



VYSOKÉ UČENÍ TECHNICKÉ V BRNĚ

BRNO UNIVERSITY OF TECHNOLOGY

FAKULTA CHEMICKÁ

FACULTY OF CHEMISTRY

ÚSTAV FYZIKÁLNÍ A SPOTŘEBNÍ CHEMIE

INSTITUTE OF PHYSICAL AND APPLIED CHEMISTRY

**PŘÍPRAVA A CHARAKTERIZACE KOMPLEXNÍCH
NANOČÁSTIC S VYUŽITÍM ZEJMÉNA FRAKCIONACE V
TOKOVÉM POLI A POKROČILÝCH
SPEKTROSKOPICKÝCH METOD**

PREPARATION AND CHARACTERIZATION OF COMPLEX NANOPARTICLES BY FIELD-FLOW
FRACTIONATION AND ADVANCED SPECTROSCOPIC METHODS

DIZERTAČNÍ PRÁCE

DOCTORAL THESIS

AUTOR PRÁCE

AUTHOR

Ing. Jan Kotouček

ŠKOLITEL

SUPERVISOR

doc. RNDr. Jaroslav Turánek, CSc., DSc.

BRNO 2020

Specification Doctoral Thesis

Department: Institute of Physical and Applied Chemistry Academic year: 2019/20
Student: **Ing. Jan Kotouček**
Study programme: Physical Chemistry
Study branch: Physical Chemistry
Head of thesis: **doc. RNDr. Jaroslav Turánek, CSc., DSc.**

Title of Doctoral Thesis:

Preparation and Characterization of Complex Nanoparticles by Field–Flow Fractionation and Advanced Spectroscopic Methods

Doctoral Thesis:

Topic: Preparation and characterization of complex nanoparticles and use of FFF for their separation and analysis

Objectives:

- 1.Preparation and characterization of nanoparticles with the use of using advanced physicochemical and spectrophotometric methods.
- 2.Surface modification on the nanoparticles with the use of bioconjugation orthogonal reactions.
- 3.Optimization and implementation of the separation techniques for nanoparticles and biopolymers.

Deadline for Doctoral Thesis delivery: 30.5.2020:

Ing. Jan Kotouček
Student

doc. RNDr. Jaroslav Turánek, CSc.,
DSc.
Head of thesis

prof. Ing. Miloslav Pekař, CSc.
Head of department

In Brno dated 1.9.2019

prof. Ing. Martin Weiter, Ph.D.
Dean

ABSTRACT

Liposomes are versatile biocompatible and biodegradable carriers for a variety of medical applications. As the first nanoparticles, they have been approved for pharmaceutical use so far, and many liposome-based preparations are in clinical trials. Classical methods of liposome preparation represent potential limitations in technology transfer from laboratory to industrial scale. New, microfluidic techniques overcome these limitations and offer new possibilities for controlled, continuous preparation of liposomal particles in a laboratory and industrial scale. An important element in the development of new nanoparticle systems is their complex characterization and purification. In addition to the established chromatographic techniques, the Field flow fractionation technique, in particular the Asymmetrical flow Field-flow fractionation, is described. This relatively new technique in conjunction with the MALS/DLS/DAD-UV/dRI online detectors enables the purification and characterization of complex samples. The main advantage of this technique lies in the possibility of separation under native conditions, which plays an important role in the separation of biopolymers in particular. Separation in the "empty" channel then eliminates sample degradation due to unwanted interactions at the stationary phase-sample interface. The theoretical part of this thesis describes the possibilities of preparation, modification, and characterization of liposomal nanoparticles. For this purpose, optical methods based on dynamic light scattering, multi-angle dynamic light scattering and nanoparticle tracking analysis techniques are described, as well as a non-optical method using "particle by the particle" analysis, tunable resistive pulse sensing method. A separate chapter of the theoretical part is dedicated to the technique Asymmetrical flow Field-flow fractionation in connection with the above-mentioned detectors. Important results associated with this work are summarized in the attached scientific paper, together with the result summaries and the author's contributions.

ABSTRAKT

Liposomy představují univerzální biokompatibilní a biodegradabilní nosiče pro celou řadu medicínských aplikací. Jako jediné z nanočástic byly doposud schváleny pro farmaceutické použití a celá řada přípravků na bázi liposomů je v klinickém testování. Klasické metody přípravy liposomů představují potenciální omezení v převádění technologie z laboratorního do průmyslového měřítko. Nové, mikrofluidní techniky tyto omezení do jisté míry překonávají a nabízejí nové možnosti kontrolované, kontinuální přípravy liposomálních částic. Důležitým prvkem při vývoji nových, nanočásticových systémů je jejich komplexní charakterizace a purifikace. Kromě ustálených chromatografických technik se dostává do popředí technika Frakcionace v tokovém v poli, a to zejména Frakcionace tokem v asymetrickém tokovém poli (Asymmetrical flow Field-flow fractionation). Tato relativně nová technika ve spojení s online detektory MALS/DLS/DAD-UV/dRI umožňuje purifikaci a charakterizaci komplexních vzorků. Hlavní výhodou této techniky spočívá v možnosti separace za nativních podmínek, což hraje důležitou roli při separaci zejména biopolymerů. Separace v „prázdném“ kanále poté eliminuje degradaci vzorku v důsledku nechtěných interakcí na rozhraní stacionární fáze. Teoretická část této práce popisuje jednak možnosti přípravy, modifikace zejména liposomálních nanočástic. Sumarizuje jejich možnosti využití a charakterizaci. K tomu účelu jsou zde popsány optické metody na bázi dynamického rozptylu světla, Multi-angle dynamic light scattering a Nanoparticle tracking analysis a také neoptická metoda využívající průchodu

částic membránou tzv. „particle by particle” metoda Tunable resistive pulse sensing. Samostatnou kapitolou teoretické části je technika Frakcionace tokem v asymetrickém tokovém poli ve spojení z výše uvedenými detektory. Důležité výsledky spojené s touto prací jsou sumarizovány v příložených vědeckých publikacích. V této práci jsou poté uvedeny krátké přehledy a autorovy přínosy k těmto příloženým publikacím.

KEYWORDS

Liposomes, microfluidic mixing, dynamic and static light scattering, asymmetrical flow field-flow fractionation, recombinant proteins.

KLÍČOVÁ SLOVA

Liposomy, mikrofluidní směšování, dynamický a statický rozptyl světla, asymetrická frakcionace v tokovém poli, rekombinantní proteiny.

KOTOUCEK, J. Příprava a charakterizace komplexních nanočástic s využitím metody frakcionace v tokovém poli a dalších pokročilých spektroskopických metod. Brno: Vysoké učení technické v Brně, Fakulta chemická, 2019. Vedoucí dizertační práce doc. RNDr. JAROSLAV TURÁNEK, CSc., DSc.

PROHLÁŠENÍ

Prohlašuji, že jsem dizertační práci vypracoval samostatně a že všechny použité literární zdroje jsem správně a úplně citoval. Dizertační práce je z hlediska obsahu majetkem Fakulty chemické VUT v Brně a může být využita ke komerčním účelům jen se souhlasem vedoucího dizertační práce a děkana FCH VUT.

.....

podpis studenta

Poděkování:

Zde bych rád poděkoval všem svým kolegům z oddělení Farmakologie a imunoterapie Výzkumného ústavu veterinárního lékařství za skvělý kolektiv. Rád bych poděkoval zejména mému vedoucímu Doc. RNDr. Jaroslav Turánek, CSc., DSc. za podporu a poskytnutí cenných rad. Dále bych zde chtěl poděkovat své rodině za oporu v náročných momentech doprovázejících studium.

CONTENT

1	INTRODUCTION.....	8
2	THEORETICAL BACKGROUND.....	10
2.1	Liposomes.....	10
2.1.1	Methods of preparation of the liposomes	11
2.1.2	Surface modification of the liposomes	13
2.1.3	Use of lipid nanoparticles and other nanoparticles of medical interest	14
2.2	Field-flow fractionation.....	17
2.2.1	Detectors	22
2.2.1.1	Light scattering detectors.....	23
2.2.2	Application of Asymmetric flow Field-flow fractionation.....	24
2.3	Offline physicochemical methods of nanoparticle characterization	27
2.3.1	Dynamic light scattering	27
2.3.1.1	Multi-angle dynamic light scattering.....	30
2.3.2	Electrophoretic light scattering.....	31
2.3.2.1	Zeta potential	32
2.3.3	NTA (Nanoparticle tracking analysis).....	34
2.3.4	Tunable Resistive Pulse Sensing	35
3	GOALS OF THE THESIS	38
4	PUBLISHED RESULTS IN THE CHRONOLOGICAL ORDER	39
5	SUBMITTED RESULTS	40
6	MANUSCRIPTS IN PREPARATION.....	40
7	COMMENTS AND AUTHOR CONTRIBUTION TO THE ENCLOSED PUBLICATIONS	41
7.1	[P1] Preparation of nanoliposomes by microfluidic mixing in herring-bone channel and the role of membrane fluidity in liposomes formation	41
7.2	[P2] Proinflammatory Effect of Carbon-Based Nanomaterials: In Vitro Study on Stimulation of Inflammasome NLRP3 via Destabilisation of Lysosomes.....	42
7.3	[P3] Targeting Human Thrombus by Liposomes Modified with Anti-Fibrin Protein Binders.....	42
7.4	[P4] N-Oxy lipid-based click chemistry for orthogonal coupling of mannan onto nanoliposomes prepared by microfluidic mixing: Synthesis of lipids, characterisation of mannan-coated nanoliposomes and in vitro stimulation of dendritic cells	43

7.5	[P5] Application of Advanced Microscopic Methods to Study the Interaction of Carboxylated Fluorescent Nanodiamonds with Membrane Structures in THP-1 Cells: Activation of Inflammasome NLRP3 as the Result of Lysosome Destabilization.....	44
7.6	[S1] Characterization and purification of the pentameric chimeric protein particles using Asymmetrical Flow Field-Flow Fractionation coupled with MALS/DLS/UV detector	44
7.7	[M1] Expression, purification and characterization of chimeric VP1-PCV2bCap protein as antigen for construction of recombinant vaccine against porcine circovirus.....	45
7.8	[M2] Sublingual allergen-specific immunotherapy delivered by nanofibre-based mucoadhesive film in a pig model.....	45
8	CONCLUSION.....	46
9	REFERENCES.....	47
9.1	LIST OF ABBREVIATIONS AND SYMBOLS	56
10	LISTED PUBLICATIONS.....	60

1 INTRODUCTION

The PhD thesis is consisting of two main topics; the first topic is focusing on preparation, modification, and characterization of nanoparticles, especially nanoliposomes. The second topic deals with the Asymmetrical flow Field-flow fractionation technique coupled with multiple detectors, such as Multi-angled light scattering detector, Dynamic light scattering detector, UV absorption, and Different refractive index detector.

Liposomes, the name of these vesicular particles, comes from the two Greek words *Lipos*, meaning Fat and *Soma*, the Body. Liposomes were first described by Dr Alec D. Bangham in 1965 and have since become a versatile, modular biodegradable and biocompatible platform for a variety of applications. The first liposome-based pharmaceutical products were launched in the late 1980s (for example, Ambisome-liposomal amphotericin). Not only liposomes but other nanoparticles as well are subject of the development of modern vaccines, drug carriers, contrast agents or in general theranostics. A prerequisite for successful clinical applications is the production of nanoparticles on an industrial scale. The introduction of new techniques, especially in the field of microfluidics, allows the transition from laboratory to industrial scale, leading to extensive research in this field. The development of microfluidics is directing towards the design of integrated microfluidic chips enabling complex, controlled preparation of nanoparticle carriers.

Modularity/surface modification of nanoparticles is another prerequisite for their successful clinical application. The surface modification affects their biodistribution and biocompatibility. The new bioconjugation reactions have been developed, including the so-called click chemistry and orthogonal bioconjugation reactions. Novel characterization and separation methods are associated with the development of the new nanoparticles. The most commonly used characterization techniques include light scattering techniques. In addition to established chromatographic techniques, a new Field-flow fractionation technique finds its place and application in various fields.

The beginning of the Field-flow fractionation technique is dated back to the year 1966 when professor Giddings first introduced the concept. Since then, multiple sub-techniques have been developed, including the most robust and hence the most used Asymmetrical flow Field-flow fractionation technique (AF4). Modern, versatility AF4 technology makes it possible to characterize a wide range of pharmaceutical substances, polymers, nanoparticles and recently found a place as a technique for quality control departments besides Size-exclusion chromatography. As a well-described theoretical technique, AF4 allows calculating the size of eluting particles based on retention time. Often, however, the AF4 is connected with light scattering detectors, both static and dynamic, concentration detectors such as UV absorption and different refractive index detector. The platform AF4-MALS/DLS/DAD-UV/dRI allow the determination of the molecular weight, concentration, conformation, and size of the individual eluting fractions.

Results within the PhD thesis had been published in a total of five published, and three prepared/submitted scientific papers. These scientific papers are presented together with a brief commentary and evaluation of the author's contribution.

The thesis Preparation and characterization of complex nanoparticles by Field-flow fractionation and advanced spectroscopic methods is constructed as a „thematically arranged set of published works and works accepted for publication according to article 42 of paragraph 1b, of The study and examination rules of Brno University of Technology.

2 THEORETICAL BACKGROUND

The theoretical background in this thesis describes the physical and chemical properties of, especially liposomes. Liposomes, as universal particles, find various applications as described in chapter 2.1.3. Besides, other types of nanoparticles, such as virus-like particles, bacterial ghost, and nanodiamonds, are briefly described in the same chapter. Chapter 2.3 describes the offline/batch methods of nanoparticle characterization, especially with the use of light scattering techniques. Furthermore, the thesis describes the characterization and separation method, Asymmetrical flow Field-flow fractionation in chapter 2.2.

2.1 Liposomes

Liposomes are typically closed bilayer vesicles composed of amphiphilic substances, most commonly phospholipids, ranging in size from about 20 nm to micrometre particles. Their self-assembly in the aquatic environment is controlled mainly by the hydrophobic effect. Phospholipid acyl chains are minimizing the interaction (the entropic disadvantage) with the surrounding aqueous phase by the organization into the bilayers and subsequent vesiculation resulting in the formation of liposomes. The structure is influenced by the geometry of individual molecules. If the polar head is larger than the non-polar acyl chain, the molecules forming structures with a large radius of curvature, micelles. If the polar and non-polar parts are comparatively large, the molecules tend to form into bilayers. Invert structures (invert hexagonal structure) are forming in the case of a smaller polar head than the acyl chain [1].

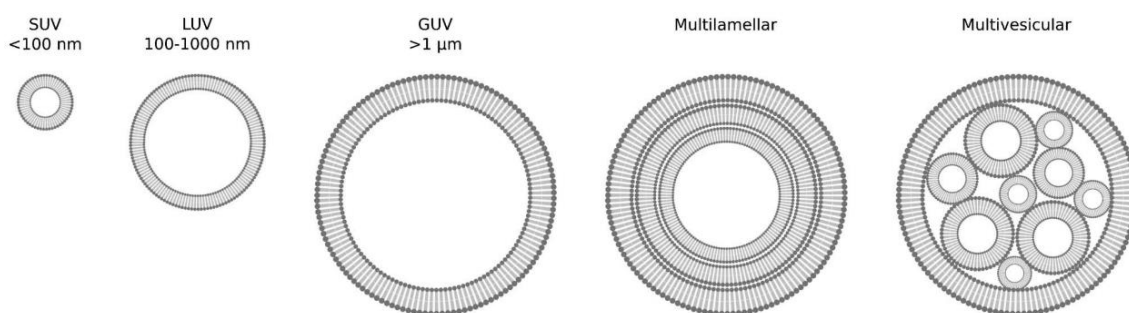


Fig. 1 – *The schematic representation of different liposomes morphologies* [2].

The lipid composition and the method of preparation determine the physicochemical properties of the liposomes (rigidity, structure, and size). By the size, liposomes can be categorized as **SUV** (small unilamellar vesicles), **LUV** (large unilamellar vesicles) and **GUV** (giant unilamellar vesicles). Another criterium is the number of lamellas. Liposomes can be categorized as multilamellar, multivesicular or multivesicular-multicentric particles. The lamellas arrangement can be concentrically or non-concentrically (see **Fig. 1**). And according to the phospholipid charge to neutral, anionic or cationic. According to their function, liposomes are conventional, stealth, ligand-targeted, long-term-release, triggered-release or as a combination of these listed properties, multi-functional (more in chapter 2.1.3) [3]. An important factor, especially in the preparation of liposomes, is the transition temperature (T_m) of the phospholipid (temperature of the transition from an ordered, rigid state to a fluid membrane). The transition temperature depends on the degree of saturation and the length of

the acyl chain. The typical range is from $-20\text{ }^{\circ}\text{C}$ for unsaturated dioleoyl to about $55\text{ }^{\circ}\text{C}$ for saturated chains of the distearoylphosphatidylcholine [1].

2.1.1 Methods of preparation of the liposomes

There are several liposome preparation methods. They can be divided into the *bulk method* (where liposomes are formed during the transfer of the lipids from dissolved organic/detergent phase into aqueous phase), and the *film method* (where the formation of the liposomes is preceded by the formation of a lipid film on a substrate and its subsequent hydration) [3].

The **Hydration of phospholipid film** is the oldest, and the most commonly used method. The phospholipid composition is dissolved in an organic solvent, for example, chloroform or chloroform/methanol mixture. The solvent is then evaporated under vacuum in a rotary evaporator. By the evaporation, a thin film/stacks of phospholipid bilayers on the glass bulb wall is formed. The film is then hydrated with a suitable buffer with stirring at a given temperature, according to the highest transition temperature of the given phospholipid. If the film "peeling" is relatively slow, the bilayer edges are allowed to merge into the multilamellar (MLV) liposomes. By increasing the rate of the film separation by application of electric field, large unilamellar vesicles are formed. This method is called **Electro-formation**, in which the lipid film is deposited on a planar electrode to which direct current is applied during subsequent hydration. Lipids interact with the aqueous buffer solution and the electric field, "peeling" the film from the electrode surface in layers to form large vesicles (GUVs) [4]. This technique requires the use of a low salt buffer, which complicates the encapsulation of active proteins, and the application of an electric field can lead to a disruption of the structure of particularly charged proteins [2]. The lipid film can be deposited into solid particles substrate, proliposomes are formed. By the **Hydration of the proliposomes**, the substrate is dissolved, and MLVs are formed [3].

Additionally, secondary methods are often needed for targeted size and homogeneity of the resulting vesicles [1,5,6]. The secondary method includes **Freezing and thawing** of the suspension to form unilamellar liposomes with a larger volume of the encapsulated aqueous phase. **Extrusion**: The liposome suspension is repeatedly pushed through the uniform cylindrical pores of the polycarbonate membrane, thereby reducing the vesicle size according to the pore size [1,7]. **Sonication**: Disruption of the MLV suspension by sonication (using sonication bath or sonication titanium probe) leads to the formation of SUVs of various sizes. For sonication baths, the suspension should be kept above the phase transition temperature. Titanium probes are capable of delivering the necessary amount of energy, but there is a risk of phospholipids degradation. Also, there is a possible sample contamination risk due to the released titanium particles [1]. **High-pressure homogenization**: During homogenization, the liposome suspension is continuously driven through the homogenizer. The suspension is divided into two streams, which then collide with the wall at high pressure (up to 138 MPa), thereby reducing the size of the vesicles. The disadvantages of this method are the above-mentioned high pressure and the necessity of relatively large volumes, depending on the design of the homogenizer [1].

Detergent Removal method is an example of bulk liposomes preparation. At first, mixed micelles of phospholipid and a suitable detergent (octyl glucoside or deoxycholate) are formed.

The detergent is then removed by dialysis, ultrafiltration, sorbents or gel chromatography. Removal converts small mixed phospholipid micelles into disc-like micelles which are fusing and finally vesiculate to form the liposomes. This process is driven by decreasing the detergent concentration and creates homogeneous SUV-LUV [6,8]. The **Evaporation of the reverse phase**: this method involves hydrating the phospholipids dissolved in an organic solvent by adding water with rapid stirring, creating a water-in-oil emulsion. The organic solvent is then evaporated, and LUV and MLV are formed [9]. The **Alcohol injection**: Lipids are dissolved in a water-miscible solvent, most commonly ethanol, then they are rapidly diluted with the aqueous phase. Rapid dilution causes precipitation and formation of the lipid bilayer fragments. The fragments subsequently vesiculate, as a result of the efforts to minimize contact of the hydrophobic chain with the hydrophilic environment. The resulting vesicle size is, in addition to the lipid composition and concentration, also determined by process parameters such as the rate of injection of the alcohol solution, the temperature of both the alcoholic and aqueous phases, and the stirring rate [10,11].

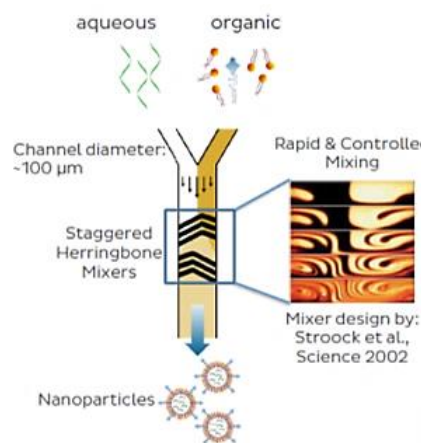


Fig. 2 – Schematic representation of microfluidic chip with detail of mixing profile herringbone structure [12].

The **Microfluidic mixing** method is an adaptation of the alcohol injection method. Rapid mixing of the lipid organic phase with the aqueous phase results in a step change of the polarity. The example of microfluidic technology is staggered herringbone micromixer (**Fig. 2**). Technology enables better control of the process parameters, which are responsible for reproducibility and quality of resulting vesicles. The process parameters are *Total Flow Rate* (TFR) and *Flow Rate Ratio* (FRR). The *Total Flow Rate* (TFR) represents the flow rate of the solution in the microfluidic channel, and the *Flow Rate Ratio* (FRR) represents the aqueous and organic phases mixing ratio. The TFR and FRR, together with the lipid concentration and lipid composition, enables the precise control of the liposomal properties such as size, and polydispersity. The principle of the liposome formation inside the microfluidic mixers, regardless of their geometry, is to reduce diffusion length and accelerate diffusion so that the mixing time (t_{mix}) is shorter than the time required to form the liposomal vesicles (t_{agg}). If the t_{mix} is smaller than the t_{agg} , liposome self-organization proceeds homogeneously [3,13,14].

2.1.2 Surface modification of the liposomes

The surface modification allows improving the functionality of the liposomes. As further described in chapter 2.1.3, rapid uptake of the plain liposomes by phagocytic cells of the reticuloendothelial system (RES) upon intravenous administration limits their clinical application. Surface modifications allow the tuning of the physicochemical properties of the liposomes for potentially more extensive therapeutic use by minimizing the fast clearance and enables specific targeting to the point of interest. These modifications are performed using various techniques such as physical adsorption, electrostatic or covalent bonding. The so-called *click-chemistry* represents a set of orthogonal biocompatible reactions with relatively high reaction rates and minimal by-products. As a concept was first introduced in 1998 by Dr Barry Sharpless: “*Click chemistry is a group of chemical reactions that must be stereospecific, modular, have a wide range with large yields and relatively harmless by-products that can be removed by non-chromatographic methods. The products of these reactions must be stable under physiological conditions*” [15].

In particular, there are four significant *click* reactions types:

Azide-alkyne cycloadditions (Huisgen cycloaddition): reactions involving primarily 1,3-dipolar cycloaddition of azides and terminal alkynes to form 1,2,3-triazoles. The reaction requires a copper Cu^{I} catalyst, usually prepared in situ by reduction of Cu^{II} ($\text{CuSO}_4 \cdot 5\text{H}_2\text{O}$) with sodium ascorbate. The reaction proceeds under standard laboratory conditions (without the need for temperature elevation due to the Cu^{I} catalyst) and over a wide pH range of 4 to 12 [15].

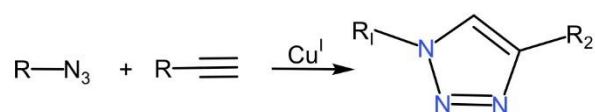


Fig. 3 – Huisgen 1,3-dipolar cycloaddition of azides and terminal alkynes.

Nucleophilic ring-openings: a group of reactions including heterocyclic electrophiles such as aziridines, epoxides or cyclic sulfates.

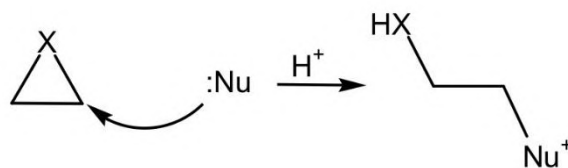


Fig. 4 – Nucleophilic ring-opening reaction, $X=\text{O}$, NR , ^+SR , $^+\text{NR}_2$.

Carbonyl reactions (Non-aldol reactions): include urea, thiourea, hydrazones, oxime ethers, amides, aromatic heterocycles.

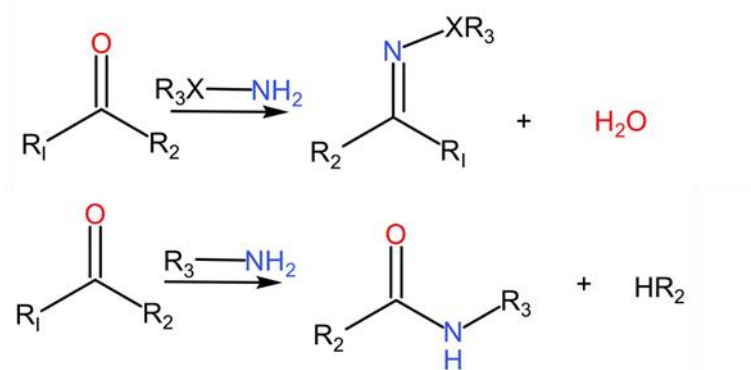


Fig. 5 – Hydrazone/oxime ether formation, X= O, NR (top), Amine/isourea formation (bottom).

Double or triple bond addition: reactions including for example epoxidation, aziridation, or Michael reactions.

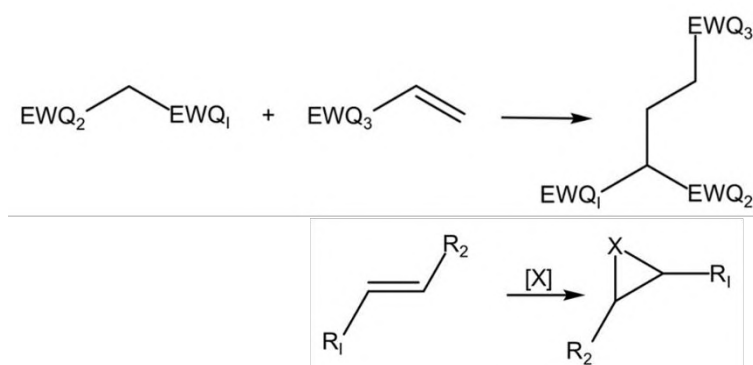


Fig. 6 – The top reaction represents certain Michael additions where EWG stands for Electron Withdrawing Group such as halogens (F, Cl), carbonyl group (RCOR) or nitro group (NO₂). The bottom reaction leads to the formation of various by-products, X=O, NR, ⁺SR, ⁺NR₂.

2.1.3 Use of lipid nanoparticles and other nanoparticles of medical interest

As was mentioned above, liposomes are biodegradable, and biocompatible vesicles that have been firstly described in 1965 by Alec Bangham [16]. Since then, liposomes found various applications in the field of drug delivery systems, gene therapy and diagnostic. The first pharmaceutical preparations based on liposome technology were launched in the late 1980s (Ambisome-liposomal amphotericin) and several other liposomal cytostatic, antibiotics and dermatological products were commercially available or in clinical trials (Doxil®/Caelyx® (doxorubicin) and DaunoXome® (daunorubicin)) [17,18].

Their unique structure enables the encapsulation of both hydrophobic compounds (located into the lipid bilayers), and hydrophilic compounds (entrapped in the aqueous centre) [18]. Encapsulation has several advantages such as increased of efficacy and increased of the therapeutic index (the comparison of the amount of a drug that causes the therapeutic effect to the amount that causes toxicity [19]). Further, encapsulation reducing potential obstacles with cellular uptake, increased stability and solubility of the drug and last but not least, with surface modification, active drug targeting can be achieved [20,21]. The design and surface functionalization of the liposomes can be generalized into several groups/generations (**Fig. 7**).

The 1st generation or *Conventional liposomes* are plain liposomes made from phospholipid bilayers. Such liposomes, as shown in **Fig. 7 A** serve as basic carriers, but their use *in vivo* encounters several obstacles. One of them is the insufficient retention of the substances inside the vesicles [22]. Incorporation of cholesterol into the bilayer, the fluidity of the membrane can be tuned. The lower fluid of the bilayers reducing the potential leakage of an encapsulate compound from the vesicles [23]. Also, it has been demonstrated that the liposomes formed from phospholipids with a higher transition temperature (in general with saturated acyl chains phospholipid) are more stable upon the intravenous administration compares to the liposomes formed from unsaturated phospholipids [24]. Another obstacle is relative short circulation time upon intravenous administration. The reason is the uptake of vesicles by phagocytic cells of the reticuloendothelial system (RES), which reduces their distribution potential. Long-term circulation is required for *Passive targeting*. One of the driving elements of passive targeting is the size and charge of the liposomes. Charged and relatively large liposomal particles are more captured by the RES than small neutral liposomes (especially positively charged liposomes due to the toxicity, are removed with priority) [25,26]. Nanoparticles with a diameter below 100 nm will passively target liver tissue [27]. Nanoparticles in the range of 40 to 200 nm will accumulate in tumour tissue due to the so-called EPR effect (Enhanced permeability and retention) [28,29]. Larger particles then accumulate more frequently in the lung tissue [30]. Fast clearance is desirable if the target site is especially the liver and spleen. There are commercially available or in clinical trials, some formulation categorized as the Conventional liposomes such as Ambisome® (antifungal amphotericin B), Myocet® (anticancer agent doxorubicin), and Daunoxome® (anticancer agent daunorubicin) [31]. For the increasing of the circulation time, liposomes can be coated with a polymer, i.e., polyethene glycol (PEG), which increasing repulsive forces between liposomes and serum components (which promotes opsonization). Such surface-modified liposomes have been termed as PEGylated or in general *Stealth liposomes* **Fig. 7 B**. The presence of the polymer on the surface, improving the colloidal stability of the vesicles. The modification of the surface can be performed by absorption of the polymer, by the covalent bond of the polymer with a reactive group on phospholipid molecule after the liposome formulation or by incorporation of the PEG-lipid conjugate into the lipid bilayer (for example DSPE-PEG (1,2-distearoylphosphatidylethanolamine(polyethene glycol))) [31]. The first product with the concept of PEG-liposomes was Doxil®/Caelyx® [32]. There are other polymers which can be used as potential protective layers such as polyvinyl pyrrolidone (PVP), synthetic poly-amino acid (PAA) polymers, poly(2-ethyl-2-oxazoline) and poly(2-methyl-2-oxazoline) polymers [31,33].

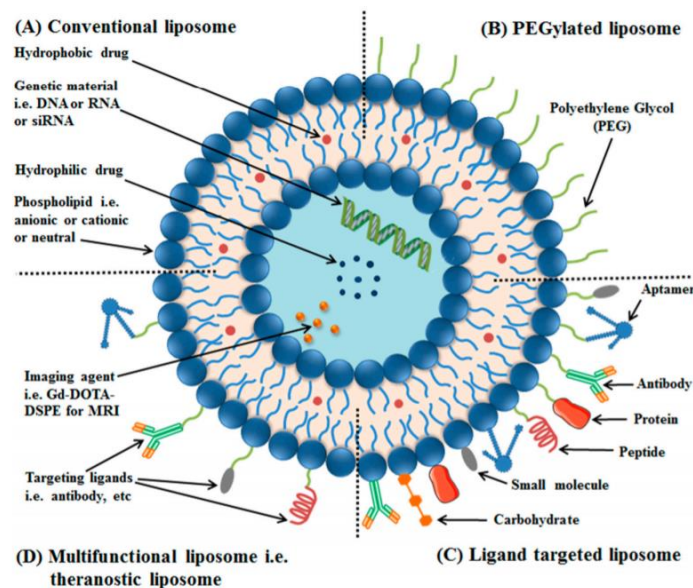


Fig. 7 – Schema of individual types of liposomes based on surface modification: A) Conventional, plain liposomes; B) PEGylated, Stealth liposomes; C) Ligand targeted liposomes; D) Theranostic liposomes [34].

Another functionalization of the surface of the liposomes promotes **Active targeting**. Active targeting involves the introduction of functional elements such as antigens or fragments, peptides or proteins. The introduction of a given ligand on a liposomal particle allows specific binding to the respective receptors on the surface of target cells [35]. Such modified liposomes are collectively referred to as *Ligand targeted liposomes* (**Fig. 7 C**). Liposomes combining both a suitable surface modification, an active compound, and a suitable imaging contrast agent are collectively referred to as *Theranostic liposomes* (**Fig. 7 D**) [34]. Besides nanoliposomes, there are additional nanoparticles with the potential clinical application such as:

Virus-like particles (VLP) are a group of particles that includes a variety of structures from empty viral particles without nucleic acids, non-infectious viruses or recombinant, structural viral proteins resulting from expression in host systems self-assembled into particles. By their structure, VLP can stimulate both non-specific and an adaptive immune response [36]. According to their structure, they can be distinguished into non-enveloped VLP, which are further distinguished according to the layers of the protein envelope - capsids, into one or more capsid VLP. Another type of particles is VLP with lipid membrane expression cells (Enveloped VLPs). Single-capsid VLP can be produced from both prokaryotic and eukaryotic cells or only by self-assembly of the synthesized proteins. Multiple capsids VLP already require higher eukaryotic host cells that allow co-expression of various capsid proteins and complex VLP assembly in the cell. Yeast, plant cells or insect cells are used as expression organisms. Novel antigens are located on the surface of VLP either by molecular fusion or by chemical conjugation [36–38].

Nanodiamonds with polyhedra geometry are belonging to a group of carbon-based particles (in addition to nanodiamonds, fullerenes, carbon nanotubes or graphene particles) [39]. They can be divided base on size into nanocrystalline (up to 100 nm) and ultrananocrystalline (below 10 nm). Their fluorescence properties, especially in the near-infrared (NIR) region, arising from

defects in the crystal grid, nitrogen-vacancy (NV). The intensity of the fluorescence depends on the number of NVs and hence the size of nanodiamonds [40]. Nanodiamonds show relatively low toxicity [41–43]. There are several possibilities for preparing fluorescent nanodiamonds. DNDs (detonation NDs): Nanodiamonds are prepared by controlled detonation (for example detonation of hexogen). The resulting soot contains clusters of nanoparticles about 4 nm in diameter, which is then released by milling and disintegration by ultrasound. CVD (chemical vapour deposition): Nanodiamonds are produced by gas-phase deposition in the form of nanocrystalline films. HPHT (high-pressure, high temperature): Nanodiamonds are formed from larger crystals growing at high pressure (up to 5 GPa) and temperature (above 1400 °C), the crystals are then crushed. Fluorescence properties are induced by irradiating the particles with a high energy beam at high temperatures, thereby migrating vacancies in the crystalline grids to the nitrogen atom and forming a stable NV conjugate [40,42]. Colloidal stability is required for biological application. Especially esters, amides, hydroxyls and silane groups are introduced by the surface treatment of ND, allowing further modification, for example, with polymers [44] or proteins [45]. Such modified NDs are sterically stable.

Bacterial ghosts represent an empty, non-living envelope of Gram-negative bacteria. The morphology of the inner and outer membrane is similar to the native cell. The envelope contains membrane proteins, lipopolysaccharides and peptidoglycans. The preparation of bacterial ghosts can be performed by both genetic and chemical way. The genetic approach involves a control expression of the gene *E*, which causes the fusion of outer and inner cell membrane. The fusion creates a gap which causes cytoplasmic secretion. The limitation of the genetic approach is with the use only of the Gram-negative bacteria [46]. The chemical approach involves the use of suitable chemicals (for example sodium hydroxide or surfactants like sodium dodecyl sulfate or tween 80), optimization of the concentration, and physical parameters (such as temperature or stirring) but maintaining the same preparation concept. The chemical approach enables preparation of bacterial ghost from Gram-positive bacterial [47]. The particles themselves serve as self-adjuvants, the native cell membrane structure is recognized and taken up by immune cells and induce a humoral and cellular immune response. Besides self adjuvants properties, the bacterial ghost can serve as delivery vehicles for anti-cancer drugs, pesticides and additional foreign antigens [48].

2.2 Field-flow fractionation

The *Field-flow fractionation* (FFF) is the separation one phase chromatography technique; the concept of Field-flow fractionation was first introduced in 1966 by prof. Giddings [49]. Since then, the technique has evolved into several sub-techniques like Thermal (ThFFF), Gravitation or Sedimentation (GrFFF), Magnetic (MgFFF), Electric (EFF) and Flow-field (FIFFF) [50]. The instrumentally most developed and universal is the FIFFF sub-technique called *Asymmetric flow Field-flow fractionation* (AF4) [51–53]. In general, the separation is carried in the narrow, empty channel in which the carrier liquid is pumped with an established laminar, parabolic flow profile, called a *channel* or *detector flow*. Detector flow carries the analyte from inlet to outlet with different velocity base on the different displacement of the sample due to an external force. The velocity of the detector flow, $v(x)$, is a function of the distance from the accumulation wall of the channel x [54]:

$$v(x) = 6\langle v \rangle \left(\frac{x}{w} - \frac{x^2}{w^2} \right) \quad (1)$$

where the w is a thickness of the channel and $\langle v \rangle$ is the average liquid velocity in the cross-section along the channel axis (cm/s). Equation (1) assuming zero velocity at the bottom of the accumulation wall (in the distance $x = 0$) and that the flow profile is constant along the channel separation axis. The external force, based on different sub-techniques, is applied perpendicularly to the detector flow and forcing the analyte against the accumulation wall. The separation force in the Asymmetric flow Field-flow fractionation is a perpendicular hydrodynamic field called *cross-flow*. Perpendicular cross-flow is formed by the passage of the carried liquid through a semipermeable bottom channel wall. The accumulation wall allows only carrier liquid to pass, which created the grading pushing the sample towards the accumulation wall. The cross-flow velocity is given by equation as a function of the distance from the accumulation wall [54]:

$$u(x) = u_0 \left(1 - \frac{3x^2}{w^2} + \frac{2x^3}{w^3} \right) \quad (2)$$

where u_0 (cm/s) is the cross-flow velocity at the accumulation wall (equal to zero at the upper channel wall and increasing towards the bottom wall of the channel). The diffusion drives the sample away from the accumulation wall until the equilibrium between the external force, cross-flow, and diffusion is reached. Equilibrium results in a different displacement of the sample according to the hydrodynamic differences. The higher the sample's coefficient is, the greater is a distance from the accumulation wall resulting in higher velocity along the channel axis when the detector flow is applied. The concentration profile of the sample in equilibrium is given by equation (3):

$$c(x) = c_0 e^{\left(\frac{-x}{l}\right)} \quad (3)$$

where c_0 is the concentration at the accumulation wall, and l is the distance of the centre of the sample layer from the accumulation wall and is given by the equation:

$$l = \frac{D}{u_0} \quad (4)$$

where D is the diffusion coefficient of the sample. The parameter l is dependent on the channel thickness w . The retention parameter λ expresses the distance of the sample layer relative to the channel thickness:

$$\lambda = \frac{l}{w} \quad (5)$$

The velocity is given in the volumetric flow (ml/min) [54]:

$$u_0 = \frac{V_c}{bL} \quad (6)$$

$$\langle v \rangle = \frac{V_{in}}{bw} \quad (7)$$

$$V_0 = bLw \quad (8)$$

where V_c and V_{in} are the volumes of the cross and inlet flow, respectively, L and b are the length and width of the channel and w is a thickness of the channel [53]. The equation (5) can be extended to:

$$\lambda = \frac{DbL}{wV_c} \quad (9)$$

A distance of the sample from the accumulation wall depends on the diffusion coefficient, the dimension of the channel and the cross-flow rate. The parameter describing the elution velocity v of the sample with a given diffusion coefficient in the average detector flow velocity $\langle v \rangle$ is called the *Retention ratio* [53]:

$$R = \frac{v}{\langle v \rangle} \quad (10)$$

The simplified relation between the Retention factor and Retention ratio is given by equation (11):

$$R = 6\lambda \quad (11)$$

The elution of the sample in order of increasing hydrodynamic radius it's *normal elution* mode, and it's valid for equation (11). Normal elution mode is applied to a size of approximately 1 μm . Separation up to 1 μm is a *steric elution* and its carried in a reverse elution order [55]. For the steric elution, the equation (11) is extended by the dimensionless steric correction parameter γ and by the diameter of the particles d [53,56]:

$$R = 6\lambda + 3\frac{\gamma d}{w} \quad (12)$$

Retention ratio can also be expressed as the equation (13):

$$R = \frac{t_0}{t_R} \quad (13)$$

there the t_0 is the void time (time of the imaginary sample which is not retained in the channel), and t_R is the time of the separated sample, called *retention time*. By the AF4 theory, the retention time can be expressed as:

$$t_R = \frac{w^2}{6D} \ln \left(1 + \frac{V_c}{V} \right) \quad (14)$$

where w is the channel thickness, D is the diffusion coefficient of the sample, V_c and V are the cross-flow and detector flow rates, respectively. From equation (14), the diffusion coefficient of the sample can be calculated, knowing the channel parameter and retention time. The diffusion coefficient is related to the hydrodynamic size R_h of the sample by the Stokes-Einstein equations (24), the equation (14) can be then extended as [53,56]:

$$t_R = \frac{w^2 \pi \eta R_h}{kT} \ln \left(1 + \frac{V_c}{V} \right) \quad (15)$$

where T is the thermodynamic temperature, η is the viscosity of the mobile phase, and k is the Boltzmann's constant.

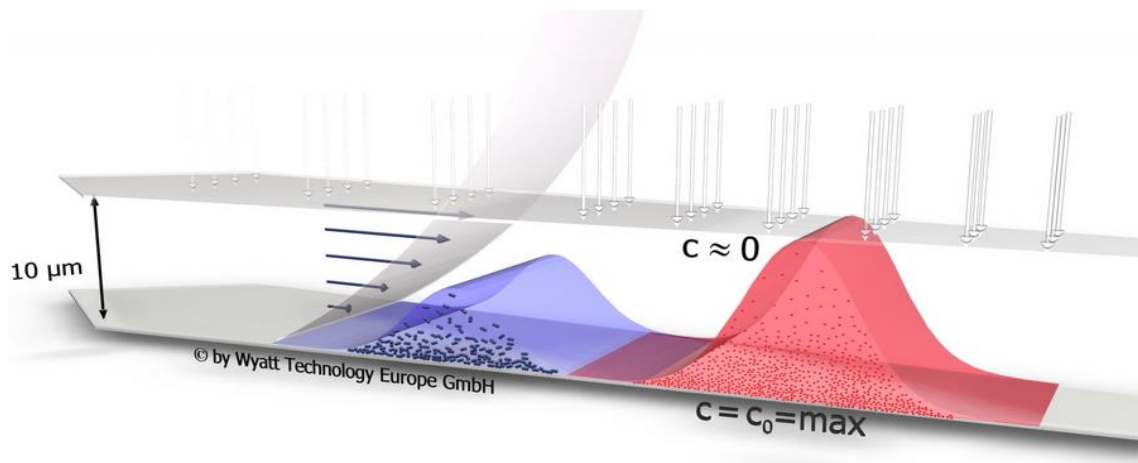


Fig. 8 – The scheme of the AF4 channel with the parabolic longitudinal flow, analyte distribution is given by equilibrium between the cross-flow and the diffusion (© Wyatt Technology Corporation).

As mentioned above, the AF4 separation is carried in an empty channel. The channel is usually formed by an upper and a lower part, between which a trapezoidal moulding and membrane are placed (**Fig. 9**). The moulding is called spacer with a given thickness (typically between 190 to 490 μm) which gives the channel thickness. The membrane (polyethene sulfonate or cellulose) with the specific cut of (5 to 30 kDa) together with the bottom support frit is responsible for the semi-permeability of the channel.

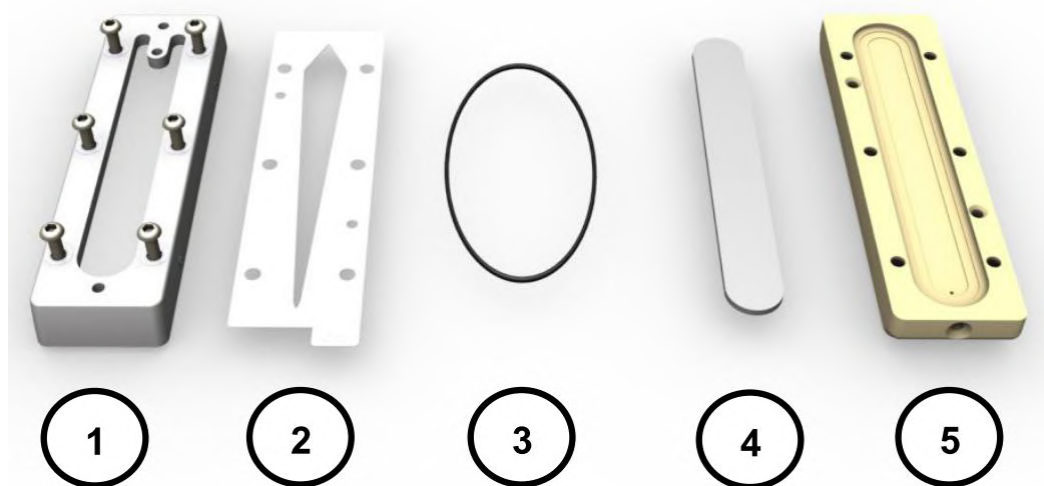


Fig. 9 – Different parts of the AF4 standard channel: 1) represents the upper part; 2) is the spacer; 3) is the sealing O-ring; 4) is the porous frit and 5) is the bottom part of the channel (© Wyatt Technology Corporation).

The separation by AF4 in the standard channel involves primarily three phases. *Injection* of the sample followed by the *focusing and relaxation* and the *elution* itself. During focusing, the mobile phase is pumped through the inlet and outlet port at the same time in a given ratio. The ratio is adjusted in a way that enables the sample to be focused on a specific focus distance from

the original sample injection site. The focusing position is given by the channel and can be adjusted by the ratio of input and output flow according to equation [53]:

$$z_f = L \frac{V_{in,f}}{V_{in,f} + V_{out,f}} \quad (16)$$

where the z_f is a focus position, L is the length of the channel, $V_{in,f}$ and $V_{out,f}$ are flow rates of the inlet and outlet ports. Equation (15), which applies when the elution starts directly from the channel inlet, can be then extended as:

$$t_R = \frac{w^2 \pi \eta R_h}{kT} \ln \left(\frac{\frac{z_f}{L} - \frac{V_{in}}{V_c}}{1 - \frac{V_{in}}{V_c}} \right) \quad (17)$$

Beside the “standard” AF4 channel, there are other types of Flow filed Filed-flow fractionation channels that differ in the geometry of the separation channel and the configuration of the channel flow and cross-flow. In this thesis, the *Frit Inlet channel* (FIAF4) and the *Hollow fibre channel* (HF5) are mentioned.

The *Frit-Inlet AF4 channel* (**Fig. 10**): The separation itself is preceded by the focusing phase, where the sample is focused near the accumulation wall of the channel to establish equilibrium between the cross-flow and diffusion of the analyte. Insufficient focusing will result in high band broadening. Although one of the advantages of the FFF technique is the absence of a stationary phase, the analyte may interact with the membrane at the bottom of the accumulation wall [57]. It has also been reported that the focusing phase can cause sample aggregation [58,59]. The separation process in FIAF4 is carried out without interruption of the longitudinal flow (detector flow) and the need for a focusing phase. Hydrodynamic relaxation is achieved by injecting the sample at a relatively low flow rate. At the same time, the mobile phase is driven through the inlet frit, whereby the analyte components are carried into the channel. The result is a continuous relaxation of the sample in the region of the inlet frit. After the sample injection, the equilibrium is established, and the analyte is eluting according to the standard AF4 principle. The absence of the focusing phase can be particularly useful for samples susceptible to aggregation [57,60], Another advantage is a relative reduction in the analyte separation time and a reduction in sudden pressure increase caused by the change of the focusing phase to the elution phase [60].

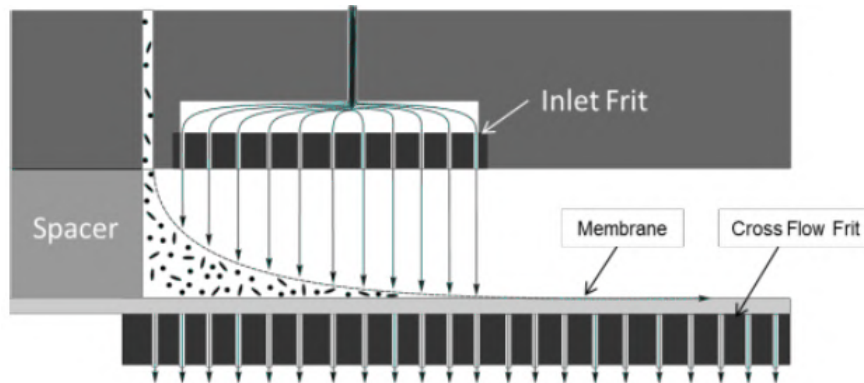


Fig. 10 – The schematic representation of the Frit-Inlet AF4 channel [60].

Another alternative to the classical separation channel is the use of the *Hollow Fibre channel*. The HF5 uses an entirely different, cylindrical, geometry (**Fig. 11**) based on a polymer or ceramic hollow fibres with porous walls. The permeability of the walls forms the radial flow (cross-flow); the remaining volume creates the detector flow. The separation is carried by the same mechanism as the classical AF4 elution, according to the hydrodynamic differences. The HF5 has smaller void volume compared to the conventional channel; less analyte is needed for sufficient separation due to a relatively low dilution. The channel is designed to be disposable, sterile and applicable to one sample type, reducing the risk of cross-contamination [61].

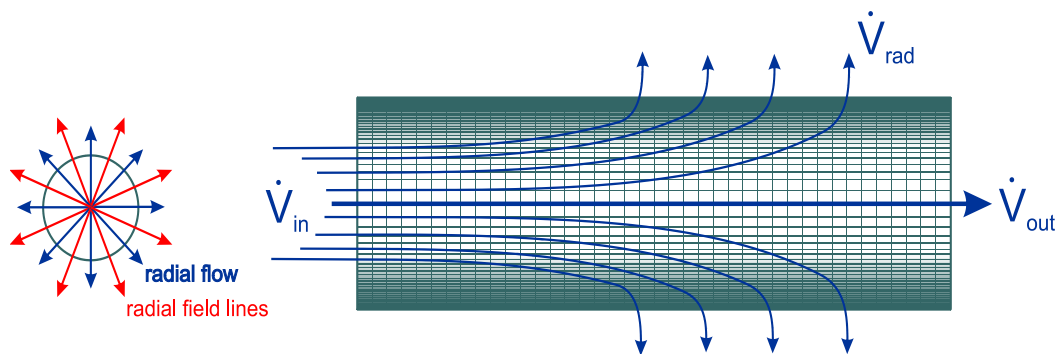


Fig. 11 – The schematic representation of the HF4 channel, V_{in} is the total flow that is divided into V_{rad} forming cross-flow and V_{out} forming flow detector (© Wyatt Technology Corporation).

2.2.1 Detectors

The separation is followed by the detection of individual fractions eluting from the separation channel. Several detectors are used to monitor the eluting analyte in the mobile phase. The most common detectors in conjunction with FFF (or with SEC) are concentration sensitive detectors, the UV-VIS and RI (refractive index) detectors, whose signal is proportional to the concentration in the elution volume. Fluorescence detector, measuring emission and excitation properties of the analyte. Next in line is the light-scattering detector. Where the signal is proportional to the molecular weight and eluate concentration. The **UV-VIS detector** can be used for the detection of the compounds with, for example, double bond, conjugated double bond, aromatic ring or carbonyl function group. The detector measures the absorbance A which is defined by Lambert-Beer law as [53]:

$$A = \log\left(\frac{I_0}{I}\right) = \varepsilon c L \quad (18)$$

where the I_0 and I represent the intensities of primary and transmitted light, respectively. The absorbance is related to the length of the measuring cell L , the concentration c and the absorption/extinction coefficient ε [53,62]. The **RI detector** is a universal detector for analyte with a non-zero increment of the refractive index dn/dc . In general, the sensitivity of the RI detector can be lower, compared to the UV detector, especially for highly absorbing analytes. But can be used for the detection of non-absorbing compounds. The measurement itself takes place in a cell that is divided into two compartments, sample, and referent (**Fig. 12**).

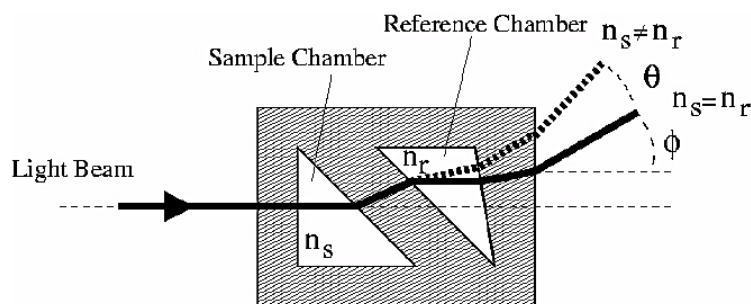


Fig. 12 – Diagram of the Optilab T-rEX™ Flow Cell Flow (© Wyatt Technology Corporation).

If the refractive index n_s (sample) and n_r (reference liquids) are identical, then the light beam emits from the cell in a direction parallel to the incoming beam. If n_s differs from n_r , the light beam emits from the cell at an angle θ . The angle is proportional to the difference in refractive index between n_s and n_r , i.e. the *differential refractive index* (dRI). With the known value of the dn/dc , eluate concentration can be determined. The reference cell has one chamfered edge. The chamfer additionally deforms the light beam at an angle ϕ . The angle ϕ depends on the skew angle and the difference between the refractive index between the reference fluid and the quartz cell. If the sample is present in both the reference cell and the sample cell, the refractive index difference is zero, and any angular distortion of the light beam is only due to the *absolute refractive index* (aRI) [53,63].

2.2.1.1 Light scattering detectors

Light scattering can be divided in particular into two types: **Dynamic light scattering** (or Quasi-Elastic Light Scattering, i.e. QELS) discussed in Chapter 2.3.1, and **Static light scattering**. Type of the static light scattering detector is a *Multi-angle light scattering detector* (MALS) where the intensity of scattered light is detected from several detection angles. The information from scattering analyte in angular or concentration dependence can be used for the determination of molar mass; size expressed as the radius of gyration and second virial coefficient [53,64]. The dependence of the intensity of scattered light on the characteristics of the sample is shown as:

$$\frac{K^*c}{R(\theta)} = \frac{1}{MP(\theta)} + 2A_2c \quad (19)$$

where c is the analyte concentration, M the molecular weight A_2 the second virial coefficient, K^* is the optical constant, $P(\theta)$ the scattering function of the particles and $R(\theta)$ is the excess Rayleigh ratio. The excess Rayleigh ratio expresses the scattered light intensity of the analyte (by subtracting the scattered light intensity of the solvent, $I_{\theta, \text{solvent}}$ from the scattered light intensity of the eluate I_{θ}) [53]:

$$R_{\theta} = \frac{(I_{\theta} - I_{\theta, \text{solvent}})r^2}{I_0V} \quad (20)$$

where I_0 is the intensity of the primary light, V is the scattering volume, r is the distance between scattering volume and detector. The Rayleigh ratio is independent of the intensity of the primary light and on the geometry of the measuring cell. The optical constant in equation (19) is defined as:

$$K = \frac{4\pi^2 n_0^2}{\lambda_0^4 N_A} \left(\frac{dn}{dc} \right)^2 \quad (21)$$

where n_0 is the refractive index of the solvent at a given laser wavelength λ_0 , N_A is the Avogadro constant, and dn/dc represents the refractive index change with the concentration of the so-called refractive index increment [53]. The particle scattering function describes the decrease of the intensity of the scattered light with increasing detection angle due to the interference of the light coming from different parts of the same particle. Scattered light from different parts will destructively interfere, and intensity will be lower compared to the individual light beams. Approximation for small angles is given as:

$$\lim_{\theta \rightarrow 0} P(\theta) = 1 - \frac{16\pi^2 n_0^2}{3\lambda_0^2} \sin^2\left(\frac{\theta}{2}\right) \langle R_g^2 \rangle \quad (22)$$

where λ_0 is a wavelength of the incident light in a solvent with a refractive index of n_0 . The $\sqrt{Kc/R(\theta)}$ can be plotted against $\sin^2(\theta/2)$, the abscissa is constructed, and from the slope, the R_g can be determined [53,65].

2.2.2 Application of Asymmetric flow Field-flow fractionation

How was mentioned in chapter 2.2, Asymmetric flow Field-flow fractionation is one of the universal separation techniques, which has recently found application in a wide range of sectors including nano/biotechnology, pharmacy, and medicine [66,67]. The recent application shows the AF4 as a reliable technique for the quantitation and characterisation of viruses during the process of vaccine development [68–70]. Another application of AF4 is in the field of the development and scale-up of the gene delivery vehicles based on virus-like particles (VLP) [71,72]. The AF4 technique enables whole lysate purification. In the study of Lampi M. et al. (2018) the infection enveloped virus (bacteriophage $\Phi 6$) were purified with 2–3-fold higher purity compared to the common purification method such as precipitation and ultracentrifugation. The study also shows that the membrane (at the bottom of the AF4 channel) cut-off enables the flow-through of small components which reduced the impurities content with high recoveries of infectious viruses [73]. There are previous studies that indicated that the regenerated cellulose membrane could be applied for different viruses with different biophysical properties with high mass recovery [73–75].

In addition to the above studies, the AF4 technique is used for the characterization of liposomal nanoparticles. Separation conditions and their effect on liposomal retention characteristics are elaborated by S. Hupfeld et al. (2009). The change in analyte retention time with an increased amount of injected sample is described as an over-loading effect. At high concentrations, the analyte is not sufficiently equilibrated at the bottom of the accumulation wall during the focusing phase, and a part of the sample is in the higher layer, which, due to the parabolic profile, elutes at a higher rate. The over-loading effect is particularly evident in monodisperse analytes both for liposomes [59] and for standards polystyrene particles as well [76]. Another parameter affecting retention characteristics is the nature of the mobile phase. In S. Hupfeld's study, the effect of the ionic strength of NaNO_3 on neutral liposomal particles (1,2-dioleoyl-sn-glycero-3-ethylphosphocholine, EPC) was assessed. At low ionic strengths, repulsive interactions between particles and the channel's accumulation wall predominate. The liposome particles do not reach equilibrium at the correct height above the accumulation wall and elute

earlier than might be expected according to the FFF theory [59]. Similarly, negatively charged liposomes in Tris buffer or PBS (phosphate buffer saline) with different ionic strength, were studied. The retention times in the mobile phase of low and high ionic strength (8–160 mM) both deviated from FFF theory. The optimal concentration is about 16 mM salt [77,78]. The AF4 separation technique is most often followed by a MALS detector (2.2.1). The light scattering detector record is then a series of individual points, for each point the Rayleigh ratio, relative to each angle is recorded. Since the sample is diluted during fractionation, the second virial coefficient A_2 can be neglected in equation (19). For the molecular weight and particle size, the resulting angular dependence is interleaved by different models according to the character of the analysed sample. The Zimm model is generally used for small particles below 100 nm. The Zimm model is also linear for high molecular weights, with the ratio $(K \cdot c \cdot R(\theta)^{-1})$ plotted on the y-axis. The Berry model $(K^{0.5} \cdot c^{0.5} \cdot R(\theta)^{-0.5})$ is generally applicable for particles above 100 nm and is universal for diverse conformations of polymers of different molecular weights, unlike Zimm model it is also suitable to determine the conformation of the polymer. The Debye model $(K^{-1} \cdot c^{-1} \cdot R(\theta))$ generally requires a higher polynomial degree with increasing molecular weight and is more suitable for larger particles (size above 100 nm) [53]. An alternative to the above-mentioned models is a “shape-dependent model” that uses a theoretical model of the angular dependence of light scattering according to particle shape, *random coil*, *sphere*, *coated sphere*, or *rod structure*. In his work, S. Hupfeld assessed, among other things, the influence of individual models on the resulting characteristics of liposomes of different sizes. By comparing the results of DLS measurements and electron microscopy, the *coated sphere* appears to be a suitable model for liposomal particles [79].

Although the AF4 is one phase separation technique with no packing material and thus no sample-stationary phase interaction, possibly leading to the degradation and losses of the sample. On the bottom of the separation channel polyethersulfone (PES) or regenerated cellulose (RC), the membrane is present. The membrane can be responsible for lower sample mass recovery. Study of Jochem A. et al. describes the mechanism of sample-membrane interaction on gold nanoparticles with different PEG polymer coating. In general, the polymer coating preventing degradation of the nanoparticles, also electrostatic repulsion prevents adsorption of the charged PEGylated particles on the membrane at the low ionic strength. With increasing ionic strength, the repulsion is weaker, and the particles are in closer distance from the accumulation wall. Increased ionic strength has an additional effect; the PEG chain length is increased as well. At sufficient ionic strength, the particles are in the close distance, and the polymer can bridge the remaining gap between particle and membrane, resulting in so-called bridging adsorption. The bridge adsorption also explains why the longer PEG does not increase the mass recoveries. Adsorption was particularly evident in the case of 5 and 10 kDa PEG at an ionic strength of 5 mM [80]. Interaction of the gold nanoparticles (AuNP) with the membrane is investigated in the work of Saenmuangchin R. et al. In the study, the strong, attractive interaction between the particle and hydrophobic PES membrane was observed with the surfactant mobile phase modification (0.05% sodium dodecyl sulphate, SDS). Based on the results, the author evaluates the ideal mobile phase of de-ionized water (in case of PEGylated AuNP) [81]. The selection of the molecular weight of the PEG has an impact on the separation behaviour. The effect was presented in the study of Hansen M. et al., where the four types of

PEG (2, 5, 10 and 20 kDa) were investigated under ideal separation conditions without the stabilizing surfactants in the mobile phase. The study shows that the PEG orientation is not responsible for the differences in retention time, which were observed in the 10 and 20 kDa PEGylated AuNP but the coating density is. With higher molecular weight, the PEG density is lower; thus, the particle behaves as smaller and eluting earlier compared to the 2 and 5 kDa PEGylated AuNP under define separation conditions [82].

Other types of particles that can be effectively separate and characterized using AF4 are exosomes. These small extracellular vesicles participate in the process of the cancer metastasis. In the work of Petersen K. et al., exosomes from aggressive melanoma cells were fractionated using AF4 coupled with MALS/DLS/UV detectors under native condition using PBS as a mobile phase. The study proves that the AF4 can separate exosomes by different subtypes without using specific affinity tags. Their study suggests the possibility of AF4 for the separation of large quantities of exosomes for diagnostic and therapeutic applications in the field of cancer treatment [83]. The Field-flow fractionation is capable of the separation of whole bacteria cells. Lee H. et al. used the FFF technique as a precursor to MALDI-MS analysis of the intact bacteria cell (*P. putida* and *E. coli*). The submicrometric-sized cells are separate according to the so-called **hyperlayer mechanism**, in addition to the elution modes described in chapter 2.2 (normal and steric elution mode). During the hyperlayer elution mode, the high channel flow generates a hydrodynamic lift force that drifts the sample from the bottom accumulation wall. The established equilibrium between lift forces and the cross-flow is then decisive for the distance of the sample from the accumulation wall of the channel. Larger particles with greater lift forces elute earlier than the smaller ones. The separation, according to the hyperlayer elution mode, provides high-resolution in relatively short elution times. Fractions in different elution times contained non-degraded bacteria of different sizes due to the different growth stages [84]. The A4F technique enables separation of proteins or in general, biopolymers under native conditions while the original conformation remains unchanged. In the study of Dou H. et al., the usage of AF4 coupled with MALS/DLS and UV detector on the characterization of the egg yolk plasma under the native condition were demonstrated. The use of programmed separation force, cross-flow enables separation of a sample with broad size distribution in reducing separation time. The combination of MALS and DLS online detector can be used for conformation determination of the low-density lipoprotein (LDL) and aggregates base on the ratio of the radius of gyration to the hydrodynamic radius (R_g/R_h) [85]. In general, the R_g/R_h ratios provide information about the conformations of the sample (see **Table 1**).

Table 1 – R_g/R_h ratios values and resulting conformations.

R_g/R_h	Conformation
< 0.7	A highly expanded macromolecule or swollen microgel structure [86]
0.778	Hard sphere [87]
0.998	Soft sphere [88]
1.0–1.5	Branched molecule [89]
1.5–2.1	Random coil [90]
> 2	Rod like structure [91]

With the increasing use of proteins in clinical applications, the need to control qualitative and quantitative properties is needed. Well established Size Exclusion Chromatography (SEC) technique is commonly used for the separation of proteins. But the loading of SEC columns and thus the shear force generated during separation can easily lead to disruption of the complex protein structure, especially proteins with higher molecular weight. Besides, limited size range does not enable high resolutions of large soluble aggregates. AF4 is a complementary technique to SEC for analysis of biopolymers, proteins, nanoparticles and whole cells [92].

2.3 Offline physicochemical methods of nanoparticle characterization

2.3.1 Dynamic light scattering

The dynamic light scattering correlates Brown's motion with the hydrodynamic size of the particles. Brownian motion is a random particle motion caused by the thermal movement of a solvent that collides with the particles of the analyte. The scattered radiation at a certain time by different particles shows a phase shift, and the individual rays interact with each other. The interaction can be positive or negative, depending on the relative position of the particles. Over a given time, the particle changes its position precisely due to Brown's motion, small particles being more affected by this motion than the large particles. As the relative position of the particles changes, the phase shift and thus the total intensity of the scattered light fluctuates. The intensity fluctuation correlates with particle velocity. For the small particles moving fast, there will be a higher fluctuation of the intensity of the scattered light than in a case of large, slower-moving particles [93]. Measurement of such an intensity changes-fluctuation is expressed by the *autocorrelation function*. The device, the correlator, assesses the degree of similarity between two signals over short period (**Fig. 13**).

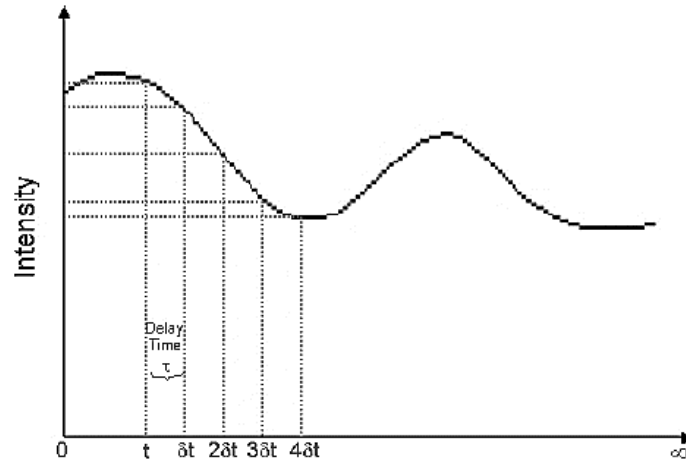


Fig. 13 – The fluctuation of the intensity of the scattered light as a function of time [94].

The initial intensity of the scattered light is compared with the intensity over time $t + dt$, $t + 2dt$, $t + 3dt$, and $t = \infty$. Time slots (dt) are in the order of nanoseconds/microseconds. The individual intensities deviate in time; time $t = \infty$ mean time in the order of tens of milliseconds, when the correlation no longer occurs and the correlation factor equals zero (for the ideal correlation, the correlation factor equals one). The graph of correlation function versus time is called *correlogram*. The time at which the correlation function begins to decrease sharply is an expression of the average particle size of the sample. The slope of the curve is then characteristic of the polydispersity of the sample. A steeper slope indicates greater homogeneity of the sample (**Fig. 14**) [93,94].

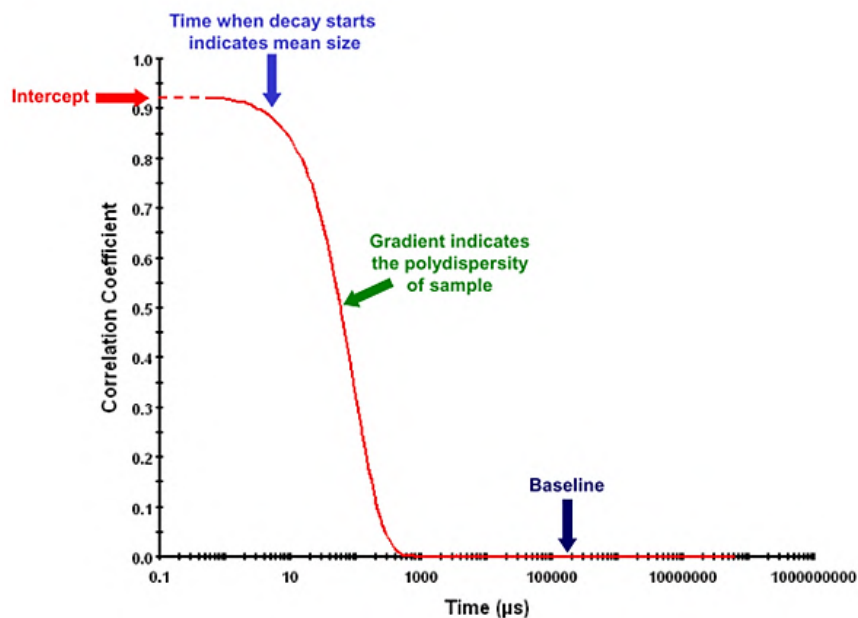


Fig. 14 – Example of the correlation function (© Malvern Panalytical Ltd.).

For monodisperse particles, the correlation function G has an exponential form and is expressed by the equation:

$$G(\tau) = [1 + B \cdot \exp(-2D\mu^2\tau)]$$

$$\mu = \frac{4\pi n}{\lambda_0} \sin\left(\frac{\theta}{2}\right) \quad (23)$$

where τ is the time lag between individual measurements, B is the amplitude of the function; the velocity of particle caused by the Brown's motion is expressed by the diffusion coefficient D , n is the refractive index of the dispersion medium, λ_0 is the wavelength of the laser, and θ is the angle of observation with respect to the initial laser beam. For the heterogeneous sample, the sum of all exponential decreases is involved in the correlation function equation. The particle size, hydrodynamic radius, is calculated from the translational diffusion coefficient using the Stokes-Einstein equation:

$$R_h = \frac{kT}{6\pi\eta D} \quad (24)$$

where R_h is the hydrodynamic radius, D is the diffusion coefficient, k is the Boltzmann constant, T is the thermodynamic temperature, and η is the viscosity of the medium. The hydrodynamic radius is an approximation whose value refers to a spherical particle of a given diameter having the same diffusion coefficient as the measured analyte. The diffusion coefficient is dependent on the particle core, structure and ionic strength of the dispersion medium. The total concentration of ions in the solution affects the rate of diffuse movement of the particle by changing the thickness of the electric bilayer - Debye length [93]. By evaluation of the correlation function using the *Cumulants analysis*, both the mean particle size (z-average diameter) and the polydispersity index (width of the distribution) are obtained. Or by fitting a multiple exponential to the correlation function to obtain the distribution of particle sizes. The size distribution can be expressed as the *Intensity distribution*, where the relative intensity of light scattered by particles is plotted in various size classes. The intensity distribution is given:

$$\%I_a = \frac{100 N_a a^6}{N_a a^6 + N_b b^6} \quad (25)$$

where N_a is the number of particles of the fraction, $\%I_a$ expresses the relative intensity of particles of size a , similarly the number of particles N_b for size b . The ratio of the intensity of the scattered light of between population a and b will be 1:1 000 000 (assuming the same concentration and varying in size by one order). The ratio results from the Rayleigh approximation: the intensity of the scattered light is proportional to the particle diameter d^6 [94]. In addition to intensity distribution, the distribution by *volume* and *number* are listed as well. For the two populations of the same concentration and size differences by one order, the *volume distribution*, the relative volume of the particle $\%V_a$ is given [94]:

$$\%V_a = \frac{100 N_a a^3}{N_a a^3 + N_b b^3} \quad (26)$$

The individual populations will differ by the ratio 1:1000 due to the sphere volume proportionality to the particle diameter, d^3 . The last type is the *number distribution* where the individual populations will be in ratio 1:1 due to the same concentration of the population a and b . The relative number is given:

$$\%N_a = \frac{100 N_a}{N_a + N_b} \quad (27)$$

The graphical representation of the distributions described above is shown in **Fig. 15** [94].

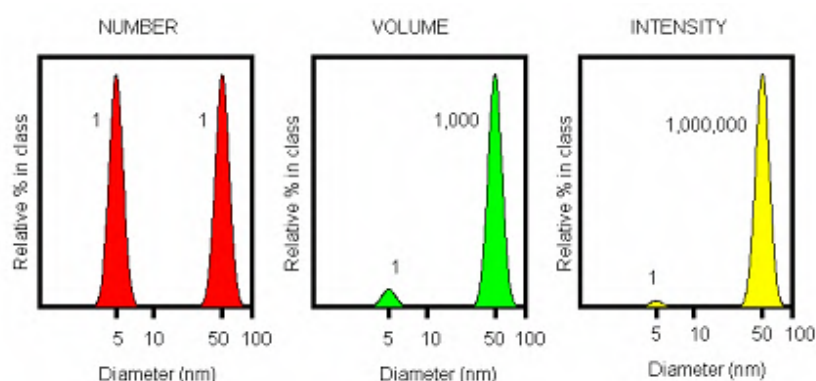


Fig. 15 – Example of theoretical distribution of two particles of size 5 and 50 nm according to number (red), volume (green) and intensity (yellow) distribution [94].

2.3.1.1 Multi-angle dynamic light scattering

The *Multi-angle dynamic light scattering* technique (MADLS®) is based on the dynamic light scattering principle; the measurement is a series of single-angle measurements: *backscatter* 173°, *side scatter* 90° and *forward scatter* 12°, that are combined. Particle size distribution is evaluated from multiple autocorrelation functions. Limitations resulting from the use of one specific angle are shown in the Mie diagram (**Fig. 16**). Fractions of the sample may be weakly scattering at one detection angle but are revealed in the other detection angles, and then included in the combined distributions [95,96].

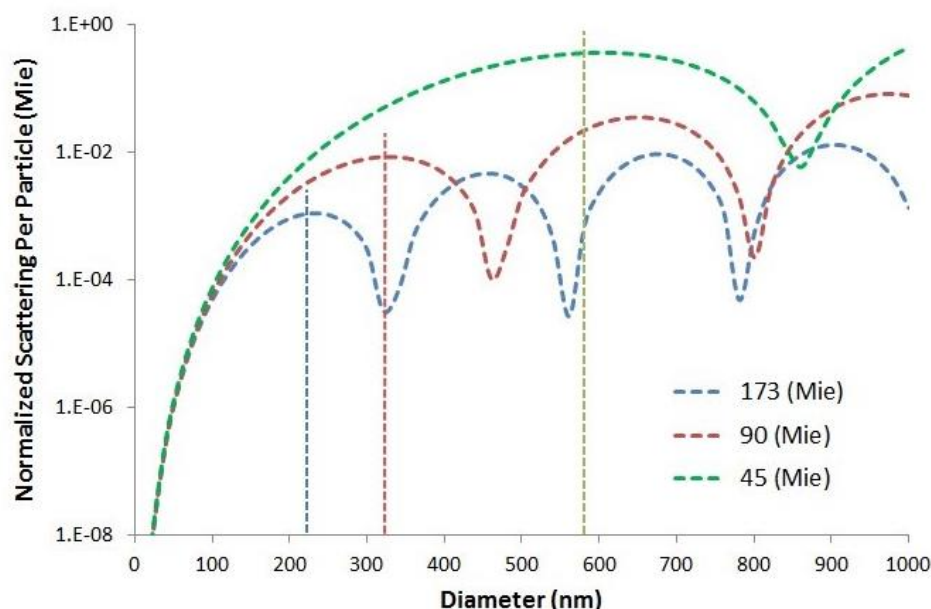


Fig. 16 – Mie diagram with the intensity minima and maxima. Particles that fall within the minima area will exhibit the low scattered light intensity and the low resolution at the given angle [96].

The MADLS increase the sensitivity to particles with sizes in the regions of the single angle Mie minima. The MADLS also introduces the so-called *adaptive correlation*, which compares

individual correlograms and isolates those that exhibit events that do not reflect the overall nature of the sample, such as the appearance of a dust particle or random aggregates. Adaptive correlation isolates (but it doesn't delete them) these random events, which is reflected in the quality of the resulting correlation curve. In comparison to single angle DLS algorithms, the MADLS provides better resolution using the algorithm which utilizes more size histogram bins. The increase in the number of bins is possible due to the noise reduction (by using adaptive correlation and multi-angle correlograms). By combining the scattered light intensity from all three angles together with the particle size and from the refractive index and absorption information of the particles and the environment, the MADLS technique also allows calculating the particle concentration in volume [96].

2.3.2 Electrophoretic light scattering

The *Electrophoretic light scattering* (ELS) technique (or *Laser Doppler Electrophoresis*) is based on the dynamic light scattering technique. It is primarily used for measuring the electrophoretic mobility of particles in suspension by measuring the small frequency shifts in the intensity of the scattered light. The frequency shifts (Equation (30)) resulting from the movement of the particles in an applied electric field. The electrophoretic mobility can be evaluated as the zeta potential. The electrophoretic mobility U_e is given by the equation:

$$U_e = \frac{v_e}{E} \quad (28)$$

where v is the velocity of the particle movement, and E represents the intensity of the electric field. The influence of zeta potential on particle velocity describes Henry's equation:

$$v_e = \frac{2\varepsilon\zeta f(\kappa a)}{3\eta} \quad (29)$$

where ε is the dielectric constant, η is the viscosity of the medium, ζ represents the zeta potential, and $f(\kappa a)$ denotes Henry's function. The parameter κ represents the Debye length whose reciprocal value, κ^{-1} , is the thickness of the electric bilayer. The parameter refers to the radius of the particle a . Thus, Henry's function correlates the radius of the particle to the thickness of the electric bilayer. For aqueous electrolytes, the value is 1.5 (**Fig. 11**) [97,98].



Fig. 17 – The scheme of Henry's function for aqueous media, where a represents the radius of the particle and κ^{-1} the layer of the electric bilayer [98].

The frequency shift Δf can be determinate as:

$$\Delta f = \frac{2v_e}{\lambda} \sin \frac{\theta}{2} \quad (30)$$

where λ is the laser wavelength and θ the scattering angle [98]. The Phase Analysis Light Scattering (PALS) technique is a modification of the ELS, where the phase shift of the scattered light is determined instead of frequency changes. The phase shift is proportional to the change in particle position. The use of phase shift increases the sensitivity of the measurement. It allows the characterization of samples with high ionic strength/conductivity or reduced mobility with a low applied voltage to minimize negative effect as Joule heating [99]. The measurement itself uses a Mixed Mode Measurement; PALS-M3 technique. The Mixed mode is referring to the use of the **Slow Field Reversal** (SFR) and **Fast Field Reversal** (FFR) measurements. In general, the electrophoretic analyses are performed by measuring the particles at the cell wall, in the stationary layer. The cell wall has a charge itself that is responsible for liquid stream along the wall when the potential is applied, called electroosmosis. The stationary layer is point/distance where the flow is cancelled due to the reverse fluid flow. The colloidal particles can respond faster to the applied electric field compared to the fluid. Using the alternating, high-frequency electric field, the electroosmosis effect is cancelled. The high-frequency alternation of the electric field is called the Fast Field Reversal technique and its use for determination of the mean zeta potential value at any position in the measuring cell [100]. Compared to that, the Slow Field Reversal technique gives zeta potential distribution, but the mobility is shifted due to the electroosmosis. By measuring FFR and SFR values, the electroosmotic flow can be determined and used for normalization of the slow field reversal distribution. The M3-PALS enables measurement of the zeta potential of high and low mobility samples and determination of the mean zeta potential and distribution [101].

2.3.2.1 Zeta potential

Most colloidal dispersions in an aqueous solution contain an electrical charge, resulting, for example, from ionization of functional groups on the surface or by adsorption of ions. Counter ions from the solution are then attracted to the charged surface to form an electric bilayer. The electric bilayer can be divided into an inner region, the **Stern layer** where the ions strongly bound to the surface of the particle are predominantly adsorption forces and the **Diffusing layer** consisting of ion bound electrostatic forces, neutralizing the remainder of the charge of the inner layer. There is a theoretical boundary within the diffusion layer within which ions and particles form a stable entity. This boundary is called the **Slip plane**. The potential that exists at this boundary is called the electrokinetic potential or ζ (zeta) potential (**Fig. 18**) [98,102].

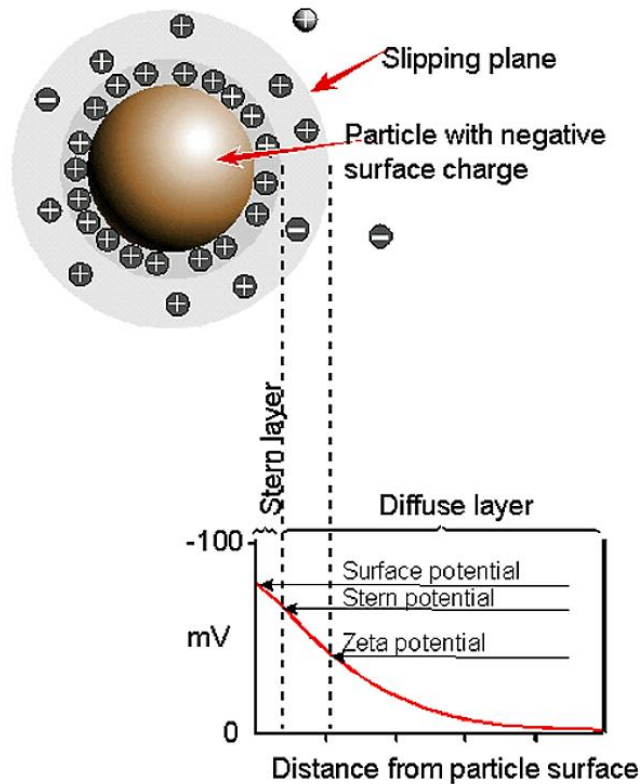


Fig. 18 – Schematic representation of the Zeta potential [98].

The zeta potential determines the stability of the colloidal particles in solution. The particles may be stabilized by two primary mechanisms: The **Steric stabilization** (adsorption of the for-example polymer to the particle surface to prevent particle adhesion) or the **Electrostatic stabilization** which preventing the particle interaction due to surface repulsiveness. The theory of electrostatic stability of particles in solution is called the **DLVO theory** (Derjaguin, Landau, Verwey, and Overbeek). The DLVO theory describes the balance between the electrostatic repulsive force and attractive interaction due to the van der Waals forces (mainly by the London dispersion interaction). The assumption is that the stability of the system is given by the sum of the attractive van der Waals forces and the repulsive electrostatic forces that penetrate between the particles at a sufficient approximation (**Fig. 19**) [98].

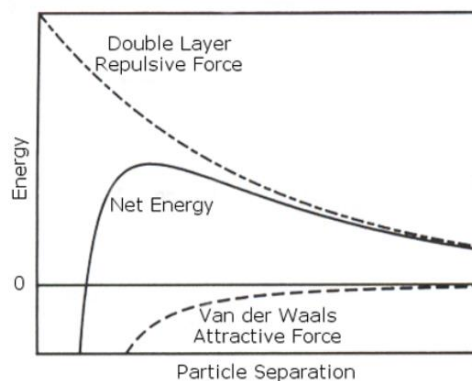


Fig. 19 – The diagram of the interaction energy dependence on the distance of the particles [98].

If the system exhibits a sufficiently large repulsion due to the high surface charge, the system can be considered as colloidally stable. If the zeta potential is reduced, for example, by changing the pH (**Fig. 20**) or by increasing the ionic strength of the solution, the repulsive forces are reduced. In general, for a zeta potential outside the range of ± 30 mV, the system is considered as colloidally stable [98].

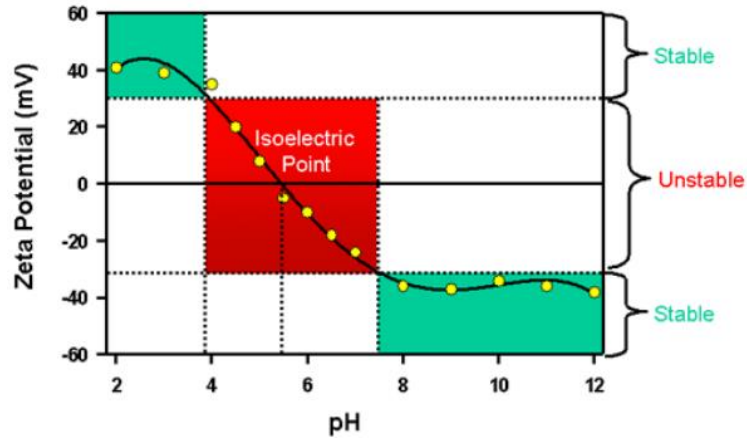


Fig. 20 – The zeta potential dependence on the pH with a marked isoelectric point (isoelectric point depends on the nature of the analyte) [98].

2.3.3 NTA (Nanoparticle tracking analysis)

The NTA technique, like DLS, utilizes laser light beam scattering on colloidal particles under the Brownian motion. The laser beam is entering into the measuring cell at a minimum angle so that the scattered light is observed at an angle close to 90° (**Fig. 21**). Light scattering is recorded near the point of entry of the laser beam into the measuring cell so that the resulting light scattering records are not affected by secondary light scattering [103].

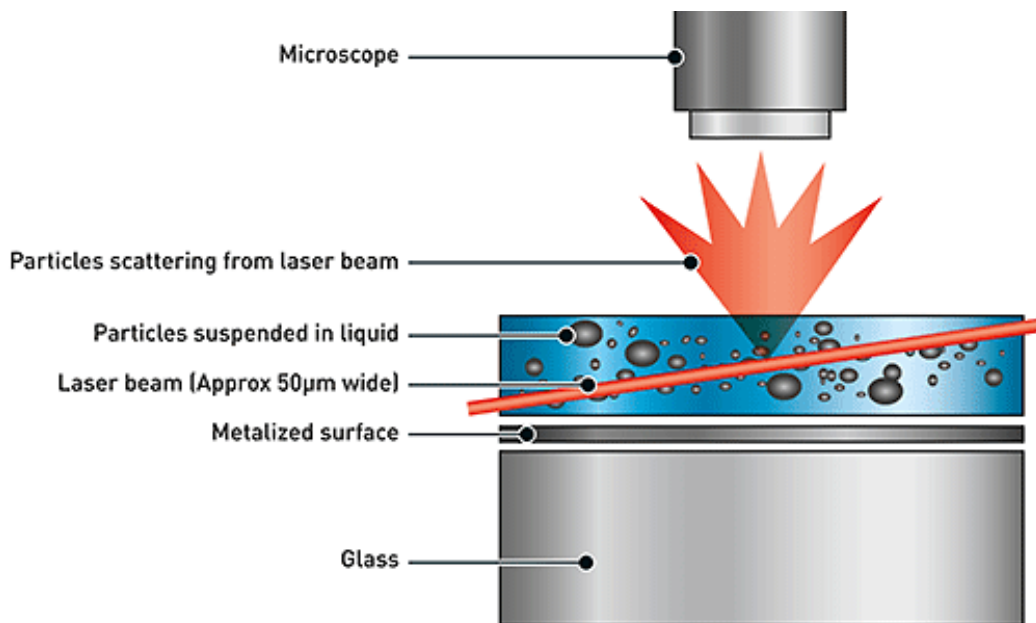


Fig. 21 – Schema of the configuration of the NTA optical elements [103].

The particles, respectively, the light they scatter are visualized using a microscope and a CCD (Charged-coupled device) camera. The recording of the particle motion is then evaluated by the "frame-by-frame" technique, with the software marking the centre of one of each particle, and then determining the mean square shift. The mean square shift is proportional to the square root of the interval τ between defined frames, whose proportionality constant is the diffusion coefficient D in Einstein-Smoluchowski equation [103]:

$$\overline{\Delta x} = \sqrt{2D\tau} \quad (31)$$

by modification of the Stokes-Einstein equation for the x -axis is given as:

$$\begin{aligned} \overline{(x)}^2 &= \frac{2TK_B t}{3\pi\eta d} \\ \overline{(x, y)}^2 &= \frac{4TK_B t}{3\pi\eta d} \end{aligned} \quad (32)$$

The movement of particles in the x , the y -axis is then expressed as:

$$\frac{\overline{(x, y)}^2}{4} = \frac{tTK_B}{3\pi\eta d} = D \quad (33)$$

With the known temperature and viscosity of the solvent, the hydrodynamic radius of the particle can be calculated from the diffusion coefficient using the Stokes-Einstein equation (24). The motion of individual particles is monitored in a fixed specific volume, which allows the calculation of the particle concentration [103].

2.3.4 Tunable Resistive Pulse Sensing

The *Tunable resistive pulse sensing* (TRPS) is a technique for measuring the size and the concentration of individual particles (particle by particle analysis) in an electrolyte solution. It is a modification of the "Coulter counter" method, where suspended particles pass through a defined pore located between two electrodes. When particles pass through the pore, a change in the flow of electric current is recorded, which results in a so-called *resistance pulse*. The size of the resistive pulse is proportional to the volume of the passing particle; the pulse frequency is then proportional to the number of particles, concentration. The use of an elastic polyurethane membrane enables the tuning of the size of the conical nanopore by axial stretching for optimal analyte characterization [104,105]. The total current is dependent on the applied voltage, the ionic strength, on the size and the resistance of the pore. The conical profile (**Fig. 22 A**) gives rise to an asymmetric resistance pulse. The resistance is highest at the top of the pore resulting in a sharp drop in current as the particle passes through the pore. The drop is followed by the gradual return of the initial current value [102].

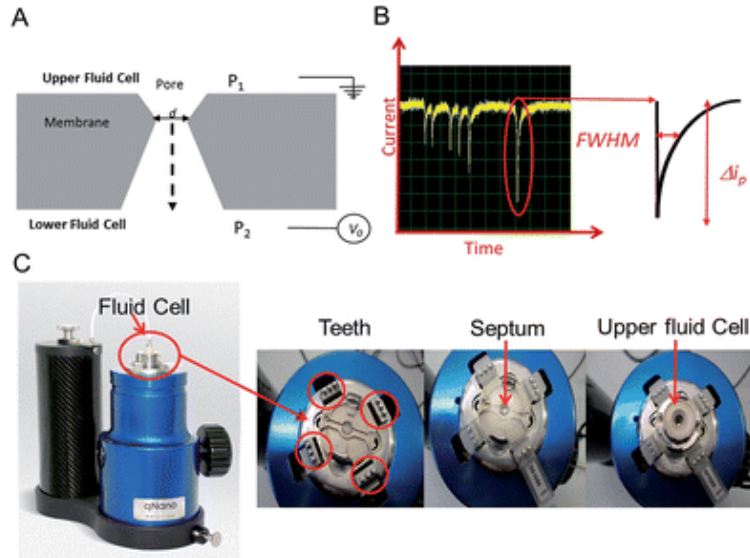


Fig. 22 – A) Schematic representation of the nanopore; B) Recording of current changes, resistive pulse, due to the passage of the particle. Resistance pulse is characterized by FWHM (Full Width Half Maximum), i.e. width at half peak and also by a total change of passing current ΔI ; C) qNano (Izon Science) instrument with polyurethane membrane placed between two Ag/AgCl electrodes [104].

For conical pore, the resistance R is given by the equation:

$$R = \frac{4L\rho}{\pi D_L D_S} \quad (34)$$

where ρ is the electrolyte resistance, L the pore length, D_L is the largest diameter and D_S the smallest diameter of the pore. The passage of particle results in an increase of the resistance and a decrease in the total current (see **Fig. 22 B**), the difference in the resistance is then given by the equation:

$$\Delta R = \frac{4\rho d^3}{\pi D_p^4} \quad (35)$$

where D_p is the mean pore diameter and d is the particle diameter. Since the pore size can be tuned by stretching/contracting of the polyurethane membrane, the analyte size calculation is evaluated based on the calibration with the particles of known diameter and concentration, measured under the same conditions [102,104,106]. The external pressure can be applied to optimize particle flow. The pressure is proportional to the frequency at which the particles are pushed through the nanopore. The ratio of P_1 to P_2 determines the optimum particle velocity. In general, the $P_1 > P_2$ is applied for the low concentrations of the sample. For concentrated suspensions, the pressure is reversed, $P_1 < P_2$ [104]. In addition to the pore size and pressure, the membrane voltage can also be tuned. The voltage is adjusted to achieve an optimum signal-to-noise ratio or to pass particles with different surface charges through the pore [107]. The rate at which the particles pass through a pore is influenced by several factors, electric field, nanopore geometry, pressure, and by the behaviour of the particles in the electrolyte. The particle flow J is defined by the Nernst-Planck theory. The theory describes electrophoretic forces, electroosmotic flow, and fluid flow. The flow of the particles is proportional to the particle concentration C_s and velocity of the passing particles v_p [104]:

$$J = C_s \times v_p \quad (36)$$

Electrophoretic mobility is the movement of charged particles in a solution due to the external electric field. This movement may be inhibited by the interference of counter ions moving in the opposite direction in a solution. The ions were forming a diffuse bilayer around the particle, the Stern bilayer (2.3.2.1), which will move in the electric field in the opposite direction than the particle itself, this phenomenon is called electrophoretic retardation. The electrophoretic mobility is then expressed by the Helmholtz–Smoluchowski equation:

$$v_E = \frac{\varepsilon \varepsilon_0 \zeta_{particle}}{\eta} E \quad (37)$$

where ε is the relative permittivity of the electrolyte, ε_0 is the relative permittivity of the vacuum, η is the dynamic viscosity, ζ is the zeta potential of the particle and E represents the intensity of the electric field. Electro-osmosis is an electric field-induced movement of an electrolyte relative to a stationary surface, so-called electroosmotic flow.

$$v_O = \frac{\varepsilon \varepsilon_0 \zeta_{pore}}{\eta} E \quad (38)$$

If the diffusion is neglected, the particle velocity v_p is given by (23), where Q represents the volume of flow:

$$v_p = v_F + v_E + v_O$$

$$v_p = \frac{Q}{\pi \left(\frac{D_s}{2}\right)^2} + \frac{\varepsilon \zeta_{particle}}{\eta} E - \frac{\zeta_{pore}}{\eta} E \quad (39)$$

$$Q = \frac{3\pi D_s^3 \Delta P}{128\eta \left(\frac{L}{D_L - D_s}\right)}$$

The particle velocity is mainly controlled by pressure differences. The resistive pulses frequency is proportional particles flow. As in the case of the size determination, the concentration analysis is based on the standard, polystyrene particles, of known concentration, measured under the same conditions as the analyte [104,107].

3 GOALS OF THE THESIS

1. Preparation and characterization of nanoparticles with the use of advance spectrophotometric methods.
 - The thesis is mainly focused on the preparation of liposomal nanoparticles using microfluidic mixing technique, lipid film hydration, detergent dilution, and high-pressure extrusion. Other nanoparticles are be obtained by biotechnological procedures within the department or are be obtained from cooperating laboratories within the OPVVV projects.
 - The characterization of nanoparticles is performed using advanced physicochemical and spectrophotometric methods. Especially dynamic light scattering/multi-angled dynamic light scattering, Nanoparticle tracking analysis for measurement of size distribution, concentration and their ζ -potential. And technique Tunable resistive pulse sensing for particle by particle analysis to obtain particle size and number distributions.
2. Surface modification on the nanoparticles with the use of bioconjugation orthogonal reactions.
3. Optimization and implementation of the separation techniques for nanoparticles and biopolymers.
 - The thesis deals mainly with the Asymmetrical flow Field-flow fractionation for separation various types of nanoparticles and biopolymers coupled with multiple detectors.
 - Furthermore, the thesis deals with additional online analytical techniques such as online dynamic light scattering/multiangled light scattering, UV-VIS absorption detector and different refractive index detector.

4 PUBLISHED RESULTS IN THE CHRONOLOGICAL ORDER

- [P1] **Kotoucek J.**, Hubatka F., Masek J., Kulich P., Velinska K., Bezdekova J., Fojtikova M., Bartheldyova E., Tomeckova A., Straska J., Hrebik D., Macaulay S., Kratochvilova I., Raska M., Turanek J. **Preparation of nanoliposomes by microfluidic mixing in herring-bone channel and the role of membrane fluidity in liposomes formation.** *Scientific Reports* (Q1, IF 4.1). 2020, 10(1). DOI: 10.1038/s41598-020-62500-2. ISSN 2045-2322.
- [P2] Svadlakova T., Hubatka F., Turanek Knotigova P., Kulich P., Masek J., **Kotoucek J.**, Macak J., Motola M., Kalbac M., Kolackova M., Vankova R., Vicherkova P., Malkova A., Simeckova P., Volkov Y., Prina-Mello A., Kratochvilova I., Fiala Z., Raska M., Krejsek J., Turanek J. **Proinflammatory Effect of Carbon-Based Nanomaterials: In Vitro Study on Stimulation of Inflammasome NLRP3 via Destabilisation of Lysosomes.** *Nanomaterials* (Q1, IF 4.0). 2020, 10(3). DOI: 10.3390/nano10030418. ISSN 2079-4991.
- [P3] Petrokova H., Mašek J., Kuchař M., Vítečková Wünschová A., Štikarová J., Bartheldyová E., Kulich P., Hubatka F., **Kotouček J.**, Knotigová T. P., Vohlídalová E., Héžová R., Mašková E., Macaulay S., Dyr J.E., Raška M., Mikulík R., Malý P., Turánek J. **Targeting Human Thrombus by Liposomes Modified with Anti-Fibrin Protein Binders: In Vitro Study on Stimulation of Inflammasome NLRP3 via Destabilisation of Lysosomes.** *Pharmaceutics* (Q1, IF 4.2). 2019, 11(12). DOI: 10.3390/pharmaceutics11120642. ISSN 1999-4923.
- [P4] Bartheldyova, E.; Turanek Knotigova, P.; Zachova, K.; Masek, J.; Kulich, P.; Effenberg, R.; Zyka, D.; Hubatka, F.; **Kotoucek, J.**; Celechovska, H.; Hezova, R.; Tomeckova, A.; Maskova, E.; Fojtikova, M.; Macaulay, S.; Bystricky, P.; Paulovicova, L.; Paulovicova, E.; Droz, L.; Ledvina, M.; Raska, M.; Turánek, J. **N-Oxy lipid-based click chemistry for orthogonal coupling of mannan onto nanoliposomes prepared by microfluidic mixing: Synthesis of lipids, characterisation of mannan-coated nanoliposomes and in vitro stimulation of dendritic cells.** *Carbohydrate Polymers* (Q1, IF 6.0). 2019, 207(12), 521-532. DOI: 10.1016/j.carbpol.2018.10.121. ISSN 01448617.
- [P5] Knötigová, P.; Mašek, J.; Hubatka, F.; **Kotouček, J.**; Kulich, P.; Šimečková, P.; Bartheldyová, E.; Machala, M.; Švadlákova, T.; Krejsek, J.; Vaškovická, N.; Skoupý, R.; Krzyžánek, V.; MacAulay, S.; Katzuba, M.; Fekete, L.; Ashcheulov, P.; Raška, M.; Kratochvílová, I.; Turánek J. **Application of Advanced Microscopic Methods to Study the Interaction of Carboxylated Fluorescent Nanodiamonds with Membrane Structures in THP-1 Cells: Activation of Inflammasome NLRP3 as the Result of Lysosome Destabilization.** *Molecular Pharmaceutics* (Q1, IF 4.4). 2019, 16(8), 3441-3451. DOI: 10.1021/acs.molpharmaceut.9b00225. ISSN 1543-8384.

5 SUBMITTED RESULTS

- [S1] **Kotoucek J.**, Hezova R., Vrablikova A., Hubatka F., Kulich P., Roessner D., Macaulay S., Raska M., Psikal I., Turanek J. **Characterization and purification of the pentameric chimeric protein particles using Asymmetrical Flow Field-Flow Fractionation coupled with MALS/DLS/UV detector.** (The Journal of Chromatography A (Q1, IF 3.9); submitted 2020).

6 MANUSCRIPTS IN PREPARATION

- [M1] Hezova R., Vrablikova A., **Kotoucek J.**, Hubatka F., Kulich P., Turanek-Knotigova P., Gebauer J., Macaulay S., Roessner D., Raska M., Psikal I., Turanek J. **Expression, purification and characterization of chimeric VP1-PCV2bCap protein as antigen for construction of recombinant vaccine against porcine circovirus.** (Allergy (Q1 IF 6.8); 2020)
- [M2] Turanek J., Masek J., Knotigova P., Kulich P., Hubatka F., **Kotoucek J.**, Lubasova D., Maskova E., Goepfert E., Raska M., Sorensen P., Leenhouts K. **Sublingual allergen-specific immunotherapy delivered by nanofibre-based mucoadhesive film in a pig model.** (Vaccine (Q1 IF 3.3); 2020).

7 COMMENTS AND AUTHOR CONTRIBUTION TO THE ENCLOSED PUBLICATIONS

The data measured within the author's dissertation thesis were published in the bellow mentioned scientific papers. Manuscripts [M1] and [M2] are in preparation and will be submitted in 2020. The results include the implementation of nanoparticle characterization techniques, where the author participated in the optimization of measurements and data evaluation. The techniques used by the author are given in the theoretical part of this thesis. The results further include the development of the nanoparticle itself. Here, the author focused on liposomes and their preparation using mainly microfluidic mixing technique. The preparation of the liposomes using microfluidic mixing technique is dealt with within the author's first article [P1]. In the following scientific papers, the author also deals with the characterization of carbon-based materials and bacterial ghost particles. Other publications focus on the preparation of liposomes and their post-modification and subsequent application. The author's second first article [S1] deals exclusively with the A4F technique. Here, the author focus on the development of purification and characterization methods of pentameric protein particles. With his work, the author contributed to the broader topic of the development of recombinant, mRNA vaccines, targeted cytostatic, and theragnostic.

7.1 [P1] Preparation of nanoliposomes by microfluidic mixing in herring-bone channel and the role of membrane fluidity in liposomes formation

This work aimed to clarify the mechanism of liposomes formulation, by microfluidic mixing technique, via the vesiculation of the phospholipid bilayer fragment. The liposomes were formulated using “herring bone” mixing channel. The liposome composition included unsaturated 1,2-distearoyl-sn-glycero-3-phosphocholine (DSPC) or saturated 1,2-dioleoyl-sn-glycero-3-ethylphosphocholine (EPC) phospholipids with the different cholesterol content. After the formulation, fluorescence membrane probe DPH-TMA (N,N,N-Trimethyl-4-(6-phenyl-1,3,5-hexatrien-1-yl)) was incorporated into the phospholipid bilayer, and the steady-state fluorescence anisotropy was measured. Liposomes prepared under the same process parameters such as the Flow Rate ratio and Total Flow rate ratio exhibits various sizes based on the cholesterol content and saturation or unsaturation of the acyl chain. In the case of the liposomes with unsaturated phospholipid (EPC) with the increasing cholesterol contend (from 0 mol% to 50 mol%) the size of the resulting liposomes increased as well. The effect of the cholesterol lies in the decrease in the fluidity of the bilayer. During the liposomal formulation by microfluidic mixing the phospholipid bilayer fragment is formed as a metastable structure. The instability cause bending, resulting in vesiculation and liposome formulation. The critical parameter for bending is the fluidity of the phospholipid bilayer fragment expressed as the steady-state fluorescence anisotropy of the DPH-TMA. With the decrease of the fluidity, the lipid bilayer fragment can form larger structures and vesiculation results in larger liposomes. An opposite effect is observed, when the fluidity is larger, due to the composition. The flexible fragment may vesiculate faster, and the resulting liposomes are smaller. In the study, the measured fluidity is in a good correlation with the size of the liposomes and composition. For unsaturated phospholipid (EPC) the cholesterol decreases the fluidity of the membrane, for the saturated phospholipid (DSPC) the effect for the opposite. Also, the experimental data and

theoretical calculations are in good accordance with the theory of lipid disc micelle vesiculation. Clarification of the mechanism of liposome formation by microfluidic mixing is important for optimising the process of formulating liposomes of different sizes for specific applications. Microfluidic mixing also minimizing potential problems with chemical and morphological stability and enables in situ preparation of therapeutics and contrast agents (as is shown in the study on the Ga-liposomal contrast formulation).

The author participated in the design of the study and experiments, was responsible for the preparation of liposomal samples with different cholesterol content using the NanoAssemblr Benchtop (Precision NanoSystems, Canada). The author characterized the size, polydispersity and distributions of the resulting liposomes using Multi-angle DLS technique, Zetasizer Ultra (Malvern Panalytical, UK). The author also characterized the steady-state anisotropy of the incorporated membrane probe using a fluorescence spectrometer Chronos DFD Fluorescence spectrometer (ISS, USA). The author evaluated the measured data and participated in manuscript writing and editing during the review process.

7.2 [P2] Proinflammatory Effect of Carbon-Based Nanomaterials: In Vitro Study on Stimulation of Inflammasome NLRP3 via Destabilisation of Lysosomes

This work is a follow-up of the previous work [P5]. In the publication, the disruption of the lysosome membrane due to the accumulation of nanodiamonds was observed. The disruption leads to the induction of inflammation via the inflammasome pathway. In this study, the same cell model (THP1) was exposed to the different carbon-based nanomaterials such as multi-walled carbon nanotubes (MWCNT) and two types of graphene platelets (GP1 and GP2). Both of the GP types formed aggregates with different morphology, GP2 aggregates were larger with sharp edges indicates potential more substantial cellular damage. The study shows an extensive accumulation of carbon-based nanomaterials in the cytoplasm but also demonstrates that the increased dose does not lead to cell death. The carbon-based nanomaterial particles did not exert acute toxicity. But they are not degradable, and the accumulation in different tissues may lead to chronic inflammation. The possible proinflammatory and immunomodulatory effects of above mention particles were confirmed in *in vitro* models. The bio-resistance and proinflammatory effect of the carbon-based materials are limiting for their medicinal applications.

The author was responsible for the characterization of carbon-based nanomaterials by application of the DLS method for measuring the size distribution and zeta potential, and for evaluating partial results using Zetasizer Ultra (Malvern Panalytical, UK). The author participated in the writing and editing of the manuscript during the review process.

7.3 [P3] Targeting Human Thrombus by Liposomes Modified with Anti-Fibrin Protein Binders

The publication presents the platform for surface modification of the liposomes by the selective fibrin binders for direct thrombus imaging and therapy. Liposomes were prepared using DOGS NTA-Ni (1,2-di-(9Z-octadecenoyl)-sn-glycero-3-[(N-(5-amino-1-carboxypentyl)iminodiacetic acid)succinyl] (nickel salt)). DOGS NTA-Ni creates an anchor in the phospholipid bilayer which enables functionalization of the liposomes with the anti-insoluble fibrin protein binder

(D7) via the metallochelating bond. Protein binder attachment was reflected as an increase of the hydrodynamic radius. The modification was also visualized using immunogold staining and direct TEM analysis. The ability of the resulting proteo-liposomal platform to bind to the fibrin fibres of the thrombus was tested and proven *in vitro* on the coronary artery flow model. The proteo-liposomal platform is a first step for developing of the theranostic for thrombus imaging. The liposomes with protein binders surface modification represent a potential platform for MRI imaging of the thrombus and delivery of the specific thrombolytic drugs.

The author was responsible for data evaluation, and characterization of various liposomal preparations. The characterisation includes measurement of the size, size distributions and zeta potential using Multi-angle DLS technique Zetasizer Ultra (Malvern Panalytical, UK). The author also participated in the manuscript writing and editing in the review process.

7.4 [P4] N-Oxy lipid-based click chemistry for orthogonal coupling of mannan onto nanoliposomes prepared by microfluidic mixing: Synthesis of lipids, characterisation of mannan-coated nanoliposomes and *in vitro* stimulation of dendritic cells.

The study describes a new drug delivery platform based on the mannan coated monodisperse liposomes prepared by microfluidic mixing technique. Liposomes were prepared using custom synthesized aminoxy lipid. The aminoxy-group on the surface of the liposomes and reducing termini of mannan molecule enables an orthogonal bond by aminoxy ligation. The one-step orthogonal reaction forms well-orientated patterns of the mannan molecules imitating of the native structures which can be found of various microorganisms. The structure was confirmed with the DLS, NTA and TRPS measurements. Increase of the hydrodynamic size and reduction of the zeta potential after the reaction were observed. Mannan bound on the liposomal surface retained its affinity for the recombinant mannan receptor, as was demonstrated by immunogold TEM. Also, the functionality of the whole platform was tested *in vitro* on human and mouse dendritic cells. The results show a positive interaction between mannan coating liposomes and dendritic cells compare to the plain liposomes or lipopolysaccharides. Described liposomes can be potential self-adjuvant drug delivery platform, targeting on the mannan receptor. The aminoxy reaction seems optimal for post-forming modification of liposomes with polysaccharides (containing the reducing hemiacetal group in the terminal end).

The author was responsible for the design of methods for characterization of the size distribution and zeta potential of the plain and modified liposomes using batch DLS Zetasizer ZSP (Malvern Panalytical, UK) and TRPS technique qNano instrument (iZON Science, UK). The author participated in the liposome preparation using NanoAssemblr Benchtop (Precision NanoSystems, Canada). The author also participated in the manuscript writing and editing in the review process.

7.5 [P5] Application of Advanced Microscopic Methods to Study the Interaction of Carboxylated Fluorescent Nanodiamonds with Membrane Structures in THP-1 Cells: Activation of Inflammasome NLRP3 as the Result of Lysosome Destabilization.

The publication is focused on the study of the physical-chemical properties of the fluorescence nanodiamonds and their potential application as the drug carrier and *in vitro* and *in vivo* imaging agents. Furthermore, the work deals with the intracellular distribution of nanodiamonds, the effect on cell membranes and cell immunity activation of the inflammasome of the THP-1 cell line model. The measured pH dependence on zeta potential shows that the acidification of the aqueous medium reduces the zeta potential of the carboxylated ND, resulting in aggregation, which occurs near pH 6. The NTA analysis further shows that even due to the relatively high negative zeta potential at neutral pH, the suspension contains an aggregate fraction. The specific, irregular shape of the NB is responsible for mechanical penetration of the cell membrane, and NDs are further accumulated in lysosomes in immune cells. The lysosome's destabilization leads to the activation of inflammasome NLRP3. The lysosome destabilization is induced by aggregation of ND due to the different pH values in the lysosome environment. The study is filling the lack of publications dealing with toxicological aspects of ND. In particular, their mechanical disruption of membranes resulting from their biodistribution must be considered for further application as *in vitro* and *in vivo* imaging agents.

The author developed and performed methods for characterization of ND by measuring the size distribution, zeta potential and the effect of the pH on zeta potential using batch DLS Zetasizer Nano ZSP (Malvern Panalytical, UK) and NTA, NanoSight NS500 (Malvern Panalytical, UK) techniques. The author also participated in data evaluation, and on the manuscript writing and editing in the review process

7.6 [S1] Characterization and purification of the pentameric chimeric protein particles using Asymmetrical Flow Field-Flow Fractionation coupled with MALS/DLS/UV detector

This manuscript deals with the influence of AF4 separation conditions on the separation of cell lysate with recombinant vaccination protein particles assembled from identical subunits into pentamer structure. The chimeric fusion proteins were derived from circovirus capsid antigen Cap and the multimerizing subunit of mouse polyomavirus capsid protein VP1 (VP1-PCV2bCap protein). Different elution profiles (constant, linear, and exponential cross-flow) were tested. A combination of the exponential decrease, followed by the constant cross-flow profile reduced separation time with good separation efficiency. The results show that the AF4 separation process doesn't promote the aggregation of the individual pentameric particles and preserves their native state. The R_g/R_h ratio obtained from online MALS/DLS shows a soft sphere structure on the individual pentameric particles, which can be separated from larger, super unit pentameric clusters with a branched structure. The theoretical hydrodynamic radius obtained from the FFF theory using the full retention equation is in correlation with the measured radius showing minimal sample to membrane interaction. Individual fractions were collected and subjected to offline DLS, TEM, and SDS-PAGE analysis. The results show maintaining the native structure of the pentameric antigen during the AF4 separation.

The author designed the experiments and performed the analysis of the lysate sample using AF4-MALS/DLS/UV (Wyatt Technology Europe GmbH, GE). The author developed the FFF analytical method, confirmed the theoretical model, measured the size distribution and denaturation temperature using batch Multi-angle DLS technique using Zetasizer Ultra (Malvern Panalytical, UK). The contribution of the author is in the writing of the manuscript and additional editing during the review process.

7.7 [M1] Expression, purification and characterization of chimeric VP1-PCV2bCap protein as antigen for construction of recombinant vaccine against porcine circovirus

This work describes the expression, purification, and immunity testing of the chimeric VP1-PCV2bCap protein sequences based on the mouse polyomavirus (MPyV). The chimeric protein based on the mouse polyomavirus was expressed in a baculovirus expression system. The circovirus is a small non-enveloped DNA virus, PCV2 is one of the four types representing the pathogenic form causing the post-weaning multi-systemic wasting syndrome. The chimeric protein forms super-unit structures, pentamers which have been characterized elsewhere [S1].

The aggregates and residual proteins were separated from the lysate using A4F. Fractions containing pentamers of VP1-PCV2bCap protein were collected. The humoral immune response of the mice immunized by purified pentameric protein was tested. The strong immunity response was detected upon first mice vaccination. The response gradually increased with the second and third immunization.

The author was responsible for the design and purification of the lysate sample using the AF4-MALS/DLS/UV (Wyatt Technology Europe GmbH, GE) system. The author also participated in the writing of the manuscript.

7.8 [M2] Sublingual allergen-specific immunotherapy delivered by nanofibre-based mucoadhesive film in a pig model

This study proves the concept of sublingual anti-allergic vaccination using non-invasive mucoadhesive films with bacteria ghost as adjuvants. The vaccination was performed *in vivo* on piglet animal model of allergy against egg albumin. Results showed rapid penetration of antigens into animal model submucosa. Prior to the vaccination, release test from the reservoir layer of the mucoadhesive film were performed *in-vitro*. An almost complete release of the particles was measured in 15 minutes. With the know concentration of the particles and area of the film, the results show sufficient adjacent mucosal surface covering with bacterial ghosts.

The author performed DLS (Malvern Panalytical, UK), NTA, NanoSight NS500 (Malvern Panalytical, UK) analysis and TRPS analysis using qNano instrument (iZON Science, UK) of different bacterial ghosts samples. The author evaluates the data and participates in manuscript writing and editing.

8 CONCLUSION

In my PhD thesis "Preparation and characterization of complex nanoparticles by Field-flow fractionation and advanced spectroscopic methods" I summarize modern methodological approaches and instrumentation for the preparation and characterization of nanoparticles. My work is part of wider research aiming at the development of modern recombinant, and mRNA vaccines, targeted cytostatics, and theranostics.

The first section of the PhD thesis is dedicated to the liposomes. The novel method of preparation is presented. The results describe the mechanism of liposomal formulation via the vesiculation of the lipid bilayer fragment. The size of the resulting vesicle is given by the fluidity of the fragment, which can be tuned using cholesterol with respect to the saturated/unsaturated nature of the phospholipid acyl chains. The application of liposomal nanoparticles with different surface modification are presented as well. The application, including orthogonal binding of the mannan on the surface of the liposome. The mannan coated liposomes stimulating the murine dendritic cells represent the self-adjuvants platform for targeting the mannan receptor. Another application includes nanoliposomes with surface binder domain for targeting the fibrin fibres. The second part of the thesis describes different characterization techniques. By determination of size, size distribution, polydispersity, zeta potential and concentration, this thesis contributes to the characterization of the different carbon-based nanoparticles in the study of proinflammatory effects. Another participation is described in the study of the anti-allergic vaccination using bacterial ghosts. The last part is focused on the Asymmetrical flow Field-flow fractionation technique coupled with multiple detectors. The results show the possible application in the field of vaccine development, especially for purification and characterization of the pentameric chimeric protein particles VP1-PCV2bCap. Maintaining the native state of the protein particles is crucial for the purification process. The series of additional post purification analysis show maintaining the native structure of the pentameric antigen during the AF4 purification. In another study, the immunity response of purified pentameric protein was tested *in vivo* on mice animal models.

9 REFERENCES

- [1] D.D. Lasic, *Liposomes in gene delivery*, CRC Press, Boca Raton, FL, 1997.
- [2] D. Van Swaay, A. Demello, Microfluidic methods for forming liposomes, *Lab Chip*. 13 (2013) 752–767. <https://doi.org/10.1039/c2lc41121k>.
- [3] Y.P. Patil, S. Jadhav, Novel methods for liposome preparation, *Chem. Phys. Lipids*. 177 (2014) 8–18. <https://doi.org/10.1016/j.chemphyslip.2013.10.011>.
- [4] M.I. Angelova, D.S. Dimitrov, Liposome electroformation, *Faraday Discuss. Chem. Soc.* 81 (1986) 303. <https://doi.org/10.1039/dc9868100303>.
- [5] A.D. Bangham, M.W. Hill, N.G.A. Miller, *Methods in Membrane Biology*, Plenum Press, New York, 1974. <https://doi.org/10.1007/978-1-4615-8960-0>.
- [6] Jaroslav Turánek, *Liposomy pro konstrukci cílených terapeutik a vakcín*, Přírodovědecká fakulta, Masarykova univerzita, 2016.
- [7] D.G. Hunter, B.J. Frisken, Effect of Extrusion Pressure and Lipid Properties on the Size and Polydispersity of Lipid Vesicles, *Biophys. J.* 74 (1998) 2996–3002. [https://doi.org/10.1016/S0006-3495\(98\)78006-3](https://doi.org/10.1016/S0006-3495(98)78006-3).
- [8] A. Helenius, Reconstitution of Semliki forest virus membrane, *J. Cell Biol.* 75 (1977) 866–880. <https://doi.org/10.1083/jcb.75.3.866>.
- [9] D. Deamer, A.D. Bangham, Large volume liposomes by an ether vaporization method, *Biochim. Biophys. Acta - Nucleic Acids Protein Synth.* 443 (1976) 629–634. [https://doi.org/10.1016/0005-2787\(76\)90527-X](https://doi.org/10.1016/0005-2787(76)90527-X).
- [10] S. Batzri, E.D. Korn, Single bilayer liposomes prepared without sonication, *BBA - Biomembr.* 298 (1973) 1015–1019. [https://doi.org/10.1016/0005-2736\(73\)90408-2](https://doi.org/10.1016/0005-2736(73)90408-2).
- [11] C. Charcosset, A. Juban, J.P. Valour, S. Urbaniak, H. Fessi, Preparation of liposomes at large scale using the ethanol injection method: Effect of scale-up and injection devices, *Chem. Eng. Res. Des.* 94 (2015) 508–515. <https://doi.org/10.1016/j.cherd.2014.09.008>.
- [12] I. V. Zhigaltsev, N. Belliveau, I. Hafez, A.K.K. Leung, J. Huft, C. Hansen, P.R. Cullis, Bottom-up design and synthesis of limit size lipid nanoparticle systems with aqueous and triglyceride cores using millisecond microfluidic mixing, *Langmuir*. 28 (2012) 3633–3640. <https://doi.org/10.1021/la204833h>.
- [13] L. Capretto, D. Carugo, S. Mazzitelli, C. Nastruzzi, X. Zhang, Microfluidic and lab-on-a-chip preparation routes for organic nanoparticles and vesicular systems for nanomedicine applications, *Adv. Drug Deliv. Rev.* 65 (2013) 1496–1532. <https://doi.org/10.1016/j.addr.2013.08.002>.
- [14] D. Carugo, E. Bottaro, J. Owen, E. Stride, C. Nastruzzi, Liposome production by microfluidics: potential and limiting factors, *Sci. Rep.* 6 (2016) 25876. <https://doi.org/10.1038/srep25876>.
- [15] C.D. Hein, X.-M. Liu, D. Wang, *Expert Review Click Chemistry, A Powerful Tool for Pharmaceutical Sciences*, (n.d.). <https://doi.org/10.1007/s11095-008-9616-1>.

- [16] A.D. Bangham, M.M. Standish, J.C. Watkins, Diffusion of univalent ions across the lamellae of swollen phospholipids, *J. Mol. Biol.* 13 (1965) 238–252. [https://doi.org/10.1016/S0022-2836\(65\)80093-6](https://doi.org/10.1016/S0022-2836(65)80093-6).
- [17] Y. Barenholz, Doxil® - The first FDA-approved nano-drug: Lessons learned, *J. Control. Release.* 160 (2012) 117–134. <https://doi.org/10.1016/j.jconrel.2012.03.020>.
- [18] U. Bulbake, S. Doppalapudi, N. Kommineni, W. Khan, Liposomal formulations in clinical use: An updated review, *Pharmaceutics.* 9 (2017) 1–33. <https://doi.org/10.3390/pharmaceutics9020012>.
- [19] A.J. Trevor, B.G. Katzung, M. Kruidering-Hall, *Pharmacology Examination & Board Review a LANGE medical book Eleventh Edition*, 2015. www.mhprofessional.com. (accessed March 5, 2020).
- [20] A. Akbarzadeh, R. Rezaei-Sadabady, S. Davaran, S.W. Joo, N. Zarghami, Y. Hanifehpour, M. Samiei, M. Kouhi, K. Nejati-Koshki, Liposome: classification, preparation, and applications, *Nanoscale Res. Lett.* 8 (2013) 102. <https://doi.org/10.1186/1556-276X-8-102>.
- [21] A.D. Miller, Delivering the promise of small ncRNA therapeutics, *Ther. Deliv.* 5 (2014) 569–589. <https://doi.org/10.4155/tde.14.23>.
- [22] G. Gregoriadis, Drug entrapment in liposomes, *FEBS Lett.* 36 (1973) 292–296. [https://doi.org/10.1016/0014-5793\(73\)80394-1](https://doi.org/10.1016/0014-5793(73)80394-1).
- [23] T.M. Allen, L.G. Cleland, Serum-induced leakage of liposome contents, *BBA - Biomembr.* 597 (1980) 418–426. [https://doi.org/10.1016/0005-2736\(80\)90118-2](https://doi.org/10.1016/0005-2736(80)90118-2).
- [24] J. Senior, G. Gregoriadis, Is half-life of circulating liposomes determined by changes in their permeability?, *FEBS Lett.* 145 (1982) 109–114. [https://doi.org/10.1016/0014-5793\(82\)81216-7](https://doi.org/10.1016/0014-5793(82)81216-7).
- [25] J.H. Senior, Fate and behavior of liposomes in vivo: a review of controlling factors., *Crit. Rev. Ther. Drug Carrier Syst.* 3 (1987) 123–93. <http://www.ncbi.nlm.nih.gov/pubmed/3542245> (accessed April 6, 2019).
- [26] K. Cho, X. Wang, S. Nie, Z. Chen, D.M. Shin, Therapeutic Nanoparticles for Drug Delivery in Cancer, *Clin. Cancer Res.* 14 (2008) 1310–1316. <https://doi.org/10.1158/1078-0432.CCR-07-1441>.
- [27] S. Kolli, S.P. Wong, R. Harbottle, B. Johnston, M. Thanou, A.D. Miller, PH-triggered nanoparticle mediated delivery of siRNA to liver cells in vitro and in vivo, *Bioconjug. Chem.* 24 (2013) 314–332. <https://doi.org/10.1021/bc3004099>.
- [28] G.D. Kenny, N. Kamaly, T.L. Kalber, L.P. Brody, M. Sahuri, E. Shamsaei, A.D. Miller, J.D. Bell, Novel multifunctional nanoparticle mediates siRNA tumour delivery, visualisation and therapeutic tumour reduction in vivo, *J. Control. Release.* 149 (2011) 111–116. <https://doi.org/10.1016/j.jconrel.2010.09.020>.
- [29] H. Maeda, H. Nakamura, J. Fang, The EPR effect for macromolecular drug delivery to solid tumors: Improvement of tumor uptake, lowering of systemic toxicity, and distinct tumor imaging in vivo, *Adv. Drug Deliv. Rev.* 65 (2013) 71–79. <https://doi.org/10.1016/j.addr.2012.10.002>.

- [30] A. Aissaoui, M. Chami, M. Hussein, A.D. Miller, Efficient topical delivery of plasmid DNA to lung in vivo mediated by putative triggered, PEGylated pDNA nanoparticles, *J. Control. Release.* 154 (2011) 275–284. <https://doi.org/10.1016/j.jconrel.2011.06.017>.
- [31] Maria Laura Immordino, Franco Dosio, Luigi Cattel, Stealth liposomes: review of the basic science, rationale, and clinical applications, existing and potential, *Int. J. Nanomedicine.* 1 (2006) 297–315. <https://doi.org/10.1023/A:1020134521778>.
- [32] S.E. Krown, D.W. Northfelt, D. Osoba, J.S. Stewart, Use of liposomal anthracyclines in Kaposi's sarcoma, *Semin. Oncol.* 31 (2004) 36–52. <https://doi.org/10.1053/j.seminoncol.2004.08.003>.
- [33] O.K. Nag, V. Awasthi, Surface engineering of liposomes for stealth behavior, *Pharmaceutics.* 5 (2013) 542–569. <https://doi.org/10.3390/pharmaceutics5040542>.
- [34] M. Riaz, C. Lin, X. Chen, G. Zhang, A. Lu, Z. Yang, K. Wong, X. Zhang, Surface Functionalization and Targeting Strategies of Liposomes in Solid Tumor Therapy: A Review, *Int. J. Mol. Sci.* 19 (2018) 195. <https://doi.org/10.3390/ijms19010195>.
- [35] V. Kumar Khanna, Targeted delivery of nanomedicines., *ISRN Pharmacol.* 2012 (2012) 571394. <https://doi.org/10.5402/2012/571394>.
- [36] J. Fuenmayor, F. Gòdia, L. Cervera, Production of virus-like particles for vaccines, *N. Biotechnol.* 39 (2017) 174–180. <https://doi.org/10.1016/j.nbt.2017.07.010>.
- [37] B. Forouhar Kalkhoran, A Short Review on Virus-Like Particles as Vaccine and Delivery Systems, 2017. <https://pdfs.semanticscholar.org/3a9d/aec2cadbd422ea921f22bd2e41065003d7b9.pdf> (accessed March 16, 2019).
- [38] L.H.L. Lua, N.K. Connors, F. Sainsbury, Y.P. Chuan, N. Wibowo, A.P.J. Middelberg, Bioengineering virus-like particles as vaccines, *Biotechnol. Bioeng.* 111 (2014) 425–440. <https://doi.org/10.1002/bit.25159>.
- [39] O.A. Shenderova, V. V. Zhirnov, D.W. Brenner, Carbon Nanostructures, *Crit. Rev. Solid State Mater. Sci.* 27 (2002) 227–356. <https://doi.org/10.1080/10408430208500497>.
- [40] A. Gruber, A. Dräbenstedt, C. Tietz, L. Fleury, J. Wrachtrup, C. von Borczyskowski, Scanning Confocal Optical Microscopy and Magnetic Resonance on Single Defect Centers, *Science* (80-.). 276 (1997) 2012–2014. <https://doi.org/10.1126/science.276.5321.2012>.
- [41] O.A. Williams, Nanocrystalline diamond, *Diam. Relat. Mater.* 20 (2011) 621–640. <https://doi.org/10.1016/J.DIAMOND.2011.02.015>.
- [42] J. Slegerova, I. Rehor, J. Havlik, H. Raabova, E. Muchova, P. Cigler, Nanodiamonds as Intracellular Probes for Imaging in Biology and Medicine, in: 2014: pp. 363–401. https://doi.org/10.1007/978-94-017-8896-0_18.
- [43] H. Huang, E. Pierstorff, E. Osawa, D. Ho, Active Nanodiamond Hydrogels for Chemotherapeutic Delivery, *Nano Lett.* 7 (2007) 3305–3314. <https://doi.org/10.1021/nl071521o>.
- [44] L. Zhao, T. Takimoto, M. Ito, N. Kitagawa, T. Kimura, N. Komatsu, Chromatographic

- Separation of Highly Soluble Diamond Nanoparticles Prepared by Polyglycerol Grafting, *Angew. Chemie Int. Ed.* 50 (2011) 1388–1392. <https://doi.org/10.1002/anie.201006310>.
- [45] S.A. Dahoumane, M.N. Nguyen, A. Thorel, J.-P. Boudou, M.M. Chehimi, C. Mangeney, Protein-Functionalized Hairy Diamond Nanoparticles, *Langmuir*. 25 (2009) 9633–9638. <https://doi.org/10.1021/la9009509>.
- [46] P. Kudela, V.J. Koller, W. Lubitz, Bacterial ghosts (BGs)-Advanced antigen and drug delivery system, *Vaccine*. 28 (2010) 5760–5767. <https://doi.org/10.1016/j.vaccine.2010.06.087>.
- [47] S. Rabea, M.M. Salem-Bekhit, F.K. Alanazi, A.S. Yassin, N.A. Moneib, A.E.M. Hashem, A novel protocol for bacterial ghosts' preparation using tween 80, *Saudi Pharm. J.* 26 (2018) 232–237. <https://doi.org/10.1016/j.jsps.2017.12.006>.
- [48] I.A. Hajam, P.A. Dar, G. Won, J.H. Lee, Bacterial ghosts as adjuvants: Mechanisms and potential, *Vet. Res.* 48 (2017) 1–13. <https://doi.org/10.1186/s13567-017-0442-5>.
- [49] J.C. Giddings, A New Separation Concept Based on a Coupling of Concentration and Flow Nonuniformities, *Sep. Sci.* 1 (1966) 123–125. <https://doi.org/10.1080/01496396608049439>.
- [50] M. Baalousha, B. Stolpe, J.R. Lead, Flow field-flow fractionation for the analysis and characterization of natural colloids and manufactured nanoparticles in environmental systems: A critical review, *J. Chromatogr. A.* 1218 (2011) 4078–4103. <https://doi.org/10.1016/j.chroma.2011.04.063>.
- [51] S. Podzimek, J. Machotova, J. Snuparek, M. Vecera, L. Prokupek, Characterization of molecular structure of acrylic copolymers prepared via emulsion polymerization using A4F-MALS technique, *J. Appl. Polym. Sci.* 131 (2014). <https://doi.org/10.1002/app.40995>.
- [52] S. Podzimek, J. Machotova, H. Zgoni, P. Bohacik, J. Snuparek, Application of A4F-MALS for the Characterization of Polymers Prepared by Emulsion Polymerization: Comparison of the Molecular Structure of Styrene-Acrylate and Methyl Methacrylate-Acrylate Copolymers, *Polym. - Plast. Technol. Eng.* 55 (2016) 1365–1372. <https://doi.org/10.1080/03602559.2016.1146957>.
- [53] S. Podzimek, *Light Scattering, Size Exclusion Chromatography and Asymmetric Flow Field Flow Fractionation*, John Wiley & Sons, Inc., Hoboken, NJ, USA, 2011.
- [54] K.G. Wahlund, J.C. Giddings, K.-G. Wahlund1, J.C. Giddings, K.G. Wahlund, J.C. Giddings, K.-G. Wahlund1, J.C. Giddings, Properties of an asymmetrical flow field-flow fractionation channel having one permeable wall, *Anal. Chem.* 59 (1987) 1332–1339. <https://doi.org/10.1021/ac00136a016>.
- [55] M.H. Moon, Flow field-flow fractionation: Recent applications for lipidomic and proteomic analysis, *TrAC - Trends Anal. Chem.* 118 (2019) 19–28. <https://doi.org/10.1016/j.trac.2019.05.024>.
- [56] S. Lee, J.C. Giddings, Experimental observation of steric transition phenomena in sedimentation field-flow fractionation, *Anal. Chem.* 60 (1988) 2328–2333. <https://doi.org/10.1021/ac00172a004>.

- [57] A. Litzén, K.-G. Wahlund, Zone Broadening and Dilution in Rectangular and Trapezoidal Asymmetrical Flow Field-Flow Fractionation Channels, 1991. <https://pubs.acs.org/sharingguidelines> (accessed December 19, 2019).
- [58] S. Hupfeld, D. Ausbacher, M. Brandl, Asymmetric flow field-flow fractionation of liposomes: 2. Concentration detection and adsorptive loss phenomena, *J. Sep. Sci.* 32 (2009) 3555–3561. <https://doi.org/10.1002/jssc.200900292>.
- [59] S. Hupfeld, D. Ausbacher, M. Brandl, Asymmetric flow field-flow fractionation of liposomes: Optimization of fractionation variables, *J. Sep. Sci.* 32 (2009) 1465–1470. <https://doi.org/10.1002/jssc.200800626>.
- [60] Wyatt Technology Corporation, Application Note : Frit Inlet Channel for the Usage with Organic Solvents, (n.d.) 1–5.
- [61] C. Johann, S. Elsenberg, U. Roesch, D.C. Rambaldi, A. Zattoni, P. Reschiglian, A novel approach to improve operation and performance in flow field-flow fractionation, *J. Chromatogr. A.* 1218 (2010) 4126–4131. <https://doi.org/10.1016/j.chroma.2010.12.077>.
- [62] I. Agilent Technologies, Agilent 1200 Series Diode Array and Multiple Wavelength Detectors, (2006) 1–182.
- [63] Wyatt Technology Corporation, Optilab® T-rEX™ and UT-rEX™ User's Guide, (2014) 1–109.
- [64] B.H. Zimm, The Scattering of Light and the Radial Distribution Function of High Polymer Solutions, *J. Chem. Phys.* 16 (1948) 1093–1099. <https://doi.org/10.1063/1.1746738>.
- [65] S. Hupfeld, H.H. Moen, D. Ausbacher, H. Haas, M. Brandl, Liposome fractionation and size analysis by asymmetrical flow field-flow fractionation/multi-angle light scattering: influence of ionic strength and osmotic pressure of the carrier liquid, *Chem. Phys. Lipids.* 163 (2010) 141–147. <https://doi.org/10.1016/j.chemphyslip.2009.10.009>.
- [66] A. Zattoni, B. Roda, F. Borghi, V. Marassi, P. Reschiglian, Flow field-flow fractionation for the analysis of nanoparticles used in drug delivery, *J. Pharm. Biomed. Anal.* 87 (2014) 53–61. <https://doi.org/10.1016/j.jpba.2013.08.018>.
- [67] W. Fraunhofer, G. Winter, The use of asymmetrical flow field-flow fractionation in pharmaceuticals and biopharmaceuticals, *Eur. J. Pharm. Biopharm.* 58 (2004) 369–383. <https://doi.org/10.1016/j.ejpb.2004.03.034>.
- [68] T. Bousse, D.A. Shore, C.S. Goldsmith, M.J. Hossain, Y. Jang, C.T. Davis, R.O. Donis, J. Stevens, Quantitation of influenza virus using field flow fractionation and multi-angle light scattering for quantifying influenza A particles, *J. Virol. Methods.* 193 (2013) 589–596. <https://doi.org/10.1016/j.jviromet.2013.07.026>.
- [69] L.F. Pease, D.I. Lipin, D.-H. Tsai, M.R. Zachariah, L.H.L. Lua, M.J. Tarlov, A.P.J. Middelberg, Quantitative characterization of virus-like particles by asymmetrical flow field flow fractionation, electrospray differential mobility analysis, and transmission electron microscopy, *Biotechnol. Bioeng.* 102 (2009) 845–855. <https://doi.org/10.1002/bit.22085>.
- [70] Z. Wei, M. Mcevoy, V. Razinkov, A. Polozova, E. Li, J. Casas-Finet, G.I. Tous, P. Balu,

- A.A. Pan, H. Mehta, M.A. Schenerman, Biophysical characterization of influenza virus subpopulations using field flow fractionation and multiangle light scattering: Correlation of particle counts, size distribution and infectivity, *J. Virol. Methods.* 144 (2007) 122–132. <https://doi.org/10.1016/j.jviromet.2007.04.008>.
- [71] F. Caputo, A. Arnould, M. Bacia, W. Li Ling, E. Rustique, I. Texier, A. Prina Mello, A.-C. Couffin, W.L. Ling, E. Rustique, I. Texier, A.P. Mello, A.-C. Couffin, W. Li Ling, E. Rustique, I. Texier, A. Prina Mello, A.-C. Couffin, Measuring Particle Size Distribution by Asymmetric Flow Field Flow Fractionation: A Powerful Method for the Preclinical Characterization of Lipid-Based Nanoparticles., *Mol. Pharm.* 16 (2019) 756–767. <https://doi.org/10.1021/acs.molpharmaceut.8b01033>.
- [72] A. Citkowicz, H. Petry, R.N. Harkins, O. Ast, L. Cashion, C. Goldmann, P. Bringmann, K. Plummer, B.R. Larsen, Characterization of virus-like particle assembly for DNA delivery using asymmetrical flow field-flow fractionation and light scattering, *Anal. Biochem.* 376 (2008) 163–172. <https://doi.org/10.1016/j.ab.2008.02.011>.
- [73] M. Lampi, H.M. Oksanen, F. Meier, E. Moldenhauer, M.M. Poranen, D.H. Bamford, K. Eskelin, Asymmetrical flow field-flow fractionation in purification of an enveloped bacteriophage $\phi 6$, *J. Chromatogr. B Anal. Technol. Biomed. Life Sci.* 1095 (2018) 251–257. <https://doi.org/10.1016/j.jchromb.2018.07.008>.
- [74] K. Eskelin, M. Lampi, F. Meier, E. Moldenhauer, D.H. Bamford, H.M. Oksanen, Halophilic viruses with varying biochemical and biophysical properties are amenable to purification with asymmetrical flow field-flow fractionation, *Extremophiles.* 21 (2017) 1119–1132. <https://doi.org/10.1007/s00792-017-0963-x>.
- [75] K. Eskelin, M. Lampi, F. Meier, E. Moldenhauer, D.H. Bamford, H.M. Oksanen, Asymmetric flow field flow fractionation methods for virus purification, *J. Chromatogr. A.* 1469 (2016) 108–119. <https://doi.org/10.1016/j.chroma.2016.09.055>.
- [76] M.E. Hansen, J.C. Giddings, R. Beckett, Colloid characterization by sedimentation field-flow fractionation: VI. Perturbations due to overloading and electrostatic repulsion, *J. Colloid Interface Sci.* 132 (1989) 300–312. [https://doi.org/10.1016/0021-9797\(89\)90245-2](https://doi.org/10.1016/0021-9797(89)90245-2).
- [77] M.H. Moon, I. Park, Y. Kim, Size characterization of liposomes by flow field-flow fractionation and photon correlation spectroscopy: Effect of ionic strength and pH of carrier solutions, *J. Chromatogr. A.* 813 (1998) 91–100. [https://doi.org/10.1016/S0021-9673\(98\)00325-2](https://doi.org/10.1016/S0021-9673(98)00325-2).
- [78] P.J. Wyatt, Submicrometer particle sizing by multiangle light scattering following fractionation, *J. Colloid Interface Sci.* 197 (1998) 9–20. <https://doi.org/10.1006/jcis.1997.5215>.
- [79] S. Hupfeld, Size Characterisation of Liposomes Using Asymmetrical Flow Field-Flow Fractionation Factors Influencing Fractionation and Size Determination, 2009.
- [80] A.-R.R. Jochem, G.N. Ankah, L.-A.A. Meyer, S. Elsenberg, C. Johann, T. Kraus, Colloidal Mechanisms of Gold Nanoparticle Loss in Asymmetric Flow Field-Flow Fractionation, *Anal. Chem.* 88 (2016) 10065–10073. <https://doi.org/10.1021/acs.analchem.6b02397>.

- [81] R. Saenmuangchin, A. Siripinyanond, Flow field-flow fractionation for hydrodynamic diameter estimation of gold nanoparticles with various types of surface coatings, (n.d.). <https://doi.org/10.1007/s00216-018-1284-3>.
- [82] The use of asymmetrical flow field-flow fractionation in pharmaceuticals and biopharmaceuticals, *J. Chromatogr. A.* 1218 (2018) 217–224. <https://doi.org/10.1016/j.ejpb.2004.03.034>.
- [83] K.E. Petersen, E. Manangon, J.L. Hood, S.A. Wickline, D.P. Fernandez, W.P. Johnson, B.K. Gale, A review of exosome separation techniques and characterization of B16-F10 mouse melanoma exosomes with AF4-UV-MALS-DLS-TEM, *Anal. Bioanal. Chem.* 406 (2014) 7855–7866. <https://doi.org/10.1007/s00216-014-8040-0>.
- [84] H. Lee, S.K.R. Williams, K.L. Wahl, N.B. Valentine, Analysis of whole bacterial cells by flow field-flow fractionation and matrix-assisted laser desorption/ionization time-of-flight mass spectrometry, *Anal. Chem.* 75 (2003) 2746–2752. <https://doi.org/10.1021/ac020698u>.
- [85] H. Dou, Y. Li, J. Choi, S. Huo, L. Ding, S. Shen, S. Lee, Asymmetrical flow field-flow fractionation coupled with multiple detections: A complementary approach in the characterization of egg yolk plasma, *J. Chromatogr. A.* 1465 (2016) 165–174. <https://doi.org/10.1016/j.chroma.2016.08.062>.
- [86] P. Guo, Y. Li, J. An, S. Shen, H. Dou, Study on structure-function of starch by asymmetrical flow field-flow fractionation coupled with multiple detectors: A review, *Carbohydr. Polym.* 226 (2019). <https://doi.org/10.1016/j.carbpol.2019.115330>.
- [87] A.K. Brewer, A.M. Striegel, Characterizing the size, shape, and compactness of a polydisperse prolate ellipsoidal particle via quadruple-detector hydrodynamic chromatography, *Analyst.* 136 (2011) 515–519. <https://doi.org/10.1039/c0an00738b>.
- [88] A.K. Brewer, A.M. Striegel, Particle size characterization by quadruple-detector hydrodynamic chromatography, *Anal. Bioanal. Chem.* 393 (2009) 295–302. <https://doi.org/10.1007/s00216-008-2319-y>.
- [89] C. Zielke, A. Stradner, L. Nilsson, Characterization of cereal β -glucan extracts: Conformation and structural aspects, *Food Hydrocoll.* 79 (2018) 218–227. <https://doi.org/10.1016/j.foodhyd.2017.12.036>.
- [90] J.R. Runyon, M. Ulmius, L. Nilsson, J. Ray Runyon, M. Ulmius, L. Nilsson, J.R. Runyon, M. Ulmius, L. Nilsson, A perspective on the characterization of colloids and macromolecules using asymmetrical flow field-flow fractionation, *Colloids Surfaces A Physicochem. Eng. Asp.* 442 (2014) 25–33. <https://doi.org/10.1016/j.colsurfa.2013.04.010>.
- [91] T. Coviello, K. Kajiwara, W. Burchard, M. Dentini, V. Crescenzi, Solution properties of xanthan. 1. Dynamic and static light scattering from native and modified xanthans in dilute solutions, *Macromolecules.* 19 (1986) 2826–2831. <https://doi.org/10.1021/ma00165a027>.
- [92] G. Yohannes, M. Jussila, K. Hartonen, M.L. Riekkola, Asymmetrical flow field-flow fractionation technique for separation and characterization of biopolymers and bioparticles, *J. Chromatogr. A.* 1218 (2011) 4104–4116.

- <https://doi.org/10.1016/j.chroma.2010.12.110>.
- [93] R.B. Perry, Principles of Colloid and Surface Chemistry, Second Edition (Hiemenz, P. C.), *J. Chem. Educ.* 64 (1987) A328. <https://doi.org/10.1021/ed064pA328.3>.
- [94] Malvern Instruments, Dynamic Light Scattering, Tech. Note. (2014) 15. <https://www.malvernpanalytical.com/en/support>.
- [95] P.G. Cummins, E.J. Staples, Particle size distributions determined by a "multiangle" analysis of photon correlation spectroscopy data, *Langmuir*. 3 (1987) 1109–1113. <https://doi.org/10.1021/la00078a040>.
- [96] P. Size, Malvern Instruments Limited, P. Size, Improved component resolution with Multi- Angle DLS (MADLS), Grovewood Road, Malvern, Worcestershire, UK. WR14 1XZ, 2018. <https://www.malvernpanalytical.com/en/learn/knowledge-center/whitepapers/WP180926ImprovedComponentResolutionMADLS> (accessed February 5, 2019).
- [97] L. Bartovská, M. Šišková, Fyzikální chemie povrchů a koloidních soustav, Vysoká škola chemicko-technologická, 2005. http://147.33.74.135/knihy/uid_isbn-80-7080-579-X/pages-img/ (accessed February 3, 2019).
- [98] Malvern Panalytical Ltd, Malvern Instruments Limited, Malvern Panalytical Ltd, Malvern Instruments Limited, Zeta potential: An Introduction in 30 minutes, Zetasizer Nano Serles Tech. Note. MRK654-01. (2017) 1–18. <https://www.malvernpanalytical.com/en/learn/knowledge-center/technical-notes/TN101104ZetaPotentialIntroduction.html> (accessed January 31, 2019).
- [99] Malvern Panalytical Ltd, The influence of ionic strength on surface zeta potential, (2017) 1–5.
- [100] Malvern Instruments, Measuring zeta potential using phase analysis light scattering (PALS), Malvern Guid. (2014) 1–3. <http://www.malvern.com/en/pdf/secure/TN101104PhaseAnalysisLightScattering.pdf>.
- [101] Malvern Panalytical Ltd, Measuring Zeta Potential - Laser Doppler Electrophoresis Explained, 2018. <https://www.malvernpanalytical.com/en/learn/knowledge-center/technical-notes/TN150611LDEExplained> (accessed February 12, 2020).
- [102] E. Weatherall, G.R. Willmott, B. Glossop, Individual nanoparticle zeta potential measurements using tunable resistive pulse sensing, in: 2013 Seventh Int. Conf. Sens. Technol., IEEE, 2013: pp. 874–878. <https://doi.org/10.1109/ICSensT.2013.6727775>.
- [103] Malvern Panalytical Ltd, Zeta potential - An introduction in 30 minutes, (2015) 1–18.
- [104] E.L.C.J.C.J. Blundell, L.J. Mayne, E.R. Billinge, M. Platt, Emergence of tunable resistive pulse sensing as a biosensor, *Anal. Methods*. 7 (2015) 7055–7066. <https://doi.org/10.1039/C4AY03023K>.
- [105] D. Kozak, W. Anderson, R. Vogel, M. Trau, Advances in resistive pulse sensors: Devices bridging the void between molecular and microscopic detection, *Nano Today*. 6 (2011) 531–545. <https://doi.org/10.1016/j.nantod.2011.08.012>.
- [106] G.R. Willmott, M.G. Fisk, J. Eldridge, Magnetic microbead transport during resistive

pulse sensing, *Biomicrofluidics*. 7 (2013) 064106. <https://doi.org/10.1063/1.4833075>.

- [107] Izon Science Support Centre, The Technology TRPS, Izon Sci. (2016). <https://izon.freshdesk.com/support/solutions/articles/14000030802-what-is-tunable-and-why->.

9.1 LIST OF ABBREVIATIONS AND SYMBOLS

A	Absorption of light
$\%I_a$	Relative intensity of particle of the size a
$V_{in,f}$	Input and output flow
$V_{out,f}$	Output flow
u_0	Transverse flow velocity at the accumulation wall
$\langle v \rangle$	Average liquid velocity in cross-section along the channel axis
α_{UV}	Calibration constant of UV detector
A_2	Second virial coefficient
$AF4$	Asymmetrical flow Field-flow fractionation
aRI	Absolute refractive index
B	Amplitude of correlation function
b	Separation channel width
c_0	Analyte concentration at the accumulation wall
CCD	Charged-coupled device
C_s	Particles concentration
CVD	Chemical vapour deposition
d	Diameter of the particle
D	Diffusion coefficient
D_L	The largest pore diameter
DLS	Dynamic light scattering
DLVO	Derjaguin, Landau, Verwey, and Overbeek
DND	Detonation nanodiamonds
DOGS NTA-Ni	1,2-di-(9Z-octadecenoyl)-sn-glycero-3-[(N-(5-amino-1-carboxypentyl)iminodiacetic acid)succinyl] (nickel salt)
D_p	Mean pore diameter
DPH-TMA	(1-(4-Trimethylammoniumphenyl)-6-Phenyl-1,3,5-Hexatriene p-Toluenesulfonate)
dRI	Differential refractive index
D_s	The smallest pore diameter
DSPC	1,2-distearoyl-sn-glycero-3-phosphocholine
DSPE	Distearoylphosphatidylethanolamine
E	Electric field intensity
EFF	Electric Field-flow fractionation
ELS	Electrophoretic light scattering
EPC	1,2-dioleoyl-sn-glycero-3-ethylphosphocholine
EPR	Enhanced permeability and retention
EWG	Electron withdrawing group
$f(ka)$	Henry's function

FFR	Fast field reversal
FIAF4	Frit-Inlet Asymmetrical flow Field-flow fractionation
FIFFF	Flow field Field-flow fractionation
FRR	Flow rate ratio
G	Correlation functions
GP	Graphene platelets
GrFFF	Gravitation/Sedimentation Field-flow fractionation
GUV	Giant unilamellar vesicles
HF5	Hollow fiber Field-flow fractionation
HPHT	High-pressure, high temperature
I	Intensity of transmitted light
I_0	Primary beam intensity
I_θ	Sample scattered light intensity
$I_{\theta,\text{solvent}}$	Solvent scattered light intensity
J	Particle flow
K	Optical constant
k, K_B	Boltzmann constant
l	Distance of the centre of the sample from the accumulation wall
L	Optical path of the flow cell, pore length, and separation channel length
LDL	Low-density lipoprotein
LUV	Large unilamellar vesicles
M	Molecular weight
MADLS	Multi-angle dynamic light scattering
MALDI	Matrix-assisted laser desorption ionization
MALS	Multi-angle light scattering
MgFFF	Magnetic Field-flow fractionation
MLV	Multilamellar
MS	Mass spectrometry
MWCNT	Multi-walled carbon nanotubes
N_a	Avogadro constant
$N_a; N_b$	Number of particles of size $a; b$
ND	Nanodiamond
NIR	Near-infrared
$n_r; \eta_0$	Refractive index of the reference liquid
n_s	Refractive index of the sample
NTA	Nanoparticle tracking analysis
Nu	Nucleophile
NV	Nitrogen-vacancy
P	Pressure

$P(\theta)$	Particle scattering factor
PAA	Poly-amino acid
PALS	Phase analysis light scattering
PBS	Phosphate buffer saline
PEG	Polyethene glycol
PES	Polyethersulfone
PVP	Polyvinyl pyrrolidone
Q	Volume flow
QELS	Quasi-elastic light scattering
r	Detector distance from the source of the scattering light, and radius
R	Rayleigh ratio, and pore resistance
RC	Regenerated cellulose
RES	Reticuloendothelial system
R_g	Radius of gyration
R_h	Hydrodynamic radius
RI	Refractive index
RMS	Root mean square
SDS	Sodium dodecyl sulphate
SEC	Size extrusion chromatography
SFR	Slow Field Reversal
SUV	Small unilamellar vesicles
T	Thermodynamic temperature
t, t_0	Time, and void time
t_{agg}	Aggregation time
TFR	Total flow rate
ThFFF	Thermal Field-flow fractionation
t_{mix}	Mixing time
t_R	Retention time
TRPS	Tunable resistive pulse sensing
$u(x)$	Transverse flow velocity at a distance x
U_e	Electrophoretic mobility
UV	Ultraviolet
v	Analyte migration rate, and scattering volume
$v(x)$	Flow rate
V_0	Volume of the entire channel
V_a	Relative volume of the particle a
V_c	Cross-flow
v_e	Particle movement speed
V_{in}	Inlet flow



VLP	Virus-like particles
v_p	Particle velocity
w	Channel thickness
x	Distance from the accumulation wall of the channel
z_f	Focusing position
γ	Spherical correlation parameter
ε	Dielectric constant
ε_0	Relative permittivity of vacuum
ζ	Zeta potential
η	Dynamic viscosity
θ	Detection angle
κ	Debye length
λ	Retention parameter
λ_0	Laser wavelength
ρ	Electrolyte resistance
τ	Interval between defined frames in NTA analysis
dn/dc	Refractive index increment

10 LISTED PUBLICATIONS

The full scientific papers included in this thesis are listed in chronological order below

OPEN

Preparation of nanoliposomes by microfluidic mixing in herring-bone channel and the role of membrane fluidity in liposomes formation

Jan Kotouček^{1,8}, František Hubatka^{1,8}, Josef Mašek¹, Pavel Kulich¹, Kamila Velínská¹, Jaroslava Bezděková^{1,2}, Martina Fojtíková¹, Eliška Bartheldyová¹, Andrea Tomečková¹, Jana Stráská³, Dominik Hrebík⁴, Stuart Macaulay⁵, Irena Kratochvílová ^{6*}, Milan Raška ^{1,7*} & Jaroslav Turánek^{1*}

Introduction of microfluidic mixing technique opens a new door for preparation of the liposomes and lipid-based nanoparticles by on-chip technologies that are applicable in a laboratory and industrial scale. This study demonstrates the role of phospholipid bilayer fragment as the key intermediate in the mechanism of liposome formation by microfluidic mixing in the channel with “herring-bone” geometry used with the instrument NanoAssemblr. The fluidity of the lipid bilayer expressed as fluorescence anisotropy of the probe N,N,N-Trimethyl-4-(6-phenyl-1,3,5-hexatrien-1-yl) was found to be the basic parameter affecting the final size of formed liposomes prepared by microfluidic mixing of an ethanol solution of lipids and water phase. Both saturated and unsaturated lipids together with various content of cholesterol were used for liposome preparation and it was demonstrated, that an increase in fluidity results in a decrease of liposome size as analyzed by DLS. Gadolinium chelating lipids were used to visualize the fine structure of liposomes and bilayer fragments by CryoTEM. Experimental data and theoretical calculations are in good accordance with the theory of lipid disc micelle vesiculation.

Liposomes, self-assembled nanoparticles based on lipid bilayers are widely employed for biomedical and biotechnological purposes¹. Liposomes are composed of one or more lamellae, consisting of a phospholipid bilayer and enclosing a small volume of aqueous liquid. The diameter of liposomes can vary from tens of nanometers up to hundreds of micrometers depending on the method used for their preparation. Unilamellar or oligolamellar liposomes with an average size of about 80 nm are typically produced and used in medical applications as anti-cancer drug delivery systems².

Phospholipids and lipids, the main components of liposomal membranes, are well soluble in various organic solvents, therefore most present methods use organic solvents (e.g. methanol, ethanol, tert-butanol, chloroform, ethers) to solubilize lipids as a first step in the whole procedure. If the organic solvent is miscible with water, liposomes can be prepared by mixing an alcoholic solution of lipids with aqueous phase. Ethanol injection method² and proliposome-liposome method^{2,3} represent well-established techniques used in the laboratory as well as on an industrial scale^{4–6}.

The advent of microfluidics opens a new door for the on-chip preparation of liposomes and other lipid-based nanoparticles⁷. Microfluidic methods have demonstrated their ability to control the process of mixing the organic

¹Department of Pharmacology and Immunotherapy, Veterinary Research Institute, v.v.i., Hudcova 70, 621 00, Brno, Czech Republic. ²Mendel University in Brno, Department of Chemistry and Biochemistry, Zemedelska 1, 61300, Brno, Czech Republic. ³Regional Centre of Advanced Technologies and Materials, Palacký University, Šlechtitelů 11, 78371, Olomouc, Czech Republic. ⁴Central European Institute of Technology CEITEC, Structural Virology, Masaryk University, Kamenice 753/5, 62500, Brno, Czech Republic. ⁵Malvern Panalytical, Malvern, Worcestershire, United Kingdom. ⁶Institute of Physics, Czech Academy of Sciences, Na Slovance 2, Prague 8, Czechia. ⁷Department of Immunology, Faculty of Medicine and Dentistry, Palacký University Olomouc, Hněvotínská 3, 775 15, Olomouc, Czech Republic. ⁸These authors contributed equally: Jan Kotouček and František Hubatka. *email: krat@fzu.cz; milan.raska@upol.cz; turanek@vri.cz

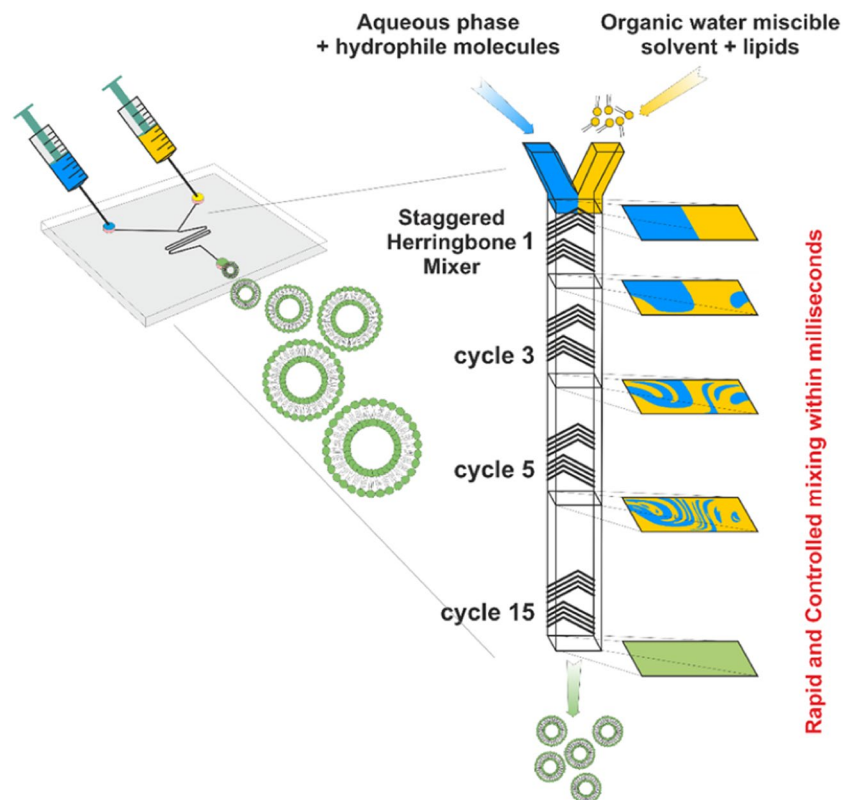


Figure 1. Principle of microfluidic mixing in herring bone channel and formation of liposomes. Organic water miscible solvent (ethanol) contains lipids forming liposomes while water phase contains water soluble components that are to be encapsulated. The mixing process is finished within millisecond and liposomes are formed by the self-assembled mechanism. Various linear injector syringe pumps controlled by computer are used to drive the mixing process.

and water phases, therefore the required parameters of final liposomal products like size, polydispersity, morphology, and lamellarity are achieved in a more reproducible way.

Various systems were designed and constructed for laboratory use and also for the application of this technology on an industrial scale. Microfluidic approaches to liposome production are based on the application of various geometries of mixing channel as well as the application of shear forces, electric field or various microfluidics effects taking place in the channel. A comprehensive review was published recently by Carugo *et al.*⁸, Wang *et al.*⁹ and Maeki^{10,11}. Theoretical models describing kinetic and thermodynamic parameters that determine the formation of liposomes from lipid bilayer disc were described^{12–15}. The process of microfluidic mixing can help in optimizing the method, especially for the production in industrial scale using complex on-chip technology as recently demonstrated^{16,17}.

Here we used the microfluidic mixing channel with “herring bone” geometry to perform nanoprecipitation within milliseconds and nanoliter reaction volumes. “Herring bone” geometry of mixing channel differentiates this process from microfluidic mixing based on microfluidic hydrodynamic flow focusing of an alcohol stream with two aqueous buffer streams¹⁸.

“Herring bone” geometry mixing channels are now available as commercial products together with computer-controlled instruments for laboratory and industrial scale preparation of lipid and polymeric nanoparticles. Therefore, the method is available for wide use to prepare nanoliposomes. The schematic illustration of the preparation of liposomes by microfluidic mixing in herring bone chamber is presented in Fig. 1.

In this study, we applied gadolinium-chelating lipids and cryo-electron transmission microscopy to visualize in detail the structure of liposomes, liposomal membrane, and intermediates formed within the whole process. We tested the effect of lipid membrane fluidity on the final morphology of liposomes expressed as the size distribution, polydispersity, and lamellarity. Based on exact measurements of lipid membrane fluidity (polarization of fluorescence) we predicted the effect of this parameter on the critical size of disc micelle intermediates and therefore their tendency to vesiculate and form liposomes^{3,19,20}. Experimental data were compared with theoretical prediction following from the model based on Helfrich bending energy and analyses of the energetics and thermodynamics of vesicle formation¹⁵.

Lipid type	$D_{\min, \text{calculated}}^{\#}$ (nm)	$D_{\text{sonication}}^{\#}$ (nm)	$D_{\min, \text{calculated}}^*$ (nm)	$D_{\text{microfluidic}}$ (nm)
EPC	17.3	21.8	ND	22.0
DMPC	13.4	16.8	14.1	14.3
SOPC	ND	ND	17.1	22.3

Table 1. Comparison of liposomal theoretical diameter with sonicated vesicles and vesicles prepared by microfluidic mixing. From the number distribution ($D_{\text{microfluidic}}$) the minimal size of the vesicles was compared with theoretical values ($D_{\min, \text{calculated}}^{\#}$), vesicles based on the sonication method ($D_{\text{sonication}}^{\#}$). [#]Data from citation¹⁵. ^{*} D_{\min} calculation based on d_0 and d published in Handbook of lipid bilayers, second edition, Derek Marsh³³.

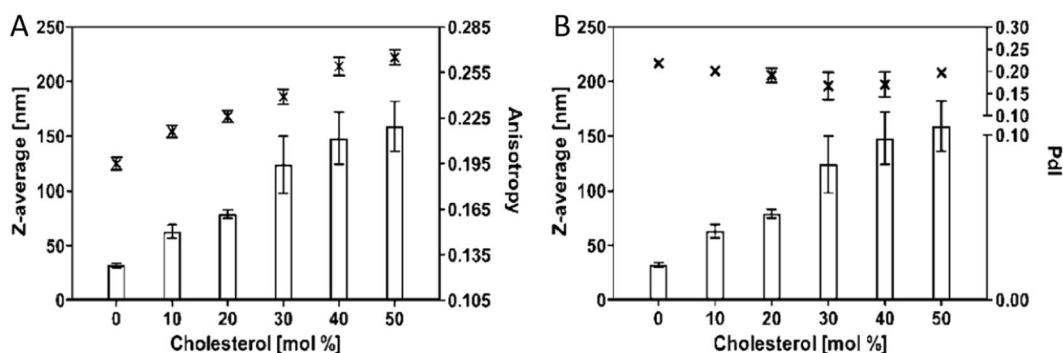


Figure 2. Effect of cholesterol on size, polydispersity, and anisotropy of liposomes prepared from unsaturated phospholipids (EPC). **(A)** The plot of cholesterol concentration (mol %) versus Z-average diameter (nm) on the major axis and steady state fluorescence anisotropy of the DPH-TMA on the minor axis. **(B)** The plot of cholesterol concentration (mol%) versus Z-average diameter (nm) on the major axis and polydispersity index (PDI) and on the minor axis.

Results

The size distribution of liposomes composed saturated and unsaturated lipids. In the first experiment, the prediction based on the theoretical model describing the critical size of liposomes composed of various lipids was verified¹⁵. The sizes of liposomes composed of EPC, SOPC, and DMPC were compared to published theoretical and experimental data^{21,22}. The size distribution of liposomes prepared by microfluidic mixing were in a good accordance with the theoretical prediction. The results are summarized in Table 1. We were not able to prepare liposomes composed only from DSPC without the addition of cholesterol. Therefore, the data on pure DSPC were not included in Table 1 and also in distribution analyses.

Effect of cholesterol on the size distribution of liposomes prepared by microfluidic mixing. Liposomes prepared by microfluidic mixing exhibit various size properties based on the saturated/unsaturated chains of lipids and on the cholesterol content while maintaining the same preparation conditions as the Flow Rate Ratios (3:1) and Total Flow Rate (7 ml/min).

By Flow Rate Ratios (FRR) is meant the volumetric ratio of the organic and aqueous medium mixed through the microfluidic channel and Total Flow Rate is defined as a sum of the volumetric ratio of organic and aqueous medium pumped through the two inlets.

Preparation of liposomes composed of unsaturated lipids. For unsaturated lipids as EPC, the increase of cholesterol content resulted in an increase in the size of the liposomes (Fig. 2). Increased cholesterol content in the lipid bilayer composed of unsaturated phospholipids resulted in a decrease in the fluidity/elasticity of liposomal lipid bilayer. This effect was demonstrated by both complementary physical-chemical parameters as an increase of anisotropy and a decrease of fluidity which is directly related to the elasticity of the phospholipid bilayer. Fluidity was expressed as anisotropy of steady state fluorescence of molecular probe DPH-TMA. Steady-state anisotropy of the probe in non-organized systems such as in n-heptane reached values 0.001. In organized systems such as liposomes, DPH-TMA is oriented along the hydrocarbon chains²⁰ in which rotation is reduced and anisotropy is increased. With decreasing fluidity of the bilayer structure, anisotropy values increased from 0.195 (without cholesterol) to 0.265 (50 mol% of cholesterol) (Fig. 2). PDI of prepared liposomes was not substantially changed by cholesterol content and the PDI values were within the range 0.17–0.23.

Preparation of liposomes composed of saturated lipids. Saturated lipids such as DSPC exhibit different properties. Cholesterol in bilayer structure is increasing the fluidity of the fragment which allows the formation of smaller vesicles (Fig. 3). Steady state anisotropy is gradually decreasing with increasing cholesterol content from 0.288 to 0.187 for 10 mol% and 50 mol% respectively. In comparison to unsaturated phospholipids, PDIs

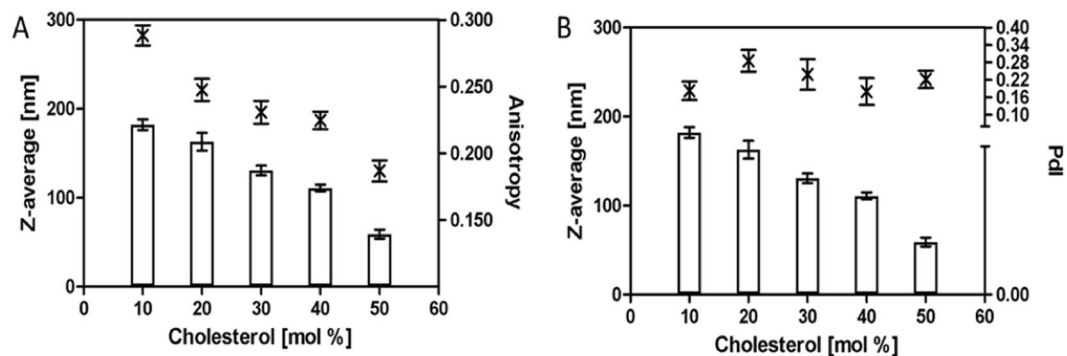


Figure 3. Effect of cholesterol on size, polydispersity, and anisotropy of liposomes prepared from saturated phospholipids (DSPC). (A) The plot of cholesterol concentration (mol %) versus Z-average diameter (nm) on the major axis and steady state fluorescence anisotropy of the DPH-TMA on the minor axis. (B) The plot of cholesterol concentration (mol %) versus Z-average diameter (nm) on the major axis and polydispersity index (PDI) and on the minor axis.

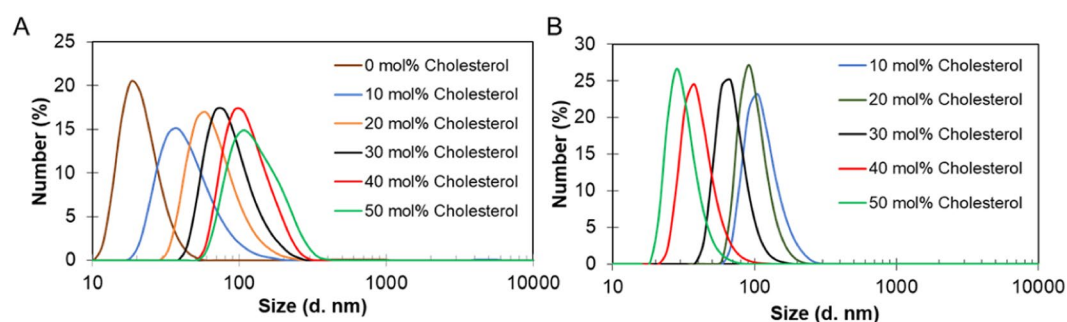


Figure 4. Size distribution by the number of (A) EPC/Cholesterol and (B) DSPC/Cholesterol liposomes with increasing cholesterol concentration from 10 mol% to 50 mol%.

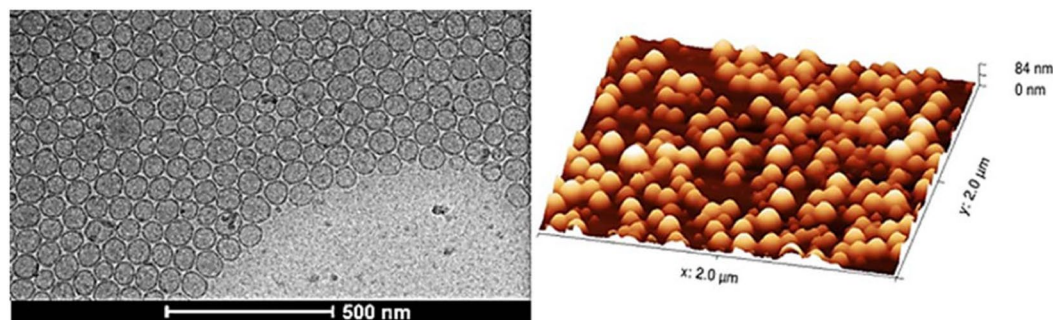


Figure 5. Structure of liposomes revealed by cryoelectron transmission microscopy and atomic force microscopy. Liposomes were prepared by the microfluidic mixing method. The composition was DSPC:Chol 70:30 Cryo-TEM picture (left) and AFM picture (right).

of liposomes composed of saturated phospholipids were slightly higher, but again they were not substantially changed by cholesterol content and were within the range 0.20–0.28.

Size distribution by number reflects the most numerous population of liposomes. The effect of cholesterol on the size distribution of liposomes composed of unsaturated and saturated phospholipids is presented in Fig. 4. The example of liposomes (DSPC:Chol 70:30) prepared by microfluidic mixing and visualized by cryoTEM and AFM is in Fig. 5. Unilamellarity of liposomes and homogeneity in the size distribution is in correlation with DLS data.

Electron microscopy of Gd-labelled liposomes. Phosphorus atoms in phospholipids are responsible for contrast in cryo-electron microscopy enabling visualization of the phospholipid bilayer. Atoms of gadolinium

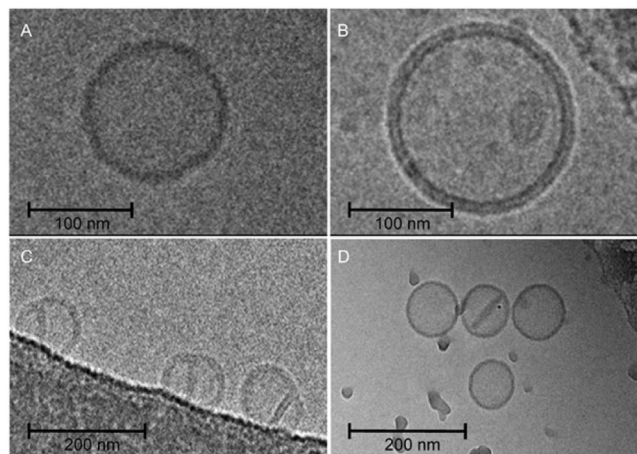


Figure 6. Cryo-TEM images of a liposomes: (A) control sample (Table 1, composition 3), width of phospholipid bilayer ≈ 4.3 nm, (B) liposomes containing 5% of Gd-lipid (Table 1, composition 3), width of phospholipid bilayer ≈ 5.8 nm, (C) liposomes (Table 1, composition 1) with a lipid membrane fragment and (D) conjugated liposomes (Table 1, composition 3).

chelated in Ga-lipids represent much more dense material for electrons, therefore sharp and strong visualization of the lipid bilayer in liposomes can be achieved.

The resolution of the outer and inner lipid layers of the liposomal bilayer can be clearly observed because of the larger distance of Gd in the bilayer when compared to phosphorus atoms (Fig. 6A,B). Therefore, the bilayer character of fragments of bilayers (Fig. 6D), as well as a bilayer partition separating two conjugated liposomes (Fig. 6C), were demonstrated by cryo-electron transmission microscopy. The presence of Gd in liposomes was confirmed by TEM-EDX (Supporting data Fig. S1A,B) and three Gd peaks were identified when liposome was scanned (Supporting data Fig. S1B).

Discussion

Microfluidic mixing represents a promising technology for the production of complex liposomal preparations¹⁵ and the application of on-chip technology as demonstrated recently^{3,10}. Gadolinium complexes are used as MRI contrast agents and liposomes represents a versatile platform for the application of gadolinium *in vivo* imaging and development of theranostics^{23–25}. Gadolinium lipid complexes represent also a useful tool for visualization of lipid structures by cryoTEM as we demonstrated in this article.

Knowledge of mechanisms of liposome formation during microfluidic mixing is of importance to optimize the process on both laboratory and industrial scale. Various forms of bilayer phospholipid fragments (BPF) were supposed as intermediates during the process of liposome formation²⁶. For example, disc-like bilayer micelles (DBM) are intermediates formed during the process of the detergent removal method and vesiculation of these disc micelles creates liposomes very homogeneous in their size distribution^{27,28}. On the other hand, stacked bilayer fragments are the main intermediates formed in the proliposome-liposome method^{12,13}. Because the liposome preparation by application of microfluidic mixing method is based on similar principles, such as the proliposome-liposome method or ethanol injection method, it is reasonable to assume that BPF in the form of DBM is also an intermediate in the process of liposome formation.

Vesiculation of bilayer disc micelles in aqueous milieu is a spontaneous process driven by the minimization of the line tension energy originated in the exposure of the nonpolar hydrophobic tails of lipid molecules, which are presented along the edge of the disc membrane micelles, to polar water molecules. Vesiculation, as the process of transformation of a planar bilayer membrane into a sphere, is hindered by the resistance of the lipid membrane towards bending. Therefore, it becomes possible only when the driving force is sufficiently high to overcome the corresponding resistance towards bending.

The formation of vesicles starts within milliseconds from small aggregates of individual amphiphilic lipid molecules to disk-like bilayer structures formed in the rapid process of self-assembly. (Fig. 7A). Growing bilayer structures generally tend to maintain a circular disc configuration to keep the overall line tension energy at a minimum. After reaching a certain critical size the bilayer structure tends to curve to further reduce the line energy. (Fig. 7B,C). Finally, the cup-like structure closes to form a spherical vesicle, as shown in Fig. 7D. This mechanism implies the formation of a vesicle of minimal size related to the minimal size of disc micelle.

The reduction in line energy during the transition from a planar DBM to a closed vesicle is countered by an increase in the membrane bending energy. The size of vesicles depends on membrane size growth kinetics, but there is a critical membrane size below which vesiculation is energetically unfavorable. It means that below the critical diameter of DMB vesicles are not formed and it implies also a critical diameter of vesicles, which depends on lipid composition determining the fluidity/flexibility of lipid bilayer.

Basic equations describing the energy of various intermediates in the process of liposome formation was recently described by Huang *et al.*¹⁵. Planar disc bilayer micelle with a diameter of $D = 2l$, as shown in Fig. 7, was considered by the authors and they described the system energy by the equation:

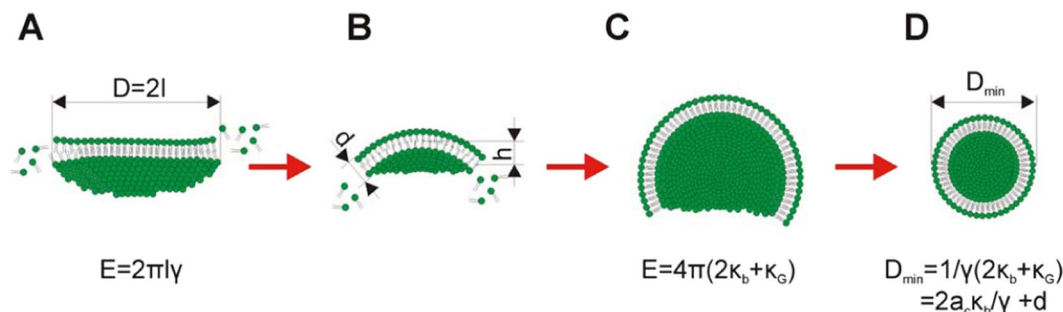


Figure 7. A schematic illustration of vesicle formation in the process of self-assembly. A planar disc-like micelle (A) curves into a spherical cap (B and C) and finally closes to form a vesicle (D). Equations are described in the text.

$$E = \frac{1}{2}\pi\kappa_b \cdot \left(\frac{4h}{l} - l c_0\right)^2 + 4\pi\kappa_G \cdot \left(\frac{h}{l}\right)^2 + \frac{16}{l^2}\pi B \cdot \left(\frac{h}{l}\right)^4 2\pi\sqrt{l^2 - h^2}\gamma \quad (1)$$

where $h \in [0, l]$ is the height of the spherical cap that effectively indicates vesicle shape evolution ($h = 0$) corresponds to a planar patch; $h = l$ corresponds to a spherical vesicle, $B = \kappa_1 + \kappa_2 + \kappa_3$, where κ_1 , κ_2 , and κ_3 are fourth-order moduli; γ is line tension; κ_G is Gaussian bending stiffness, κ_b is the bending stiffness, and c_0 is the spontaneous curvature. The last term in Eq. (1) is the line energy along the free edge, where γ is the line tension.

Based on assumption that the number of lipid molecules in the micelle and formed liposome remains constant (it implies the same surface of micelle and vesicle formed from it), during the process of vesiculation, the membrane is assumed to maintain a uniform curvature. For an initially flat disc-like membrane micelle $h = 0$ and the system energy in Eq. (1) reduces to $E_1 = 2\pi l\gamma$. For a fully vesiculated sphere $h = l$ and Eq. (1) is reduced to $E_2 = 8\pi\kappa_b + 4\pi\kappa_G + 16\pi B/l^2$, which can be further reduced to $E_2 = 4\pi\kappa_b$ for the case of linear elasticity $B = 0$ and $\kappa_G \approx -\kappa_b$ ²⁹.

For the transition from the DBM configuration into a spherical vesicle, it must stand that $E_2 \leq E_1$. Based on above assumption the lower diameter of the circular DBM that can possibly form a spherical vesicle is given by $l^* = 2\kappa_b/\gamma$, $l = a l^*$, where the scaling parameter $a \geq 1$ ¹⁵.

The lower outer diameter of spontaneously self-assembled vesicles can be expressed as:

$$D_{\min} = a_c l^* + d = 2a_c \frac{\kappa_b}{\gamma} + d \quad (2)$$

where d is the thickness of the membrane bilayer and a critical membrane size $l = a_c l^*$, where a_c is the critical scaling parameter. Because differences in the thickness of the membrane formed from different phospholipids are relatively small, the main factor effecting D_{\min} is the value of κ_b . While κ_b is related to the elasticity of the membrane reflected also by its fluidity, parameter γ depends presumably on the character of hydrocarbon chain (e.g. content of saturated and unsaturated acyls in phospholipid molecule) and its length. Therefore, the critical diameter of the disc micelle l^* is strongly dependent of κ_b , as demonstrated by the effect of cholesterol on the size of liposomes (Figs. 1–3). Bending energy determines the critical size of DBM and is the crucial thermodynamic parameter ruling the process of vesiculation of DBM. Lipid composition of DBM and temperature are the main factors effecting bending energy and therefore the final size of formed vesicles. Direct mathematical relation of bending stiffness (generally obtained from measurements on giant liposomes), linear tension and anisotropy are not described by theoretical models. We used fluorescence anisotropy data as a parameter reflecting the relative fluidity of phospholipid bilayers with the different cholesterol content. Parameters like fluidity/elasticity of the lipid bilayer reflect bending energy can be obtained experimentally by independent methods e.g. measurement of anisotropy of fluorescence, as we applied in this study.

During the process of microfluidic mixing of water and alcohol-lipid phases, the edges of DBM are not stabilized and any formed DBMs are short lived metastable structures. The thermodynamic instability at the edges of the DBM causes bending and when the DBM closes upon itself, a vesicle is formed. Therefore, the vesiculation of DBM is driven by minimizing their edge energy. As the bilayer rearranges from a flat disc into a sphere, the total energy of the system first increases due to contributions from the bending energy of the bilayer. Subsequently, the total energy decreases as the edges disappear during the process of closing of DBM and finally disappear when vesicles are formed.

Fluidity (reflected by the value of anisotropy) correlated well with the final size of liposomes (Figs. 1–3) and their lipid composition. The solidification effect of cholesterol on lipid membranes composed of unsaturated phospholipids (in our study we used EPC) was reflected by a decrease of the fluidity of the membrane. The size of the liposomes was increased as predicted by the model based on DBM. An opposite effect of cholesterol was observed on membranes formed by saturated phospholipids (in our study we use DPPC). The softening of the phospholipid membrane was reflected by an increase of fluidity. The final size distribution of liposomes increased with increasing cholesterol content in the membrane. The role of fluidity as the crucial parameter ruling

the vesiculation of DBM is supported by the comparison of the values of anisotropy and the size of liposomes prepared from unsaturated or saturated lipids mixed with cholesterol (compare Figs. 1 and 2).

Nevertheless, present models of liposome formation are static while the formation of disc micelles and their vesiculation are highly dynamic processes. Therefore, kinetic aspects of vesicle formation are responsible for an increase of the final size of liposomes above theoretical values, predicted from static models. Moreover, static models do not involve the important factors such as shearing forces occurring during rapid flow mixing in the herring-bone like channel.

Formation of larger vesicles can be eliminated by shearing forces and septum in coalescent liposomes can be forced apart of the bilayer to form disc micelles encapsulated inside the liposomes (Fig. 6C,D), as discussed below. One has to keep in mind, that the DLS method gives an average size of liposomes, while the critical size of liposomes (smallest liposomes) can be measured only by cryoTEM.

Jahn and colleagues used cryo-SEM methods to visualize lipid structures formed during the process based on microfluidic hydrodynamic flow focusing on an alcohol stream with two aqueous buffers streams¹⁹. In this study, the authors used cryo-SEM imaging to demonstrate a mixture of spherical vesicles as well as disc-like lipid structures, fractured or incomplete vesicles, and flat aggregate structures. The disc-like bilayer fragments were presented in rapidly frozen samples observed by cryo-SEM. Application of the above-mentioned method is technically difficult if impossible for a herring bone like channel in the compact cartridge. Therefore, we used the approach based on cryo-TEM and Gd-chelating lipids to search for residual traces of various intermediates and to visualize a detailed structure of the lipid double layer in liposomal membranes. Firstly, we confirmed the presence of Gd in the liposomal bilayer by TEM with EDX to rule out possible misinterpretations. The spatial co-localization of Gd with liposomes was proved by this method. Therefore, the clear resolution of both lipid layers forming a liposomal bilayer can be attributed to Gd providing strong electron contrast (Fig. 4). Among many perfectly formed liposomes, we were able to find several liposomes preserving imperfections pointing to intermediates formed during the process of liposome formation. In Fig. 6C we can see conjugated liposomes with a bilayer septum dividing their internal space. One liposome with a disc-like bilayer fragment inside the internal volume is presented (Fig. 6D). These two morphological structures point to the mechanism of liposome formation based on the assembly of DBMs and their vesiculation when their critical size is reached. The proposed mechanism is described in Fig. 8.

The Fig. 8 indicates that morphological and size distribution uniformity of liposomal preparations produced by the microfluidic mixing method is ruled by the physical-chemical character of DBM, which can be expressed in well-defined and quantifiable terms as the fluidity of the lipid double-layer membrane.

Application of Gd-lipids and cryoTEM revealed some residual “witness” of bilayer structures formed in the process of microfluidic mixing. BPF is first formed in the early stages of mixing. This was also supposed by Maeki and colleagues who studied the effect of flow rate on the size of POPC liposomes prepared by microfluidic mixing in herring-bone channel¹¹.

The mechanism of vesiculation is the reason for the high uniformity of liposomal preparations obtained by the method of microfluidic mixing. Of course, at higher concentration of lipids the rapid growth of DBM can lead to the formation of imperfection in DBMs like forks on their rims and finally coalescent liposomes are formed. These rare liposomal structures can be stabilized by various morphological transformations to decrease tension in the lipid bilayer. In principle, fusion and splitting are processes taking place in this case. The formation of two smaller liposomes (splitting) or one larger liposome (fusion) is the result of this transformation. The presence of a small amount of larger and smaller liposomes is demonstrated in Fig. 3. The incomplete fusion process can also lead to larger liposomes with fragments of the bilayer inside entrapped (Fig. 6C,D).

It is known that various sterols, especially cholesterol, affect structure and fluidity of phospholipid membranes. The influence of sterols like cholesterol or β -sitosterol at various concentrations up to 50 mol% on liposomal membrane fluidity, liposome size and thermal transition was tested on small unilamellar liposomes (SUV) prepared by lipid hydration methods and sonication^{30,31}. The authors confirmed concentration dependent impact of sterols on membrane fluidity, but only small effect was observed with respect to the final size of SUV liposomes prepared by ultrasonication. In comparison to ultrasonication characterised by the application of high energy for disruption of large liposomes to form smaller ones, during microfluidic mixing different mechanisms are acting in liposome formation. Moreover, lower energy is used for running the process.

Microfluidic mixing as the method using low dispersive energy represents a promising technology to produce complex liposomal preparations¹⁰ and the application of on-chip technology as demonstrated recently^{2,11}. Gadolinium complexes are used as MRI contrast agents and liposomes represents a versatile platform for the application of gadolinium *in vivo* imaging and development of theranostics^{18–20}. Our manuscript describes the application of microfluidic mixing for the preparation of Ga-liposomal contrast for MRI. *In vitro* toxicological study proved potential biocompatibility as documented by Simeckova at al Gadolinium labelled nanoliposomes as the platform for MRI theranostics: *in vitro* safety study in liver cells and macrophages, in press, Scientific Reports.

Conclusions

Lipid composition affects fluidity and elasticity of the bilayer and represents an important factor for the preparation of liposomes by microfluidic mixing. The right setting of the fluidity of lipid composition allows the preparation of liposomes with desired physical properties like size distribution, morphology. Microfluidic mixing can also be used for *in situ* preparation of therapeutics and contrast agents for diagnostics, minimizing problems with chemical (e.g. lipid oxidation and hydrolysis) and morphological instability (e.g. aggregation, fusion). These future perspectives are of interest as point-of-care personalized liposome therapeutic treatments.

lipid	composition (molar % of lipid)				
	1	2	3	4	5
18:0 PE DTPA (Gd)	5	—	—	—	—
DMPC	—	—	—	—	100
SOPC	—	—	—	—	100
DSPC	—	—	(90–50)	—	—
EPC	65	70	—	(100–50)	—
Cholesterol	30	30	(10–50)	(0–50)	—

Table 2. Lipid compositions of the liposome formulation.

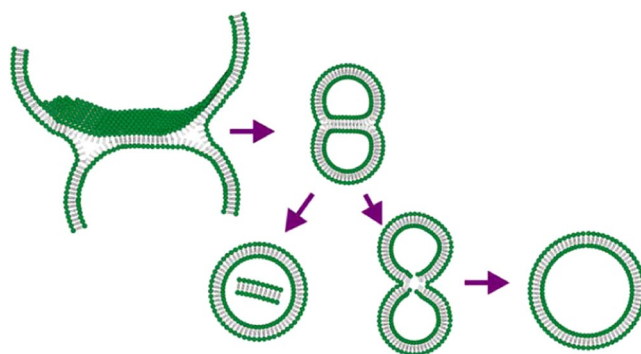


Figure 8. Schematic description of possible rare transition intermediates in the process of liposome formation by microfluidic mixing.

A proper understanding of the physical-chemical factors and processes leading to the formation of liposomes by microfluidic techniques to which this work contribute is very important for the development of a new technological process.

In this work, the way of liposome formation by microfluidic mixing in a “herring bone” channel is presented. The fluidity of the lipid bilayer expressed as fluorescence anisotropy of the probe N,N,N-Trimethyl-4-(6-phenyl-1,3,5-hexatrien-1-yl) was found to be the basic parameter affecting the final size of formed liposomes prepared by microfluidic mixing of an ethanol solution of lipids and water phase. Both saturated and unsaturated lipids together with various content of cholesterol were used for liposome preparation and it was demonstrated, that an increase in fluidity results in a decrease of liposome size as analyzed by DLS.

We were the first who showed the impact of fluidity on the size of liposomes produced by microfluidic mixing in herring-bone like channel and who confronted experimental results with theory (Huang *et al.*)¹⁵. The models of liposome formation are static while the formation of disc micelles and their vesiculation is a highly dynamic process. Static models of liposomes formation do not involve the important factors such as shearing forces occurring during rapid flow mixing in the herring-bone like channel. In our case, kinetic aspects of vesicle formation were responsible for an increase of the final size of liposomes above theoretical values.

Experimental Section

Chemicals. Fluorescence probes: N,N,N-Trimethyl-4-(6-phenyl-1,3,5-hexatrien-1-yl) (DPH-TMA) was purchased from Sigma-Aldrich, USA.

Lipids: 1,2-distearoyl-sn-glycero-3-phosphoethanolamine-N-diethylenetriaminepentaacetic acid (18:0 PE DTPA (Gd)), 1,2-dimyristoyl-sn-glycero-3-phosphocholine (DMPC), 1-stearoyl-2-linoleoyl-sn-glycero-3-phosphocholine (SOPC) 1,2-dioleoyl-sn-glycero-3-ethylphosphocholin (EPC 95%), 1,2-distearoyl-sn-glycero-3-phosphocholine (DSPC) and cholesterol were purchased from Avanti lipids USA, with purity of 99%. All other chemicals were purchased from Sigma-Aldrich, USA.

Microfluidic mixing. The required amount of individual lipids according to the desired composition (Table 2) were dissolved in anhydrous ethanol and in a mixture of EtOH:DMSO (1:1) for composition 2,3,4 and 1, respectively at 4 mg/ml. The organic and aqueous phase (Milli-Q water) were rapidly mixed using the NanoAssemblr Benchtop instrument (Precision NanoSystems, Canada) at defined Flow Rate Ratios (FRR) 1:3 and Total Flow Rate (TFR) 7 ml/min to form unilamellar liposomes 1 mg/ml of lipid. During the mixing process, the temperature was controlled using NanoAssemblr Benchtop Heating Controller accessory (Precision NanoSystems, Canada). For preparation of liposomes containing DSPC, the temperature was set to 65 °C, respectively. NanoAssemblr instrument setting is presented at Fig. 9.

Characterization of liposomes by dynamic light scattering (DLS). Samples of liposomes suspension (1 mg/ml and 2 mg/ml) were diluted 1:10 using Milli-Q water. The diluted suspension was placed in a disposable,

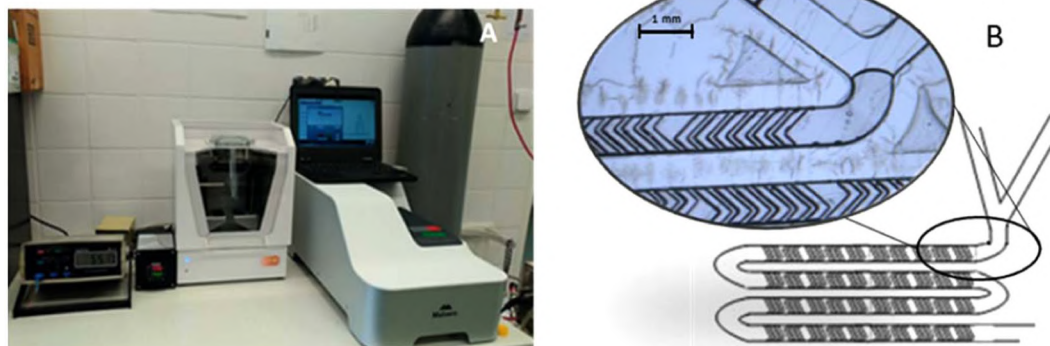


Figure 9. NanoAssemblr instrument settings with precise measurement of the temperature in the mixing cartridge and Zetasizer Ultra for size distribution measurement (A), Detail of microfluidic mixing “herringbone” structure in the NanoAssemblr Microfluidic Cartridge (B).

low volume cuvette with path length 10 mm (Malvern Instruments, UK). For the liposomes size distribution, the Zetasizer Ultra (Malvern Panalytical, UK) operating at detection angle of 173° at room temperature was used.

Characterization of liposomes by electron microscopy (TEM, EDX, Cryoelectron microscopy).

Transmission electron microscopy. Liposomes have been suspended inside a drop of PBS. The subsequent suspension got included with a grid coated with Formvar (Sigma-Aldrich, Czech Republic) and carbon (Agar Scientific, Austria). The lattice got expelled from the suspension after 1 min, and the leftover water dried with a segment of filtration paper. Philips 208 S Morgagni (FEI, Czech Republic) at $7,500\times$ amplification and a quickening voltage of 80 kV was used for samples visualization.

Identification of Gd in liposomes by TEM-EDX. We used liposomes without negative staining, only labelled by gadolinium lipid. Transmission electron microscope Jeol 2100, 100 kV coupled with energy dispersed spectroscopy system (Silicon Lithium Detector, Oxford x-MAX 80 T, SSD, England) was used for chemical analysis and detection of gadolinium in liposomes.

Cryo-EM sample preparation and micrograph acquisition. Previously published methods were applied for sample preparation⁶.

Characterization of liposomes by Atomic force microscopy (AFM)³². This picture has been obtained by the NanoWizard 4 (JPK) instrument. The measurement was proceeded in the QI Mode in combination with qp-BioAC-10 cantilever. Liposomes were resuspended in PBS buffer and fixated on freshly cleaved mica slides.

Measurement of anisotropy as a parameter of fluidity of liposomal membrane. Steady-state fluorescence anisotropy measurements were obtained in the L-format using Chronos DFD Fluorescence spectrometer (ISS, USA) equipped with 300 W Cermax xenon arc lamp (ISS, USA), calcite Glan-Thompson polarizer, concave holographic grating monochromator and PMT detector. Monochromator was set up at 355 nm and 430 nm for excitation and emission wavelength respectively. The correction factor of emission monochromator transmission efficiency was obtained from the ratio of emission intensity at 0° and 90° with the excitation polarizer oriented at 90° . Measurements were performed at 25°C and 55°C for liposomes containing EPC (composition 4) and DSPC (composition 3). Values were recorded using Vinci software (ISS, USA) in a twenty-fold repeat (Fig. 9).

Received: 28 June 2019; Accepted: 10 March 2020;

Published online: 27 March 2020

References

- Zylberberg, C. & Matosevic, S. Pharmaceutical liposomal drug delivery: a review of new delivery systems and a look at the regulatory landscape. *Drug Deliv.* **23**, 3319–3329 (2016).
- Belfiore, L. *et al.* Towards clinical translation of ligand-functionalized liposomes in targeted cancer therapy: Challenges and opportunities. *J. Control. release* **277**, 1–13 (2018).
- Perrett, S., Golding, M. & Williams, W. P. A Simple Method for the Preparation of Liposomes for Pharmaceutical Applications: Characterization of the Liposomes. *J. Pharm. Pharmacol.* **43**, 154–161 (1991).
- Pons, M., Foradada, M. & Estelrich, J. Liposomes obtained by the ethanol injection method. *Int. J. Pharm.* **95**, 51–56 (1993).
- Turanek, J. *et al.* Linkup of a fast protein liquid chromatography system with a stirred thermostated cell for sterile preparation of liposomes by the proliposome-liposome method: Application to encapsulation of antibiotics, synthetic peptide immunomodulators, and photosens. *Anal. Biochem.* **249**, 131–139 (1997).
- Bartheldyová, E. *et al.* Hyaluronic Acid Surface Modified Liposomes Prepared via Orthogonal Aminoxy Coupling: Synthesis of Nontoxic Aminoxy lipids Based on Symmetrically α -Branched Fatty Acids, Preparation of Liposomes by Microfluidic Mixing, and Targeting to Cancer Cells Expressi. *Bioconjug. Chem.* **29**, 2343–2356 (2018).

7. Capretto, L., Carugo, D., Mazzitelli, S., Nastruzzi, C. & Zhang, X. Microfluidic and lab-on-a-chip preparation routes for organic nanoparticles and vesicular systems for nanomedicine applications. *Adv. Drug Deliv. Rev.* **65**, 1496–1532 (2013).
8. Carugo, D., Bottaro, E., Owen, J., Stride, E. & Nastruzzi, C. Liposome production by microfluidics: potential and limiting factors. *Sci. Rep.* **6**, 25876 (2016).
9. Wang, X. *et al.* Synthesis of Biomaterials Utilizing Microfluidic Technology. *Genes (Basel)*. **9**, 283 (2018).
10. Maeki, M., Kimura, N., Sato, Y., Harashima, H. & Tokeshi, M. Advances in microfluidics for lipid nanoparticles and extracellular vesicles and applications in drug delivery systems. *Adv. Drug Deliv. Rev.* **128**, 84–100 (2018).
11. Maeki, M. *et al.* Understanding the formation mechanism of lipid nanoparticles in microfluidic devices with chaotic micromixers. *PLoS One* **12**, e0187962 (2017).
12. Campelo, F., Arnarez, C., Marrink, S. J. & Kozlov, M. M. Helfrich model of membrane bending: From Gibbs theory of liquid interfaces to membranes as thick anisotropic elastic layers. *Adv. Colloid Interface Sci.* **208**, 25–33 (2014).
13. Guida, V. Thermodynamics and kinetics of vesicles formation processes. *Adv. Colloid Interface Sci.* **161**, 77–88 (2010).
14. Patil, Y. P. & Jadhav, S. Novel methods for liposome preparation. *Chem. Phys. Lipids* **177**, 8–18 (2014).
15. Quinn, D. *et al.* Formation and size distribution of self-assembled vesicles. *Proc. Natl. Acad. Sci.* **114**, 2910–2915 (2017).
16. Hood, R. R., Vreeland, W. N. & DeVoe, D. L. Microfluidic remote loading for rapid single-step liposomal drug preparation. *Lab Chip* **14**, 3359 (2014).
17. Dimov, N., Kastner, E., Hussain, M., Perrie, Y. & Szita, N. Formation and purification of tailored liposomes for drug delivery using a module-based micro continuous-flow system. *Sci. Rep.* **7**, 1–13 (2017).
18. Stroock, A. D. *et al.* Chaotic Mixer for Microchannels. *Science (80-)*. **295**, 647–651 (2002).
19. Jahn, A. *et al.* Microfluidic mixing and the formation of nanoscale lipid vesicles. *ACS Nano* **4**, 2077–2087 (2010).
20. do Canto, A. M. T. M. *et al.* Diphenylhexatriene membrane probes DPH and TMA-DPH: A comparative molecular dynamics simulation study. *Biochim. Biophys. Acta - Biomembr.* **1858**, 2647–2661 (2016).
21. Venetiä, R., Leunissen-Bijvelt, J., Verkleij, A. J. & Ververgaert, P. H. J. T. Size determination of sonicated vesicles by freeze-fracture electron microscopy, using the spray-freezing method. *J. Microsc.* **118**, 401–408 (1980).
22. Maulucci, G. *et al.* Particle Size Distribution in DMPC Vesicles Solutions Undergoing Different Sonication Times. *Biophys. J.* **88**, 3545–3550 (2005).
23. Koudelka, S. *et al.* Liposomal nanocarriers for plasminogen activators. *J. Control. Release* **227**, 45–57 (2016).
24. Busquets, M. A., Estelrich, J. & Sánchez-Martín, M. J. Nanoparticles in magnetic resonance imaging: from simple to dual contrast agents. *Int. J. Nanomedicine* **1727**, <https://doi.org/10.2147/IJN.S76501> (2015).
25. Lux, J. & Sherry, A. D. Advances in gadolinium-based MRI contrast agent designs for monitoring biological processes *in vivo*. *Curr. Opin. Chem. Biol.* **45**, 121–130 (2018).
26. Lasic, D. D. Mechanisms of Liposome Formation. *J. Liposome Res.* **5**, 431–441 (1995).
27. Schubert, R. Liposome Preparation by Detergent Removal. In 46–70. [https://doi.org/10.1016/S0076-6879\(03\)67005-9](https://doi.org/10.1016/S0076-6879(03)67005-9) (2003).
28. Mašek, J. *et al.* Immobilization of histidine-tagged proteins on monodisperse metallochelation liposomes: Preparation and study of their structure. *Anal. Biochem.* **408**, 95–104 (2011).
29. Hu, M., Briguglio, J. J. & Deserno, M. Determining the Gaussian Curvature Modulus of Lipid Membranes in Simulations. *Biophys. J.* **102**, 1403–1410 (2012).
30. Jovanović, A. A. *et al.* Comparative Effects of Cholesterol and β -Sitosterol on the Liposome Membrane Characteristics. *Eur. J. Lipid Sci. Technol.* **120**, 1800039 (2018).
31. Macdonald, A. G., Wahle, K. W. J., Cossins, A. R. & Behan, M. K. Temperature, pressure and cholesterol effects on bilayer fluidity: a comparison of pyrene excimer/monomer ratios with the steady-state fluorescence polarization of diphenylhexatriene in liposomes and microsomes. *BBA - Biomembr.* **938**, 231–242 (1988).
32. Fekete, L., Kúsová, K., Petrák, V. & Kratochvílová, I. AFM topographies of densely packed nanoparticles: a quick way to determine the lateral size distribution by autocorrelation function analysis. *J. Nanoparticle Res.* **14**(1), 1062 (2012).
33. Marsh, D. *Handbook of Lipid Bilayers*. (Boca Raton, FL.: CRC Press, Taylor & Francis Group, 2013).

Acknowledgements

This work was supported by the following grants: The Ministry of Education, Youth and Sports OPVVV PO1 project “FIT” (Pharmacology, Immunotherapy, nanoToxicology) CZ.02.1.01/0.0/0.0/15_003/0000495 (JT, MR), European Structural and Investment Funds and the Czech Ministry of Education, Youth and Sports (Project No. SOLID21 - CZ.02.1.01/0.0/0.0/16_019/0000760, LO1409) (IK) the Ministry of Health CZ AZV-ČR 16–30299 A (JT, JM); Supported by the Ministry of Agriculture of the Czech Republic, institutional support MZE-RO0518. Access to instruments in the laboratory NanoPharm (join project of Veterinary Research Institute and International Clinical Research Center (FNUSA-ICRC)(JT) is acknowledged, as well as support by Education and Research Centre VRI-Malvern (JT, MK).

Author contributions

J. Turánek, Milan Raška and Irena Kratochvílová – design of experiments, evaluation of results, and preparation of the manuscript. Stuart Macaulay, Jan Kotouček, Eliška Bartheldyová, Josef Mašek, František Hubatka, Kamila Velínská, Jaroslava Bezděková, Martina Fojtíková, Andrea Tomečková – development of the procedure and preparation of liposomes by nanofluidisation, evaluation of liposome size by dynamic light scattering, measurement of anisotropy of fluorescence. Pavel Kulich, Josef Mašek, Jana Stráská, Dominik Hřebík – SEM, TEM, TEM-EDX and cryo-TEM microscopy. This manuscript has not been published and will not be submitted elsewhere for publication while being considered by the Scientific Reports.

Competing interests

The authors declare no competing interests.

Additional information

Supplementary information is available for this paper at <https://doi.org/10.1038/s41598-020-62500-2>.

Correspondence and requests for materials should be addressed to I.K., M.R. or J.T.

Reprints and permissions information is available at www.nature.com/reprints.

Publisher's note Springer Nature remains neutral with regard to jurisdictional claims in published maps and institutional affiliations.



Open Access This article is licensed under a Creative Commons Attribution 4.0 International License, which permits use, sharing, adaptation, distribution and reproduction in any medium or format, as long as you give appropriate credit to the original author(s) and the source, provide a link to the Creative Commons license, and indicate if changes were made. The images or other third party material in this article are included in the article's Creative Commons license, unless indicated otherwise in a credit line to the material. If material is not included in the article's Creative Commons license and your intended use is not permitted by statutory regulation or exceeds the permitted use, you will need to obtain permission directly from the copyright holder. To view a copy of this license, visit <http://creativecommons.org/licenses/by/4.0/>.

© The Author(s) 2020



Article

Proinflammatory Effect of Carbon-Based Nanomaterials: In Vitro Study on Stimulation of Inflammasome NLRP3 via Destabilisation of Lysosomes

Tereza Svadlakova ^{1,2}, Frantisek Hubatka ³, Pavlina Turanek Knotigova ³, Pavel Kulich ³, Josef Masek ³, Jan Kotoucek ³, Jan Macak ⁴, Martin Motola ⁴, Martin Kalbac ⁵, Martina Kolackova ¹, Radka Vankova ¹, Petra Vicherkova ¹, Andrea Malkova ², Pavlina Simeckova ³, Yuri Volkov ^{6,7}, Adriele Prina-Mello ⁶, Irena Kratochvilova ⁸, Zdenek Fiala ², Milan Raska ^{3,9}, Jan Krejsek ^{1,*} and Jaroslav Turanek ^{3,*}

¹ Institute of Clinical Immunology and Allergology, University Hospital Hradec Kralove and Faculty of Medicine in Hradec Kralove, Charles University, 50005 Hradec Kralove, Czech Republic; svadlakovat@lfhk.cuni.cz (T.S.); kolackovam@lfhk.cuni.cz (M.K.); vankovr@lfhk.cuni.cz (R.V.); petraavicherkova@gmail.com (P.V.)

² Institute of Hygiene and Preventive Medicine, Faculty of Medicine in Hradec Kralove, Charles University, 50003 Hradec Kralove, Czech Republic; Malka8AR@lfhk.cuni.cz (A.M.); fiala@lfhk.cuni.cz (Z.F.)

³ Veterinary Research Institute, 62100 Brno, Czech Republic; hubatka@vri.cz (F.H.); knotigova@vri.cz (P.T.K.); kulich@vri.cz (P.K.); masek@vri.cz (J.M.); kotoucek@vri.cz (J.K.); simeckova@vri.cz (P.S.); milan.raska@upol.cz (M.R.)

⁴ Center of Materials and Nanotechnologies, Faculty of Chemical Technology, University of Pardubice, 53002 Pardubice, Czech Republic; Jan.Macak@upce.cz (J.M.); martin.motola@upce.cz (M.M.)

⁵ J. Heyrovsky Institute of Physical Chemistry of the Czech Academy of Sciences, 18223 Prague, Czech Republic; martin.kalbac@jh-inst.cas.cz

⁶ Department of Clinical Medicine/Trinity Translational Medicine Institute (TTMI), Trinity College Dublin, D08 W9RT, Dublin, Ireland; yvolkov@tcd.ie (Y.V.); prinamea@tcd.ie (A.P.-M.)

⁷ Department of Histology, Cytology and Embryology, First Moscow State Sechenov Medical University, 119992 Moscow, Russia

⁸ Institute of Physics, Czech Academy of Sciences, 18200 Prague, Czech Republic; krat@fzu.cz

⁹ Department of Immunology and Institute of Molecular and Translational Medicine, Faculty of Medicine and Dentistry, Palacky University Olomouc, 77515 Olomouc, Czech Republic

* Correspondence: jan.krejsek@fnhk.cz (J.K.); turanek@vri.cz (J.T.)

Received: 7 February 2020; Accepted: 24 February 2020; Published: 27 February 2020



Abstract: Carbon-based nanomaterials (C-BNM) have recently attracted an increased attention as the materials with potential applications in industry and medicine. Bioresistance and proinflammatory potential of C-BNM is the main obstacle for their medicinal application which was documented in vivo and in vitro. However, there are still limited data especially on graphene derivatives such as graphene platelets (GP). In this work, we compared multi-walled carbon nanotubes (MWCNT) and two different types of pristine GP in their potential to activate inflammasome NLRP3 (The nod-like receptor family pyrin domain containing 3) in vitro. Our study is focused on exposure of THP-1/THP1-null cells and peripheral blood monocytes to C-BNM as representative models of canonical and alternative pathways, respectively. Although all nanomaterials were extensively accumulated in the cytoplasm, increasing doses of all C-BNM did not lead to cell death. We observed direct activation of NLRP3 via destabilization of lysosomes and release of cathepsin B into cytoplasm only in the case of MWCNTs. Direct activation of NLRP3 by both GP was statistically insignificant but could be induced by synergic action with muramyl dipeptide (MDP), as a representative molecule of the family of pathogen-associated molecular patterns (PAMPs). This study demonstrates a possible proinflammatory potential of GP and MWCNT acting through NLRP3 activation.

Keywords: graphene platelets; carbon nanotubes; inflammasome NLRP3; cathepsin B; macrophages; THP-1

1. Introduction

Over the past decades, nanomaterials have attracted great attention with C-BNM being among the most studied ones. Their extraordinary physicochemical properties, namely, tuneable electronic (e.g., band gap) and electrical properties (e.g., conductivity), thermal and chemical stability, and large surface area, make C-BNM appropriate candidates for a wide range of high-tech applications, as well as for biomedical applications [1–6]. Chemical industry is capable of producing C-BNM in large quantities and, therefore, their impact on the environment is inevitable. C-BNM, predominantly graphene oxide (GO) and carbon nanotubes (CNT), were tested for their potential use in nanomedicine as drug carriers. However, incomplete toxicology data together with an increasing demand on the production of these materials dictate the necessity for toxicological studies to answer questions about their safety with respect to guidance issued by FDA and EMEA.

An important concern relates to the C-BNM interaction with the immune system and their ability to induce an inflammation. Even though both CNT and graphene have been extensively investigated over the recent years, the results are still inconsistent and often contradictory. Asbestos-like shape of CNT leads to the assumption that both single and multi-walled carbon nanotubes (SWCNT and MWCNT) have a capacity to induce acute and chronic inflammation [7–9]. Depending on the shape, length, functionalization and presence of impurities, the mechanical disruption associated with oxidative stress, mitochondrial damage, and production of pro-inflammatory cytokines are considered principal mechanisms of cytotoxicity [10–12]. A similar situation could arise for graphene, the 2D layered nanomaterial, which can also be expected to cause mechanical damage to cell membranes via flat and sharp edges [13,14]. Many studies are focused on graphene oxide (GO), which is described as a promising nanomaterial in nanomedicine despite the fact, that many reports point to its potential cytotoxicity [15–25]. However, there are limited data on biological effects of other derivatives such as GP and graphene sheets to which humans are exposed during development, processing or manufacturing [26,27]. These non-biodegradable materials could pose a risk, especially for the respiratory system after exposure by inhalation [28]. It has been confirmed that GP, which are up to 25 μm in diameter, can be delivered beyond the ciliated airways and deposited in alveoli, where they can either persist in intercellular spaces, or are internalized by alveolar macrophages [29–31]. This may lead to inflammation, disruption of homeostasis, and subsequent fibrosis and tissue damage [28,32–34]. For example, multi-layered graphene platelets induced a substantial inflammatory response and cytotoxicity in rat lungs [33]. Another pulmonary in vivo study which compared six different surface modifications of GP showed increased oxidative stress and acute inflammation [35]. Moreover, positively-charged GP also showed significant inflammation characterized by the accumulation of neutrophil granulocytes [31]. On the other hand, single-layered graphene oxide platelets did not cause acute cytotoxicity or inflammation in a 3D human lung model and similarly, no acute toxicity was demonstrated after 28 days of in vivo exposure to multi-layered graphene platelets [29,36]. Obviously, a focus on deeper details on the mechanism of cytotoxicity and the inflammation of C-BNM is still necessary.

One of the key mediators of nanomaterials-induced inflammation could be activation of NLRP3 inflammasome [37]. Activation of NLRP3 is a complex process, which is evoked in response to infectious stimuli like whole pathogens or individual PAMPs, which escaped to the cytoplasm, as well as by cellular stress signals represented by sterile damage signals (DAMPs). Some studies focused on the assembly of this complex as the leading mechanism of pulmonary inflammation after exposure to all nanotubes and nanowire materials [38–40]. As a principal mediator of inflammasome assembly, activation of NADPH oxidase, which led to the oxidative burst and, subsequently, to lysosomal

damage and a release of cathepsin B, was suggested [38]. In our previous study we found that nanodiamonds (ND) can disrupt lysosomal membrane and subsequently activate NLRP3 via cathepsin B activation pathway [6]. This leads to a hypothesis whether pristine graphene and its derivatives are also capable of induction of inflammation via the inflammasome pathway. Therefore, we used the same model of THP1-Null cells (derived from THP-1 human monocytic cells). This cell line represents a well-established in vitro system for the studies of canonical NLRP3 inflammasome pathway, as it expresses high levels of NLRP3, ASC and pro-caspase 1. Upon activation of caspase-1 in THP1 cells, bioactive IL-1 β is detected with high sensitivity and specificity by HEK-Blue™IL-1 β reporter cell-based assay. In this study, we assessed MWCNT and two types of GP by their potential to penetrate the cells, affect cell viability, destabilise lysosomes, and activate inflammasome NLRP3 by canonical and non-canonical pathways. All these nanomaterials are assumed to cause chronic inflammation. For this reason, we focussed on their ability to induce NLRP3 stimulation as a main mechanism of their proinflammatory effects. We demonstrate here that GP and MWCNT possess proinflammatory potential executed both via canonical and alternative pathways.

2. Materials and Methods

2.1. Carbon-Based Nanomaterials Characterization

Two different types of GP and MWCNT were used in this study. GP1 was purchased from PlasmaChem GmbH (Berlin, Germany) as a powder (product number PL-P-G750). According to the manufacturer's specifications, the particle size was up to 2 μ m and the thickness of graphene sheets was 1–4 nm. GP2 was kindly donated by CRANN (the Centre for Research on Adaptive Nanostructures and Nanodevices), Trinity College Dublin (Dublin, Ireland) as a powder. MWCNT were purchased from Sigma-Aldrich (St. Luis, MO, USA) as a powder (product number 659258).

All three types of materials were thoroughly investigated for composition, structure, and thermal stability. Results of the X-ray diffractometry, energy dispersive X-ray spectroscopy, Raman spectroscopy and thermogravimetric analyses are introduced and discussed in detail in the Supplementary Information. Briefly, all obtained physico-chemical characterisation results were in line with specifications of the producers of these materials.

2.2. Preparation of Suspensions

Stock suspensions of GP at a concentration 250 μ g/mL were prepared by dispersing powders in 0.02% sodium cholate, followed by sonication using a sonic probe (QSonica, Q700 ultrasonic processor with a 1/4" microtip probe) for 30 min with 65% of amplitude. The average shape and size were assessed by transmission electron microscopy (TEM, Philips 208 S Morgagni, FEI) at an accelerating voltage of 80 kV and by scanning electron microscopy (SEM, Magellan 400L, FEI). The hydrodynamic diameters (D_H) of GP were determined using Zetasizer Nano-Ultra (Malvern Panalytical Ltd, Malvern, UK). Measurements were provided in several dilution of stock solutions in Milli-Q water and cell culture media containing of 10% FBS.

Stock suspension of MWCNT at a concentration 500 μ g/mL was prepared by dispersing powder in 0.02% sodium cholate and sonicating using QSonica (Melville, NY, USA), Q700 5 min with 55% of amplitude. The average length and diameters of all used materials were assessed by TEM at an accelerating voltage of 80 kV and by SEM.

2.3. Zeta Potential

Zeta potential measurements were performed on a Zetasizer Nano ZSP instrument equipped with MPT-2 Titrator (Malvern Panalytical Ltd, Malvern, UK). The instrument is using a He–Ne laser (wavelength of 633 nm) and detector angles of 173° and 13°. Data were recorded and analysed using Zetasizer Software v7.11. Prior to all zeta potential measurements, all C-BNM were diluted in 10 mM

Na₂HPO₄ solution with pH 7.2. ζ -potential values were calculated using the Smoluchowski equation. Each data value represents an average of three measurements.

2.4. Cell Culture

Human cell line THP-1 was purchased from The European Collection of Authenticated Cell Cultures (ECACC, Salisbury, UK). All human reporter cell lines, THP1-null, THP1-defNLRP3, THP1-defASC and HEK-Blue™ IL-1 β were purchased from InvivoGen (San Diego, CA, USA). THP-1 were maintained in RPMI 1640 media without phenol red (Corning, NY, USA) supplemented with 10% heat inactivated ultra-low endotoxin fetal bovine serum (FBS_{LE}; Biosera, France), 2 mM L-alanyl-L-glutamine (GlutaMAX; Life Technologies, Carlsbad, CA, USA), 1 mM sodium pyruvate (Life Technologies, Carlsbad, CA, USA), 10 mM HEPES (Sigma-Aldrich, St. Luis, MO, USA), 0.05 mM 2-mercaptoethanol and with penicillin (100 U/mL) and streptomycin (100 μ g/mL) (Sigma-Aldrich, St. Luis, MO, USA). THP1-null, THP1-defNLRP3 and THP-1 defASC were maintained in RPMI 1640 media supplemented with heat inactivated 10% foetal FBS_{LE}, 25 mM HEPES, Normocin (100 μ g/mL; InvivoGen, San Diego, CA, USA) and selection antibiotic Hygromycin B Gold (200 μ g/mL; InvivoGen, San Diego, CA, USA). HEK-Blue™ IL-1 β were maintained in Dulbecco's modified Eagle's High Glucose medium (DMEM; Sigma-Aldrich, St. Luis, MO, USA) supplemented with 10% FBS_{LE} and with selection antibiotics Hygromycin B Gold (200 μ g/mL) and Zeocin (100 μ g/mL; InvivoGen, San Diego, CA, USA). All cells were incubated in a humidified atmosphere of 5% CO₂ at 37 °C.

Peripheral blood samples were obtained from healthy volunteers after an informed consent and approval by the Ethics Committee, University Hospital Hradec Kralove, Sokolska 581, 500 05 Hradec Kralove (reference number 201902 S22P), Czech Republic. Peripheral monocytes were isolated from whole blood using RosetteSep™ Human Monocyte Enrichment Cocktail (STEMCELL Technologies Inc., Vancouver, Canada) according to manufacturer's protocol. The purified monocytes were verified by flow cytometry (~94%) and maintained in RPMI 1640 supplemented with 20% human autologous serum and Primocin™ (100 μ g/mL, InvivoGen, San Diego, CA, USA). The cells were incubated in a humidified atmosphere of 5% CO₂ at 37 °C.

2.5. Cell Viability and Plasma Membrane Integrity

Cell viability was assessed through lactate dehydrogenase (LDH) assay. THP-1 cells were seeded in flat bottom 96-well plates at the density 4×10^4 cells per well and treated with phorbol 12-myristate 12-acetate (PMA; 25 ng/mL, Sigma-Aldrich, St. Luis, MO, USA) for 72 h. After differentiation, cells were washed and exposed to increasing concentration of GP and MWCNT in media (5–60 μ g/mL) for 24–72 h. Cells with no exposure and cells exposed to sodium cholate were used as controls. Supernatants were centrifuged at 10,000 $\times g$ for 10 min to eliminate GP and MWCNT and transferred into a new flat bottom 96-well plate. The LDH assay was performed according to the manufacturer's protocol. Absorbance was measured in a microplate spectrophotometer Synergy HTX (Biotek, Bad Friedrichshall, Germany) at 490 nm, with 690 nm set as the reference wavelength.

2.6. Mitochondrial Potential Detection

PMA differentiated THP-1 cells exposed to all C-BNM samples were washed with a phosphate buffered solution (PBS) and subsequently treated with cell permeable probe tetramethylrhodamine ethyl ester (TMRE, 750 nM, Sigma-Aldrich, St. Luis, MO, USA) for 30 min. TMRE intensity fluorescence was determined by the microplate spectrophotometer with excitation/emission wavelengths of 549/575 nm. GP and MWCNT were incubated with fluorescence probes to determine possible interferences. TMRE-stained mitochondria were also observed using a holotomographical microscope Nanolive 3D Cell Explorer – fluo with software STEVE version 1.6.3496 (Nanolive, Ecublens, Switzerland).

2.7. Intracellular Localization of C-BNM

THP-1 cells were prepared as described above for the viability assays. Cells exposed to 25 and 50 $\mu\text{g/mL}$ C-BNM were collected and fixed in 3% glutaraldehyde. GP and MWCNT samples were centrifuged and the pellet was rinsed in Milonig buffer, post-fixed in 1% OsO_4 solution in Milonig buffer, dehydrated in 50%, 70%, 90%, 100% ethanol, embedded in Epon-Durcupan mixture (Epon 812 Serva, Heidelberg, Germany; Durcupan, ACM Fluka, Buchs, Switzerland) and polymerized at 60 °C for 72 h. Ultrathin (60 nm) sections were cut with glass knives on UC 7 ultramicrotome (UC 7, Leica, Vienna, Austria) and contrasted by 2% uranyl acetate and 2% lead citrate. The sections were examined using TEM (Philips 208 S Morgagni, FEI, San Jose, CA, USA).

2.8. Activation of NLRP3

THP1-null cells, as they express high levels of NLRP3, adaptor protein ASC (apoptosis-associated Speck-like protein with a caspase recruitment domain) and pro-caspase 1 were seeded in the flat bottom 96-well plates at density 360×10^3 cells per well and primed with ultrapure lipopolysaccharide (LPS, 1 $\mu\text{g/mL}$, Invivogen) for 3 h. Cells were subsequently washed and stimulated with C-BNM (5–60 $\mu\text{g/mL}$) and with sodium cholate as a control for 24–48 h. Collected supernatants were centrifuged at $10,000 \times g$ for 10 min to eliminate free C-BNM and transferred (50 μL) to new flat bottom 96-well plates. Mature (cleaved) IL-1 β in supernatants was detected by cell-based assay using HEK-Blue™ IL-1 β cells. HEK-Blue™ cells respond specifically to IL-1 β . Binding of IL-1 β to its receptor IL-1R on the surface of HEK-Blue™ allows sensitive specific detection of bioactive interleukins via colorimetric assay of enzyme activity of expressed reporter gene SEAP. SEAP was quantified using QUANTI-Blue™ a SEAP detection medium, which turns blue in its presence. THP1-defNLRP3 and THP-1 defASC cell lines, which are deficient of NLRP3 and ASC, respectively, were primed and exposed in the same way as the THP1-null cells and were used as negative controls. Absorbance was measured in a microplate spectrophotometer at 630 nm wavelength.

Supernatants from isolated monocytes exposed to all C-BNM (5–60 $\mu\text{g/mL}$ for 24–48 h) were collected and centrifuged at $10,000 \times g$ for 10 min to get rid of non-internalised free GP and MWCNT and transferred (50 μL) to a new flat-bottom 96-well plate. LPS (100 ng/mL) was used as a positive control and the specific inhibitor MCC950 (Invivogen, Paris, France) was used as a verification of a specific NLRP3 inflammasome activation. Mature IL-1 β in supernatants was detected by cell-based assay using HEK-Blue™ IL-1 β cells. Absorbance was measured in a microplate spectrophotometer at 630 nm wavelength.

2.9. Release of Cathepsin B

Detection of cathepsin B in THP1-null cells exposed to GP and MWCNT (30 $\mu\text{g/mL}$) was performed by cathepsin B detection kit (Enzo, LifeSciences, Farmingdale, NY, USA) according to the manufacturer's protocol. CV-(RR)2 was used as a substrate for cathepsin B cleavage. As a positive control, cells were pre-treated by lysosomal disruptor Leu-Leu methyl ester hydrobromide LLME (100 μM , Sigma-Aldrich, St. Luis, MO, USA) for 2 h. Cells not exposed to GP and MWCNT were used as negative controls.

2.10. Inflammatory Cytokines Production

For cytokine detection in supernatants from exposed THP-1 cells and primary monocytes, ELISA kits for IL-6, TNF- α and IL-10 (R&D Systems, Minneapolis, MN, USA) human cytokines were used. Kits were used according to the manufacturer's protocol.

2.11. Statistical Analysis

Data are expressed as mean values ($n_{\text{tests}} = 3$) \pm standard deviation and are normalized to the control untreated cells (control). Differences have been considered significant for p values < 0.05 .

Two-way ANOVA with Bonferroni post hoc test was performed, using GraphPad Prism™ software version 7.00 (GraphPad Software Inc., San Diego, CA, USA).

3. Results

3.1. C-BNM Characterization

The morphology characterization, carried out using electron microscopes, is presented in Figure 1 for all C-BNM. Both TEM and SEM images clearly show shape heterogeneity of GP. Both GP form small aggregates, whereas clearly smaller GP1 (80~300 nm of lateral size; Figure 1a–c) form lumps-like flakes indicating a significantly lower quality of this GP. On the other hand, as seen in Figure 1d–f, GP2 form flakes with lateral size about 250~400 nm blade-like edges which could cause damage of intracellular membranes. These results correspond with the average size distribution measured by DLS using Zetasizer (Figure 2). The calculated zeta-average diameters of R_h are 178.5 ± 110 nm and 315 ± 78 nm for GP1 and GP2, respectively. However, as the DLS method is the most suitable for the measurement of spherical particles, therefore the flat shape of GP and presence of aggregates must be considered for the evaluation of these analyses. Figure 1g–i shows the 10 μ m long MWCNT with a diameter of 110~200 nm. Detailed physical characterisation (Raman spectra, X-ray diffraction, elemental composition, thermogravimetric analyses) is provided in the Supplementary Material.

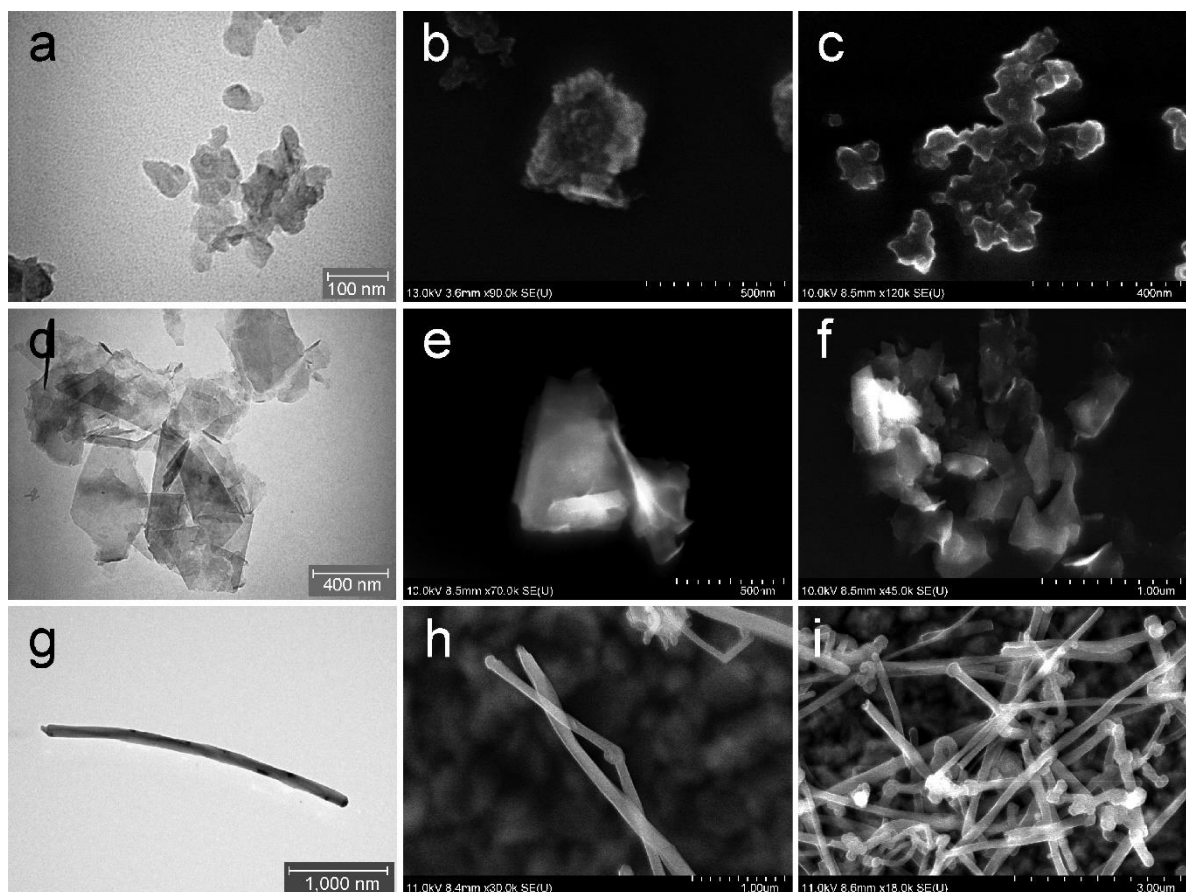


Figure 1. Characterisation of C-BNM by electron microscopy: (a) TEM and (b,c) SEM detail of the GP1 forming small aggregates; (d) TEM detail of the GP2; (e) SEM detail of a structure of GP2 single platelet and (f) forming clusters; (g) TEM detail of single MWCNT; (h) SEM detail of a structure of MWCNT with (i) forming clusters.

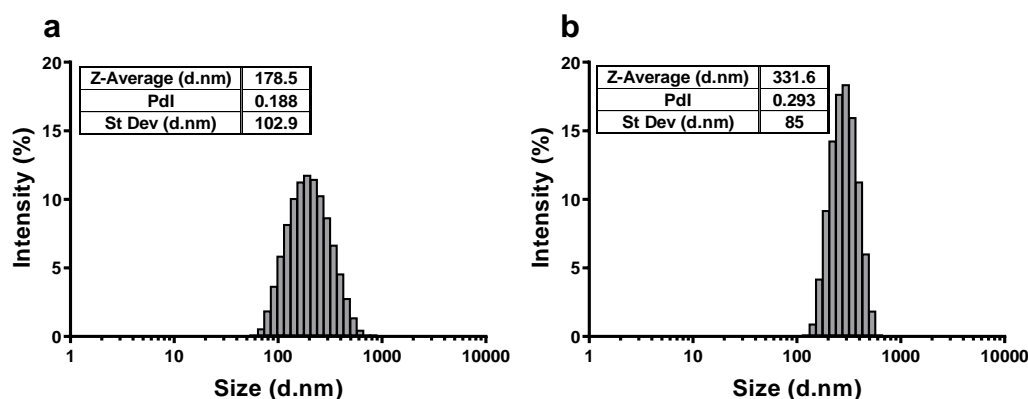


Figure 2. Average size distribution measured by dynamic light scattering: (a) GP1 and (b) GP2 in 0.02% sodium cholate; PDI: polydispersity index; Z-average: R_n ; St Dev: standard deviation

3.2. Zeta Potential

Figure 3 shows pH-dependence of the (a) ζ potential of C-BNM and (b) aggregation state of GP1 and GP2. Negative ζ potential of C-BNM ($\zeta < -40$ mV) in neutral pH corresponds with presence of sodium cholate and residual oxygen (see Supplementary Material) on the surface of these materials. In the pH range 6–8, the aggregation of particles was also significantly less pronounced than in acidic pH. Acidification to pH 3 led to an increase of ζ potential to $\zeta > -20$ mV and a considerable increase of aggregation which is reflected by an increase in the average size (Z-average) (Figure 3b). Below pH 4 GP2 exerted formation of significantly larger aggregates in comparison to GP1. Transferring of these well dispersed C-BNM into cell medium with FBS caused formation of biocorona which was reflected by changing an average ζ potential to values: -8.52 mV for GP1; -10.8 mV for GP2; and -13.1 mV for MWCNT.

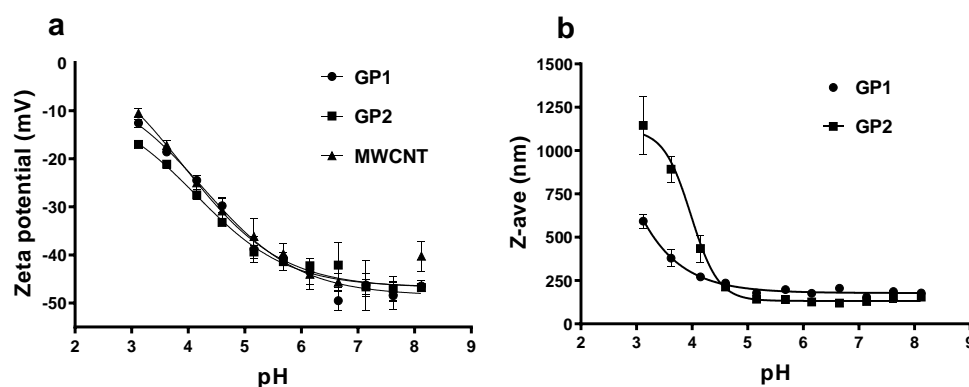


Figure 3. Effect of pH on (a) ζ -potential of C-BNM in 0.02% sodium cholate; (b) average diameter of C-BNM in 0.02% sodium cholate

3.3. Intracellular Localization of C-BNM

TEM confirmed presence of all GP and MWCNT in cytoplasm of THP-1 macrophages after 24 h of exposure (Figure 4). As seen in Figure 4a–c, GP particles were observed in endosomes and no particles were localized in nucleus. GP1 formed large aggregates (Figure 4b) whereas GP2 formed smaller aggregates (Figure 4c) located in vesicles. Moreover, in the case of GP2, free particles were found sporadically in cytoplasm. We observed a similar pattern of GP distribution in human primary monocytes (Figure 4e,f). Further, MWCNT were located as free particles in whole cytoplasm, where they could possibly interact with multiple organelles (Figure 4d). Damaged cell structures suggest an escape of tubes from endosomes or lysosomes as it corresponds with the release of cathepsin B (see

Section 3.5. Activation of NLRP3 and Release of Pro-Inflammatory Cytokines). Individual nanotubes were observed to penetrate also through the nucleus membrane.

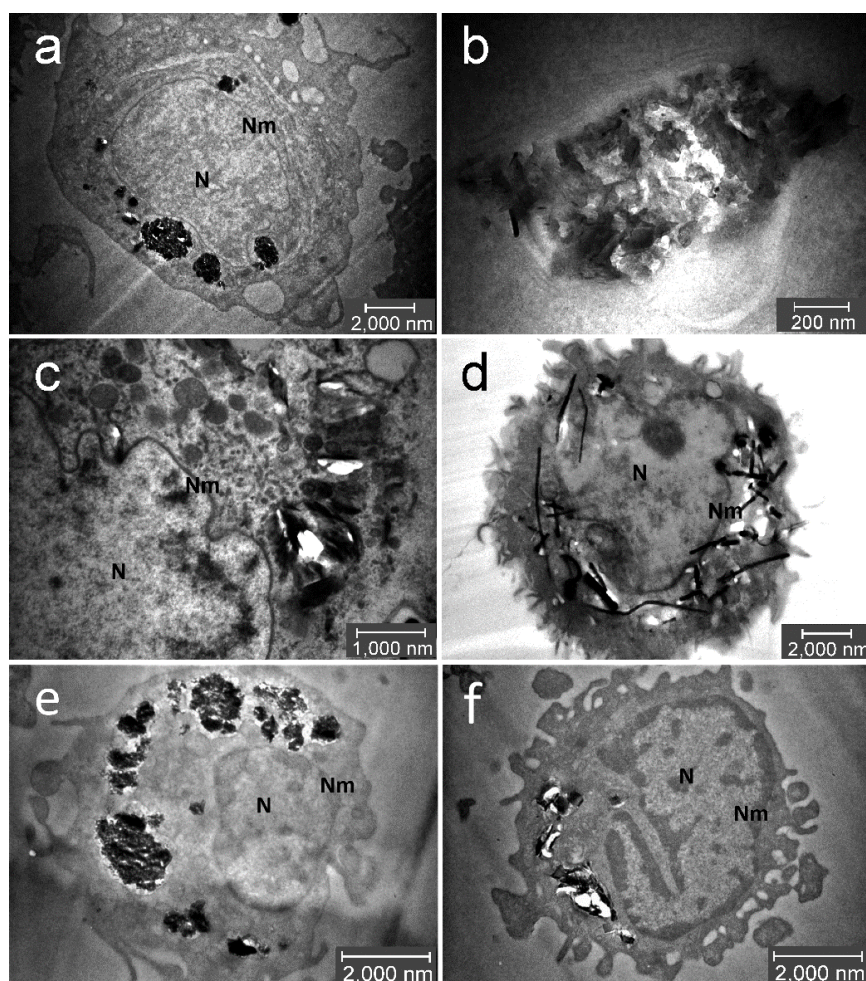


Figure 4. Intracellular localisation of C-BNM after 24 h exposure in THP-1 (a–d) and primary monocytes (e,f): GP1 (a,b,e) forms large aggregates in cytoplasm apparently in vesicles. No particles are found in nucleus (N); (c,f) GP2 forms smaller aggregates in cytoplasm, apparently in vesicles. Occasionally, free particles are detected in cytoplasm; (d) MWCNT were found as free needle-like objects in the cytoplasm, possibly from damaged lysosomes. Sporadically, they can be found in nucleus or penetrating through the nuclear membrane (Nm).

3.4. Cell Viability

Cell viability, assessed with LDH assay, was determined after 24 h, 48 h and 72 h of cell exposure to C-BNM (5–60 $\mu\text{g/mL}$). Cytosolic enzyme LDH which is released into the cell medium after damage of the plasma membrane during cell death, serves as a well-established and reliable indicator of cellular toxicity. Studied C-BNM did not induce any significant cell membrane damage and subsequent release of LDH into cytoplasm (Figure 5a). We also evaluated the mitochondrial membrane potential via TMRE staining after 24 h, 48 h and 72 h of cell exposure to C-BNM (5–60 $\mu\text{g/mL}$). In TMRE labelled active mitochondria, a decrease of the fluorescent intensity corresponds with a decrease of the mitochondrial activity or its damage. All C-BNM induced only slight dose dependent decrease (10–20%) in mitochondrial activity (Figure 5b). Moreover, microscopy studies did not reveal any significant mitochondrial damage (Figure 5c). Finally, no statistical difference was observed in the mitochondrial potential decrease, between all types of C-BNM.

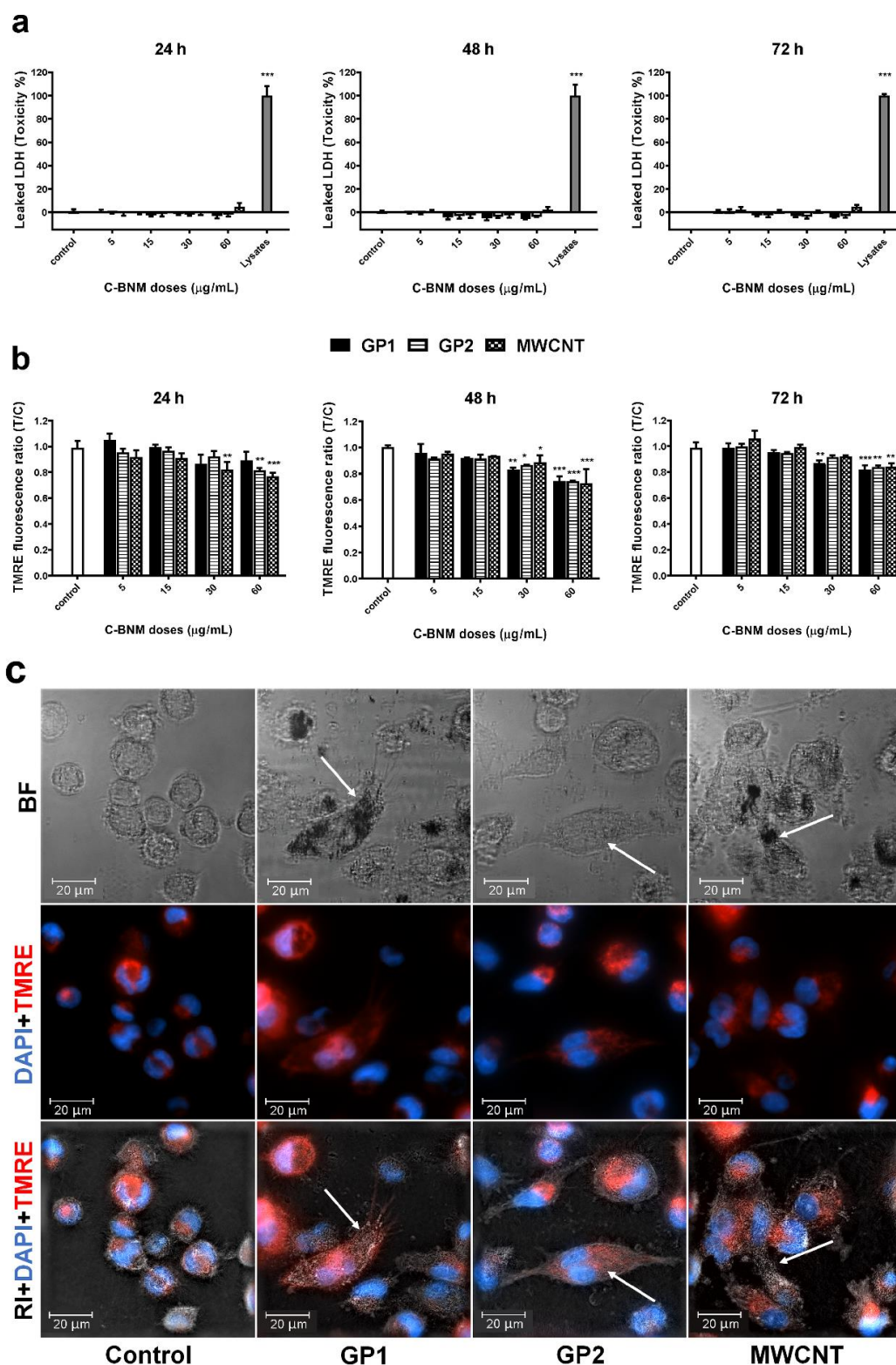


Figure 5. Cell responses to C-BNM: (a) Percentage of cytotoxicity via LDH assay after 24 h, 48 h and 72 h exposure. Data are reported as average \pm standard error of the mean ($\text{Toxicity \%} = (T - C)/(L - C) \times 100$); T —test cells; C —untreated control; L —lysates. The symbol *** $p < 0.001$ highlights statistical significance as compared to the corresponding C ; (b) mitochondrial potential via TMRE staining after 24 h, 48 h and 72 h exposure. Data normalised to control (untreated cells) represent an average \pm standard error of the mean. The symbols * $p < 0.05$; ** $p < 0.01$; *** $p < 0.001$ highlight the statistical significance

as compared to the corresponding control; (c) representative images of THP-1 cells loaded with C-BNM (white arrows), after 24 h exposure, with labelled active mitochondria (TMRE) and nuclei (DAPI) detected using a holotomographical microscopy; RI—refractive index; BF—bright field.

3.5. Activation of NLRP3 and Release of Pro-Inflammatory Cytokines

Activation of inflammasome is a key step in the release of pro-inflammatory cytokine IL-1 β . In this study, we measured IL-1 β in supernatants of THP1-null cells which represent a model of canonical pathway activation of NLRP3. The cells were exposed to increased concentrations of C-BNM (5–60 μ g/mL) and to ATP (5 mM) as a positive control. Results are summarized in Figure 6a. Both GP induced a slight, but statistically not significant increase of IL-1 β secretion at the highest dose tested. In contrast to GP, MWCNT were able to activate inflammasome and subsequently release IL-1 β in a dose-dependent manner. To observe possible activation of other inflammasomes than NLRP3, we examined supernatants of exposed THP1-defNLRP3 and THP1-defASC, which are deficient in NLRP3 receptor and ASC adaptor protein, respectively. The results confirmed specific activation of NLRP3 by MWCNT (Figure 6b). The effect of PAMP molecules was tested with the muramyl dipeptide. Both GP were able to activate NLRP3 in the presence of muramyl dipeptide (Figure 6c,d).

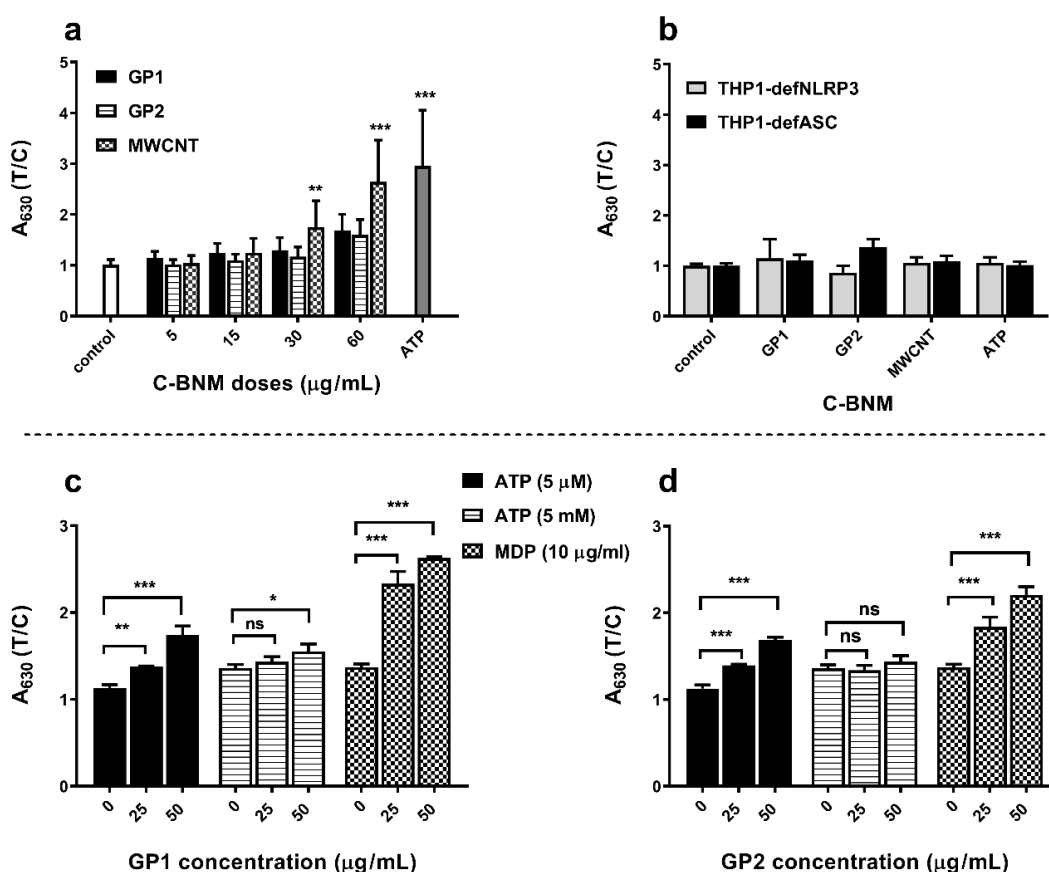


Figure 6. Effect of C-BNM on activation of inflammasome NLRP3 after 24 h exposure: (a) NLRP3 activation in THP1 null cells was measured as conversion of proIL-1 β to IL-1 β , which was detected using HEK-Blue™ IL-1 β cells. Data were normalised to the control (untreated THP1-null cells). ATP was used as positive standard of NLRP3 induction. The symbols ** $p < 0.01$; *** $p < 0.001$ highlight the statistical significance as compared to the corresponding control; (b) Activation of NLRP3 in deficient cells THP1-defNLRP3 and THP1-defASC, which were treated the same way as THP1-null cells; (c,d)

activation of NLRP3 in THP-1 null macrophages by GP in presence of MDP and ATP: ATP (5 mM; 5 μ M) and MDP (10 μ g/mL) were used as a standard activators of NLRP3 (control) in presence of 0, 25 and 50 μ g/mL of GP. The symbols * $p < 0.05$; ** $p < 0.01$; *** $p < 0.001$ highlight statistical significance as compared to the corresponding controls (0) without GP.

For the evaluation of the possible mechanism of NLRP3 assembly, we measured the release of cathepsin B into cytoplasm using a cell-penetrating fluorogenic substrate (Figure 7). Under normal conditions, this protease is localized in lysosomes. Destabilization of lysosomes by various lysosomal disruptors leads to the release of cathepsin B into the cytoplasm and subsequently the activation of NLRP3 is induced. Figure 7 shows micrographs of C-BNM, visualized by the confocal microscopy in the light scattering mode at wavelengths corresponding to the excitation spectrum of the fluorescent product of CV-(RR)2 substrate cleavage by cathepsin B. The fluorescence was measured after 2 h, 6 h and 24 h after treatment of THP1-null cells with C-BNM. Fluorescent dots represent penetration of a substrate to lysosomes and the disperse signal points to the release of cathepsin B from damaged lysosomes. In addition to the positive control, the most significant release of cathepsin B was observed using MWCNT (Figure 7a), which corresponds to our previous findings on NLRP3 activation (Figure 6a).

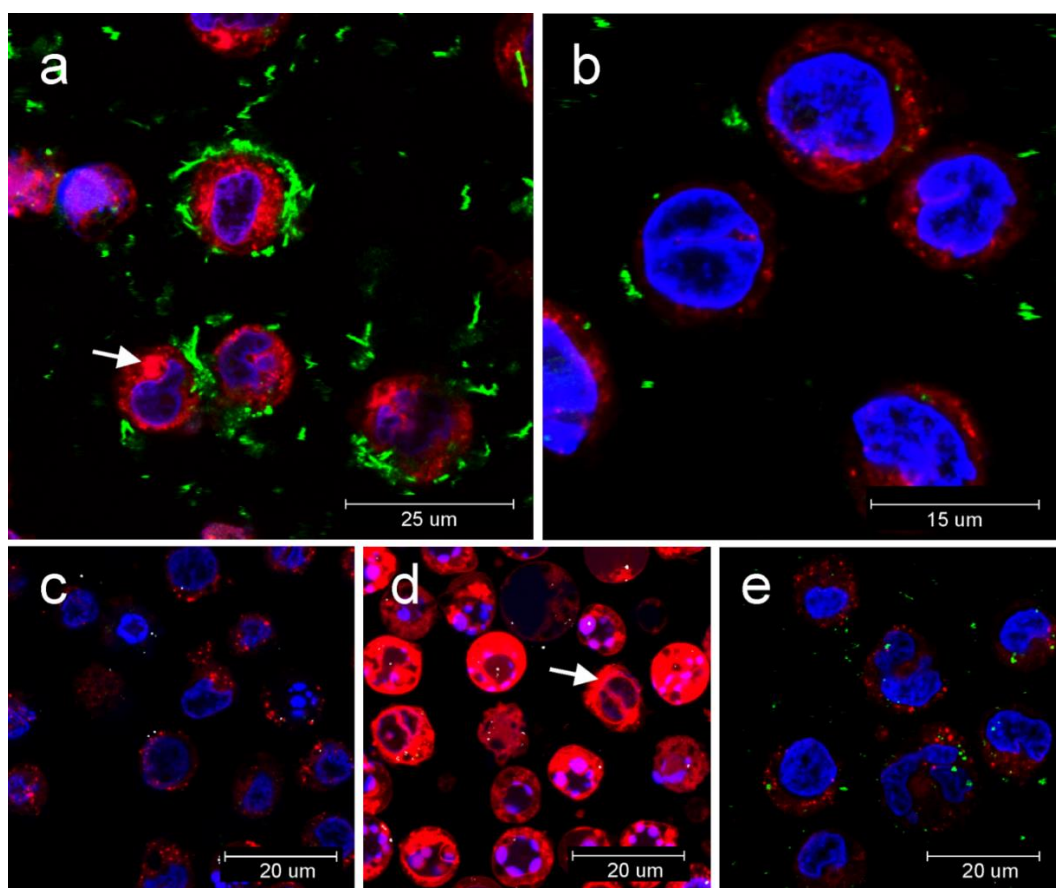


Figure 7. Release of cathepsin B from lysosomes into cytoplasm in THP1-null cell revealed by confocal microscopy: Proteolytic activity of cathepsin B was determined by fluorogenic substrate with red emission; (a) release of cathepsin B (red fluorescence) into cytoplasm after 24 h incubation with MWCNT (light scattering in green). Cytoplasm stained with fluorogenic substrate (white arrow); (b) Release of cathepsin B after 24 h incubation with GP2 (light scattering in green); (c) Negative control; (d) release of cathepsin B after incubation with lysosomal disruptor LLME with burst of cathepsin B into cytoplasm (white arrow); (e) release of cathepsin B after 24h incubation with GP1 (light scattering in green).

Activation of NLRP3 in Isolated Monocytes

Verification of NLRP3 activation by an alternative pathway was performed using primary monocytes isolated from human blood. Additionally, in this more complex in vitro model, MWCNT induced strong and concentration-dependent activation of NLRP3 (Figure 8). Application of MCC950 inhibitor confirmed specific activation of NLRP3 inflammasome by MWCNT. When exposed to graphene, only GP2 increased the activity of NLRP3, but without statistical significance when compared to GP1. Viability of monocytes exposed to various C-BNM was confirmed by LDH assay (see supplementary data, Figure S4).

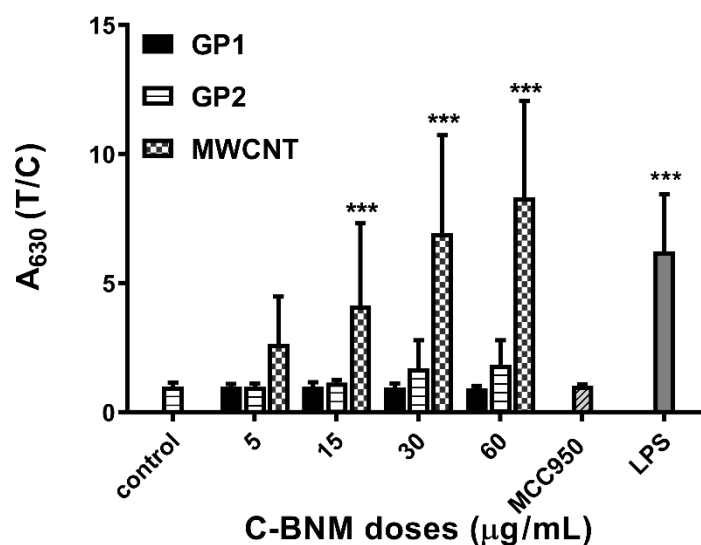


Figure 8. Activation of NLRP3 in isolated monocytes after 24 h exposure was measured as conversion of proIL-1 β to IL-1 β , which was detected using HEK-Blue™ IL-1 β cells. Untreated isolated monocytes were used as a negative control. LPS was used as positive standard of NLRP3 induction. MCC950 was used as specific inhibitor of MWCNT induction of NLRP3. The symbol *** $p < 0.001$ highlights the statistical significance as compared to the corresponding control.

The secretion of the pro-inflammatory cytokines IL-6 and TNF α as well as of the anti-inflammatory cytokine IL-10 was quantified after 24 h and 48 h exposure of THP-1 and primary monocytes to C-BNM and LPS (100 ng/mL) as a positive control. There was no significant release of these cytokines after 24 h or 48 h exposure to all C-BNM (results not shown).

4. Discussion

The aim of this study was to evaluate possible proinflammatory and immunomodulatory effects of C-BNM, notably of GP, toxicological data on which are still insufficient. Generally, C-BNM were found to affect complement and all immune cells including macrophages, dendritic cells, lymphocytes, monocytes, neutrophils, eosinophils, NK cells and mast cells. There is no wonder that inflammation is among the general side effects observed by toxicologists after application of C-BNM [41]. Acute or chronic inflammation responses are interfering with the normal physiological functions of important organs [42,43]. C-BNM are known to induce either physical or biological damage to the cell membrane, membranes of organelles along with destabilization of actin filaments, the cytoskeleton and effecting the cell cycle [44–46]. At the tissue and cellular levels, the mechanisms responsible for inflammation are based on disruption of various barriers (e.g., alveolar–capillary barrier, blood–brain barrier), infiltration of immune cells and their interaction with molecules released from injured cells (disease associated molecular patterns) or with nanoparticles themselves [47]. A recent study demonstrating destabilisation of phospholipid membranes by carbon nanosheets was published recently by [48].

As inflammasomes play a central role in the process of inflammation we used a well-established model on THP-1 and THP1-null cells to study the key mechanism responsible for the adverse effect of C-BNM. In our previous study we demonstrated the effect of 100 nm nanodiamonds on the injury of lysosomal membranes and the release of cathepsin B resulting in activation of inflammasome NLRP3 and release of IL-1 β [6]. Therefore, we used a similar model also for testing of various GP and MWCNT. In this study, we used two types of sterile non-oxidized graphene platelets and commercially available MWCNT to determine their proinflammatory potential. We confirmed the ability of C-BNM to penetrate cytoplasmic membranes and, in the case of MWCNT, nuclear membranes, and accumulate inside the cells (Figure 4). We observed direct stimulation of inflammasome NLRP3 by MWCNT through a release of the proinflammatory cytokine IL-1 β (Figure 6). Activation of NLRP3 is a complex process which is evoked in the response to infectious stimuli like whole pathogens or individual microbial components (PAMPs), as well as by cellular stress signals represented by sterile DAMPs. In the canonical pathway, two signals precede the oligomerization of NLRP3. In the case of macrophages/THP1-null model, the first one requires the transcription of inflammasome components including pro-caspase-1 and pro-IL-1 β . The second one includes the DAMP/PAMP signals, which are sensed by NLR receptors. In the non-canonical pathway, NLRP3 can be activated through endogenous caspases 4 and 5 (caspase 11 in murine macrophages), which specifically binds lipopolysaccharide from Gram-negative bacteria and triggers misbalance of ions and ATP. ATP then works as an autostimulator of NLRP3 assembly. The result of this stimulus is the cleavage of pro-caspase-1, pro-IL-1 β , pro-IL-18 and pro-gasdermin D. Gasdermin D (GSDMD) forms pores in the cell membrane, through which mature IL-1 is released. Increased pore formation together with mitochondrial disbalance may lead to failure of cell homeostasis and, subsequently, to cell death by pyroptosis followed by the leakage of intracellular content, such as LDH [49,50].

Neither GP nor MWCNT induced a significant release of LDH even after 72 h incubation (Figure 5a). It means that short term cytotoxicity via pyroptosis was not a direct effect of GP and MWCNT. A slight decrease of mitochondrial potential was observed for all tested materials at concentrations above 30 $\mu\text{g}/\text{mL}$ (Figure 5b). These data are in a good accordance with published observations regarding C-BNM as summarised by [51].

ELISA assays confirmed the absence of proinflammatory cytokines IL-6 or TNF α for all C-BNM used in the study. Release of these cytokines is typical of pyrogenic stimulation, so these data confirm the absence of LPS or another PAMPs on the surface of nanomaterials. On the other hand, we observed a proinflammatory potential of MWCNT via activation of NLRP3. While the NLRP3 serves as a sensor of DAMPs and (in the case of macrophages), its own assembly does not depend only on stimulation with LPS (unlike the alternative pathway), making it the most suitable tool for the evaluation of proinflammatory potential [40]. According to images from TEM (Figure 4) we assumed that especially carbon nanotubes may cause a nonspecific intracellular damage of membrane structures, which we confirmed by the detection of Cathepsin B release from the damaged lysosomes (Figure 7a). Cathepsin B is considered as one of the DAMPs sensed by NLR and its presence in cytoplasm leads to NLRP3 oligomerization [6,52]. Interestingly, according to TMRE staining, we detected only a slight decrease of the mitochondrial potential. It can be assumed that mitochondrial damage did not play a pivotal role in inflammasome activation in THP1-null macrophages. However, it correlates with our observation of cell viability even after 72h after stimulation with C-BNM and rejects the possibility of non-canonical activation of inflammasome, which usually leads to pyroptosis through misbalance of ATP [49,53]. This ability to secrete IL-1 β while retaining viability is similar to the situation in primary monocytes, whose NLRP3 (Figure 8) is activated via an alternative pathway, and also has been described in human bone marrow derived macrophages as a hyperactivation state [50,54]. It has been proven that several self-derived DAMPs as isolated lipid components, like self-encoded oxidized phospholipids (oxPAPC), led to the GSDMD-dependent release of IL-1 β without cell death and LDH release [54]. Participation of other inflammasomes (e.g., AIM2, NLRC4, NLRP1, etc.) was excluded by using specific THP-1 macrophages deficient in NLRP3 and ASC in our study (Figure 6b).

It has been reported that oxidized forms of graphene and nanotubes caused the release of proinflammatory cytokines IL-6, TNF α and IL-8 through oxidative stress as a main mechanism [15,17]. On the other hand, pristine graphene without specific carboxyl or hydroxyl groups should not specifically interact with pattern recognition receptors (PRR) on the surface of cells. Thus, its potential cytotoxicity strongly depends on its shape and size [30,55]. Unlike MWCNT, GP were found enclosed as smaller (GP2) or bigger (GP1) aggregates in endosomes (Figure 4). We detected either no or only slight release (GP2) of cathepsin B (Figure 7) to cytoplasm and together with the results from LDH assay and TMRE staining (Figure 5) it corresponded with a slight, nonsignificant release of IL-1 β (Figure 6a). Autophagy, which inhibits NLRP3 activation, could be a possible reason and has been referred to as a common phenomenon in graphene-focussed studies [56]. Generally, despite the different character of used GP, neither of them alone was able to activate NLRP3 to a significant level. A quite different situation occurred when muramyl MDP was added as the prominent representative of DAMP. There was a significantly stronger activation of NLRP3 by both GP1 and GP2 together with MDP than in the case of using MDP alone (Figure 6c,d). These results relate to the contention that GP and MWCNT may serve as a “Trojan horse” and inhaled particles of GP or MWCNT may carry contaminants on its surface. It must be considered that NLRP3 strongly responds to accumulated signals, and it is possible that “harmless” nanomaterial may boost a stimulus from adsorbed PAMPs/DAMPs. There is also an important fact that C-BNM are considered not fully biodegradable materials which are facing the continuous surveillance of the immune system. Therefore, although not acutely toxic, it may cause chronic problems under long-term exposure, owing to accumulation in tissues [43,57]. If the accumulation reaches the certain threshold, the second signals like DAMP or PAMP originating from damages can trigger activation of inflammasome. On the other hand, recent studies suggested a possibility of partial degradation of GP and MWCNT by macrophages via enzymes like myeloperoxidase. This means that inflammatory mechanisms are inevitably involved in the elimination of C-BNM [58].

THP1-null cells represent a pure model to study activation of NLRP3 inflammasome and the proinflammatory potential was confirmed in the case of both GP and especially MWCNT. The data obtained on THP1-null cells were verified on peripheral blood monocytes which represent a model closer to the realistic in vivo scenario and possibility of activation of NLRP3 via an alternative pathway. Contrary to THP-1 null cells, one must consider possible genetic variations among the healthy volunteers from whom the monocytes were isolated. Nevertheless, both models convincingly pointed to a proinflammatory potential of C-BNM, especially MWCNT. An example is the study in which the pulmonary exposure of MWCNT in mice not only led to local inflammation, but also promoted systemic inflammation and systemic inflammation together with dysfunction of the NOS system [59].

5. Conclusions

In our study using a well-established in vitro model, we have demonstrated a clear proinflammatory potential of GP and MWCNT which can be enhanced by various PAMP. Therefore, it must be considered that, in in vivo conditions, accumulation of PAMPs and DAMP signals can act synergistically with nanomaterials, even if they are considered “harmless” on their own. Such a synergic action can lead to activation of inflammatory mechanisms, e.g., via NLRP3. There is also an important fact that graphene as well as CNT are not fully biodegradable materials and, therefore, although rendered not acutely toxic due to various surface modifications, they may cause chronic problems under long-term exposure owing to accumulation in tissues and organs. Questions regarding the effects of C-BNM accumulated for instance, in brain, lungs, liver or spleen in the course of real infection (e.g., influenza, hepatitis or EBV) of these organs are of additional importance. Studies focused on aspects of interaction between C-BNM and organisms at the molecular, cellular, tissue and whole body level are necessary to fully understand mechanisms of toxicity and to evaluate possible risks imposed by such materials to humans and the environment, if broad application of C-BNM were accomplished. Therefore, GP and MWCNT may serve as a “Trojan horse” and inhaled particles

of C-BNM in real environment may carry contaminants on its surface, which can have a nature characteristic of PAMPs.

Supplementary Materials: The following are available online at <http://www.mdpi.com/2079-4991/10/3/418/s1>. Figure S1: XRD patterns of studied C-BNM. Table S1: Elemental composition of C-BNM. Figure S1: Raman spectra of MWCT, GP1 and GP2. Figure S3: TGA (left Y-axis) and TGA (right Y-axis) curves recorded for C-BNM under oxygen atmosphere with a heating rate of 10 K/min. Figure S4: Monocytes response to C-BNM; Percentage of cytotoxicity via LDH assay after 24 and 48 h.

Author Contributions: T.S., M.K. (Martina Kolackova), R.V., P.V., A.M. and P.S. performed cell culture experiments, F.H., J.K., J.M. (Jan Macak), M.M. and M.K. (Martin Kalbac). performed C-BNMs physical-chemical characterization and data analysis, T.S., P.T.K., J.M. (Josef Masek), A.P.-M. and J.T. designed experiments and analyzed data, P.K., I.K. and M.R. analyzed data and revised manuscript, Y.V., A.P.-M. and J.K. revised the manuscript and provided materials, Z.F., J.K. and J.T. supervised team and provided support, T.S. and J.T. wrote manuscript, Y.V., Z.F. and I.K. reviewed manuscript. The authors declare no competing financial interests. All authors have read and agreed to the published version of the manuscript.

Funding: This work was supported by the Ministry of Education, Youth and Sports of the Czech Republic and The European Union—European Structural and Investments Funds in the frame of Operational Programme Research Development and Education—projects “FIT” (project no. CZ.02.1.01/0.0/0.0/15_003/0000495), “NANOBIIO” (project no. CZ.02.1.01/0.0/0.0/17_048/0007421), “Modernization and upgrade of CEMNAT infrastructure” (project no. CZ.02.1.01/0.0/0.0/16_013/0001829), “Pro-NanoEnviCz” (project no. CZ.02.1.01/0.0/0.0/16_013/0001821), and “SOLID21” (project no. CZ.02.1.01/0.0/0.0/16_019/0000760), the Ministry of Education, Youth and Sports of the Czech Republic “SAFMAT” LM 2015088 and by the Ministry of Agriculture of the Czech Republic under the project RO0518, Project Centre of Excellence for Nanotoxicology CENATOX GAP503/12/G147. This work was also funded by the institutional support from Charles University, Faculty of Medicine in Hradec Kralove: project PROGRES Q40/10 and Q40/09.

Acknowledgments: Access to instruments in the laboratory NanoPharm (join project of Veterinary Research Institute and International Clinical Research Center (FNUSA-ICRC) (J.T.) is acknowledged, as well as support by Education and Research Centre VRI-Malvern (J.T.).

Conflicts of Interest: The authors declare no conflict of interest.

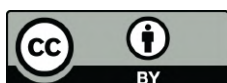
References

1. Raphey, V.R.; Henna, T.K.; Nivitha, K.P.; Mufeedha, P.; Sabu, C.; Pramod, K. Advanced biomedical applications of carbon nanotube. *Mater. Sci. Eng. C Mater. Biol. Appl.* **2019**, *100*, 616–630. [[CrossRef](#)] [[PubMed](#)]
2. Bei, H.P.; Yang, Y.; Zhang, Q.; Tian, Y.; Luo, X.; Yang, M.; Zhao, X. Graphene-Based Nanocomposites for Neural Tissue Engineering. *Molecules* **2019**, *24*, 658. [[CrossRef](#)] [[PubMed](#)]
3. Tadzyszak, K.; Wychowaniec, J.K.; Litowczenko, J. Biomedical Applications of Graphene-Based Structures. *Nanomaterials* **2018**, *8*, 944. [[CrossRef](#)] [[PubMed](#)]
4. Li, Q.; Wen, J.; Liu, C.; Jia, Y.; Wu, Y.; Shan, Y.; Qian, Z.; Liao, J. Graphene-Nanoparticle-Based Self-Healing Hydrogel in Preventing Postoperative Recurrence of Breast Cancer. *ACS Biomater. Sci. Eng.* **2019**, *5*, 768–779. [[CrossRef](#)]
5. Kratochvílová, I.; Šebera, J.; Ashcheulov, P.; Golan, M.; Ledvina, M.; Míčová, J.; Mravec, F.; Kovalenko, A.; Zverev, D.; Yavkin, B.; et al. Magnetical and Optical Properties of Nanodiamonds Can Be Tuned by Particles Surface Chemistry: Theoretical and Experimental Study. *J. Phys. Chem. C* **2014**, *118*, 25245–25252. [[CrossRef](#)]
6. Knötigová, P.T.; Mašek, J.; Hubatka, F.; Kotouček, J.; Kulich, P.; Šimečková, P.; Bartheldyová, E.; Machala, M.; Švadláková, T.; Krejsek, J.; et al. Application of Advanced Microscopic Methods to Study the Interaction of Carboxylated Fluorescent Nanodiamonds with Membrane Structures in THP-1 Cells: Activation of Inflammasome NLRP3 as the Result of Lysosome Destabilization. *Mol. Pharma.* **2019**, *16*, 3441–3451. [[CrossRef](#)]
7. Møller, P.; Christophersen, D.V.; Jensen, D.M.; Kermanizadeh, A.; Roursgaard, M.; Jacobsen, N.R.; Hemmingsen, J.G.; Danielsen, P.H.; Cao, Y.; Jantzen, K.; et al. Role of oxidative stress in carbon nanotube-generated health effects. *Arch. Toxicol.* **2014**, *88*, 1939–1964. [[CrossRef](#)]
8. Wan, B.; Wang, Z.X.; Lv, Q.Y.; Dong, P.X.; Zhao, L.X.; Yang, Y.; Guo, L.H. Single-walled carbon nanotubes and graphene oxides induce autophagosome accumulation and lysosome impairment in primarily cultured murine peritoneal macrophages. *Toxicol. Lett.* **2013**, *221*, 118–127. [[CrossRef](#)]
9. Duke, K.S.; Bonner, J.C. Mechanisms of carbon nanotube-induced pulmonary fibrosis: A physicochemical characteristic perspective. *Wiley Interdiscip. Rev. Nanomed. Nanobiotechnol.* **2018**, *10*, e1498. [[CrossRef](#)]

10. Brown, D.M.; Kinloch, I.A.; Bangert, U.; Windle, A.H.; Walter, D.M.; Walker, G.S.; Scotchford, C.A.; Donaldson, K.; Stone, V. An in vitro study of the potential of carbon nanotubes and nanofibres to induce inflammatory mediators and frustrated phagocytosis. *Carbon* **2007**, *45*, 1743–1756. [[CrossRef](#)]
11. Schinwald, A.; Donaldson, K. Use of back-scatter electron signals to visualise cell/nanowires interactions in vitro and in vivo; frustrated phagocytosis of long fibres in macrophages and compartmentalisation in mesothelial cells in vivo. *Part. Fibre Toxicol.* **2012**, *9*, 34. [[CrossRef](#)] [[PubMed](#)]
12. Ghanbari, F.; Nasarzadeh, P.; Seydi, E.; Ghasemi, A.; Taghi Joghataei, M.; Ashtari, K.; Akbari, M. Mitochondrial oxidative stress and dysfunction induced by single- and multiwall carbon nanotubes: A comparative study. *J. Biomed. Mater. Res. Part A* **2017**, *105*, 2047–2055. [[CrossRef](#)] [[PubMed](#)]
13. Akhavan, O.; Ghaderi, E. Toxicity of Graphene and Graphene Oxide Nanowalls Against Bacteria. *ACS Nano* **2010**, *4*, 5731–5736. [[CrossRef](#)] [[PubMed](#)]
14. Matesanz, M.C.; Vila, M.; Feito, M.J.; Linares, J.; Goncalves, G.; Vallet-Regi, M.; Marques, P.A.; Portoles, M.T. The effects of graphene oxide nanosheets localized on F-actin filaments on cell-cycle alterations. *Biomaterials* **2013**, *34*, 1562–1569. [[CrossRef](#)]
15. Chen, G.Y.; Yang, H.J.; Lu, C.H.; Chao, Y.C.; Hwang, S.M.; Chen, C.L.; Lo, K.W.; Sung, L.Y.; Luo, W.Y.; Tuan, H.Y.; et al. Simultaneous induction of autophagy and toll-like receptor signaling pathways by graphene oxide. *Biomaterials* **2012**, *33*, 6559–6569. [[CrossRef](#)]
16. Russier, J.; Treossi, E.; Scarsi, A.; Perrozzi, F.; Dumortier, H.; Ottaviano, L.; Meneghetti, M.; Palermo, V.; Bianco, A. Evidencing the mask effect of graphene oxide: A comparative study on primary human and murine phagocytic cells. *Nanoscale* **2013**, *5*, 11234–11247. [[CrossRef](#)]
17. Qu, G.; Liu, S.; Zhang, S.; Wang, L.; Wang, X.; Sun, B.; Yin, N.; Gao, X.; Xia, T.; Chen, J.-J.; et al. Graphene Oxide Induces Toll-like Receptor 4 (TLR4)-Dependent Necrosis in Macrophages. *ACS Nano* **2013**, *7*, 5732–5745. [[CrossRef](#)]
18. Tkach, A.V.; Yanamala, N.; Stanley, S.; Shurin, M.R.; Shurin, G.V.; Kisin, E.R.; Murray, A.R.; Pareso, S.; Khaliullin, T.; Kotchey, G.P.; et al. Graphene oxide, but not fullerenes, targets immunoproteasomes and suppresses antigen presentation by dendritic cells. *Small* **2013**, *9*, 1686–1690. [[CrossRef](#)]
19. Wibroe, P.P.; Petersen, S.V.; Bovet, N.; Laursen, B.W.; Moghimi, S.M. Soluble and immobilized graphene oxide activates complement system differently dependent on surface oxidation state. *Biomaterials* **2016**, *78*, 20–26. [[CrossRef](#)]
20. Jarosz, A.; Skoda, M.; Dudek, I.; Szukiewicz, D. Oxidative Stress and Mitochondrial Activation as the Main Mechanisms Underlying Graphene Toxicity against Human Cancer Cells. *Oxid. Med. Cell. Longev.* **2016**, *2016*, 5851035. [[CrossRef](#)]
21. Orecchioni, M.; Jasim, D.A.; Pescatori, M.; Manetti, R.; Fozza, C.; Sgarrella, F.; Bedognetti, D.; Bianco, A.; Kostarelos, K.; Delogu, L.G. Molecular and Genomic Impact of Large and Small Lateral Dimension Graphene Oxide Sheets on Human Immune Cells from Healthy Donors. *Adv. Healthc. Mater.* **2016**, *5*, 276–287. [[CrossRef](#)] [[PubMed](#)]
22. Fahmi, T.; Branch, D.; Nima, Z.A.; Jang, D.S.; Savenka, A.V.; Biris, A.S.; Basnakian, A.G. Mechanism of graphene-induced cytotoxicity: Role of endonucleases. *J. Appl. Toxicol.* **2017**, *37*, 1325–1332. [[CrossRef](#)] [[PubMed](#)]
23. Kang, Y.; Liu, J.; Wu, J.; Yin, Q.; Liang, H.; Chen, A.; Shao, L. Graphene oxide and reduced graphene oxide induced neural pheochromocytoma-derived PC12 cell lines apoptosis and cell cycle alterations via the ERK signaling pathways. *Int. J. Nanomed.* **2017**, *12*, 5501–5510. [[CrossRef](#)] [[PubMed](#)]
24. Mohammadinejad, R.; Moosavi, M.A.; Tavakol, S.; Vardar, D.O.; Hosseini, A.; Rahmati, M.; Dini, L.; Hussain, S.; Mandegary, A.; Klionsky, D.J. Necrotic, apoptotic and autophagic cell fates triggered by nanoparticles. *Autophagy* **2019**, *15*, 4–33. [[CrossRef](#)] [[PubMed](#)]
25. Fadeel, B.; Bussy, C.; Merino, S.; Vázquez, E.; Flahaut, E.; Mouchet, F.; Evariste, L.; Gauthier, L.; Koivisto, A.J.; Vogel, U.; et al. Safety Assessment of Graphene-Based Materials: Focus on Human Health and the Environment. *ACS. Nano* **2018**, *12*, 10582–10620. [[CrossRef](#)] [[PubMed](#)]
26. Wang, E.N.; Karnik, R. Graphene cleans up water. *Nat. Nanotechnol.* **2012**, *7*, 552. [[CrossRef](#)]
27. Petersen, E.J.; Zhang, L.; Mattison, N.T.; O’Carroll, D.M.; Whelton, A.J.; Uddin, N.; Nguyen, T.; Huang, Q.; Henry, T.B.; Holbrook, R.D.; et al. Potential release pathways, environmental fate, and ecological risks of carbon nanotubes. *Environ. Sci. Technol.* **2011**, *45*, 9837–9856. [[CrossRef](#)]

28. Schinwald, A.; Murphy, F.A.; Jones, A.; MacNee, W.; Donaldson, K. Graphene-based nanoplatelets: A new risk to the respiratory system as a consequence of their unusual aerodynamic properties. *ACS Nano* **2012**, *6*, 736–746. [[CrossRef](#)]
29. Kim, J.K.; Shin, J.H.; Lee, J.S.; Hwang, J.H.; Lee, J.H.; Baek, J.E.; Kim, T.G.; Kim, B.W.; Kim, J.S.; Lee, G.H.; et al. 28-Day inhalation toxicity of graphene nanoplatelets in Sprague-Dawley rats. *Nanotoxicology* **2016**, *10*, 891–901. [[CrossRef](#)]
30. Schinwald, A.; Murphy, F.; Askounis, A.; Koutsos, V.; Sefiane, K.; Donaldson, K.; Campbell, C.J. Minimal oxidation and inflammogenicity of pristine graphene with residence in the lung. *Nanotoxicology* **2014**, *8*, 824–832. [[CrossRef](#)]
31. Lee, J.K.; Jeong, A.Y.; Bae, J.; Seok, J.H.; Yang, J.-Y.; Roh, H.S.; Jeong, J.; Han, Y.; Jeong, J.; Cho, W.-S. The role of surface functionalization on the pulmonary inflammogenicity and translocation into mediastinal lymph nodes of graphene nanoplatelets in rats. *Arch. Toxicol.* **2017**, *91*, 667–676. [[CrossRef](#)] [[PubMed](#)]
32. Lammel, T.; Navas, J.M. Graphene nanoplatelets spontaneously translocate into the cytosol and physically interact with cellular organelles in the fish cell line PLHC-1. *Aquat. Toxicol.* **2014**, *150*, 55–65. [[CrossRef](#)] [[PubMed](#)]
33. Park, E.J.; Lee, S.J.; Lee, K.; Choi, Y.C.; Lee, B.S.; Lee, G.H.; Kim, D.W. Pulmonary persistence of graphene nanoplatelets may disturb physiological and immunological homeostasis. *J. Appl. Toxicol.* **2017**, *37*, 296–309. [[CrossRef](#)] [[PubMed](#)]
34. Katsumiti, A.; Tomovska, R.; Cajaraville, M.P. Intracellular localization and toxicity of graphene oxide and reduced graphene oxide nanoplatelets to mussel hemocytes in vitro. *Aquat. Toxicol.* **2017**, *188*, 138–147. [[CrossRef](#)]
35. Li, J.; Zhang, X.; Jiang, J.; Wang, Y.; Jiang, H.; Zhang, J.; Nie, X.; Liu, B. Systematic Assessment of the Toxicity and Potential Mechanism of Graphene Derivatives In Vitro and In Vivo. *Toxicol. Sci.* **2019**, *167*, 269–281. [[CrossRef](#)]
36. Drasler, B.; Kucki, M.; Delhaes, F.; Buerki-Thurnherr, T.; Vanhecke, D.; Korejwo, D.; Chortarea, S.; Barosova, H.; Hirsch, C.; Petri-Fink, A.; et al. Single exposure to aerosolized graphene oxide and graphene nanoplatelets did not initiate an acute biological response in a 3D human lung model. *Carbon* **2018**, *137*, 125–135. [[CrossRef](#)]
37. Guo, H.; Callaway, J.B.; Ting, J.P. Inflammasomes: Mechanism of action, role in disease, and therapeutics. *Nat. Med.* **2015**, *21*, 677–687. [[CrossRef](#)]
38. Sun, B.; Wang, X.; Ji, Z.; Wang, M.; Liao, Y.-P.; Chang, C.H.; Li, R.; Zhang, H.; Nel, A.E.; Xia, T. NADPH Oxidase-Dependent NLRP3 Inflammasome Activation and its Important Role in Lung Fibrosis by Multiwalled Carbon Nanotubes. *Small* **2015**, *11*, 2087–2097. [[CrossRef](#)]
39. Leso, V.; Fontana, L.; Iavicoli, I. Nanomaterial exposure and sterile inflammatory reactions. *Toxicol. Appl. Pharmacol.* **2018**, *355*, 80–92. [[CrossRef](#)]
40. Sun, B.; Wang, X.; Ji, Z.; Li, R.; Xia, T. NLRP3 inflammasome activation induced by engineered nanomaterials. *Small* **2013**, *9*, 1595–1607. [[CrossRef](#)]
41. Mukherjee, S.P.; Bottini, M.; Fadeel, B. Graphene and the Immune System: A Romance of Many Dimensions. *Front. Immunol.* **2017**, *8*, 673. [[CrossRef](#)] [[PubMed](#)]
42. Wen, K.P.; Chen, Y.C.; Chuang, C.H.; Chang, H.Y.; Lee, C.Y.; Tai, N.H. Accumulation and toxicity of intravenously-injected functionalized graphene oxide in mice. *J. Appl. Toxicol.* **2015**, *35*, 1211–1218. [[CrossRef](#)] [[PubMed](#)]
43. Li, B.; Zhang, X.Y.; Yang, J.Z.; Zhang, Y.J.; Li, W.X.; Fan, C.H.; Huang, Q. Influence of polyethylene glycol coating on biodistribution and toxicity of nanoscale graphene oxide in mice after intravenous injection. *Int. J. Nanomed.* **2014**, *9*, 4697–4707. [[CrossRef](#)] [[PubMed](#)]
44. Li, Y.; Yuan, H.; von dem Bussche, A.; Creighton, M.; Hurt, R.H.; Kane, A.B.; Gao, H. Graphene microsheets enter cells through spontaneous membrane penetration at edge asperities and corner sites. *Proc. Natl. Acad. Sci. USA* **2013**, *110*, 12295–12300. [[CrossRef](#)]
45. Tian, X.; Yang, Z.; Duan, G.; Wu, A.; Gu, Z.; Zhang, L.; Chen, C.; Chai, Z.; Ge, C.; Zhou, R. Graphene Oxide Nanosheets Retard Cellular Migration via Disruption of Actin Cytoskeleton. *Small* **2017**, *13*. [[CrossRef](#)]
46. Wang, Y.; Xu, J.; Xu, L.; Tan, X.; Feng, L.; Luo, Y.; Liu, J.; Liu, Z.; Peng, R. Functionalized graphene oxide triggers cell cycle checkpoint control through both the ATM and the ATR signaling pathways. *Carbon* **2018**, *129*, 495–503. [[CrossRef](#)]

47. Gonzalez-Carter, D.; Goode, A.E.; Kiryushko, D.; Masuda, S.; Hu, S.; Lopes-Rodrigues, R.; Dexter, D.T.; Shaffer, M.S.P.; Porter, A.E. Quantification of blood–brain barrier transport and neuronal toxicity of unlabelled multiwalled carbon nanotubes as a function of surface charge. *Nanoscale* **2019**, *11*, 22054–22069. [[CrossRef](#)]
48. Muñoz-López, R.; Guzmán, E.; Velázquez, M.M.; Fernández-Peña, L.; Merchán, M.D.; Maestro, A.; Ortega, F.; Rubio, R.G. Influence of Carbon Nanosheets on the Behavior of 1,2-Dipalmitoyl-sn-glycerol-3-phosphocholine Langmuir Monolayers. *Processes* **2020**, *8*, 94. [[CrossRef](#)]
49. He, Y.; Hara, H.; Nunez, G. Mechanism and Regulation of NLRP3 Inflammasome Activation. *Trends Biochem. Sci.* **2016**, *41*, 1012–1021. [[CrossRef](#)]
50. Evavold, C.L.; Ruan, J.; Tan, Y.; Xia, S.; Wu, H.; Kagan, J.C. The Pore-Forming Protein Gasdermin D Regulates Interleukin-1 Secretion from Living Macrophages. *Immunity* **2018**, *48*, 35–44.e6. [[CrossRef](#)]
51. Li, Y.; Liu, Y.; Fu, Y.; Wei, T.; Le Guyader, L.; Gao, G.; Liu, R.S.; Chang, Y.Z.; Chen, C. The triggering of apoptosis in macrophages by pristine graphene through the MAPK and TGF-beta signaling pathways. *Biomaterials* **2012**, *33*, 402–411. [[CrossRef](#)] [[PubMed](#)]
52. Meunier, E.; Coste, A.; Olagnier, D.; Authier, H.; Lefevre, L.; Dardenne, C.; Bernad, J.; Beraud, M.; Flahaut, E.; Pipy, B. Double-walled carbon nanotubes trigger IL-1beta release in human monocytes through Nlrp3 inflammasome activation. *Nanomedicine* **2012**, *8*, 987–995. [[CrossRef](#)] [[PubMed](#)]
53. Pellegrini, C.; Antonioli, L.; Lopez-Castejon, G.; Blandizzi, C.; Fornai, M. Canonical and Non-Canonical Activation of NLRP3 Inflammasome at the Crossroad between Immune Tolerance and Intestinal Inflammation. *Front. Immunol.* **2017**, *8*, 36. [[CrossRef](#)] [[PubMed](#)]
54. Zanoni, I.; Tan, Y.; Di Gioia, M.; Broggi, A.; Ruan, J.; Shi, J.; Donado, C.A.; Shao, F.; Wu, H.; Springstead, J.R.; et al. An endogenous caspase-11 ligand elicits interleukin-1 release from living dendritic cells. *Science* **2016**, *352*, 1232–1236. [[CrossRef](#)] [[PubMed](#)]
55. Sasidharan, A.; Panchakarla, L.S.; Sadanandan, A.R.; Ashokan, A.; Chandran, P.; Girish, C.M.; Menon, D.; Nair, S.V.; Rao, C.N.; Koyakutty, M. Hemocompatibility and macrophage response of pristine and functionalized graphene. *Small* **2012**, *8*, 1251–1263. [[CrossRef](#)] [[PubMed](#)]
56. Di Cristo, L.; Mc Carthy, S.; Paton, K.; Movia, D.; Prina-Mello, A. Interplay between oxidative stress and endoplasmic reticulum stress mediated- autophagy in unfunctionalised few-layer graphene-exposed macrophages. *2D Mater.* **2018**, *5*, 045033. [[CrossRef](#)]
57. Ou, L.; Song, B.; Liang, H.; Liu, J.; Feng, X.; Deng, B.; Sun, T.; Shao, L. Toxicity of graphene-family nanoparticles: A general review of the origins and mechanisms. *Part. Fibre Toxicol.* **2016**, *13*, 57. [[CrossRef](#)]
58. Peng, Z.; Liu, X.; Zhang, W.; Zeng, Z.; Liu, Z.; Zhang, C.; Liu, Y.; Shao, B.; Liang, Q.; Tang, W.; et al. Advances in the application, toxicity and degradation of carbon nanomaterials in environment: A review. *Environ. Int.* **2020**, *134*, 105298. [[CrossRef](#)]
59. Cao, Y.; Luo, Y. Pharmacological and toxicological aspects of carbon nanotubes (CNTs) to vascular system: A review. *Toxicol. Appl. Pharmacol.* **2019**, *385*, 114801. [[CrossRef](#)]





Article

Targeting Human Thrombus by Liposomes Modified with Anti-Fibrin Protein Binders

Hana Petroková ¹, Josef Mašek ², Milan Kuchař ¹, Andrea Vítečková Wünschová ², Jana Štikarová ³, Eliška Bartheldyová ², Pavel Kulich ², František Hubatka ², Jan Kotouček ², Pavlína Turánek Knotigová ², Eva Vohlídalová ², Renata Héžová ², Eliška Mašková ², Stuart Macaulay ⁴, Jan Evangelista Dyr ³, Milan Raška ^{2,5}, Robert Mikulík ⁶, Petr Malý ^{1,*} and Jaroslav Turánek ^{2,*}

¹ Laboratory of Ligand Engineering, Institute of Biotechnology, Czech Academy of Sciences, v.v.i., BIOCEV Research Center, Průmyslová 595, 252 50 Vestec, Czech Republic; hana.petrokova@ibt.cas.cz (H.P.); milan.kuchar@ibt.cas.cz (M.K.)

² Department of Pharmacology and Immunotherapy, Veterinary Research Institute, v.v.i., Hudcova 70, 621 00 Brno, Czech Republic; masek@vri.cz (J.M.); viteckova@vri.cz (A.V.W.); bartheldyova@vri.cz (E.B.); kulich@vri.cz (P.K.); hubatka@vri.cz (F.H.); kotoucek@vri.cz (J.K.); knotigova@vri.cz (P.T.K.); vohlidalova@vri.cz (E.V.); hezova@vri.cz (R.H.); maskova@vri.cz (E.M.); milan.raska@upol.cz (M.R.)

³ Department of Biochemistry, Institute of Hematology and Blood Transfusion, U nemocnice 2094/1, 128 20 Praha 2, Czech Republic; Jana.Stikarova@uhkt.cz (J.Š.); Jan.Dyr@uhkt.cz (J.E.D.)

⁴ Malvern Instruments Ltd., Enigma Business Park, Grove Lane, Malvern WR14 1XZ, UK; Stuart.Macaulay@malvern.com

⁵ Department of Immunology, Faculty of Medicine and Dentistry, Palacky University Olomouc, Hněvotínská 3, 775 15 Olomouc, Czech Republic

⁶ The International Clinical Research Center ICRC and Neurology Department of St. Anne's University Hospital in Brno, Pekařská 53, 656 91 Brno, Czech Republic; robert.mikulik@fnusa.cz

* Correspondence: petr.maly@ibt.cas.cz (P.M.); turanek@vri.cz (J.T.); Tel.: +420-325-873-763 (P.M.); +420-732-813-577 (J.T.)

Received: 2 October 2019; Accepted: 26 November 2019; Published: 2 December 2019



Abstract: Development of tools for direct thrombus imaging represents a key step for diagnosis and treatment of stroke. Nanoliposomal carriers of contrast agents and thrombolytics can be functionalized to target blood thrombi by small protein binders with selectivity for fibrin domains uniquely formed on insoluble fibrin. We employed a highly complex combinatorial library derived from scaffold of 46 amino acid albumin-binding domain (ABD) of streptococcal protein G, and ribosome display, to identify variants recognizing fibrin cloth in human thrombus. We constructed a recombinant target as a stretch of three identical fibrin fragments of 16 amino acid peptide of the B β chain fused to TolA protein. Ribosome display selection followed by large-scale Enzyme-Linked ImmunoSorbent Assay (ELISA) screening provided four protein variants preferentially binding to insoluble form of human fibrin. The most specific binder variant D7 was further modified by C-terminal FLAG/His-Tag or double His-tag for the attachment onto the surface of nanoliposomes via metallochelating bond. D7-His-nanoliposomes were tested using in vitro flow model of coronary artery and their binding to fibrin fibers was demonstrated by confocal and electron microscopy. Thus, we present here the concept of fibrin-targeted binders as a platform for functionalization of nanoliposomes in the development of advanced imaging tools and future theranostics.

Keywords: fibrin; thrombus targeting; thrombus imaging; binding protein; ABD scaffold; liposome; combinatorial library; metallochelation; fibrinogen B β chain

1. Introduction

Thrombosis, a critical event consisting of formation of thrombus in blood vessels, is one of the most frequent causes of death, e.g., due to ischemic stroke [1], myocardial infarction [2] or pulmonary embolism [3]. Such diseases are not only leading causes of death but have huge socioeconomic impacts worldwide despite available therapy [4]. There is clearly a significant medical need for better and rapid diagnosis and targeted treatment of acute thrombosis.

Direct thrombus imaging can be mediated by targeting surface structures of activated platelets, for instance, by single-chain antibody conjugated iron oxide microparticles [5,6]. Activated platelets can be targeted also by cyclic RGD peptides that were designed, synthesized and tested as ligands for highly specific targeting mediated by theranostic nanoparticles [7]. Another compound of the blood thrombus that can be used for targeting of the imaging agents is fibrin in the form of insoluble net of fibers. As fibrin is the end-product of proteolytic cleavage of fibrinogen followed by further coagulation process, it shares substantial sequence identity (98%) and structural similarity to its parental soluble progenitor. Concentration of fibrinogen in plasma is dominating (2–4 mg/mL), therefore, a high selectivity of fibrin-targeting ligands is required to avoid their complete scavenging by fibrinogen during in vivo circulation. To overcome this burden, several laboratories tried to develop monoclonal antibodies specific to fibrin but those recognize soluble fibrin and its D-dimer as well, or substantially cross-react with fibrinogen [8–11].

Beside antibodies, several small peptide-based ligands specifically binding fibrin were also generated. The small cyclic peptides Tn6, Tn7 and Tn10 specifically bind to fibrin and fibrin-degradation products with micromolar affinity, whereas binding to fibrinogen is about 100-fold weaker [12]. The modified version of Tn6 peptide, the peptide EP-2104R [13], was tested for thrombus imaging by MRI in the phase II clinical trials [14] but did not advanced to the next phase. In another attempt, the cyclic peptides CLT1 and CLT2 were developed to recognize fibrin-fibronectin complexes in plasma thrombi in tumors and at injured tissues sites [15].

Generation of insoluble fibrin-specific agents represents a significant challenge in the development of thrombus-specific in vivo diagnostic probes. Recently developed monoclonal antibody (mAb) clone 102-10 [16] distinguishes fibrin thrombi from precursors such as fibrinogen, soluble fibrin as an early polymerization product and insoluble fibrin precursor and degradation clot product such as D-dimer. Detail analysis of the binding specificity of this mAb identified a prominent hydrophobic region of 16 amino acid located on the B β chain as an exclusive epitope for binding of 102-10 mAb to fibrin thrombi [16]. This B β peptide epitope has been postulated to be shielded by a steric hindrance in the soluble fibrinogen but exposed in polymerized insoluble fibrin fibers. In addition, radiolabeled 102-10 mAb selectively accumulated in mouse spontaneous tumors and identified increased fibrin deposition in grade 4 glioma in comparison to lower-grade gliomas [16–18]. Tissue plasminogen activator (tPA) (an endogenous protein that has been shown to bind fibrin with high affinity) was studied as possible targeting ligand which might circumvent antibody difficulties. The use of tPA-derived proteins however, requires neutralization of remove the plasminogen-activating proteolytic activity. Targeting of echogenic liposomes towards fibrin was demonstrated, but no clinical application has not been demonstrated up to present [19,20].

Phage display technology was also used for identification of fibrin-specific antibodies or their fragments. Human single-chain antibody fragment Tomlinson I and J libraries were panned against non-cross-linked fibrin [21] and only one clone (E4) was identified that, in ELISA, showed a weak preferential binding to fibrin in comparison to fibrinogen. Monoclonal antibody AP2 was selected by phage display from a combinatorial library targeted to N-terminal peptide of α -chain of fibrin [22]. This antibody recognizes five N-terminal amino acids from fibrin and does not react with fibrinogen. The AP2 antibody also inhibits fibrin thrombus formation and localizes in fibrin-rich tumors as shown in vivo on a mouse model. All above mentioned antibodies, however, were not used for development of methods for direct thrombus imaging.

Various functionalized nanoparticles have already been tested for the purpose of *in vivo* imaging, but most of the developed nanoparticle types have not been yet approved for clinical applications. Liposomes, self-assembled membrane-like spherical vesicles, are non-toxic biocompatible nanoparticles approved by FDA and EMA for the application in human medicine with a considerable potential as diagnostic and theranostic carriers applicable for improving many imaging techniques such as Computed Tomography (CT) or magnetic resonance imaging (MRI) [23]. Several different liposomal preparations are in use as vaccines or for the treatment of infectious diseases, cancer or dermatological disorders [24–26]. Technologies for preparation and production of liposomes at industrial scale are available and bioconjugate chemistry for surface modifications of liposome by ligands of various chemical structure are currently being developed [27–29].

Therefore, we use the new approach based on ribosome display technology to identify fibrin-specific artificial protein binders derived from a small protein domain scaffold. This approach represents a valuable alternative for production of robust and high-affinity binders with a required selectivity. In this study, we used a highly complex combinatorial library derived from scaffold of albumin-binding domain (ABD) of streptococcal protein G [30–32], and ribosome display, to identify fibrin-specific protein binders that could be used as components for targeted delivery of nanoliposomes to human thrombi *in vitro* and *in vivo*. We demonstrate that one of the selected candidates preferentially binds to insoluble fibrin as well as to human thrombus *in vitro*. Thus, this ABD-derived variant can serve as a useful molecular tool for the functionalization of a liposomal surface. The concept was proved *in vitro* by application of flexible silicone replica of coronary artery as a model for visualization of thrombi by fluorescently labeled liposome-binder complexes under flow conditions. Nanoliposomes modified by small protein binders represent a basis for development of platform for MRI or CT imaging of thrombus as well as for targeted delivery of thrombolytic drugs or theranostics when combined together.

2. Materials and Methods

2.1. Production of Fusion Proteins Carrying B β Epitopes (BEP) Recognized by 102-10 mAb

For the construction of triple-B β -containing protein target (3BEP-TolA-Avi), the codon-optimized DNA sequences of triple-B β epitope (CNIPVVS β GKECEEIIR) connected with GGGGS hinges was synthesized by GeneArt (Regensburg, Germany) and inserted into pET28b vector between N-terminal His-tag and C-terminal TolA-Avi-tag using digestion with NcoI and BamHI enzymes. Protein was expressed in *Escherichia coli* (*E. coli*) BL21 (DE3) *BirA* strain as *in vivo* biotinylated product. Purification was done using 1 mL NiNTA-agarose matrice (Qiagen, Hilden, Germany) under native conditions. Column with matrice was equilibrated with TNI20 buffer (50 mM Tris, 300 mM NaCl and 20 mM imidazole pH 8.0) and the sonicated protein culture in TNI20 buffer was applied twice and washed with 10 mL of the same buffer. Elution was done by TNI250 (50 mM Tris, 300 mM NaCl and 250 mM imidazole, pH 8.0). Fractions with highest concentration of protein were pooled and polished by size exclusion chromatography on Superdex 200 10/300 column in the TN buffer (50 mM Tris, 150 mM NaCl, pH 8.0).

Fusion protein carrying the single-B β epitope (BEP-TolA-Avi) as well as a control protein lacking B β epitope (Δ EP-TolA-Avi) were also constructed and produced as above. Synthetic peptide CNIPVVS β GKECEEIIR (sBEP) was produced by Vidia s.r.o. (Vestec, Czech Republic).

2.2. Ribosome Display Selection of Binders

Combinatorial DNA library was generated as described previously [33,34] with some modifications. The assembled library was *in vitro* transcribed/translated in a single step reaction using *E. coli* extract (EasyXpress *E. coli* kit, biotechrabbit, Hennigsdorf, Germany) and used for the pre-selection in 96well Maxisorp plates (NUNC, Roskilde, Denmark). To reduce non-specific variants, two pre-selection steps were performed (each 1 h at 4 °C): first one on fibrinogen and the second on the Δ EP-TolA-Avi.

Fibrinogen (Abcam, Cambridge, UK) was coated to the wells of plate directly at concentration of 5 µg/mL for all three rounds of the selection. The biotinylated protein ΔEP-TolA-Avi was coated indirectly (10, 10 and 2.5 µg/mL for individual rounds) via streptavidin (1 µg/mL in carbonate buffer pH 9.6). The selection of binders was made in wells with 3BEP-TolA-Avi (10, 10 and 2.5 µg/mL for individual rounds) bound via biotin to coated streptavidin (1 µg/mL in carbonate buffer pH 9.6). After 1 h incubation at 4 °C, selection well was washed 5 times (10 times in second and third round) with wash buffer (50 mM Tris, 150 mM NaCl, 50 mM Mg-acetate, pH 7.5) supplemented with 0.05% Tween 20 (0.05% and 0.25% for second and third round, respectively). Collection of cDNA, obtained by reverse transcription after the third round of selection campaign, was cloned as NcoI and BamHI fragments in a pET-28b-TolA-Avi vector containing DNA sequences for spacer TolA and C-terminal Avitag [34]. The final TolA-Avi fusion proteins were expressed in *E. coli* BL21 (λDE3) GOLD strain. Whole cell lysates of individual clones were used for ELISA screening of binding to fibrin.

2.3. Binding of Protein Variants to Fibrin

Fibrin was formed directly in wells of Maxisorp 96-well plate from coated fibrinogen (10 µg/mL) by incubation with 0.001 U of thrombin (Abcam, Cambridge, UK) in the reaction buffer (50 mM Tris pH 7.4, 150 mM NaCl, 10 mM CaCl₂ and 7 mM cysteine where stated) overnight at room temperature. After washing three times with PBST buffer (phosphate buffered saline with 0.05% Tween-20) and blocking with 1% bovine serum albumin (BSA) in PBST (PBSTB), cell lysates or serially diluted protein binders in PBSTB buffer were applied. Detection was made by mouse anti-Avitag antibody (antibodies-online, Aachen, Germany) followed by anti-mouse horseradish peroxidase (HRP) conjugated secondary antibody or by streptavidin-HRP conjugate in case of detection of biotinylated protein. TMB-Complete 2 solution (TestLine Clinical Diagnostics s.r.o., Brno, Czech Republic) was used as a substrate for HRP. Reactions were stopped with 2 M sulfuric acid and absorbance was read at 450 nm. As a control, simultaneous binding to fibrinogen was also monitored.

2.4. Production and Purification of D7/E7-TolA-Avi Protein

In vivo biotinylated D7 and E7 proteins in fusion with TolA-Avi was produced in *E. coli* BL21 (DE3) cells with inserted vector bearing *BirA* gene coding biotin ligase. Upon induction of the culture, the biotin was added and the protein was *in vivo* biotinylated on the C-terminal Avitag. N-terminal His-tag was used for a native purification on Ni-NTA agarose matrice.

2.5. Preparation of Layers of Fibrin Degradation Products and Fibrinogen

MaxiSorp 96-wells flat-bottom microtiter plate was used for the immobilization of anti-human fibrinogen goat antiserum (30%) (Kamiya Biomedical Co, Seattle, WA, USA). After 1 h incubation of 100 µL of anti-fibrinogen antiserum (1:500 dilution of stock solution) wells were washed out by 200 µL 50 mM Tris, 100 mM NaCl pH 7.4 with 0.1 % Tween-20 (TB-T) for 10 times. Tween-20 was used for minimalizing of non-specific binding (5% solution; 100 µL; 1 h incubation). Wells were then washed out by 200 µL TB-T for 10 times. The next step was binding of 100 µL fibrinogen (FGL, FGP) or fibrin degradation products (FBL, FBP) for 1 h that were prepared freshly before the experiment. Lyophilized fibrinogen (Sigma-Aldrich, St. Luis, MO, USA) was used as a source for preparation of FGL and FBL, while pooled plasma was used for production of FBP and FBP production. Pooled plasma was produced by mixing twelve plasma samples from healthy donors. To prepare FBL, 1 mL of FBG (2 mg/mL) was mixed with 10 µL FXIIIa (1% solution) and 190 µL thrombin (65 U/mL), followed by 2 h incubation. Then, the formed thrombus was digested by plasminogen (0.15 U/mL) and tissue plasminogen activator (tPA, 0.3 µg/mL) in 300 µL TB during further 2 h incubation. For FBP preparation, 1 mL of pooled plasma was mixed with 190 µL thrombin (65 U/mL) and 10 µL CaCl₂ and incubated for 2 h. Then, the formed thrombus was digested by plasminogen (0.15 U/mL) and tissue plasminogen activator (tPA, 0.3 µg/mL) in 300 µL TB during further 2 h incubation. Preparations FBL and FBP were

used in preparation of ELISA plates above. FGL and FGP as controls were incubated only with 500 μ L of TB.

2.6. Binding of Protein Variants to Fibrin Layers Prepared from Lyophilized Fibrinogen or Human Plasma

Wells of 96-well plates coated with fibrin/fibrinogen layers were washed out with TB-T buffer and non-specific interactions were blocked out by 1 h sorption of serum bovine albumin (1%). After washing out of wells, 100 μ L of protein binders (D7, E7; 1 μ M) or mouse anti-fibrinogen antibody (1:1000; American Diagnostica GmbH, Pfungstadt, Germany) were added for 1 h incubation. For detection of binders or antibody, ExtrAvidin (100 μ L, 1:20000; Sigma-Aldrich, St. Luis, MO, USA) or anti-mouse IgG (100 μ L, 1:30000; Sigma-Aldrich, St. Luis, MO, USA) conjugated with alkaline phosphatase were used, respectively (1 h incubation). Para-nitrophenylphosphate (6 M) was used as a substrate for alkaline phosphatase. The change of optical properties was monitored by Sunrise ELISA Reader at 405 nm.

2.7. Construction of Truncated D7 Proteins with C-Terminal His-Tag

To produce D7 protein version lacking the TolA spacer and containing His-tag at the C-terminus, a trp leader sequence consensus (MKAI FVLNAQHDEAVDAMD) was introduced to the N-terminus. Then, a FLAG/His-tag in a tandem was attached to the C-terminus via 9- or 21-amino acid long GS-linker. The calculated Mw of all products is 11–12 kDa. The production of these proteins was performed in *E. coli* BL21 (DE3) cells at 37 °C.

2.8. Binding of D7 Protein Variants to Human Thrombus

Thrombus preparation. Human blood was donated by healthy volunteers ($n = 10$) who signed an informed consent. The informed consent was approved by the ethical committee of the International Clinical Research Center St. Anne's University Hospital Brno on 2017-03-07 (IIT/2016/30). The blood donors did not take any medication at least two weeks before blood collection.

Plasma Thrombus Preparation. Citrated blood (100 μ L per 10 mL of blood) was centrifuged at 2000 g to obtain plasma. Plasma (50 μ L) was coagulated in 8 mm glass tubes with addition of 10.9 mM CaCl₂ and NaCl and 50 mM thrombin at room temperature for 4 h. Each thrombus was cut into four pieces. Before a start of an experiment each thrombus was gently washed with 2 mL of TBS buffer.

Preparation of thrombi from whole blood. Thrombi were prepared from 10 μ L of whole blood without addition of anticoagulants in glass tubes—Target Insert 300 μ L Capacity (National Scientific Supply Company Inc., Claremont, CA)—at room temperature for 4 h. Before a start of an experiment each thrombus was gently washed with 2 mL of TBS buffer.

Confocal microscopy of D7-TolA-Avi and His-tagged D7 targeted fibrin filaments. D7-TolA-Avi (final concentration of 20 μ g/mL) was incubated with prepared thrombus in TBS buffer for 30 min. After that, each thrombus was washed twice by 200 μ L of TBS buffer and placed into TBS buffer with 6.6 μ g/mL APC streptavidin (BioLegend, San Diego, CA, USA) for 60 min. Each thrombus was washed three times with 200 μ L of TBS buffer prior to observation using confocal microscope Leica TCS SP8. Excitation and emission wavelengths were set to 633 and 645–700 nm, respectively. For visualization of His-tagged D7 variants (containing mono His-tag and Flag-tag or double His-tag) anti-Flag-tag (Monoclonal ANTI-FLAG[®] M-Cy3[™], Clone M2, Sigma-Aldrich, Prague, Czech Republic) and anti His-tag (Alexa Fluor[®] 488 anti-His Tag Antibody, BioLegend, San Diego, CA, USA) antibodies were used, respectively. The concentration was 10 μ g/mL and the incubation lasted one hour.

2.9. Preparation of D7 Liposomes Modified by Different Variants of Anti-Fibrin Protein Binder D7

Briefly, metallochelation liposomes were prepared by a method based on a hydration of a lipid film followed by extrusion through 0.4 μ m and 0.1 μ m polycarbonate filters as described previously [35,36] Liposomes were composed of EPC/DOGS-NTA-Ni/ Liss Rhod PE, 92.5/7.0/0.5 molar% *w/w/w*. All lipids were purchased from Avanti Polar Lipids ((Alabaster, AL, USA). A manually operated device Mini-Extruder (Avanti Polar Lipids) was used for the extrusion. In the following step, the solution of

D7 protein variants of binder in 50 mM Tris, pH 7.4 was mixed with the prepared solution of liposomes. The protein/lipid ratio was 1/20 *w/w*. The mixture was incubated for 30 min at room temperature.

2.10. Characterization of D7 Liposomes

Size measurement using the multiangle dynamic light scattering technique (MADLS). The hydrodynamic diameters of the binders, liposomes and proteoliposomes were determined by the MADLS technique using Zetasizer ULTRA instrument (Malvern Panalytical, Malvern, UK) at 25 °C.

Isothermal titration of liposomes by D7 protein binders. Calorimetric measurements were carried out to determine dissociation constants and thermal effects occurring during the process of formation of metallochelation bond between His-tag of protein binder and Nickel ion of DOGS-NTA-Ni lipid incorporated into liposomes. Gradual addition of the protein binder solution from a syringe with a volume of 40 µL to the titrated liposomal solution (0.5 mg/mL) with a volume of 350 µL located in a cell was performed using MicroCal PEAQ calorimeter (Malvern Panalytical, Malvern, UK). Experiments were performed in 50 mM Tris buffer, pH 7.4 at a temperature of 25 °C. The concentration of different variants of D7 protein solution was adjusted individually. The mixing rate was 750 rpm during the titration.

Transmission electron microscopy. The suspension of liposomes was covered with a Cu grid (300 Old Mesh, Agar Scientific, Austria) coated with Formvar film (Sigma Aldrich, Czech Republic) and carbon. The grid was removed from the suspension after 1 min, and the residual water was dried with a strip of lint-free filtration paper. The sample was stained with 2% Ammonium molybdate and observed under transmission electron microscope Philips 208S Morgagni (FEI, Czech Republic).

Immunogold technique was employed to prove specific binding of D7 to the surface of liposomes. Anti-FLAG antibody and 20 nm protein A colloidal gold conjugate (Electron Microscopy Science, Hatfield, PA, USA) were added to D7 liposomes and observed using transmission electron microscopy for specific staining of protein binder on the surface of liposome. The solution of Protein-A covered gold nanoparticles were diluted in ratio 1:50 and mixed with liposomal samples in the volume ratio 1:1. The mixture was incubated overnight at 4 °C and observed.

2.11. Confocal Microscopy of Thrombi Targeted with D7 Liposomes

Rhodamine-labeled D7 targeted liposomes (final concentration of 15 µg/mL) were incubated with prepared thrombus in TBS buffer for 30 min. After that, each thrombus was washed five times with 200 µL of TBS buffer prior to observation using confocal microscope Leica TCS SP8. Excitation and emission wavelengths were set to 561 and 580–650 nm, respectively.

2.12. Scanning Electron Microscopy of Whole Blood Thrombi

Samples for the scanning electron microscopy of whole blood thrombi or thrombi with fibrin-targeted liposomes were fixed in Millonig phosphate buffered glutaraldehyde (3%), post-fixed in osmium Millonig buffered (OsO₄ 2%) solution, dehydrated in 50, 70, 90, and 100% Ethanol and dried in HMDS (hexamethyldisilazane, Sigma-Aldrich, Prague, Czech Republic). Then the samples were put on the carbon tabs attached on the aluminum holder and platinum/palladium coated (Cressington sputter coater 208 HR, Watford, UK). The surface of the thrombus was observed under scanning electron microscope Hitachi SU 8010 (Hitachi High Technologies, Europe GmbH, Krefeld, Germany) at magnification of 2000× (at 14 kV, SE detector, working distance 10.8 mm).

2.13. In Vitro Binding of D7F1 Liposomes under Flow Conditions Using MCA Model

Simplified virtual middle cerebral artery (MCA) models with a branch (bifurcation) were designed with Fusion 360 (Autodesk) with anatomy resembling average middle cerebral artery diameter 3.1 mm, (after bifurcation 2.9 mm, the branch 1.4 mm). The lumen was three-dimensionally (3D) printed and cast into silicone Sylgard[®] 184 Elastomer kit (Dow Corning, Bay City, MI, USA). The silicone model was connected to a peristaltic pump Lambda Multiflow (Lambda Laboratory Instruments, Brno,

Czech Republic) with 3.1 mm (inner diameter) tubes and filled with TBS buffer (pH 7.4). Externally prepared *in vitro* clot from whole blood (100 μ L a diameter of each glass tube was 6 mm for 100 μ L of blood.) was inserted into tubing through a funnel to simulate the thromboembolic event in MCA. After MCA occlusion the buffer was flowing through a branch at 4.5 mL per minute. D7F1 liposomes were injected by Hamilton syringe into the flow system. The TBS buffer with final concentration of 15 μ g per ml D7F1 liposomes was circulating one hour before the clot inside the *in vitro* model was extracted from the *in vitro* model, washed with TBS and examined under confocal microscope (Leica) to observe penetration of fluorescently labeled liposomes into the thrombus.

3. Results

3.1. Production of Recombinant Protein Targets Carrying B β Epitope (BEP)

In this study, a short protein corresponding to B β chain epitope of human fibrinogen recognized by 102-10 mAb (BEP) as a molecular target for the ribosome display was used. This epitope discovered by Hisada et al. [16] was predicted to be sterically shielded in fibrinogen but uncovered and exposed during fibrin thrombus formation. This epitope consisting of 16 amino acid residues (CNIPVVS β GKECEEIIR) was, therefore, chosen as a major N-terminal binding motif for design and assembly of the recombinant protein, constructed in fusion with C-terminal Avi-tag. To facilitate protein purification, the sequence of His-tag was added to the N-terminus of the full-length construct (BEP-TolA-Avi, Figure 1). To significantly expose BEP moiety as a target for ABD screening, and to increase changes for the recognition during ribosome display, a variant carrying triple-BEP motives connected via GGGGS-linkers (3BEP-TolA-Avi) was also designed and assembled. As a control, protein lacking BEP epitope (Δ BEP-TolA-Avi) was also generated. All proteins were produced in *E. coli* BL21 cells and subsequently purified (Figure 1).

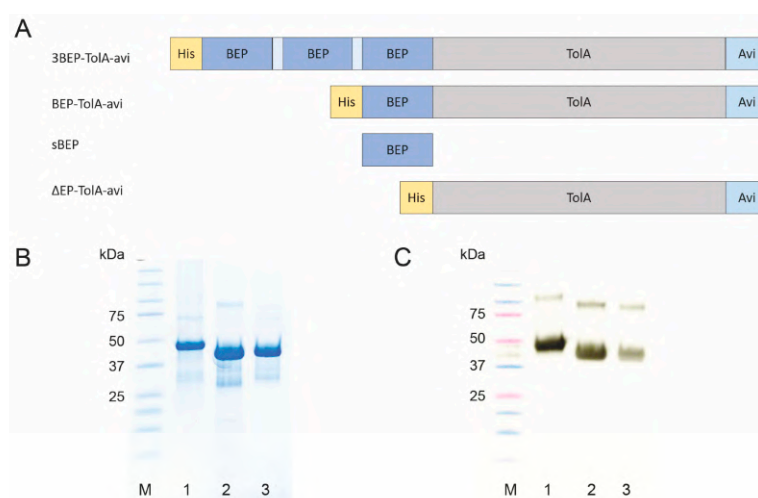


Figure 1. Schematic representation of BEP-carrying targets and their production and identification. *In vivo* biotinylated proteins carrying triple BEP epitope (3BEP-TolA-Avi), single BEP epitope (BEP-TolA-Avi), 16 amino acid synthetic BEP peptide (sBEP) and a control BEP-lacking protein (Δ BEP-TolA-Avi) shown in panel A. Visualization of produced proteins on sodium dodecyl sulphate-polyacrylamide gel electrophoresis (SDS-PAGE): molecular weight marker (lane M), 3BEP-TolA-Avi (lane 1), BEP-TolA-Avi (lane 2), Δ BEP-TolA-Avi (lane 3), respectively (panel B). Western blot of purified recombinant proteins (panel C) detected by streptavidin-HRP conjugate. Description of lanes is as presented in panel B.

3.2. Ribosome Display and Screening of Protein Variants

For ribosome display, assembled and purified 3BEP-TolA-Avi protein was chosen as a target. To minimize selection of binders raised to a TolA-Avi protein backbone, a preselection step using the

generated Δ BEP-TolA-Avi protein was used. After a three-round ribosome display campaign with an increasing stringency of the selection conditions, transcribed cDNA sequences were inserted into the pET-28b plasmid, thus generating a library of the binding candidates. Cell lysates of individual bacterial colonies were screened for binding to coated fibrin and fibrinogen by ELISA. Protein variants with a substantial binding to fibrin and that reduced to fibrinogen were selected, their proteins purified and further examined in a detail. From the collection of almost 400 tested clones, four variants named D7, E7, F7 and F11 confirmed the preferential binding to the insoluble fibrin and were, therefore, selected as the most promising ones (Figure 2A, Table 1). Sequencing of the particular cDNA cloned into the plasmid vector revealed that E7 and F7 variants are identical. Further testing demonstrated a high binding of E7 and F11 proteins to the soluble fibrinogen. D7 protein was, therefore, chosen as the only suitable binder with a substantial binding preference to insoluble fibrin and its binding curve was measured by ELISA (Figure 2B).

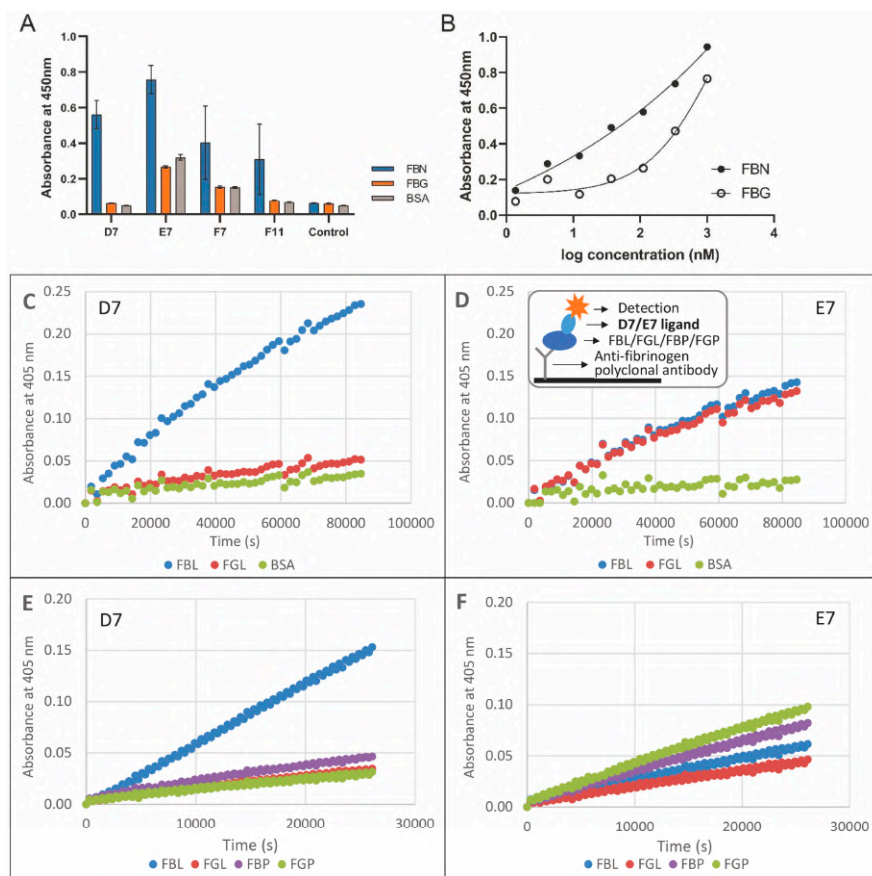


Figure 2. Binding of D7 and E7 protein variants to fibrin layer tested by ELISA. Binding of *selected in vivo* biotinylated protein variants to immobilized fibrin, fibrinogen and bovine serum albumin detected by streptavidin-HRP conjugate. Average values of triplicates with standard deviations are presented (A). Binding curves of *in vivo* biotinylated D7-TolA-Avi protein to fibrin (FBN) and fibrinogen (FBG) in ELISA (B). Binding of D7-TolA-Avi (C,E) and E7-TolA-Avi (D,F) protein variants to fibrinogen and fibrin layers tested by ELISA. Binding of protein variants to layers prepared from lyophilized fibrinogen (C,D) and those prepared from human plasma (E,F). Insert in the panel D shows a schematic representation of fibrin (FBN)/fibrinogen (FBG) layers and detection of the bound proteins. Legend: FBN—fibrin, FBG—fibrinogen, BSA—bovine serum albumin, FBL—fibrin layer prepared from lyophilized fibrinogen activated by thrombin, FGL—layer of fibrinogen produced from lyophilized product, FBP—fibrin layer prepared from human plasma activated by thrombin, FGP—layer of fibrinogen from human plasma.

Table 1. Amino acid sequences of selected protein binders. Sequence comparison of the fibrin binders. The non-mutated ABDwt was aligned with the randomized part of the ABD-derived binders selected by ribosome display. Grey boxes indicate the 11 positions at which the residues of ABD (aa 20–46) were randomized. The non-randomized N-terminal part of ABD (aa 1–19) contains sequence LAEAKVLNRELDKYGVSD.

Binder	20	21	22	23	24	25	26	27	28	29	30	31	32	33	34	35	36	37	38	39	40	41	42	43	44	45	46
ABDwt	Y	Y	K	N	L	I	N	N	A	K	T	V	E	G	V	K	A	L	I	D	E	I	L	A	A	L	P
D7	A	Y	K	N	P	I	N	L	A	R	S	V	P	T	V	K	G	A	I	D	P	I	L	A	A	L	P
E7=F7	F	Y	K	N	L	I	N	V	A	M	P	V	V	L	V	K	T	A	I	D	G	I	L	A	A	L	P
F11	G	Y	K	N	W	I	N	P	A	D	G	V	A	G	V	K	S	A	I	D	A	I	L	A	A	L	P

3.3. Binding of D7 and E7 Protein Variants to Fibrin Layer

After ribosome display, a large-scale screening of the binding variants was performed using thrombin-treated fibrinogen coated on wells of microtitre plates. To verify that the identified D7 and E7 binding candidates bind not only to a coated insoluble fibrin but also to fibrin degradation products, tests on layers of fibrin and fibrinogen captured to the plate via polyclonal antibody (Figure 2C,D) were performed. These experiments confirmed that D7 clone preferentially binds to fibrin while binding to fibrinogen is minimized and stays on the background level. Contrary this, E7 protein variant does not distinguish between fibrinogen and fibrin and binds to both proteins in a similar way. Additionally, we compared binding of D7 and E7 variants to fibrin layer prepared from a commercial lyophilized fibrinogen or from isolated human plasma (Figure 2E,F). We found that the binding to fibrin prepared from a lyophilized product is more pronounced than binding to fibrin produced from human plasma. In this experiment, E7 protein demonstrated its high binding to lyophilized fibrinogen as well as to human plasma.

3.4. Binding of D7 Protein to Human Thrombus *in Vitro*

To verify whether D7-TolA-Avi recognizes fibrin filaments in human thrombus, binding of the D7 protein to thrombus prepared from human whole blood was visualized by confocal microscopy (Figure 3). The quality of the prepared thrombus is documented in the panel A and detection of clearly visible fibrin fibers by D7-TolA-Avi protein is presented in the panels B and C. Negative staining by a control ABDWT-TolA-Avi protein (D) or in the presence of secondary reagent only (E) are also presented.

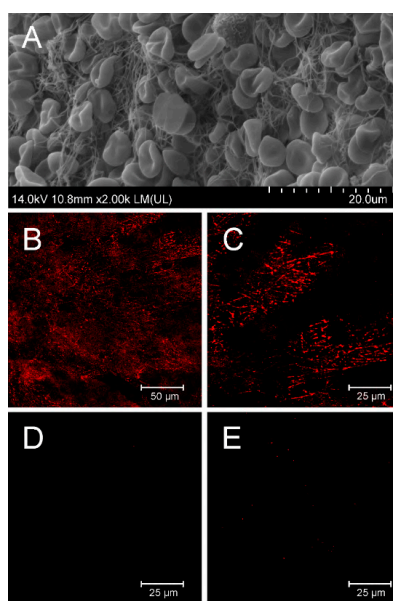


Figure 3. *In vitro* binding of fibrin filaments in the human whole blood thrombus by D7-TolA-Avi. Quality control of the structure of prepared whole blood thrombi was confirmed by SEM. Representative

picture of thrombus prepared for binding experiments with a clear structure of fibrin filaments (A). D7-TolA-Avi was tested for the ability to target fibrin filaments of the human blood clots. APC-streptavidin was used for visualization. Samples were observed using Leica TCS SP 8 confocal microscope (excitation 633 nm, emission 645–700 nm). The representative picture illustrates the specific interaction of D7-TolA-Avi with fibrin in human blood thrombus (B). Detailed picture of fibrin in the blood thrombus. Non-homogeneous distribution of the signal is given by the observation of a thin confocal plane (C). Negative control—picture of thrombus incubated with non-specific ABDwt-TolA-Avi protein and APC-streptavidin (D), and a negative control—picture of thrombus incubated with APC-streptavidin (E).

3.5. Production of Short Variants of D7 Binding Protein with C-Terminal His-Tag

For the purpose of an immobilization of the D7 protein to nanoliposomal particles via interaction of a polyhistidylated tag with Ni-NTA-modified surface, truncated proteins were designed and produced from plasmids in which D7 protein cDNA was fused to GS-linker with FLAG-tag and His-tag at the C-terminus (Figure 4A). The D7-F1 protein contains a shorter GS-linker in comparison to the D7-F3 version (nine versus 21 amino acids, respectively). To increase binding affinity to Ni-NTA-modified liposomal surface, we constructed also double-His-tag versions of the truncated D7 and ABD-WT proteins using the same GS-linker as that used for FLAG-His variants preparation (Figure 4A).

3.6. Preparation and Characterization of Liposomes

Plain metallochelating nanoliposomes (EPC/DOGS-NTA-Ni 93/7 *w/w*) of the size about 92 nm and negative ζ -potential were prepared by lipid hydration method and extrusion (Figure 4). Selected specific binders (Figure 4A) as well as their control counterparts were bound onto liposomal surface via metallochelating interaction (Figure 4B). This binding was reflected by an increase of hydrodynamic radius of formed proteoliposomes. The increase in the size of modified liposomes was in a good accordance with hydrodynamic radius of various binders used (Figure 4C–F). Binders itself possess negative charge and modification of the liposomal surface with binders did not change significantly the negative ζ -potential of liposomes, but only in the case of binder D7H2 a shift to positive value of ζ -potential was observed (Figure 4G).

Modification of liposomal surface by binders was also confirmed by TEM and immunogold TEM. Comparison of TEM pictures of plain and binder modified liposomes demonstrated direct visualization of binder molecules on the liposomal surface (Figure 5A,C,E,G). The presence of binder molecules on the surface of nanoliposomes was confirmed by immunogold staining technique. Gold nanoparticles modified with anti-FLAG antibodies recognized the protein binders on the liposomal surface and liposomes were labeled with contrast gold nanoparticles, while the plain liposomes were not labeled (Figure 5B,D,F). Figure 5H represents the schematic picture of specific binder staining directly on the surface of liposomes. The visualization of gold nanoparticles on the surface of D7 liposomes was done by different detectors (Figure 5H–J)—SE, TE and YAGBSE detectors, respectively.

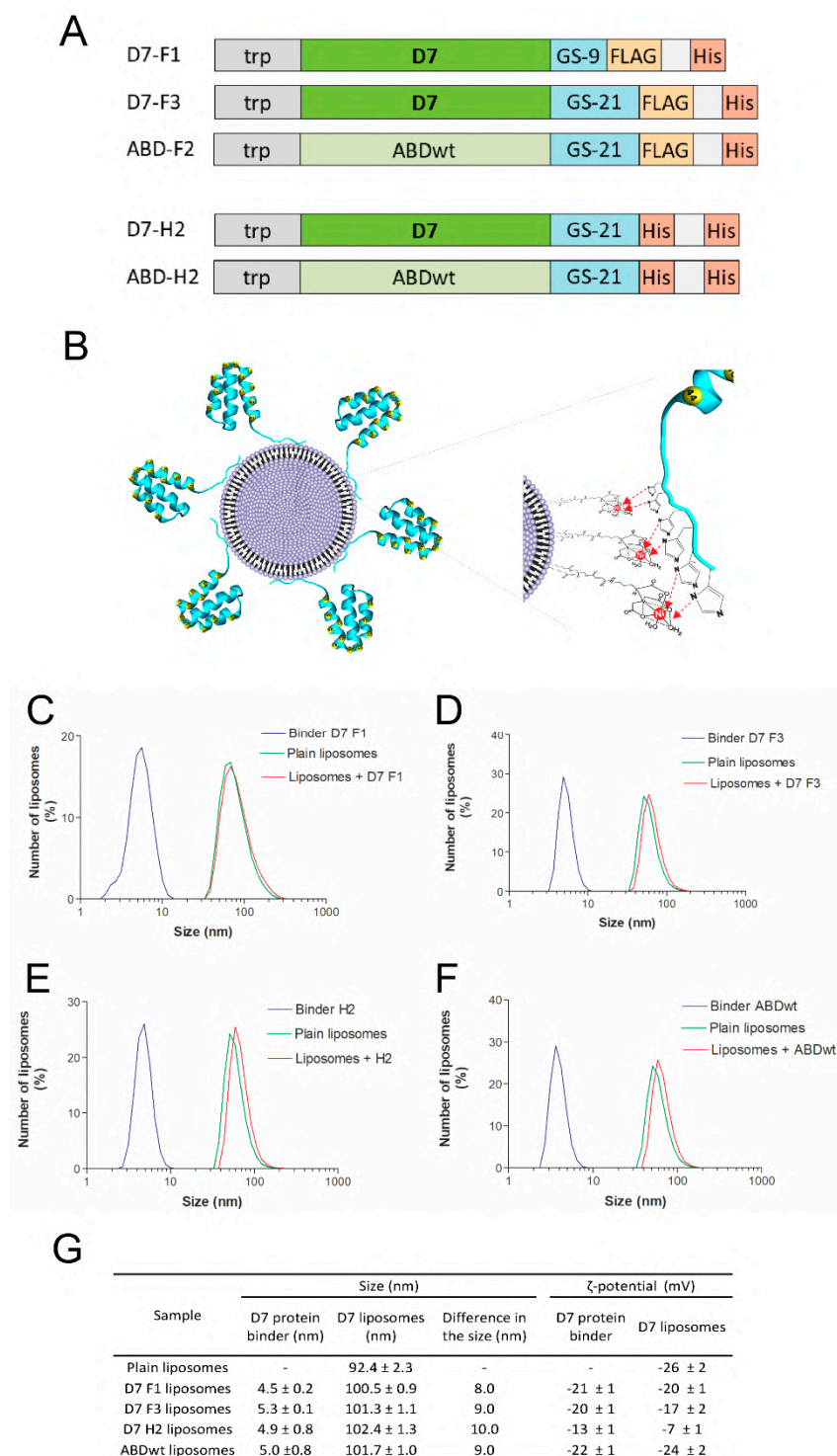


Figure 4. Characterization of liposomes modified by ABD-protein binders using MADLS. Schematic representation of C-terminally polyhistidylated variants of D7 binding proteins and ABD-WT control (A). Schematic representation of metallochelation bond of polyhistidylated variants of D7 proteins onto the surface of liposomes (B). The size distribution of mono- and double-His-tagged binders, plain liposomes and proteoliposomes was measured using MADLS technique. Increase in the size of plain liposomes followed its surface modification with both mono- and double-His-tagged binders was observed. Size distribution of D7F1 (C), D7F3 (D), D7H2 (E) and ABDwt (F) modified liposomes are shown. Inserted table summarizes the change in the size and ζ -potential followed liposome modification (G).

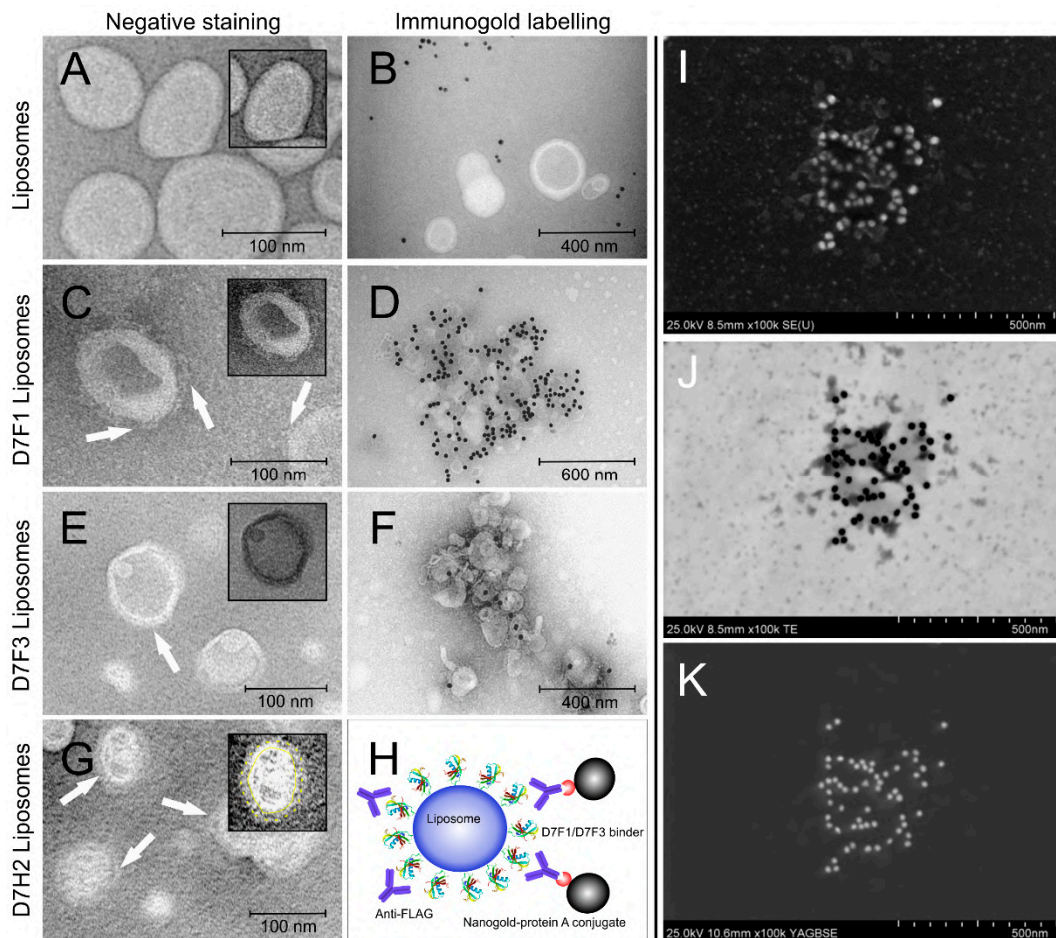


Figure 5. TEM of liposomes modified by mono His-tagged D7F1, D7F3 and double His-tagged D7H2 variants of ABD-protein binders using negative staining and immunogold labeling technique. Contrast of liposomes was enhanced using negative staining with exception of H–J. TEM micrographs are displayed of plain metallochelation liposomes (A), D7F1 (C), D7F3 (E) and D7H2 proteoliposomes (G). Binders are clearly visible on the surface of all binder-modified liposome samples. Immunogold labeling using anti-FLAG M2 antibody was used for specific detection of binder attached to the surface of metallochelation liposomes: control plain liposomes (B), D7F1 liposomes (D), D7F3 (F). Schema representing specific detection of binder molecules using the system of Anti-FLAG antibody and 20 nm protein A colloidal gold conjugate. (H–K) Detail of liposomes with binder D7H2 visualized by specific immunogold staining and detected also by using TEM equipped with SE, TE, YAGBSE detectors, respectively. Insets in (A,C,E,G): highlighted structure of selected proteoliposomes by image over contrasting, color inverting and/or labeling clearly show a protein corona formed by protein binders on the surface of liposomes.

3.7. Thermodynamic Characterization of Interaction between ABD-Protein Binders and Metallochelation Liposomes

Isothermal titration experiments enable direct measurement of $\Delta^\circ G$ and calculation of dissociation constant K_d for binder-liposome complexes prepared at 25 °C (298.15 K). Binders with double His-tag exerted lower dissociation constant in comparison to binders with one His-tag in their molecule. This means that insertion of double His-tag increased the binding of protein binders onto liposomes. Results are summarized in Table 2.

Table 2. Thermodynamic parameters of interaction between ABD-protein binders and metallochelation liposomes obtained by isothermal titration. Experimental conditions: 50 mM Tris buffer pH = 7.4; temperature of 25 °C (298.15 K).

Binder	K_d (M)	$\Delta^\circ G$ (kJ/mol)
D7 F1	$1.2 \pm 0.1 \times 10^{-7}$	-39.7 ± 0.7
ABD wt F2	$1.06 \pm 0.4 \times 10^{-7}$	-39.8 ± 1.9
D7 F3	$1.79 \pm 0.55 \times 10^{-7}$	-38.5 ± 2.8
D7 H2	$2.21 \pm 0.1 \times 10^{-9}$	-49.4 ± 1.0
ABD-wt H2	$2.35 \pm 0.2 \times 10^{-8}$	-43.5 ± 1.6

3.8. Interaction of Fibrin-Specific Binders with Thrombi

To confirm the ability of selected binders to specifically bind to human thrombus (binder variants containing one His-tag (D7F1, D7F3) and two inserts of His-tag (D7H2), fibrin fibrils in thrombi was visualized by confocal microscopy after the incubation with fluorescent conjugates (Figure 6(A1–A3)). All tested binders exerted strong binding onto fibrin in thrombi in comparison to their wild-type counterparts, which did not bind the fibrin at all (Figure 6(B1–B3)). Fluorescent conjugates (anti-FLAG and anti-His-tag) without the incubation with binders were used as controls (Figure 6(C1–C3)). Structure of fibrin thrombus with bound binders stained with fluorescence anti-FLAG and anti-His-tag antibodies is visualized in 3D projection (Figure 6(D1–D3)). In addition, the ability of D7F1 to bind to the fibrin fibrils of mouse thrombus was tested according to the same protocol. Although the observed signal was significantly lower as compared to human thrombi, the ability of binding onto fibrin fibers was confirmed (supplementary file, Figure S1).

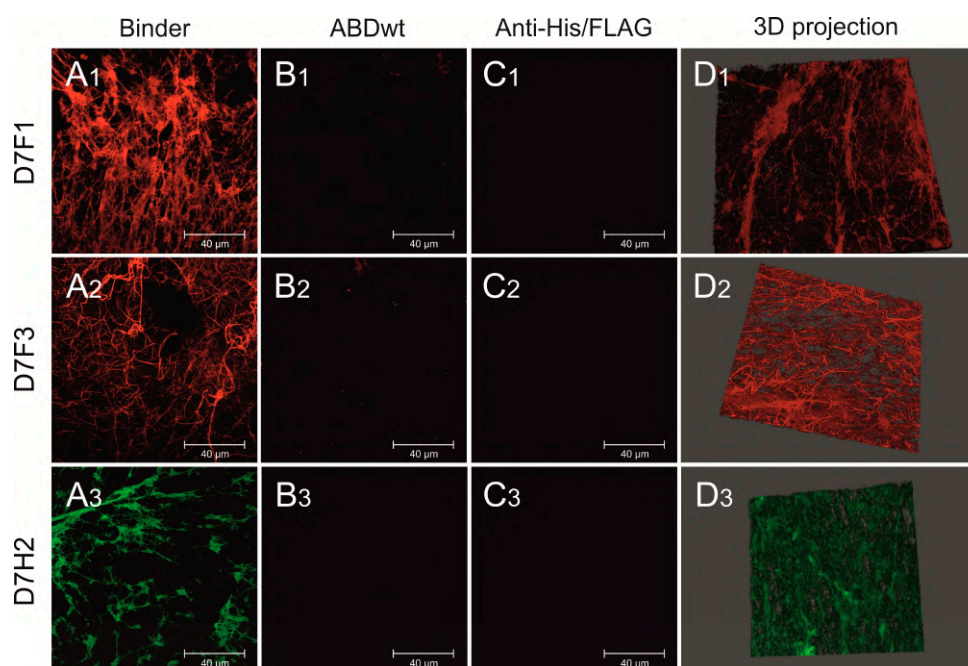


Figure 6. Confocal microscopy of fluorescently labeled D7F1, D7F3 and DFH2 variants of ABD-protein binders attached to fibrin fibrils of human thrombus. Various ABD-protein binders were incubated with human thrombus, washed and visualized using fluorescently labeled antibodies. D7F1 and D7F3 variants of ABD-protein binders were visualized using Anti-FLAG[®] M2 Cy3 Antibody Conjugate (colored in red—A1,A2). D7H2 binder was visualized using Anti-6X His tag[®] Alexa Fluor[®] 488 antibody (colored in green—A3). Non-specific ABDwt was used as a negative control (B1–B3). Anti-FLAG[®] M2 Cy3 Antibody Conjugate and Anti-6X His tag[®] Alexa Fluor[®] 488 antibody were incubated with thrombus without the presence of fibrin-specific binders as a negative control (C1–C3). 3D reconstruction of stained fibrin meshes (D1–D3). Displayed scale bar 40 µm.

3.9. Interaction of Targeted Liposomes with Thrombi

Fibrin-selective binders D7F1, D7F3 and D7H2 were bound onto the surface of metallochelating nanoliposomes labeled with fluorescence probe Rhodamine-Lyssamine PE via formation of His-tag—Nickel complexes. Binding of liposomes targeted by various types of binders onto particular thrombi was visualized by confocal microscope. Liposomes targeted by selective binders D7F1, D7F3 and D7H2, respectively, were able to bind fibrin fibers and fibrous structure of the thrombi was clearly imagined by confocal microscopy (Figure 7). Massive binding of targeted liposomes was observed (Figure 7A–C). It is interesting that plain liposomes also adhered onto fibrin fibers, but the number of bound liposomes was lower in comparison to the targeted ones (Figure 7D). Detail of interaction of D7H2 liposomes with fibrin fibers is visualized in Figure 7E. SEM picture of fixed thrombus with bound D7H2 liposomes and its negative control are in Figure 7F,G, respectively. Detailed visualization of direct interaction between liposome and surface of fibrin fiber is displayed in the Figure 7E.

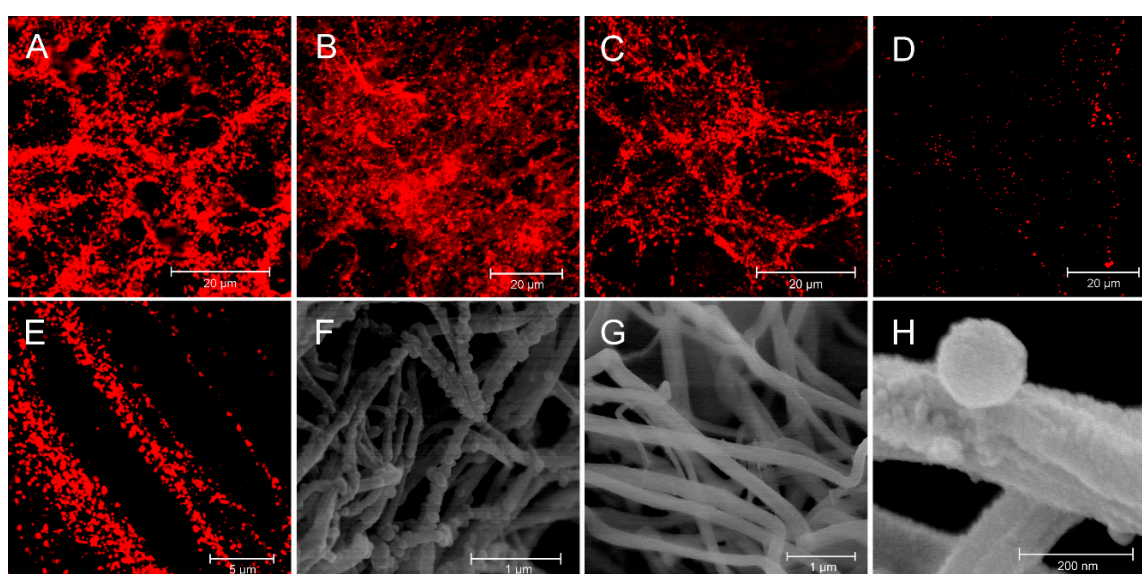


Figure 7. Binder-modified proteoliposomes targeted to fibrin fibers of human thrombus. Confocal microscopy and SEM were used for visualization of binder-modified proteoliposomes bound to the fibrin fibrils of human thrombus. Confocal microscopy of D7F1 (A), D7F3 (B) and D7H2 (C) modified liposomes labeled with fluorescent probe rhodamine-lyssamine PE. Fluorescent plain liposomes were used as control (D). Detailed picture demonstrate the binding of D7H2 liposomes onto the surface of fibrin fibrils using confocal microscopy (E). SEM—picture of fixed thrombus with attached D7H2 proteoliposomes (F) with its negative control (G). Detail of direct interaction between D7H2 liposome and surface of fibrin fiber (H).

3.10. In Vitro Model of Thrombus Obstruction in Artery for the Evaluation of in Vitro Binding of Liposomes onto the Fibrin in Thrombi

Thrombus was placed in a silicone replica of the human middle cerebral artery to mimic the situation of complete occlusion of the artery (Figure 8A,B). In vitro binding of fibrin in the thrombus by fluorescently labeled liposomes was then examined under flow conditions to mimic possible real situation occurring *in vivo*. After 20 min medium was replaced with those free of liposomes and perfusion continued for next 10 min to remove non-bound liposomes. The thrombus was removed after the completing the experiment and confocal microscopy was used to prove the perfusion of targeted liposomes into the thrombus. Liposomes penetrated into thrombus and the depth of penetration was clearly detectable by confocal microscopy. After 20 min of the incubation of the thrombus in the model under flow conditions, the depth of massive penetration of D7H2 liposomes in the range of 50–100 µm was observed (Figure 8C).

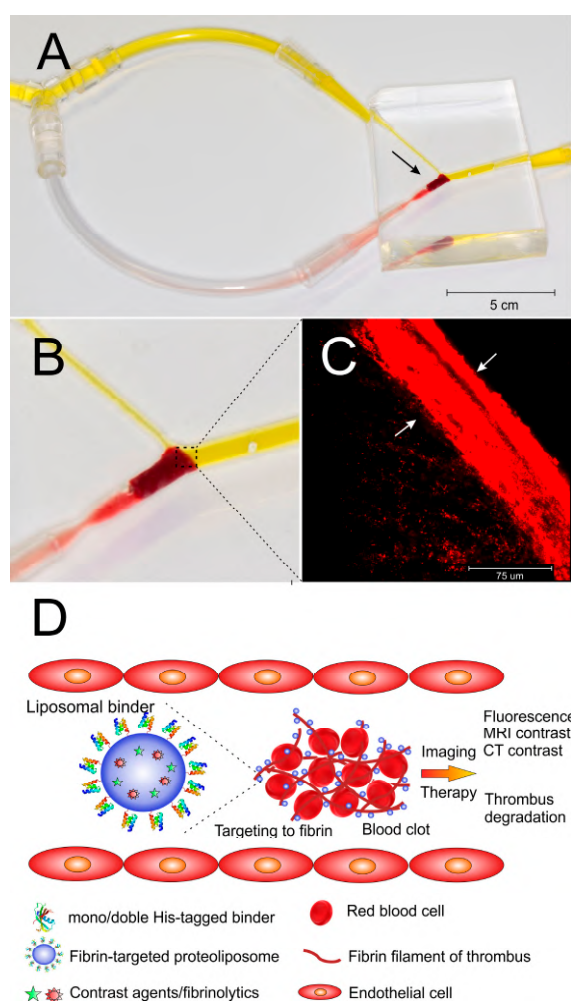


Figure 8. In vitro binding of targeted nanoliposomes to the thrombus under flow conditions. Picture of silicone replica of middle cerebral artery and its connection to the fluid circulation drawn by flow pump. The site of the occlusion caused by introduced thrombus is marked by the arrow (A). Detailed view of the site of occlusion (the circulation of fluid is highlighted by yellow color) (B). Penetration of fibrin-targeted liposomes to the thrombus withdrawn from the silicone model detected by fluorescence confocal microscopy. Depth of penetration is marked by arrows (C). Schematic picture of targeting of fibrin fibers of the thrombus under flow conditions (D).

4. Discussion

Fibrin formation is triggered by thrombin cleavage of fibrinopeptides on fibrinogen molecules, which allows them to spontaneously self-assemble into large fibers that provide the support structure of the thrombus and promote healing. Many aspects of their structure and functions still remain unknown [37,38]. The distinction between fibrinogen and fibrin is needed for determination of the size and place of thrombus formation. However, almost identical structure of fibrinogen and fibrin is hindering the process. Formation of insoluble fibrin is accompanied only by subtle changes in secondary structure and formation of very limited number of distinct new covalent bonds with new epitopes emerging. Presence of available free cysteine during polymerization process affect FXIIIa activity and possibly leads to remodeling of inter/intra molecular disulphide bonds resulting in new recognizable structures [39,40]. Interestingly, mouse and rat anti-insoluble fibrin monoclonal antibodies used in this study also significantly bind to fibrin formed in the presence of cysteine (supplementary file, Figure S2), while a diminished binding was observed in the absence of cysteine during fibrin formation.

In this work, we generated insoluble fibrin-targeted protein binders useful for development of thrombus imaging agents. For this non-immunoglobulin approach, combinatorial library derived from 5.5 kDa albumin-binding domain of streptococcal protein G was chosen as this library of theoretical complexity up to 10^{14} protein variants has already provided binders of several important protein targets [31,34,41], some of them with nanomolar or even sub-nanomolar binding affinity [30,32,33]. To stabilize small protein binders, 305 amino acid helical TolA protein is being used to form 38 kDa fusion binding variants. In combination with detection and purification tags, ABD-derived proteins can be simply modified by *in silico* and gene-fusion approaches. Therefore, ABD binders represent a suitable model for development of fibrin-targeted binders useful for development of thrombus imaging tools.

To target the insoluble form of fibrin, we used 16 amino acid peptide of the fibrinogen B β -chain (BEP epitope) [16] as an epitope for protein binder's selection. This epitope, originally recognized by 102-10 monoclonal antibody reacting only with fibrin thrombus, was suggested as a unique region sterically shielded in fibrinogen or soluble fibrin, but conformationally changed and exposed in a polymerized form of insoluble fibrin fibers. Yet this feature has not been structurally defined nor independently confirmed, BEP-specific Fab fragment probe constructed from 102-10 mAb [18] was successfully used for tumor imaging in mouse model of pancreatic ductal adenocarcinoma (PDAC). Immunohistochemistry and *ex vivo* imaging confirmed selective distribution of the 102-10 Fab in fibrin thrombus in PDAC tumors with no observed effect on fibrinolysis or blood coagulation.

BEP is a conformation epitope and we, therefore, designed and constructed single and triple versions of BEP-derived fusion proteins as targets for ribosome display selection of anti-fibrin binders. To test function of these assembled proteins, we used mouse monoclonal antibody clone L (1101) and rat monoclonal antibody clone 443, both selected as BEP-specific and immunohistochemically verified in tumor cells. Both these antibodies confirmed a specific recognition of the 3BEP-TolA-Avi fusion in ELISA (Figure S3). In a striking contrast, control Δ BEP-TolA-Avi protein lacking ABD sequences, and also synthetic 16 amino acid peptide (sBEP), were not recognized by these antibodies. This result indicates the specificity of both antibodies for the BEP recognition, and as the linear peptide is not recognized by the used antibodies, this further supports a conformation requirement carried by 3BEP-TolA-Avi fusion protein. Thus, it can be used as a target for ribosome display in combination with a pre-selection step by Δ BEP-TolA-Avi. Interestingly, rat 443 as well as mouse 1101 mAb recognize 3BEP-TolA-Avi target regardless type of immobilization—by a direct coating or via C-terminal Avitag-mediated biotinylation (Figure S4). In addition, sensitivity/specificity of the BEP recognition is demonstrated by an increased signal of the triple-BEP protein in comparison to the single-BEP one.

Presented work relied on BEP-targeting approach for the selection of anti-insoluble fibrin binders. This strategy provided several binding candidates distinguishing between formed fibrin and the soluble fibrinogen. Based on tests of specificity, only D7 variant demonstrated a substantial preference for binding to fibrin in comparison to fibrinogen. Fibrin produced for *in vitro* large-scale screening of ABD variants, however, differs from that formed during a coagulation process *in vivo*. Fibrin polymer network produced in microtiter plates by thrombin has a limited cross-linking potential due to the immobilization to plastic substrate. Additionally, absence of factor XIII and plasmin may not produce D-dimers as in the case of blood thrombus formation. Despite these limitations, D7 protein substantially binds to fibrin layer prepared from lyophilized fibrinogen (Figure 2) similarly to binding of anti-insoluble fibrin monoclonal antibody (Figure S5).

A very interesting finding was that binding of D7 fibrin variants to fibrin prepared from a lyophilized product was different than binding to fibrin produced from human plasma. The influence of residual water on the solid-state properties of freeze-dried fibrinogen and dissolution of lyophilized fibrinogen studied by combined small- and wide-angle X-ray scattering (SWAXS) showed that there were differences triggered due to the different levels of residual moisture in various samples. The dissolution rates were found to decrease with increasing specific surface, most notably in the

amorphous form, in contrast to expectations from classical thermodynamics. Protein conformational changes and hydrophobic surface formation upon depletion of water could be possible causes [42,43].

The most critical part of the development of anti-insoluble fibrin protein binders is to suppress fibrinogen recognition. The most specific variant identified after ribosome display selection, D7 protein, contains three proline residues randomized in positions 24P, 32P and 40P of the ABD scaffold structure. While amino acid residue 32 is located in a flexible loop between helix 2 and 3, position 24 and 40 can cause a local structural changes in the helices 2 and 3, respectively. Proline residues are known to change angles in helical structures, so modifications of the helical structure or reorientation of the helices in the D7 protein cannot be excluded. This can, however, support the fibrin B β epitope recognition and increase the observed anti-fibrin specificity. Beside recognition of human fibrin, confocal microscopy proved also selective binding of D7F1 binder towards fibrin in thrombi prepared from mouse blood. Binding of wild-type binder ABDwt as a negative control did exert negligible binding (see Figure S1).

Residual binding of D7 protein variant to fibrinogen, however, still remains substantial and needs to be suppressed. This can be done by generation of an optimized form of D7 protein by *in silico* docking using known structure of human fibrin D-dimer and structure of fibrinogen with the prediction of D7 protein mutations suppressing the fibrinogen recognition. Alternatively, molecular improvement of D7 variant can be performed by an affinity maturation approach using error-prone PCR-generated library and identification of variants with diminished binding to fibrinogen.

Non-covalent orthogonal binding of proteins with His-tag onto liposomes via metallochelating bond represent simple methods used for preparation of various proteoliposomes [35,44,45]. In our study, we tested protein binder constructs with one or two His-tags to compare complex stability constants (Table 2). As expected, double His-tag construct forms more stable complex with liposomes than constructs with one His-tag (Table 2). Changes of Gibbs energy differ in binders with one or two His-tag and this is reflected by the values of $\Delta^\circ G$ and dissociation constants K_d of complexes. Relatively high stability of double His-tag (K_d in nM range) makes them suitable at least for various *in vitro* experiments designed to prove the concept and the value of K_d is comparable to that published for metallochelating complexes [46]. Doubling of His-tags seems to increase the stability of complexes in physiologic fluids and the measured nanomolar K_d value was sufficient for testing of thrombus detection under flow conditions. ABD-based D7-TolA-Avi binder demonstrated also sufficient thermal stability as shown in Figure S6 in supporting information. This characteristics is of interest for a possible future industrial-scale production and application.

Under flow condition in silicone replica of the human middle cerebral artery, the liposomes with D7H2 binder were able to penetrate through the mesh of fibrin fibers by diffusion and quickly bind to form the highly fluorescent zone at the forehead of thrombus. It is worth to note that behind the thrombus forehead, which is in the direct contact with the medium flow, the concentration of liposomes was significantly lower (Figure 8C). This, again, pointed to strong binding of binder targeted liposomes onto fibrin fibers. This is an important factor for future *in vivo* applications with respect to imaging of thrombi by MRI or CT, and for the thrombolysis mediated by liposome-delivered thrombolytic drugs (Figure 8D).

The mechanism of liposome penetration into thrombus revealed by *in vitro* model could have some consequences for *in vivo* solubilization of thrombus by application of targeted thrombolytic drugs like alteplase. The model predicts that the liposomes will move through the thrombus into its deeper part as a zone. It means that penetration of liposomes into thrombus will depend on concentration of liposomes in blood because they are trapped efficiently by fibers close to the forehead of thrombus washed with blood flow. Saturation of the surface of fibrin fibers in forehead of thrombus by liposomes enables the penetration of incoming liposomes deeper into thrombus by diffusion. Our experiments confirmed that nanoliposomes with the size around 100 nm are small enough to diffuse freely through the fibrin mesh of thrombi.

5. Conclusions

In summary, we present here the anti-insoluble fibrin binder D7 derived from the ABD scaffold. Small binding proteins are suitable for large-scale production and represent an innovative approach for the development of specific ligands that are important for targeting of drug nanocarriers such as nanoliposomes. Functionalized nanoliposomes targeted by specific binders can be a platform for further development of theranostics useful for imaging and solubilization of thrombi. Our next study is focused on labeling of binder-targeted liposomes with gadolinium complexes for in vivo imaging by MRI.

Supplementary Materials: The following are available online at <http://www.mdpi.com/1999-4923/11/12/642/s1>, Figure S1: Binding of D7F1 binder to fibrin filaments of mouse thrombi, Figure S2: Binding of anti-insoluble fibrin antibodies to fibrin in the presence or absence of cysteine or to fibrinogen tested in ELISA, Figure S3: Binding of anti-fibrin monoclonal antibodies to BEP-carrying targets tested by ELISA, Figure S4: Binding of anti-fibrin monoclonal antibodies to differentially immobilized BEP targets tested by ELISA, Figure S5: Binding of mouse anti-insoluble fibrin monoclonal antibody to human fibrinogen and fibrin layers produced from a lyophilized product or from human plasma tested in ELISA, Figure S6: Thermal stability of D7-TolA-Avi protein.

Author Contributions: Conceptualization, J.E.D., M.R., R.M., P.M. and J.T.; Data curation, M.K., A.V.W., E.B., F.H., J.K., P.T.K., E.V. and R.H.; Formal analysis, H.P., E.B. and E.M.; Funding acquisition, R.M., P.M., M.R. and J.T.; Investigation, H.P., J.M., M.K., A.V.W., J.Š., E.B., P.K., F.H., J.K., P.T.K., E.V., R.H. and E.M.; Methodology, H.P., J.M., M.K., J.Š., E.B., S.M. and J.T.; Project administration, J.T., J.M., R.M. and P.M.; Resources, J.T., P.M., M.R., R.M.; Supervision, J.M., P.M. and J.T.; Writing—original draft, H.P., J.M., J.E.D., P.M. and J.T.; Writing—review & editing, H.P., J.M., E.B., J.E.D., M.R., R.M., P.M. and J.T.

Funding: This work was supported by the Czech Health Research Council, Ministry of Health of the Czech Republic [project No. 16-30299A (R.M., J.T., P.M., J.M.)]; the Institutional Research Concept RVO: 86652036; by The Ministry of Education, Youth and Sports of the Czech Republic—European Regional Development Fund [project BIOCEV No. CZ.1.05/1.1.00/02.0109], project FIT No. CZ.02.1.01/0.0/0.0/15_003/0000495 (J.T., M.R.) and project CEREBIT No. CZ.02.1.01/0.0/0.0/16_025/0007397 (M.R., J.T., P.M.); Czech Ministry of Agriculture grant MZE RO0518. R. Mikulík has been supported from the National Program of Sustainability II (MEYS CR) [project No. LQ1605] and by FNUSA-ICRC [project No. CZ.1.05/1.1.00/02.0123].

Acknowledgments: We thank Yasuhiro Matsumura, Research Center for Innovative Oncology, National Cancer Center Hospital East, Kashiwa City, Japan, for providing mouse and rat monoclonal anti-insoluble fibrin antibodies. The authors thank Michal Malý and Petra Kadlčáková from the Institute of Biotechnology CAS for excellent experimental assistance. The access to instruments in the NanoPharm laboratory (joined project of the Veterinary Research Institute and the International Clinical Research Center) (Jaroslav Turánek and Robert Mikulík) is acknowledged. The authors thank Martin Kopecký from Pragolab s.r.o., Prague, Czech Republic for collaboration and technical support in the field of confocal microscopy.

Conflicts of Interest: The authors declare no conflict of interest. The company Malvern had no role in the design of the study; in the collection, analyses, or interpretation of data; in the writing of the manuscript, and in the decision to publish the results.

References

- Skaf, E.; Stein, P.D.; Beemath, A.; Sanchez, J.; Bustamante, M.A.; Olson, R.E. Venous thromboembolism in patients with ischemic and hemorrhagic stroke. *Am. J. Cardiol.* **2005**, *96*, 1731–1733. [[CrossRef](#)] [[PubMed](#)]
- Silvain, J.; Bellemain, A.; Ecollan, P.; Montalescot, G.; Collet, J.P. Myocardial infarction: Role of new antiplatelet agents. *Presse Med.* **2011**, *40*, 615–624. [[CrossRef](#)] [[PubMed](#)]
- Doherty, S. Pulmonary embolism an update. *Aust. Fam. Phys.* **2017**, *46*, 816–820. [[PubMed](#)]
- Wendelboe, A.M.; Raskob, G.E. Global burden of thrombosis: Epidemiologic aspects. *Circ. Res.* **2016**, *118*, 1340–1347. [[CrossRef](#)]
- Heidt, T.; Ehrismann, S.; Hovener, J.B.; Neudorfer, I.; Hilgendorf, I.; Reiser, M.; Hagemeyer, C.E.; Zirlik, A.; Reinohl, J.; Bode, C.; et al. Molecular imaging of activated platelets allows the detection of pulmonary embolism with magnetic resonance imaging. *Sci. Rep.* **2016**, *6*, 25044. [[CrossRef](#)]
- Von zur Muhlen, C.; Peter, K.; Ali, Z.A.; Schneider, J.E.; McAteer, M.A.; Neubauer, S.; Channon, K.M.; Bode, C.; Choudhury, R.P. Visualization of activated platelets by targeted magnetic resonance imaging utilizing conformation-specific antibodies against glycoprotein iib/iii_a. *J. Vasc. Res.* **2009**, *46*, 6–14. [[CrossRef](#)]
- Zhang, N.; Li, C.; Zhou, D.; Ding, C.; Jin, Y.; Tian, Q.; Meng, X.; Pu, K.; Zhu, Y. Cyclic rgd functionalized liposomes encapsulating urokinase for thrombolysis. *Acta Biomater.* **2018**, *70*, 227–236. [[CrossRef](#)]

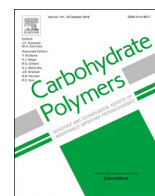
8. Gargan, P.E.; Gaffney, P.J.; Pleasants, J.R.; Ploplis, V.A. A monoclonal antibody which recognises an epitopic region unique to the intact fibrin polymeric structure. *Fibrinolysis* **1993**, *7*, 275–283. [[CrossRef](#)]
9. Soe, G.; Kohno, I.; Inuzuka, K.; Itoh, Y.; Matsuda, M. A monoclonal antibody that recognizes a neo-antigen exposed in the e domain of fibrin monomer complexed with fibrinogen or its derivatives: Its application to the measurement of soluble fibrin in plasma. *Blood* **1996**, *88*, 2109–2117. [[CrossRef](#)]
10. Wada, H.; Kobayashi, T.; Abe, Y.; Hatada, T.; Yamada, N.; Sudo, A.; Uchida, A.; Nobori, T. Elevated levels of soluble fibrin or d-dimer indicate high risk of thrombosis. *J. Thromb. Haemost.* **2006**, *4*, 1253–1258. [[CrossRef](#)]
11. Doh, H.J.; Song, K.S.; Kang, M.S.; Kim, D.S.; Kim, K.A.; Kang, J.; Jang, Y.; Chung, K.H. Novel monoclonal antibody that recognizes new neoantigenic determinant of d-dimer. *Thromb. Res.* **2006**, *118*, 353–360. [[CrossRef](#)] [[PubMed](#)]
12. Kolodziej, A.F.; Nair, S.A.; Graham, P.; McMurry, T.J.; Ladner, R.C.; Wescott, C.; Sexton, D.J.; Caravan, P. Fibrin specific peptides derived by phage display: Characterization of peptides and conjugates for imaging. *Bioconjugate Chem.* **2012**, *23*, 548–556. [[CrossRef](#)] [[PubMed](#)]
13. Overoye-Chan, K.; Koerner, S.; Looby, R.J.; Kolodziej, A.F.; Zech, S.G.; Deng, Q.; Chasse, J.M.; McMurry, T.J.; Caravan, P. Ep-2104r: A fibrin-specific gadolinium-based mri contrast agent for detection of thrombus. *J. Am. Chem. Soc.* **2008**, *130*, 6025–6039. [[CrossRef](#)] [[PubMed](#)]
14. Vymazal, J.; Spuentrup, E.; Cardenas-Molina, G.; Wiethoff, A.J.; Hartmann, M.G.; Caravan, P.; Parsons, E.C., Jr. Thrombus imaging with fibrin-specific gadolinium-based mr contrast agent ep-2104r: Results of a phase ii clinical study of feasibility. *Investig. Radiol.* **2009**, *44*, 697–704. [[CrossRef](#)] [[PubMed](#)]
15. Pilch, J.; Brown, D.M.; Komatsu, M.; Jarvinen, T.A.; Yang, M.; Peters, D.; Hoffman, R.M.; Ruoslahti, E. Peptides selected for binding to clotted plasma accumulate in tumor stroma and wounds. *Proc. Natl. Acad. Sci. USA* **2006**, *103*, 2800–2804. [[CrossRef](#)] [[PubMed](#)]
16. Hisada, Y.; Yasunaga, M.; Hanaoka, S.; Saijou, S.; Sugino, T.; Tsuji, A.; Saga, T.; Tsumoto, K.; Manabe, S.; Kuroda, J.; et al. Discovery of an uncovered region in fibrin clots and its clinical significance. *Sci. Rep.* **2013**, *3*, 2604. [[CrossRef](#)]
17. Fuchigami, H.; Manabe, S.; Yasunaga, M.; Matsumura, Y. Chemotherapy payload of anti-insoluble fibrin antibody-drug conjugate is released specifically upon binding to fibrin. *Sci. Rep.* **2018**, *8*, 14211. [[CrossRef](#)]
18. Obonai, T.; Fuchigami, H.; Furuya, F.; Kozuka, N.; Yasunaga, M.; Matsumura, Y. Tumour imaging by the detection of fibrin clots in tumour stroma using an anti-fibrin fab fragment. *Sci. Rep.* **2016**, *6*, 23613. [[CrossRef](#)]
19. Tiukinhoy-Laing, S.D.; Buchanan, K.; Parikh, D.; Huang, S.; MacDonald, R.C.; McPherson, D.D.; Klegerman, M.E. Fibrin targeting of tissue plasminogen activator-loaded echogenic liposomes. *J. Drug Target.* **2007**, *15*, 109–114. [[CrossRef](#)]
20. Klegerman, M.E.; Zou, Y.; McPherson, D.D. Fibrin targeting of echogenic liposomes with inactivated tissue plasminogen activator. *J. Liposome Res.* **2008**, *18*, 95–112. [[CrossRef](#)]
21. Yan, J.P.; Ko, J.H.; Qi, Y.P. Generation and characterization of a novel single-chain antibody fragment specific against human fibrin clots from phage display antibody library. *Thromb. Res.* **2004**, *114*, 205–211. [[CrossRef](#)] [[PubMed](#)]
22. Putelli, A.; Kiefer, J.D.; Zadory, M.; Matasci, M.; Neri, D. A fibrin-specific monoclonal antibody from a designed phage display library inhibits clot formation and localizes to tumors in vivo. *J. Mol. Biol.* **2014**, *426*, 3606–3618. [[CrossRef](#)] [[PubMed](#)]
23. Koudelka, S.; Mikulik, R.; Masek, J.; Raska, M.; Turanek Knotigova, P.; Miller, A.D.; Turanek, J. Liposomal nanocarriers for plasminogen activators. *J. Control. Release* **2016**, *227*, 45–57. [[CrossRef](#)] [[PubMed](#)]
24. Nisini, R.; Poerio, N.; Mariotti, S.; De Santis, F.; Fraziano, M. The multirole of liposomes in therapy and prevention of infectious diseases. *Front. Immunol.* **2018**, *9*, 155. [[CrossRef](#)]
25. Belfiore, L.; Saunders, D.N.; Ranson, M.; Thurecht, K.J.; Storm, G.; Vine, K.L. Towards clinical translation of ligand-functionalized liposomes in targeted cancer therapy: Challenges and opportunities. *J. Control. Release* **2018**, *277*, 1–13. [[CrossRef](#)]
26. Kumar, R.; Dogra, S.; Amarji, B.; Singh, B.; Kumar, S.; Sharma, S.; Vinay, K.; Mahajan, R.; Katare, O.P. Efficacy of novel topical liposomal formulation of cyclosporine in mild to moderate stable plaque psoriasis: A randomized clinical trial. *JAMA Dermatol.* **2016**, *152*, 807–815. [[CrossRef](#)]

27. Bartheldyova, E.; Turanek Knotigova, P.; Zachova, K.; Masek, J.; Kulich, P.; Effenberg, R.; Zyka, D.; Hubatka, F.; Kotoucek, J.; Celechovska, H.; et al. N-oxy lipid-based click chemistry for orthogonal coupling of mannan onto nanoliposomes prepared by microfluidic mixing: Synthesis of lipids, characterisation of mannan-coated nanoliposomes and in vitro stimulation of dendritic cells. *Carbohydr. Polym.* **2019**, *207*, 521–532. [[CrossRef](#)]
28. Ramasamy, T.; Ruttala, H.B.; Gupta, B.; Poudel, B.K.; Choi, H.-G.; Yong, C.S.; Kim, J.O. Smart chemistry-based nanosized drug delivery systems for systemic applications: A comprehensive review. *J. Control. Release* **2017**, *258*, 226–253. [[CrossRef](#)]
29. Bartheldyova, E.; Effenberg, R.; Masek, J.; Prochazka, L.; Knotigova, P.T.; Kulich, P.; Hubatka, F.; Velinska, K.; Zelnickova, J.; Zouharova, D.; et al. Hyaluronic acid surface modified liposomes prepared via orthogonal aminoxy coupling: Synthesis of nontoxic aminoxy lipids based on symmetrically alpha-branched fatty acids, preparation of liposomes by microfluidic mixing, and targeting to cancer cells expressing cd44. *Bioconjugate Chem.* **2018**, *29*, 2343–2356.
30. Ahmad, J.N.; Li, J.; Biedermannova, L.; Kuchar, M.; Sipova, H.; Semeradtova, A.; Cerny, J.; Petrokova, H.; Mikulecky, P.; Polinek, J.; et al. Novel high-affinity binders of human interferon gamma derived from albumin-binding domain of protein g. *Proteins* **2012**, *80*, 774–789. [[CrossRef](#)]
31. Mareckova, L.; Petrokova, H.; Osicka, R.; Kuchar, M.; Maly, P. Novel binders derived from an albumin-binding domain scaffold targeting human prostate secretory protein 94 (psp94). *Protein Cell* **2015**, *6*, 774–779. [[CrossRef](#)] [[PubMed](#)]
32. Hlavnickova, M.; Kuchar, M.; Osicka, R.; Vankova, L.; Petrokova, H.; Maly, M.; Cerny, J.; Arenberger, P.; Maly, P. Abd-derived protein blockers of human il-17 receptor as non-igg alternatives for modulation of il-17-dependent pro-inflammatory axis. *Int. J. Mol. Sci.* **2018**, *19*, 3089. [[CrossRef](#)] [[PubMed](#)]
33. Kuchar, M.; Vankova, L.; Petrokova, H.; Cerny, J.; Osicka, R.; Pelak, O.; Sipova, H.; Schneider, B.; Homola, J.; Sebo, P.; et al. Human interleukin-23 receptor antagonists derived from an albumin-binding domain scaffold inhibit il-23-dependent ex vivo expansion of il-17-producing t-cells. *Proteins* **2014**, *82*, 975–989. [[CrossRef](#)] [[PubMed](#)]
34. Krizova, L.; Kuchar, M.; Petrokova, H.; Osicka, R.; Hlavnickova, M.; Pelak, O.; Cerny, J.; Kalina, T.; Maly, P. P19-targeted abd-derived protein variants inhibit il-23 binding and exert suppressive control over il-23-stimulated expansion of primary human il-17+ t-cells. *Autoimmunity* **2017**, *50*, 102–113. [[CrossRef](#)]
35. Mašek, J.; Bartheldyová, E.; Turánek-Knotigová, P.; Škrabalová, M.; Korvasová, Z.; Plocková, J.; Koudelka, Š.; Škodová, P.; Kulich, P.; Křupka, M.; et al. Metallochelating liposomes with associated lipophilised norabumd p as biocompatible platform for construction of vaccines with recombinant his-tagged antigens: Preparation, structural study and immune response towards rhsp90. *J. Control. Release* **2011**, *151*, 193–201. [[CrossRef](#)]
36. Křupka, M.; Mašek, J.; Bartheldyová, E.; Knötigová, P.T.; Plocková, J.; Korvasová, Z.; Škrabalová, M.; Koudelka, Š.; Kulich, P.; Zachová, K.; et al. Enhancement of immune response towards non-lipidized borrelia burgdorferi recombinant ospc antigen by binding onto the surface of metallochelating nanoliposomes with entrapped lipophilic derivatives of norabumd p. *J. Control. Release* **2012**, *160*, 374–381. [[CrossRef](#)]
37. Zuev, Y.F.; Litvinov, R.I.; Sitnitsky, A.E.; Idiyatullin, B.Z.; Bakirova, D.R.; Galanakis, D.K.; Zhmurov, A.; Barsegov, V.; Weisel, J.W. Conformational flexibility and self-association of fibrinogen in concentrated solutions. *J. Phys. Chem. B* **2017**, *121*, 7833–7843. [[CrossRef](#)]
38. Koo, J.; Galanakis, D.; Liu, Y.; Ramek, A.; Fields, A.; Ba, X.; Simon, M.; Rafailovich, M.H. Control of anti-thrombogenic properties: Surface-induced self-assembly of fibrinogen fibers. *Biomacromolecules* **2012**, *13*, 1259–1268. [[CrossRef](#)]
39. Lounes, K.C.; Lefkowitz, J.B.; Henschen-Edman, A.H.; Coates, A.I.; Hantgan, R.R.; Lord, S.T. The impaired polymerization of fibrinogen longmont (bbeta166arg->cys) is not improved by removal of disulfide-linked dimers from a mixture of dimers and cysteine-linked monomers. *Blood* **2001**, *98*, 661–666. [[CrossRef](#)]
40. Schwartz, M.L.; Pizzo, S.V.; Hill, R.L.; McKee, P.A. The effect of fibrin-stabilizing factor on the subunit structure of human fibrin. *J. Clin. Investig.* **1971**, *50*, 1506–1513. [[CrossRef](#)]
41. Zadavec, P.; Mareckova, L.; Petrokova, H.; Hodnik, V.; Perisic Nanut, M.; Anderluh, G.; Strukelj, B.; Maly, P.; Berlec, A. Development of recombinant lactococcus lactis displaying albumin-binding domain variants against shiga toxin 1 b subunit. *PLoS ONE* **2016**, *11*, e0162625. [[CrossRef](#)] [[PubMed](#)]
42. Wahl, V.; Saurugger, E.; Khinast, J.; Laggner, P. Specific surface, crystallinity, and dissolution of lyophilized fibrinogen. A study by combined small- and wide-angle x-ray scattering (swaxs). *Eur. J. Pharm. Biopharm.* **2015**, *89*, 374–382. [[CrossRef](#)] [[PubMed](#)]

43. Wahl, V.; Leitgeb, S.; Laggner, P.; Pichler, H.; Liebming, A.; Khinast, J. The influence of residual water on the solid-state properties of freeze-dried fibrinogen. *Eur. J. Pharm. Biopharm.* **2015**, *91*, 1–8. [[CrossRef](#)] [[PubMed](#)]
44. Křupka, M.; Mašek, J.; Barkocziová, L.; Knotigová, P.T.; Kulich, P.; Plockova, J.; Lukac, R.; Bartheldyová, E.; Koudelka, S.; Chaloupková, R.; et al. The position of his-tag in recombinant ospc and application of various adjuvants affects the intensity and quality of specific antibody response after immunization of experimental mice. *PLoS ONE* **2016**, *11*, e0148497. [[CrossRef](#)] [[PubMed](#)]
45. Mašek, J.; Bartheldyová, E.; Korvasová, Z.; Škrabalová, M.; Koudelka, Š.; Kulich, P.; Kratochvílová, I.; Miller, A.D.; Ledvina, M.; Raška, M.; et al. Immobilization of histidine-tagged proteins on monodisperse metallochelation liposomes: Preparation and study of their structure. *Anal. Biochem.* **2011**, *408*, 95–104. [[CrossRef](#)]
46. Platt, V.; Huang, Z.; Cao, L.; Tiffany, M.; Riviere, K.; Szoka, F.C., Jr. Influence of multivalent nitrilotriacetic acid lipid-ligand affinity on the circulation half-life in mice of a liposome-attached his6-protein. *Bioconjugate Chem.* **2010**, *21*, 892–902. [[CrossRef](#)]



© 2019 by the authors. Licensee MDPI, Basel, Switzerland. This article is an open access article distributed under the terms and conditions of the Creative Commons Attribution (CC BY) license (<http://creativecommons.org/licenses/by/4.0/>).



N-Oxy lipid-based click chemistry for orthogonal coupling of mannan onto nanoliposomes prepared by microfluidic mixing: Synthesis of lipids, characterisation of mannan-coated nanoliposomes and in vitro stimulation of dendritic cells[☆]

Eliška Bartheldyová^{a,1}, Pavlína Turánek Knotigová^{a,1}, Kateřina Zachová^{b,1}, Josef Mašek^a, Pavel Kulich^a, Roman Effenberg^c, Daniel Zyka^d, František Hubatka^a, Jan Kotouček^a, Hana Čelechovská^a, Renata Héžová^a, Andrea Tomečková^a, Eliška Mašková^a, Martina Fojtíková^a, Stuart Macaulay^e, Peter Bystrický^f, Lucia Paulovičová^g, Ema Paulovičová^{g,*}, Ladislav Drož^d, Miroslav Ledvina^{c,*}, Milan Raška^{a,b,**}, Jaroslav Turánek^{a,*}

^a Department of Pharmacology and Immunotherapy, Veterinary Research Institute, v.v.i., Hudcova 70, 621 00 Brno, Czech Republic

^b Department of Immunology and Institute of Molecular and Translational Medicine, Faculty of Medicine and Dentistry, Palacky University Olomouc, Hněvotínská 3, 775 15 Olomouc, Czech Republic

^c Department of Chemistry of Natural Compounds, University of Chemistry and Technology, Technická 5, 166, 28 Prague 6, Czech Republic

^d APIGENEX s.r.o., Poděbradská 173/5, Prague 9, 190 00, Czech Republic

^e Malvern Instruments, Great Malvern, UK

^f Division of Neurosciences, Biomedical Center Martin, Jessenius Faculty of Medicine in Martin, Comenius University, Malá Hora 10701/4A, 036 01 Martin, Slovakia

^g Department of Immunochemistry of Glycoconjugates, Immunology & Cell Culture Laboratory, Institute of Chemistry, Center for Glycomics Slovak Academy of Sciences, Dubravská cesta 9, 845 38 Bratislava, Slovakia

ARTICLE INFO

Keywords:

Click chemistry – oxime ligation
Microfluidic mixing
Dendritic cells
Mannosylated liposomes
Mannan
Drug delivery

ABSTRACT

New synthetic aminoxy lipid was designed and synthesized as a building block for the formulation of functionalised nanoliposomes (presenting onto the outer surface of aminoxy groups) by microfluidic mixing. Orthogonal binding of cellular mannan (*Candida glabrata* (CCY 26-20-1) onto the outer surface of functionalised nanoliposomes was modified by orthogonal binding of reducing termini of mannans to oxime lipids via a click chemistry reaction based on aminoxy coupling (oxime ligation). The aminoxy lipid was proved as a suitable active component for preparation of functionalised nanoliposomes by the microfluidic mixing method performed with the instrument NanoAssemblr™. This “on-chip technology” can be easily scaled-up. The structure of mannan-liposomes was visualized by transmission and scanning electron microscopy, including immunogold staining of recombinant mannan receptor bound onto mannosylated-liposomes. The observed structures are in a good correlation with data obtained by DLS, NTA, and TPRS methods. In vitro experiments on human and mouse dendritic cells demonstrate selective internalisation of fluorochrome-labelled mannan-liposomes and their ability to stimulate DC comparable to lipopolysaccharide. We describe a potentially new drug delivery platform for mannan receptor-targeted antimicrobial drugs as well as for immunotherapeutics. Furthermore, the platform

[☆] The team responsible for lipid design and synthetic work is led by Dr. M. Ledvina, Dr. Drož and Ass. Prof. J. Turánek; the team responsible for mannan synthesis and characterization is headed by Ing. Ema Paulovičová, CSc., the team responsible for formulation of liposomes is led by Ass. Prof. Jaroslav Turánek; the team responsible for testing biological activities is led by Ass. Prof. Jaroslav Turánek and Prof. Milan Raška. The co-authors contributed as follows: Roman Effenberg and Daniel Zyka - synthesis and purification of lipid precursors and final products. Lucia Paulovičová, Peter Bystrický and Ema Paulovičová - preparation, purification and characterization of mannan; Eliška Bartheldyová, Josef Mašek, Stuart Macaulay, František Hubatka, Jan Kotouček, Andrea Tomečková, Eliška Mašková and Martina Fojtíková - preparation and characterization of liposomes, development of a coupling procedure and preparation of liposomes by microfluidization; Pavlína Turánek Knotigová, Kateřina Zachová, Renata Héžová and Hana Čelechovská - in vitro testing. Pavel Kulich and Josef Mašek - SEM, TEM and confocal microscopy.

* Corresponding authors.

** Corresponding author at: Department of Immunology, Faculty of Medicine and Dentistry, Palacky University Olomouc, Hněvotínská 3, 775 15, Olomouc, Czech Republic.

E-mail addresses: ema.paulovicova@savba.sk (E. Paulovičová), miroslav.ledvina@vscht.cz (M. Ledvina), raskamil@uab.edu (M. Raška), turanek@vri.cz (J. Turánek).

¹ Contribution of three first authors is equal.

<https://doi.org/10.1016/j.carbpol.2018.10.121>

Received 23 July 2018; Received in revised form 18 October 2018; Accepted 25 October 2018

Available online 29 November 2018

0144-8617/ © 2018 Elsevier Ltd. All rights reserved.

based on mannans bound orthogonally onto the surface of nanoliposomes represents a self-adjuvanted carrier for construction of liposome-based recombinant vaccines for both systemic and mucosal routes of administration.

1. Introduction

Widespread application of nanoparticle-based drug delivery systems (DDS) in nanomedicine is supported by the development of bioorthogonal ligation strategies based on the chemoselective reaction between two functional groups, whereby neither of them is present in native biomolecules. Ligation techniques which met these requirements are known as "click-chemistry" (Kolb, Finn, & Barry Sharpless, 2001). Click chemistry as a discipline of organic synthesis has accompanied this evolution of DDS by providing synthetic tools for efficient bioconjugation of drugs, polymers, or targeting ligands, and preparation of novel building blocks for the construction of DDS with new properties (Lallana, Sousa-Herves, Fernandez-Trillo, Riguera, & Fernandez-Megia, 2012).

Oxime ligation, based on spontaneous condensation of aminoxy group with an aldehyde group or ketone to give oxime linkage belongs also to the bioorthogonal "click" ligations (Ulrich, Boturyn, Marra, Renaudet, & Dumy, 2014). Oxime click chemistry has emerged as a robust strategy especially in the field of glycoconjugation, taking advantage of the fact that aldehyde functionality is available in equilibrium at the reducing end of most polysaccharides (Meng, Choudhury, & Edgar, 2016).

Coupling of saccharides, oligosaccharides, and polysaccharides like mannan onto liposomal surface via aminoxy group of lipids incorporated in liposomal lipid bilayer represents a new alternative for rapid modification of liposomes. The orthogonal character of oxime coupling reaction between aldehyde function at the reducing terminus of mannan and aminoxy group-modified lipid ensures even orientation of polysaccharide molecules on the liposomal surface, preservation of molecular pattern formed by polysaccharide molecules (e.g. mannan), and reproducibility of the technology used for such functionalized liposome preparations (Algar et al., 2011).

Recent technique for highly reproducible preparation of liposomes is based on microfluidic mixing (Carugo, Bottaro, Owen, Stride, & Nastruzzi, 2016). Here we describe for the first time the application of the NanoAssemblr™ Platform (Precision NanoSystems, Inc., Canada) for preparation of mannan-modified nanoliposomes by microfluidic mixing. The NanoAssemblr™ Platform is a scalable, microfluidics-based

system developed for preparation and manufacture of liposomes which uses custom engineered microfluidic cartridges to perform nanoprecipitation within milliseconds and nanoliter reaction volumes. This enables well controlled preparation of liposomes of tunable sizes and low polydispersity in a single step.

Mannosylated liposomes represent an alternative system to deliver antigens or antimicrobials to macrophages or DCs (Song et al., 2015; White, Rades, Furneaux, Tyler, & Hook, 2006). Adjuvant activity of various mannans was demonstrated and the induction of Th1 biased immune response as well as immune response after mucosal immunisation are favourable features for the development of antiviral vaccines and vaccines against intracellular pathogens (Fukasawa et al., 1998; Tseng, Chiou, Deng, Huang, & Der-Zen, 2010). Various chemical methods were used to bind mannan onto liposomes and lipid-based nanoparticles. Mannan can be linked to lipids by O, N or S glycosidic bond via a spacer of various length. Both length and chemical character of the spacer can affect conformational freedom of mannan and hence its ability to be recognised by appropriate receptor on cell surface. In general, mannan can be linked to preformed liposomes by chemical coupling or can be incorporated into preformed liposomes such as lipidated mannan (Engel et al., 2003; Kuramoto et al., 2009; Orr, Rando, & Bangerter, 1979; White et al., 2006; Witoonsaridsilp, Paeratakul, Panyarachun, & Sarisuta, 2012).

In this article we describe design and synthesis of new aminoxy lipid and its application for preparation of monodisperse liposomes by microfluidic mixing. These liposomes functionalized for coupling of mannan (as well as other polysaccharides) via click chemistry represent mannan-based liposomal platform for drug delivery and especially for construction of recombinant vaccines.

2. Experimental section

2.1. Chemicals

All chemicals, unless otherwise specified, were purchased from Sigma (St. Louis, MO). Tissue-culture media and media supplement were purchased from Invitrogen (Carlsbad, CA), EPC and lissamine-rhodamine from Avanti Polar Lipids (Oregon, USA).

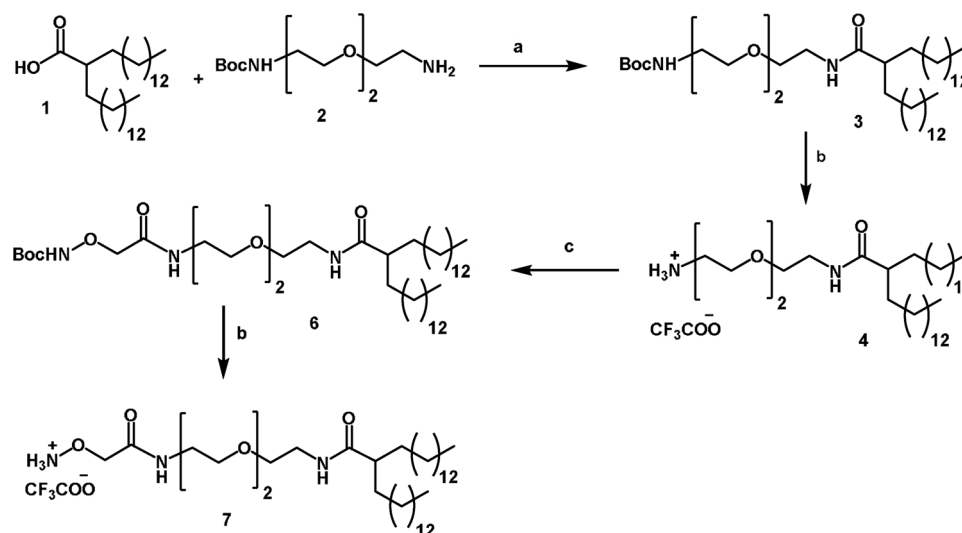


Fig. 1. Synthetic route to lipid with amino-oxo group 7 used in the study, reagents and conditions: (a) HATU, DMAP, DMF, NMM, DCM, rt, 90%. (b) DCM, TFA, rt, 3 h, quantitative yield. (c) HATU, DMF, NMM, DMAP, BocNH-O-CH₂COOH (5). Detailed description in supporting information.

2.2. Aminoxy lipids preparation

The synthetic route to the target colipid presenting an aminoxy group 7 is shown in Fig. 1. This synthetic scheme is based on the condensation of 2-tetradecylhexadecanoic acid (1) with partially N'-protected diamine 2, N'-deprotection acyl derivative 3 and subsequent N'-acylation of the free amine 4 using N-Boc-aminoxyacetic acid 5 to give fully protected intermediate 6. A final deprotection was then used to give rise to aminoxy lipid 7.

2.3. Extraction and purification of *Candida glabrata* cellular mannans

Low molecular weight cellular mannan (MW 16.7 kDa, 97.14% D-mannose, D-glucosamine 0.362%, D-glucose 1.38%, phosphorus 0.31%) was isolated from the yeast strain *C. glabrata* CCY 26-20-1 (Culture Collection of Yeasts, Institute of Chemistry of the Slovak Academy of Science, Center for Glycomics Bratislava, Slovakia). Characterization of purified mannan is described in the section "supporting information".

2.4. Preparation of liposomes

Liposomes were prepared using a method based on microfluidic mixing. Mixture of lipids (EPC and aminoxy lipid 99 : 1 M %) was dissolved in ethanol and then it was mixed with appropriate buffer using instrument NanoAssemblr equipped with the cartridge for microfluidic mixing (Precision Nanosystems, Vancouver, Canada). The ratio of water : ethanol phase was 7 : 1. The flow rate was 6 ml/min. Fluorescent liposomes were labelled by lissamine-rhodamine PA added to ethanol solution of lipids (content of lissamine-rhodamine PA was 0.4% of total lipid).

2.5. Orthogonal binding of mannan onto liposomes by oxime ligation

Mannan was dissolved in PBS. Default ratio between total lipid and mannan was 1 mg of total lipid : 0.1 mg of mannan, which corresponds to the molar ratio 2 : 1 (N-oxy : mannan). Volumes of mannan and lipid solutions were equal. The reaction was left to run overnight at room temperature at pH 4. Liposomes and unbound mannan were separated by FPLC (Pharmacia, Stockholm, Sweden) using the column *Superose 6 HR 10/30* (GE Health Care). The loading volume of samples was 200 μ l. Flow rate was set at 0.1 ml/min at start, for separation the flow rate was set at 0.3 ml/min. One ml fractions were collected.

2.6. Measuring of size and ζ -potential of liposomes

Size and ζ -potential were measured by dynamic laser scattering on a Zetasizer ZSP (Malvern, UK), nanoparticle tracking analysis was performed using NanoSight 500 (Malvern, UK) and TRPS method (Tunable Resistive Pulse Sensing) on an iZON instrument (iZON Science, UK). Zetasizer ZSP (Malvern, UK) was also used for measurement of ζ -potential. Measurements on a zetasizer Nano ZSP were conducted in a quartz cuvette ZEN 2112. Cuvette DTS1060 was used for ζ -potential measurement. Both size and ζ -potential were measured at a temperature of 25 °C and attenuator 7, at an angle of 175° (back scatter). The size and ζ -potential were measured at a total lipid concentration of 1 mg/ml in PBS, 10 mM Na-phosphate, pH 7.2.

2.7. Nanoparticle tracking analysis (NTA)

NTA measurements were performed on a NanoSight NS500 instrument (blue laser 488 nm, sCMOS) (Malvern Instruments Ltd, Malvern, UK). Data was recorded and analyzed using NTA software 3.2. Samples were prepared by appropriate dilution of stock suspensions in PBS (temperature 25 °C, sample dilution 1000x in 10 mM Na-phosphate, pH 7.2). Camera level was optimized prior to the measurement. For

analysis, detection threshold was set for each sample individually in a way to meet the manufacturer recommended quality standards. All other parameters were left in their default settings. Three runs of 60 s at 25 fps were recorded for each sample.

2.8. TRPS measurement

Polyurethane membrane (Membrane NP 150 was stretched at 47 mm) was used. Calibration was performed by carboxylated polystyrene nanoparticles (size 114 nm, particle concentration 1.1013 per ml). The applied pressure was 3 cm of water column pressure, voltage was 0.54 V, at ambient temperature. Samples were 100 x diluted to a concentration of total lipid 0.1 mg/ml. Medium: 10 mM Na-phosphate buffer, pH 7.2.

2.9. Electron microscopy

Samples of liposomes were suspended in a drop of PBS. The resulting suspension was covered with a grid coated by formvar film (Sigma-Aldrich, Czech Republic) and carbon (Agar Scientific, Austria). The grid was removed from the suspension after 1 min, and the residual water was dried with a strip of filtration paper. A drop of 2% aqueous phosphotungstic acid was placed onto the grid for a few seconds, then excess stain was dried with filtration paper. Samples were observed under an electron microscope Philips 208 S Morgagni (FEI, Czech Republic) at 7500 \times magnification and an accelerating voltage of 80 kV. For scanning electron microscopy the samples were put on the cooper grid and a special holder for STEM mode. The samples were observed under scanning electron microscope Hitachi 8010 (Hitachi, Japan) in deceleration mode at 12,000–120,000 \times magnification.

2.10. Binding of mannose receptor and labelling by gold nanoparticles

Four micrograms of recombinant human mannose receptor CD206 (MMR, R&D System; Minneapolis, USA) was dissolved in PBS in concentration 100 μ g/ml. This amount was added to 3 mg of mannosylated liposomes (10 mg/ml PBS). The mixture was stirred at ambient temperature for 1 h. Thereafter, 10 μ g of mouse anti-HisTag monoclonal antibody (1 mg/ml, ThermoFisher Scientific, Waltham, USA) was added. Protein-A covered gold nanoparticles for electron microscopy were diluted in ratio 1:50 and then gold nanoparticles (Electron Microscopy Science, USA) and the complete liposomal sample were mixed in the volume ratio 1:1. The mixture was incubated overnight at 4 °C.

The resulting suspension was covered with a Cu grid (300 Old Mesh, Agar Scientific, Austria) coated with Formvar film (Sigma Aldrich, Czech Republic) and carbon. The grid was removed from the suspension after 1 min, and the residual water was dried with a strip of lint-free filtration paper. The sample was stained with 2% Ammonium molybdate and observed under transmission electron microscope Philips 208S Morgagni (FEI, Czech Republic) at 80 Kv and magnification 18,000 \times .

2.11. Generation of monocyte-derived DCs from human buffy-coats

Immature monocyte-derived DCs were generated from peripheral blood mononuclear cells (PBMCs) obtained from buffy-coats of healthy donors at the Department of Transfusion Medicine and Blood Bank, University Hospital Brno, Brno, Czech Republic. PBMCs were separated by density gradient centrifugation on Histopaque 1077, resuspended in CellGro DC medium (CellGenix, Freiburg, Germany) supplemented with 50 μ g/ml DNase I (Roche, Mannheim, Germany), and allowed to adhere to the surface of 8.96 cm² (one well of 6-well tissue culture plate; TPP Techno Plastic Products AG, Trasadingen, Switzerland) for 2 h at + 37 °C in a humidified 5% CO₂ atmosphere. After washing, adherent monocytes were cultured for 6 days in culture medium supplemented with recombinant human GM-CSF (1000 IU/mL; PeproTech,

New Jersey, USA) and recombinant human IL-4 (400 IU/ml; PeproTech). No serum or antibiotics were added. On day 6, immature DCs were incubated in maturation medium (CellGro DC medium supplemented with recombinant human GM-CSF (1000 IU/mL), recombinant human IL-4 (400 IU/ml), and recombinant human IFN- γ (1000 IU/mL; PeproTech) for 4 h at + 37 °C in a humidified 5% CO₂ atmosphere with the maturation stimuli: mannan (0.032 mg/ml), mannosylated liposomes (0.32 mg total lipid/ml), LPS as positive control (200 ng/mL, Calbiochem, Merck Millipore, Darmstadt, Germany). As negative control, DCs without maturation stimuli were used.

2.12. DC phenotyping

Mature DCs were harvested 4 h after the incubation period with maturation stimuli, washed with FACS buffer [3% heat inactivated human AB serum, 0.1% BSA, 0.01% NaN₃ in PBS (Invitrogen)] and surface stained with fluorescence-labelled mAbs. The antibodies used included anti-CD80 (Beckman Coulter, Fullerton, CA, USA), anti-CD83 (BD Biosciences, San Jose, CA, USA) and anti-CD11c (Exbio, Vestec, Czech Republic). The cells were analyzed by flow cytometry on a BD LSR-Fortessa Flow Cytometer using BD FACSDiva Software (both BD Biosciences).

2.13. T cell proliferation assay

The stimulatory capacity of generated DCs was determined in a mixed leukocyte reaction. Allogeneic T cells (1 × 10⁵) were labelled with carboxyfluorescein succinimidyl ester (CFSE; 2.5 μ M; Invitrogen) for 10 min at + 37 °C in a humidified 5% CO₂ atmosphere and incubated with DCs matured with different stimuli or with controls (DCs/T cells ratio of 1 : 10) in 96-well flat bottom plates in X-VIVO 10 (TPP Techno Plastic Products AG, Trasadingen, Switzerland) supplemented with 5% heat inactivated human AB serum. T cells incubated alone and with phytohemagglutinin (PHA; 5 μ g/mL) served as negative and positive controls, respectively. After 6 days of incubation, the cells were collected and surface stained with fluorochrome-labelled anti-CD3 (Beckman Coulter), anti-CD4 (Exbio) and anti-CD8 (Exbio) mAbs. Proliferation of responder cells was analyzed by flow cytometry measuring the CFSE levels (fluorescence “dilution” related to mitotic cell division) in T cells.

2.14. Pulsing of murine BMDC with various formulations of mannans *in vitro*

Bone marrow-derived DC (BMDC) cells were generated by *in vitro* stimulation of bone marrow cells with GM-CSF and IL-4, as described previously (Krupka et al., 2015). In brief, tibias and femurs, aseptically removed from a BALB/c mouse sacrificed under Ketamine/Xylazine anaesthesia, were superficially washed in sterile PBS, epiphyses excised, and bone marrow cells were flushed out by RPMI 1640 medium. Cells were pelleted by centrifugation (1200 × g) for 5 min at RT, red blood cells were lysed by a Red blood cells lysis buffer. Remaining cells were washed twice with RPMI 1640 plus penicillin and streptomycin, and pellets were resuspended in differentiation RPMI 1640 medium containing 10% FBS, antibiotics, 20 ng/ml GM-CSF, and 20 ng/ml IL-4 at a final concentration of 10⁶ cells/ml, and cultivated in a humidified 5% CO₂ incubator at 37 °C for six days. Every second day 2/3 of media were replaced with fresh complete RPMI 1640 and cytokines, and then transferred into 6-well panels and pulsed in parallel with various mannan preparations and controls as specified in the Table 1 and incubated for 24 h (for flow cytometry analysis). Lipopolysaccharide (LPS) from *E. coli* was used as a positive control.

2.15. Confocal scanning laser microscopy of dendritic cells

Interaction and internalisation of nanoliposomes with human

dendritic cells was studied by confocal scanning laser microscopy (Leica SP-8, Leica, Germany). Human dendritic cells were treated using a μ -Slide 8 well chamber (Ibidi, Germany). Lissamine-rhodamine-labelled liposomes (final concentration 10 μ g/ml) were incubated with human dendritic cells for 2 h. After 2 h, samples were fixed using 1% paraformaldehyde (5 min) and stained as follows: dendritic cells were incubated with anti-human HLA-DR Alexa Fluor 488 (BioLegend, San Diego, USA) antibody (5 μ l per 10⁶ cells) for 30 min. For staining of nuclei, SYTOX™ Blue (ThermoFisher Scientific, USA) was used. Samples were observed using Leica SP8 system equipped with white laser. Excitation wavelengths of 444 nm, 488 nm and 561 nm for excitation of SYTOX™ Blue, Alexa 488 and Lissamine-Rhodamine were selected, respectively.

3. Results

Orthogonal and random binding differ in the structure of the mannan coating on liposomal surface. Schematic visualisation of chemical reaction and final structure of mannan layer on liposomal surface is presented in Fig. 2.

3.1. Preparation and characterisation of mannan-coated nanoliposomes

3.1.1. Dynamic light scattering (DLS), Tuneable Resistive Pulse sensing (TRPS) and nanoparticle tracking analysis (NTA)

Liposomes prepared by microfluidic mixing were of monodisperse character and low polydispersity as proved by dynamic light scattering and NTA analyses. These methods also confirmed binding of mannan onto their surface via oxime ligation as reflected by an increase in the size. Data are summarised in Table 1. The increase of hydrodynamic radius is in a good accordance with the expected value based on the hydrodynamic radius measured for mannan (Fig. 3, Table 2).

3.1.2. Electron microscopy

Hydrodynamic radius of isolated mannan was estimated by DLS as about 4 nm which is in a good accordance with MW 16.7 kDa measured by gel permeation chromatography. Negative ζ -potential of liposomes modified by mannan also well corresponds to the presence of residual phosphate groups in isolated mannan (residual phosphorus in mannan 0.31%). Low ionic strength (10 mM phosphate buffer, pH 7.2) was used to reveal differences in ζ -potential between plain and mannan modified liposomes.

Electron microscopy was used as an independent approach to confirm binding of mannan onto liposomal surface by oxime ligation. Contrary to plain liposomes, mannan-modified liposomes appear in TEM as “hairy” spherical objects with high contrast after staining with 2% ammonium phosphomolybdate. Hairy appearance is caused by surface modification of liposomes by mannan. Mannan-modified liposomes appear in SEM as spherical objects resembling golf balls. Clusters

Table 1
Composition of mannan liposome formulation used for murine BMDC stimulation. In all pulsing experiments performed with murine BMDC the RPMI 1640 was supplemented with 10% FBS and antibiotics. Working solution was made by diluting the stock solution 1 : 100 using RPMI + 1% FBS. In extension experiments 10 x higher doses were tested.

Formulation	Composition of stock per 1 ml			
	LPS [ng]	Mannan [μ g]	Liposome [μ g]	PBS [μ l]
LPS <i>E. coli</i>	250	0	0	1000
Mannan bound to liposome	–	5	5	1000
Mannan mixed with liposome	–	5	5	1000
Mannan	–	5	0	1000
Not pulsed	–	–	–	1000

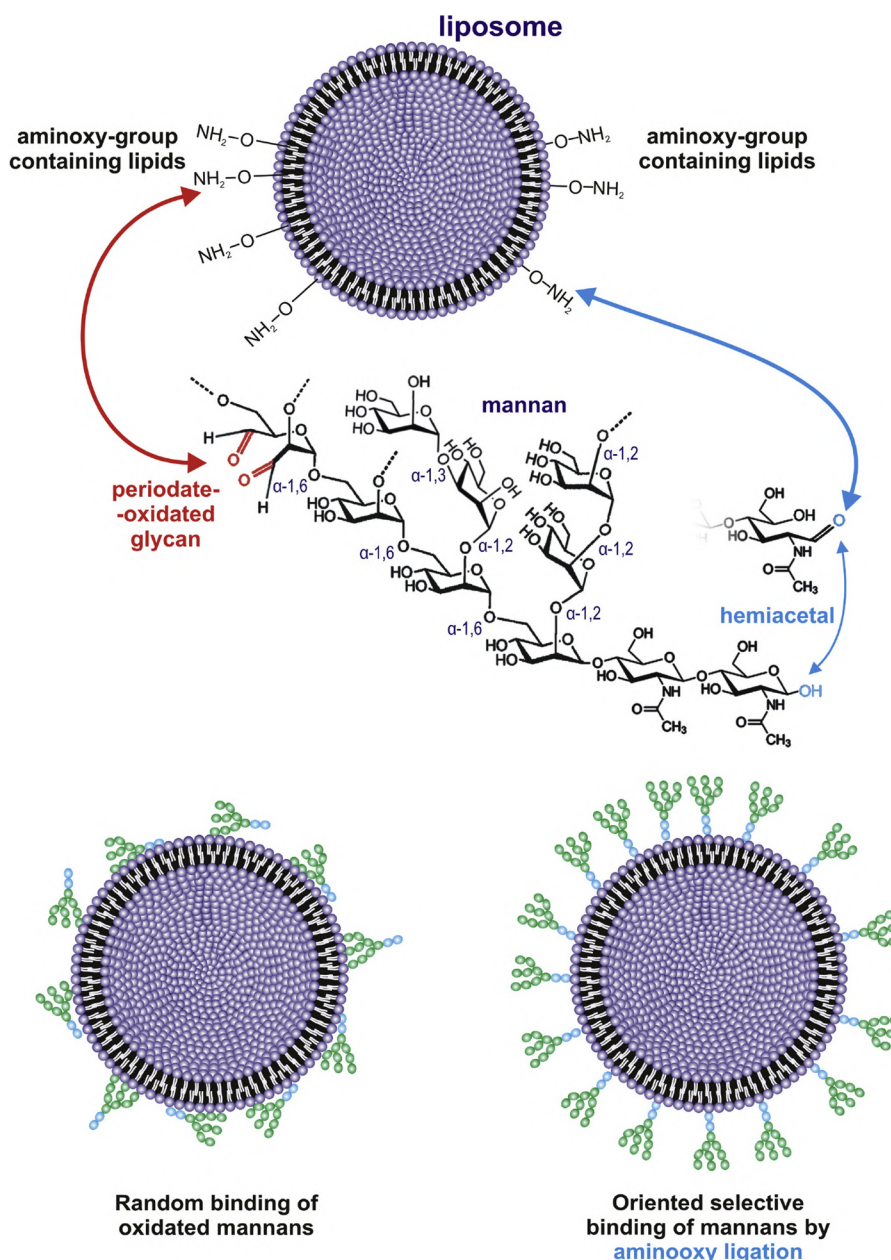


Fig. 2. Scheme describing orthogonal or random binding of mannans onto liposomal surface by oxime ligation.

Orthogonal binding of mannans onto liposomal surface by aminoxy ligation between reducing termini of mannans and aminoxy group-modified lipids preserves precise orientation of mannan molecule and forms molecular patterns resembling native structures on microorganisms. Oxidation or carboxymethylation of mannan is needed to activate mannan for subsequent reaction with primary amines on lipids. These reactions inevitably lead to random orientation of mannan molecules bound onto liposomal surface.

of mannan molecules on the surface of liposome are clearly observable (Fig. 3)

3.2. Stimulation of dendritic cells by free mannan and mannan-coated nanoliposomes

Dendritic cells belong to intended targets for mannan-modified liposomes as future self-adjuvanted carriers for construction of nanoparticulate vaccines. Therefore, we tested interaction of mannosylated liposomes with DC and their ability to stimulate DC.

Confocal microscopy demonstrated interaction of fluorochrome-labelled liposomes with the cell membrane of DC and successive internalisation of liposomes into cytoplasm (Fig. 4). Human DC derived from PBMC were used as *ex vivo/in vitro* model system to test the ability of

mannan-coated liposomes to induce stimulation of DC. Lipopolysaccharide and free mannan were used as positive controls. Stimulatory activity of mannan was not diminished by binding onto liposomes. On the contrary to mannan, modified liposomes stimulated DC in the extent similar to LPS (Table 3). Plain liposomes behaved indifferently and did not stimulate DC above control level.

3.3. Mouse dendritic cells derived from bone-marrow progenitor cells

Mouse dendritic cells were used as a model to confirm results obtained with human DC and to extend our study. In the following experiments, murine BMDC were pulsed *in vitro* with various preparations of mannan including mannan covalently bound to liposomes, mannan "simply" mixed with liposomes, or mannan alone. CD11c^{high} cells were

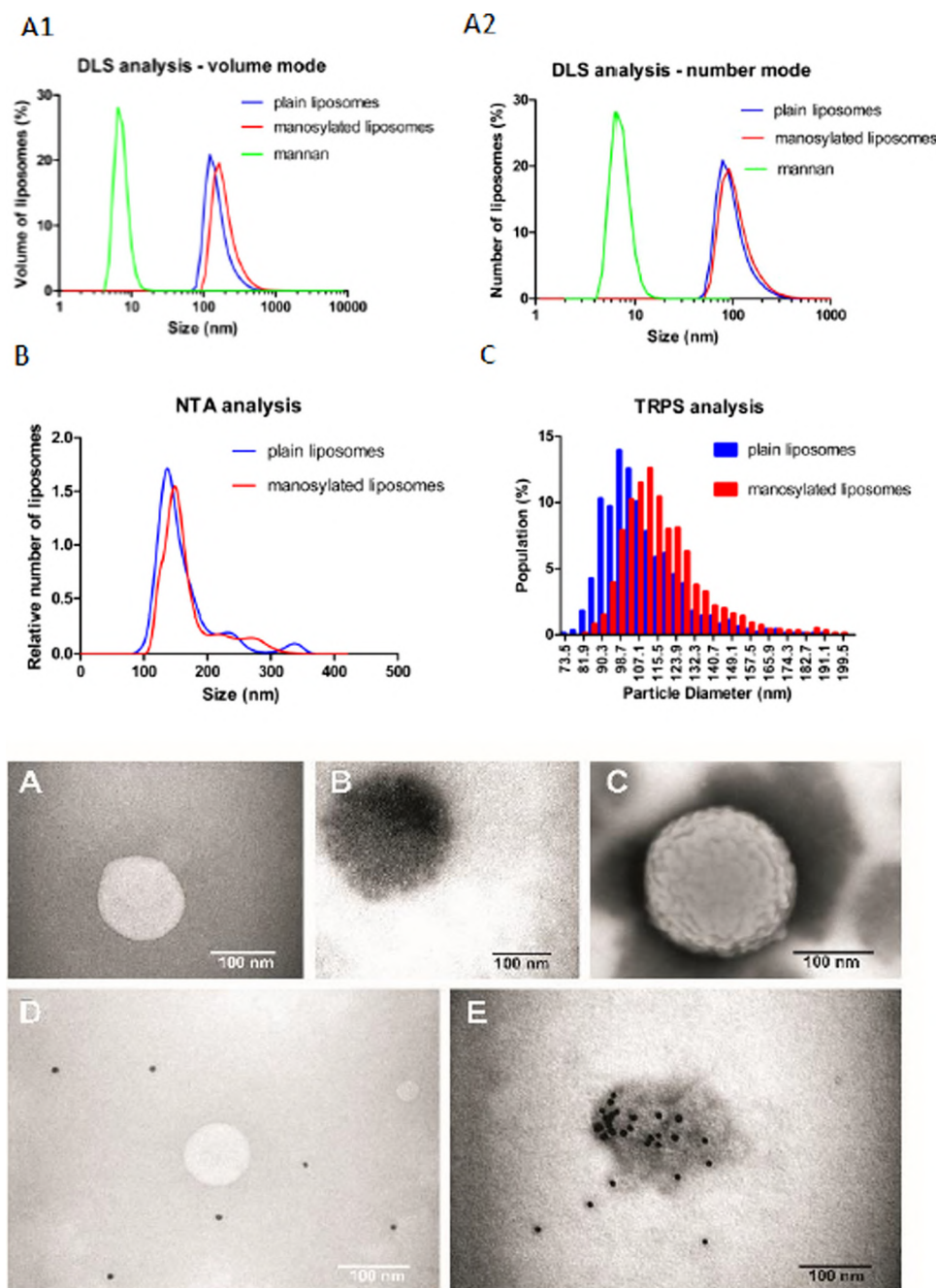


Fig. 3. Characterization of mannoseylated liposomes by size distribution and electron microscopy.

Upper part: Size distribution of mannose, plain liposomes, and liposomes modified by surface-bond mannans

A) Hydrodynamic radius distribution analyzed by DLS. A1) Size distribution expressed as volume of particles A2) Size distribution expressed as number of particles. B) Size distribution determined by NTA. C) Size distribution determined by TRPS. Size distribution expressed as histogram. For DLS data of plain liposomes see Supporting Material, Fig S3.

Bottom part: Electron microscopy photographs illustrating an orthogonal binding of mannose onto liposomal surface by oxime ligation

A) plain nanoliposome (TEM), B) mannose-modified nanoliposomes (TEM) C), mannose modified nanoliposomes (SEM). Liposomes were stained by ammonium phosphomolybdate (2%) for TEM, D) negative controls: mannoseylated liposomes + mannose (without receptor and HisTag antibody), E) mannoseylated liposomes detected by rMMR and stained by anti-HisTag antibody. TEM photo of 1:1 mixture of EPC plain liposomes (without N-oxylipid) and liposomes with N-oxylipid see Supporting Material, Fig S4.

analyzed for the expression of surface molecules CD80, CD86, MHC II acting as common DC differentiation and activation markers. As a positive control, LPS from *E. coli* was used. *E. coli* LPS was the most effective stimulator both for CD80 and CD86 (Fig. 5B, D). Mannose

covalently bound to liposome stimulated the highest increase in CD80^{bright} over CD80^{dim} among all mannose formulations tested (Fig. 5A, B). Mannose alone did not induce CD80 activation marker significantly. In the case of CD86 marker, mannose covalently bound to liposomes was as

Table 2

Characterisation of mannoseylated liposomes by various methods in terms of size, polydispersity, ζ -potential.

Parameter	Plain liposomes	Mannoseylated liposomes
Size by DLS (nm, mean from number mode)	102 ± 2	114 ± 3
Size by DLS (nm, mean from volume mode)	120 ± 1	133 ± 2
Size by DLS (nm, mean from intensity mode)	160 ± 2	177 ± 4
Polydispersity index	0.118 ± 0.008	0.128 ± 0.013
Size by NTA (nm, modus)	137 ± 1	149 ± 2
Size by TRPS (nm, mean)	108 ± 1	126 ± 3.0
Measured Mean Concentration (particles/ml) from 1 mg of total lipid	(1.25 ± 0.02)E11	(1.12 ± 0.06)E11
ζ -potential (mV)	-4.8 ± 0.2	-10.9 ± 0.9

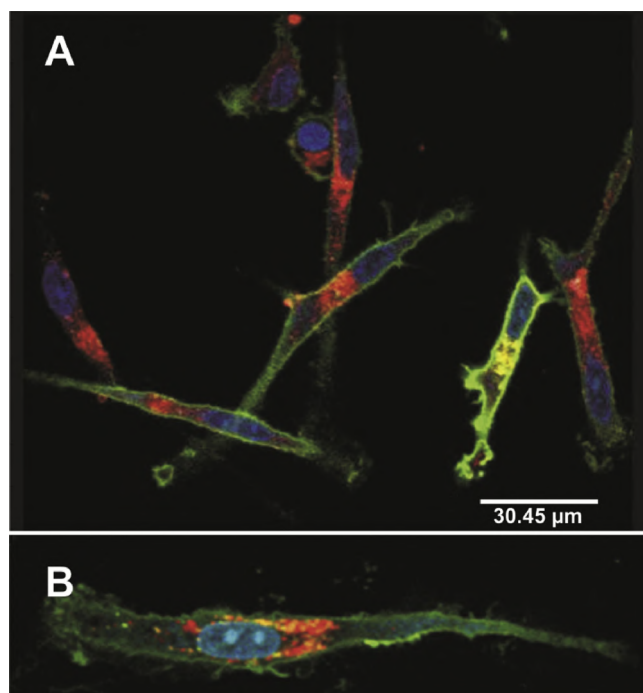


Fig. 4. Interaction of fluorochrome-labelled mannan-modified nanoliposomes with human dendritic cells derived from human peripheral blood monocytes.

Fluorochrome-labelled liposomes (Lyssamine-rhodamine PE) were found attached to the cell membrane as well as internalised in the cell interior. Blue colour – CYTOX BLUE, cell nucleus; green colour – ALEXA FLUOR 488, surface HLA-DR antigen; red colour - mannosylated liposomes stained with incorporated lyssamine-rhodamine phosphatidyl ethanolamine. A) group of DC; B) detail of single DC.

Table 3

Stimulation of human dendritic cells by mannosylated liposomes.

Parameter	Control	LPS	Mannan	Mannosylated liposomes
CD11c+/CD80+	15 ± 1	83 ± 28	62 ± 28	74 ± 23
CD11c+/CD83+	42 ± 2	88 ± 16	88 ± 16	83 ± 18
CD4+	0	15 ± 5	11 ± 6	15 ± 5
CD8+	0	21 ± 3	17 ± 14	24 ± 8
CD3+	0	17 ± 3	15 ± 3	17 ± 6

effective stimulator as mannan mixed with liposomes, whereas mannan alone did not show a significant stimulatory activity (Fig. 5C, D). When 10 x higher concentrations of mannan formulations were tested in the extension experiment, the increase in the CD80^{bright} MFI was 1.7 x and for CD86^{bright} was 2.0 x. Interestingly, low doses of mannan formulations, although significantly increased the CD80^{bright} and CD86^{bright} cell populations of CD11c^{high} BMDC, did not increase MFI over non-stimulated cells. This means that low doses of mannans increased the number of activated cells, but not the density of activation markers on the cell surface. Analysis focused on MHC II expression showed a modest but non-significant increase in the ratio between MHC II^{bright} and MHC II^{dim} cell populations for both liposomal mannan formulations similarly to LPS (Fig. 5E, F). When 10 x higher concentration of mannan liposomal formulation was used, the ratio of MHC II^{bright} over MHC II^{dim} cell population further increased by 20%, whereas mannan alone remained non stimulatory. Importantly, a higher concentration of mannan-liposome formulations did not exhibit any suppressive effect. In a limited set of experiments analyzing activation of murine BMDC by *K. pneumoniae* LPS (tested with doses identical to those of *E. coli* LPS) we detected 35 and 45% increase in cell count of CD80^{bright} and CD86^{bright} populations over respective dim populations and we also observed

+ 1.4 x and + 1.8 x shift of CD80^{bright} and CD86^{bright} MFI. In addition, individual mannan formulations or LPS distinctly affected the percentage of CD11c^{high} BMDC population when either lower or higher doses were tested. The most effective were the liposomal mannan formulations inducing for about 30–50% more CD11c^{high} BMDC in comparison to mannan alone or *E. coli* LPS.

Furthermore, we extended the analyses of mannan formulations and LPS for stimulation of CD40 and MHC I markers expression on CD11c^{high} BMDCs. As the non-stimulated cells did not separate for these markers into dim and bright subpopulations we expressed the stimulatory effect using the MFI of CD11c^{high} populations (Fig. 6) in contrast to the above analyzed CD80, CD86 and MHC II receptors (Fig. 5). Mannans bound to liposomes stimulate the most prominent MFI increase in comparison to any tested formulations including *E. coli* LPS (Fig. 6). In contrast only moderate stimulatory potential was detected when MHC I was analyzed (Fig. 6). Furthermore, in a separate experiment, we determined stimulatory potential of mannan-coupled liposomes labelled with Ni-NTA loaded with a recombinant His tagged protein antigen (Křupka, Mašek, & Bartheldyová, 2012; Mašek, Bartheldyová, Turánek-Knotigová et al. 2011). These mannan-proteoliposomes stimulated BMDC in a similar way like mannan-coated liposomes.

4. Discussion

4.1. Application of click chemistry and microfluidics mixing for preparation of mannan-modified nanoliposomes

Present methods of mannosylated liposome preparations are presumably based on mannosylated phosphatidylethanolamine prepared by condensation reaction of aldehyde function in mannan and primary amino group on lipids forming Schiff base, a sub-class of imines (Ikehara & Kojima, 2007; Ikehara et al., 2006). Direct modification of liposomal surface by incubation with mannan neoglycolipids is a slow reaction lasting days (Fukasawa et al., 1998). The procedures based on forming Schiff base or carbodiimide condensation of mythylcarboxylated mannans with aminolipids can be replaced by aminoxy coupling reaction which may be described as biorthogonal "click" ligations. This is because such reactions are based on the spontaneous condensation of aminoxy functional groups with an available aldehyde group or ketone to give rise to oxime linkage formation. Oxime formation is a one-step alternative to two-step reductive aminations, e.g., formation of imine (Schiff bases) by reaction of amino group with aldehyde or keto group followed by reduction to amine. Oxime linkages with a $K_d = 10^{-8}$ M are also much more resistant to hydrolysis than imines. Therefore, such oxime "click chemistry" is emerging as a robust strategy especially in the field of glycoconjugation, taking advantage of the fact that the reducing termini of most polysaccharides, including mannans, involve an aldehyde functional group in equilibrium with its hemiacetal form (Meng et al., 2016). Furthermore, aminoxy coupling is almost an ideal method for post-modification of liposomes with complex biologically active molecules, especially oligo and polysaccharides having a reducing hemiacetal group in the terminal part. These terminal hemiacetal groups enable orthogonal binding of polysaccharides onto the liposomal surface and such a structure resembles a native pattern existing on microorganisms. On the other hand, introduction of reactive aldehyde function into polysaccharides by e.g. periodate oxidation increases the number of reactive sites in the molecule, but orthogonality of the binding is lost, as it was schematically described in Fig. 2.

Postforming modification of liposome via aminoxy ligation is a relatively rapid process running at mild conditions and taking a few hours. The effective coupling of mannan onto liposomes was analyzed by several independent approaches (Fig. 3). Binding of mannan onto liposomal surface did not change its ability to interact with recombinant mannan receptors as demonstrated by immunogold TEM as

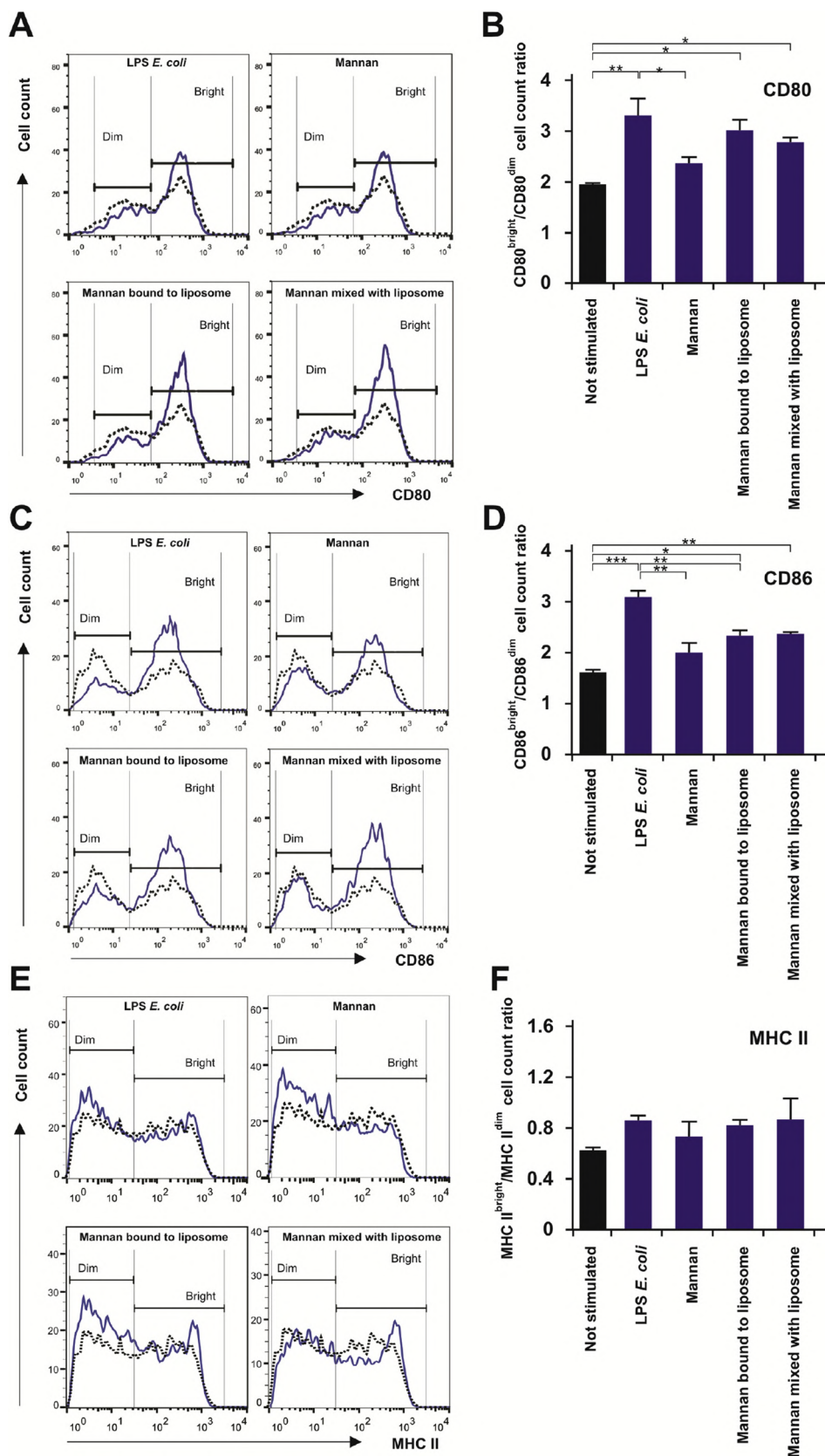


Fig. 5. Mannans pulsing of murine BMDC leads to an increase in the population of activated CD80 and CD86 highly positive cells.

Murine BMDC were stimulated (blue line and bars) with either lipopolysaccharide (LPS) (2.5 ng/ml), mannan, mannan covalently bound to liposomes or a mixture of mannan and liposomes (50 ng/ml). After five days of incubation cell were stained for CD11c, CD80, CD86, and MHC II followed by analysis by Flow cytometry. CD11^{high} BMDC population was analyzed for expression of activation markers CD80, CD86, and MHC II. Histograms showing distribution of cell counts according to CD80 (A), CD86 (C), and MHC II (E) fluorescence intensities are shown for representative experiment. Activation is expressed as a mean ± SD ratio of cell counts exhibiting Bright and Dim CD80 (B), CD86 (D), and MHC II (F) fluorescence from three independent experiments. Black bars represent the same ratio of non-stimulated CD11^{high} BMDC. Statistical analysis was performed using One-way ANOVA and Tukey's Multiple Comparison Test. P < 0.05 * P < 0.01 **, P < 0.001 ***

well as by interaction of human and mice DCs and their stimulation (Figs. 4–6; Table 3). This is an important finding with respect to further intended application of this mannan-liposome platform for the construction of recombinant vaccines based on a metallochelating

nanoliposomal platform (Křupka et al., 2012; Mašek, Bartheldyová, Turánek-Knotigová et al. 2011; Michal Krupka et al., 2016; Mašek, Bartheldyová, Korvasová et al. 2011; Effenberg et al., 2017). Modification of nanoliposomes via click chemistry based on aminoxy

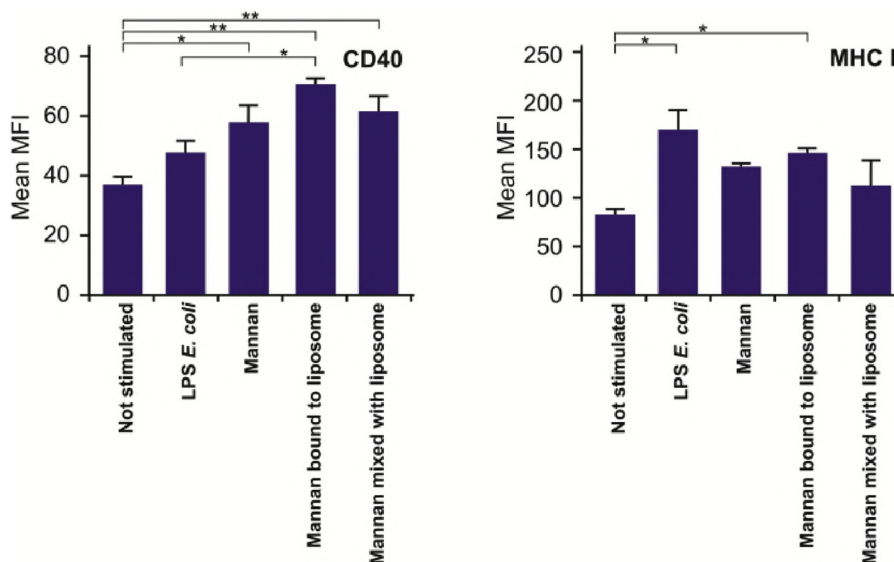


Fig. 6. Changes in MFI of CD40 and MHC I in BMDC stimulated with liposomal mannan formulations, mannan alone, or LPS. Statistical analysis was done using One-way ANOVA and Tukey's Multiple Comparison Test. $P < 0.05$ *, $P < 0.01$ **.

ligation is especially appropriate for the new microfluidic mixing method which represents a rapidly developing technique for the production of a complex liposomal preparation by on-chip technology as demonstrated recently (Hood, Vreeland, & DeVoe, 2014). Condensation of complex chemical procedures like preparation of nanoparticles (liposomes), chemical reaction (including click chemistry and photochemistry based reaction) for coupling drugs, antigens, protective polymers/biopolymers and ligands to liposomes, rapid removal of unwanted products and reactants by rapid microdialysis, etc., represent future directions in development of 4D pharmaceutical technologies.

4.2. Mannan-modified liposomes as a platform for targeted drug delivery systems and self-adjuvant carrier for antigens

Mannose-mediated binding to cell surface receptors is one of the oldest proposed mechanisms for liposome targeting (Kunimasa, Inui, Hori, Kawamura, & Endo, 1992; Okada et al., 2003; Opanasopit,

Hyoudou, Nishikawa, Yamashita, & Hashida, 2002). Mannans and mannan-modified antigens as well as mannosylated liposomes, as a corpuscular carriers for vaccine antigens, are recognised by a variety of surface receptors expressed by immune cells, especially by dendritic cells (DC) and macrophages. Such receptors include DC-SIGN (CD209), MR (CD206), Langerin (CD207), and some Dectin 2 family members (Figdor, 2002; Feinberg, Castelli, Drickamer, Seeberger, & Weis, 2006; Kerscher, Willment, & Brown, 2013). Therefore, mannans seem to be a suitable ligands for targeting of biocompatible nanoparticles like liposomes and solid lipid nanoparticles to immune cells. Antimicrobial drugs like Amphotericin B, contrast agents such as gadolinium complexes and especially vaccination nanoparticles are the examples of application of mannan-targetable delivery systems (Kang et al., 2017; Kunimasa et al., 1992; Lomakin et al., 2016; Qiao et al., 2016; Xiong et al., 2017).

Low molecular weight mannans from the opportunistic pathogenic fungus *C. glabrata* (Fidel, Vazquez, & Sobel, 1999) represent one of the

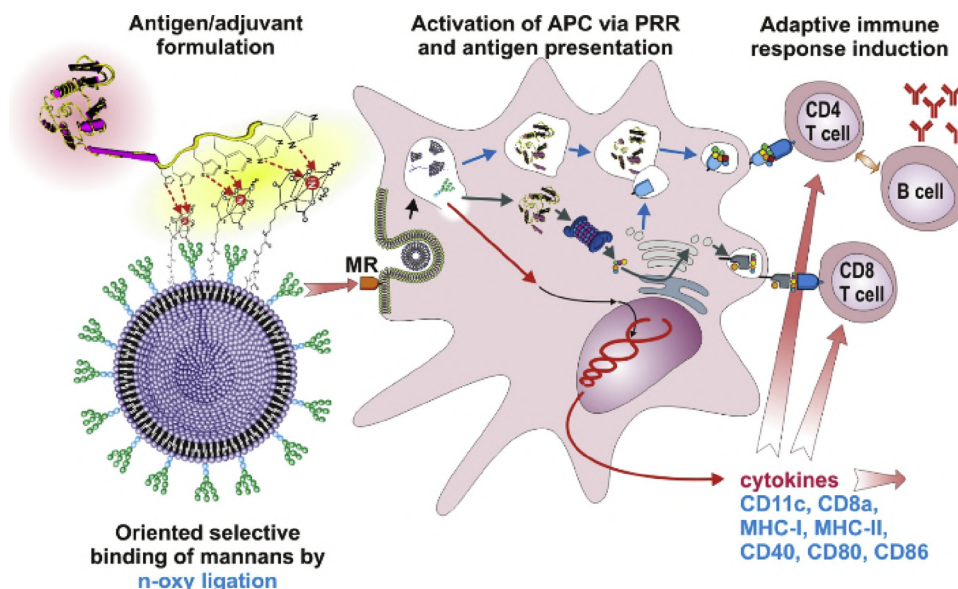


Fig. 7. Schematic presentation of self-assembling mannan-adjuvanted metallochelating nanoliposomes as self-adjuvanted carriers for construction of recombinant vaccines.

crucial antigenic components of cell wall polysaccharides (Tsuchiya, Fukazawa, Taguchi, Nakase, & Shinoda, 1974). Further studies focused on mannans expanded the knowledge of these species-specific antigenic factors (Martínez-Esparza, Sarazin, Jouy, Poulain, & Jouault, 2006; Suzuki, 1997). The structural differences accompanied by the variations in the immunostimulatory activity correspond predominantly to the difference in length and branching of mannoooligosaccharides and to the difference between binding anomers (Fradin et al., 1996; Jacquinet, Marie, Plancke, Sendid, & Poulain, 1998; Suzuki, 1997). Here we used the acid-stable part of *C. glabrata* cellular mannan with a molecular mass of 16.7 kDa containing 97.14% of D-mannose. Low MW type of mannan can be easily prepared as a well defined product for future application as a molecular adjuvant.

The enhancement of the interaction between the vaccination nanoparticles based on nanoliposomes and DCs could be a potential method for increasing vaccine immunogenicity. The principle of application of low molecular weight mannan for construction of liposomal vaccination nanoparticles is presented in Fig. 7.

Preparation of mannosylated liposomes and their interaction with peripheral blood mononuclear cells (MDDC) was reported earlier by others (Engering et al., 1997; Espuelas, Thumann, Heurtault, Schuber, & Frisch, 2008; Foged et al., 2004). In contrast to monoantennary mannose, multibranching mannosylated liposomes interact more effectively with MDDC and the interaction particularly of di- and tetra-antennary mannosylated liposomes was not inhibitable by free mannan, in contrast to monoantennary mannosylated liposomes (Espuelas et al., 2008). Inhibibility of monoantennary mannosylated liposomes was also observed by others (Perche et al., 2011). In contrast to LPS, tetraantennary branched mannose-modified liposomes did not stimulate MDDC, as measured by surface expression of CD86 and MHC II (Espuelas et al., 2008). In contrast, our mannan preparation from *Candida glabrata* exhibited BMDC stimulatory potential comparable with LPS (Figs. 5 and 6). Thus we could conclude that orthogonal bound natural mannans on liposomes could facilitate liposome endo or phagocytosis (Perche et al., 2011) and stimulation of MDDC as an initial step during induction of antigen specific immune response.

In this report, liposomes covered by orthogonally bound mannan were recognised and internalised by DCs (Fig. 4). Interaction of liposomal mannan with DCs induced the stimulatory signalling cascade leading to activation of human and murine DC as detected by expression of activation markers including CD80, CD86, CD40, MHC I and MHC II. (Figs. 4 and 5 and Table 2).

Metallochelating nanoliposomes are modified by low molecular weight mannan by orthogonal click reaction based on oxime ligation. Co-encapsulation of molecular adjuvants like monophosphoryl lipid A, trehalose dibehenate or hydrophobic derivatives of norAbu-muramyl dipeptide is feasible. Further enhancement and tuning of the immune response can be achieved. Recombinant antigens with HisTag are bound onto the surface by metallochelating noncovalent linkage to form complete vaccination nanoparticles (Krupka et al., 2012; Mašek, Bartheldyová, Turánek-Knotigová et al. 2011; Mašek, Bartheldyová, Korvasová et al. 2011; Michal Krupka et al., 2016).

Mannan bound on liposomes stimulated murine DC *in vitro* at doses of 50 ng of mannan per ml. Interestingly, this dose was as effective as 2.5 (or even 25 ng) of *E. coli* LPS per ml, when activation markers CD80, MHC I and MHC II were analyzed. In the case of CD40 activation marker, which is important for T cell maturation, the liposome-bound mannan was the most effective formulation tested (Fig. 6). In the case of CD80 activation marker, which is involved in activation of naive T cells to become armed effector T cells, the liposome-bound mannans were the most effective among all tested mannan formulations, although non-significantly weaker than LPS. The stimulatory effect of liposomal mannan rationalizes application of such carriers for the construction of self-assembly vaccination nanoparticles (Mašek, Bartheldyová, Turánek-Knotigová et al. 2011). The advantage of self-assembly liposomal systems is the possibility to combine mannan with other molecular

adjuvants (e.g. monophosphoryl lipid A or lipophilised nonpyrogenic derivatives of muramyl dipeptide) to tune and enhance the immune response towards particular antigen (Michal Krupka et al., 2016).

Corpuscular mannan proteoliposome-based vaccine approach seems to be promising also for the induction of CD8 T cell responses important for effective anti-viral and anti-tumour immunity. Here the antigen must be processed and presented by DC on MHC I molecules by one of several cross presentation pathways (Zachova, Krupka, & Raska, 2016). MR receptor is one of well characterized initiators of antigen cross presentation (Burgdorf & Lukacs-Kornek, 2006). For cross presentation of mannan proteoliposome formulated antigen we analyzed surface upregulation of MHC I on BMDC in response to various mannan formulations and we showed that oxime ligation-based covalent binding of mannan onto proteoliposome does not affect negatively mannan stimulatory potential (Fig. 5). Similarly, surface expression of MHC I induced by mannans was not affected when mannan liposomes were coupled with recombinant protein using Ni-NTA - His tag linkage (Mašek, Bartheldyová, Turánek-Knotigová et al. 2011). Pulsing experiments with murine BMDC indicate that any mannan-liposome-antigen particulate formulations did not exhibit a suppressive potential during DC pulsing in comparison to mannan alone making them a promising tool for corpuscular vaccine design.

5. Conclusions

New aminoxy lipids were designed and synthesized as reactive click chemistry components for preparation of functionalised liposomes. These lipids were proved as active components suitable for preparation of nanoliposomes by the microfluidic mixing method performed with the instrument NanoAssemblr™ and the technology can be used within the NanoAssemblr platform for scaling-up the technology and application of techniques called as “on-chip technology”. Nanoliposomes with aminoxy lipids were proved to be suitable for orthogonal binding of low MW mannan via click chemistry based on aminoxy ligation. Liposomal mannan preserved its ability to stimulate dendritic cells. This platform based on mannan bound onto the surface of nanoliposomes represents a self-adjuvant carrier for construction of liposome-based recombinant vaccines, especially for mucosal vaccination, and is now under study by our team.

Conflicts of interest

There are no conflicts to declare.

Acknowledgements

This work was supported by the following grants: the Ministry of Education, Youth and Sports OPVVV PO1 project “FIT” (Pharmacology, Immunotherapy, nanoToxicology) CZ.02.1.01/0.0/0.0/15_003/0000495 (JT, MR.), LO1304 (MR), Ministry of Education, Youth and Sports OPVVV CEREBIT CZ.02.1.01/0.0/0.0/16_025/0007397 (MR, JT, ML); Project Centre of Excellence for Nanotoxicology CENATOX GBP503/12/G147 (JT); the Ministry of Health CZ AZV-ČR 15-32198A (MR, JT); the project MZE0002716202 and RO0518 of the Czech Ministry of Agriculture (JT). The work was supported by the project “Biomedical Center Martin”, ITMS code: 6220220187 co financed from EU sources (PB). This work was supported by the Slovak Grant Agency VEGA (grant No 2/0098/17) (EP,LP).

Access to instruments in the laboratory NanoPharm (join project of Veterinary Research Institute and International Clinical Research Center (FNUSA-ICRC) is acknowledged, as well as support by Education and Research Centre VRI-Malvern.

Appendix A. Supplementary data

Supplementary material related to this article can be found, in the

online version, at doi:<https://doi.org/10.1016/j.carbpol.2018.10.121>.

References

- Algar, W. R., Prasuhn, D. E., Stewart, M. H., Jennings, T. L., Blanco-Canosa, J. B., Dawson, P. E., et al. (2011). The controlled display of biomolecules on nanoparticles: A challenge suited to bioorthogonal chemistry. *Bioconjugate Chemistry*, 22(5), 825–858. <https://doi.org/10.1021/bc200065z>.
- Burgdorf, S., Lukacs-Kornek, V., & Kurts, C. (2006). The mannose receptor mediates uptake of soluble but not of cell-associated antigen for cross-presentation. *Journal of Immunology (Baltimore, Md. : 1950)*, 176(11), 6770–6776. <http://www.ncbi.nlm.nih.gov/pubmed/16709836>.
- Carugo, D., Bottaro, E., Owen, J., Stride, E., & Nastruzzi, C. (2016). Liposome production by microfluidics: Potential and limiting factors. *Scientific Reports*, 6(1), 25876. <https://doi.org/10.1038/srep25876>.
- Effenberg, R., Knötiřová, P. T., Zyka, D., Čelechovská, H., Mašek, J., Bartheldyová, E., et al. (2017). Nonpyrogenic molecular adjuvants based on NorAbu-Muramyl dipeptide and NorAbu-Glucosaminyl muramyl dipeptide: Synthesis, molecular mechanisms of action, and biological activities in vitro and in vivo. *Journal of Medicinal Chemistry*, 60(18), 7745–7763. <https://doi.org/10.1021/acs.jmedchem.7b00593>.
- Engel, A., Chatterjee, S. K., Al-arifi, A., Riemann, D., Langner, Jürgen, & Nuhn, P. (2003). Influence of Spacer Length on Interaction of Mannosylated Liposomes with Human Phagocytic Cells. *Pharmaceutical Research*, 20(1), 51–57. <https://doi.org/10.1023/A:1022294624256>.
- Engering, A. J., Cella, M., Fluitsma, D., Brockhaus, M., Hoefsmit, E. C. M., Lanzavecchia, A., et al. (1997). The mannose receptor functions as a high capacity and broad specificity antigen receptor in human dendritic cells. *European Journal of Immunology*, 27(9), 2417–2425. <https://doi.org/10.1002/eji.1830270941>.
- Espuelas, S., Thumann, C., Heurtault, B., Tricard, F., & Frisch, B. (2008). Influence of ligand Valency on the targeting of immature human dendritic cells by mannosylated liposomes. *Bioconjugate Chemistry*, 19(12), 2385–2393. <https://doi.org/10.1021/bc8002524>.
- Feinberg, H., Castelli, R., Drickamer, K., Seeberger, P. H., & Weis, W. I. (2006). Multiple modes of binding enhance the affinity of DC-SIGN for high mannose N-Linked glycans found on viral glycoproteins. *The Journal of Biological Chemistry*, 282(6), 4202–4209. <https://doi.org/10.1074/jbc.M609689200>.
- Fidel, P. L., Vazquez, J. A., & Sobel, J. D. (1999). *Candida Glabrata*: Review of epidemiology, pathogenesis, and clinical disease with comparison to *C. Albicans*. *Clinical Microbiology Reviews*, 12(1), 80–96. <http://www.ncbi.nlm.nih.gov/pubmed/9880475>.
- Figdor, C. G., van Kooyk, Y., & Adema, G. J. (2002). C-type lectin receptors on dendritic cells and langerhans cells. *Nature Reviews Immunology*, 2(2), 77–84. <https://doi.org/10.1038/nri723>.
- Foged, C., Arigita, C., Sundblad, A., Jiskoot, W., Storm, G., & Frokjaer, S. (2004). Interaction of dendritic cells with antigen-containing liposomes: Effect of bilayer composition. *Vaccine*, 22(15–16), 1903–1913. <https://doi.org/10.1016/j.vaccine.2003.11.008>.
- Fradin, C., Jouault, T., Mallet, A., Mallet, J. M., Camus, D., Sinaÿ, P., et al. (1996). Beta-1,2-Linked oligomannosides inhibit *Candida albicans* binding to murine macrophage. *Journal of Leukocyte Biology*, 60(1), 81–87. <http://www.ncbi.nlm.nih.gov/pubmed/8699128>.
- Fukasawa, M., Shimizu, Y., Shikata, K., Nakata, M., Sakakibara, R., Yamamoto, N., Hatanaka, M., & Mizuochi, T. (1998). Liposome oligomannose-coated with Neoglycolipid, a new candidate for a safe adjuvant for induction of CD8+ cytotoxic T lymphocytes. *FEBS Letters*, 441(3), 353–356. [https://doi.org/10.1016/S0014-5793\(98\)01577-4](https://doi.org/10.1016/S0014-5793(98)01577-4) No longer published by Elsevier.
- Hood, R. R., Vreeland, W. N., & DeVoe, D. L. (2014). Microfluidic remote loading for rapid single-step liposomal drug preparation. *Lab on a Chip*, 14(17), 3359–3367. <https://doi.org/10.1039/c4lc00390j> NIH Public Access.
- Ikehara, Y., & Kojima, N. (2007). Development of a Novel Oligomannose-Coated Liposome-Based Anticancer Drug-Delivery System for Intraperitoneal Cancer. *Current Opinion in Molecular Therapeutics*, 9(1), 53–61. <http://www.ncbi.nlm.nih.gov/pubmed/17330402>.
- Ikehara, Y., Niwa, T., Le Biao, S. K., Ikehara, N., Ohashi, T. K., Shimizu, Y., Kojima, N., & Nakanishi, H. (2006). A carbohydrate recognition-Based drug delivery and controlled release system using intraperitoneal macrophages as a cellular vehicle. *Cancer Research*, 66(17), 8740–8748. <https://doi.org/10.1158/0008-5472.CAN-06-0470>.
- Jacquinet, P., Marie, Y., Plancke, B., Sendid, G. A., & Poulain, D. (1998). Nature of *Candida albicans* Derived carbohydrate antigen recognized by a monoclonal antibody in patient sera and distribution over *Candida* species. *FEMS Microbiology Letters*, 169(1), 131–138. <https://doi.org/10.1111/j.1574-6968.1998.tb13309.x> Wiley/Blackwell (10.1111).
- Kang, X.-jia, Wang, H.-yuan, Peng, H.-ge, Chen, B.-fan, Zhang, W.-yuan, Wu, A.-hua, Xu, Q., & Huang, Y.-zhuo (2017). Codelivery of Dihydroartemisinin and doxorubicin in mannosylated liposomes for drug-resistant Colon Cancer therapy. *Acta Pharmacologica Sinica*, 38(6), 885–896. <https://doi.org/10.1038/aps.2017.10>.
- Kerscher, B., Willment, J. A., & Brown, G. D. (2013). The Dectin-2 family of C-Type lectin-like receptors: An update. *International Immunology*, 25(5), 271–277. <https://doi.org/10.1093/intimm/dxt006>.
- Kolb, H. C., Finn, M. G., & Barry Sharpless, K. (2001). Click chemistry: Diverse chemical function from a few good reactions. *Angewandte Chemie (International Ed in English)*, 40(11), 2004–2021. <http://www.ncbi.nlm.nih.gov/pubmed/11433435>.
- Krupka, M., Zachova, K., Cahlikova, R., Vrbkova, J., Novak, Z., Sebela, M., Weigl, E., & Raska, M. (2015). Endotoxin-Minimized HIV-1 P24 Fused to Murine Hsp70 Activates Dendritic Cells, Facilitates Endocytosis and P24-Specific Th1 Response in Mice. *Immunology Letters*, 166(1), 36–44. <https://doi.org/10.1016/j.imlet.2015.05.010>.
- Krupka, M., Masek, J., Barkocziava, L., Knotigova, P. T., Kulich, P., Plockova, J., et al. (2016). The position of his-tag in recombinant OspC and application of various adjuvants affects the intensity and quality of specific antibody response after immunization of experimental mice. *PLoS One*, 11(2), e0148497. <https://doi.org/10.1371/journal.pone.0148497> Public Library of Science.
- Křupka, M., Mašek, J., Bartheldyová, E. Ška, Knötiřová, P. ĩna T. ěnek, Plockova, J., Korvasova, Z., Škrabalova, M., et al. (2012). Enhancement of Immune Response towards Non-Lipidized Borrelia burgdorferi Recombinant OspC Antigen by Binding onto the Surface of Metallochelating Nanoliposomes with Entrapped Lipophilic Derivatives of NorAbuMDP. *Journal of Controlled Release*, 160(2), 374–381. <https://doi.org/10.1016/j.jconrel.2012.02.017>.
- Kunimasa, J.-ichi, Inui, K.-ichi, Hori, R., Kawamura, Y., & Endo, K. (1992). Mannan-Coated Liposome Delivery of Gadolinium-Diethylenetriaminepentaacetic Acid, a Contrast Agent for Use in Magnetic Resonance Imaging. *Chemical & Pharmaceutical Bulletin*, 40(9), 2565–2567. <https://doi.org/10.1248/cpb.40.2565> The Pharmaceutical Society of Japan.
- Kuramoto, Y., Kawakami, S., Zhou, S., Fukuda, K., Yamashita, F., & Hashida, M. (2009). NOTE mannosylated cationic Liposomes/CpG DNA complex for the treatment of hepatic metastasis after intravenous administration in mice. *Pharmacists Association J Pharm Sci*, 98, 1193–1197. <https://doi.org/10.1002/jps.21475>.
- Lallana, E., Sousa-Herves, A., Fernandez-Trillo, F., Riguera, R., & Fernandez-Megia, E. (2012). Click chemistry for drug delivery nanosystems. *Pharmaceutical Research*, 29(1), 1–34. <https://doi.org/10.1007/s11095-011-0568-5>.
- Lomakin, Y., Belogurov, A., Glagoleva, I., Stepanov, A., Zakharov, K., Okunola, J., Smirnov, I., Genkin, D., & Gabibov, A. (2016). Administration of myelin basic protein peptides encapsulated in mannosylated liposomes normalizes level of serum TNF- α and IL-2 and chemoattractants CCL2 and CCL4 in multiple sclerosis patients. *Mediators of Inflammation*, 2016, 1–8. <https://doi.org/10.1155/2016/2847232>.
- Martinez-Esparza, M., Sarazin, A., Jouy, N., Poulain, D., & Jouault, T. (2006). Comparative analysis of cell wall surface glycan expression in *Candida albicans* and *Saccharomyces cerevisiae* yeasts by flow cytometry. *Journal of Immunological Methods*, 314(1–2), 90–102. <https://doi.org/10.1016/j.jim.2006.06.004>.
- Mašek, J., Bartheldyová, E. Ška, Korvasova, Z., Škrabalova, M., Koudelka, Štěpan, Kulich, P., et al. (2011). Immobilization of Histidine-Tagged Proteins on Monodisperse Metallochelation Liposomes: Preparation and Study of Their Structure. *Analytical Biochemistry*, 408(1), 95–104. <https://doi.org/10.1016/j.ab.2010.08.023>.
- Mašek, J., Bartheldyová, E. Ška, Turanek-Knötiřova, P. ĩna, Škrabalova, M., Korvasova, Z., Plockova, J., et al. (2011). Metallochelating Liposomes with Associated Lipophilised NorAbuMDP as Biocompatible Platform for Construction of Vaccines with Recombinant His-Tagged Antigens: Preparation, Structural Study and Immune Response towards RHis90. *Journal of Controlled Release*, 151(2), 193–201. <https://doi.org/10.1016/j.jconrel.2011.01.016>.
- Meng, X., Choudhury, S. R., & Edgar, K. J. (2016). Multifunctional cellulose esters by Olefin Cross-Metathesis and thiol-michael addition. *Polymer Chemistry*, 7(23), 3848–3856. <https://doi.org/10.1039/C6PY00539J> Royal Society of Chemistry.
- Okada, K., Sonoda, K., Koyama, M., Yin, S., Ikeda, M., Goryo, M., Chen, S. L., Kabeya, H., Ohishi, K., & Onuma, M. (2003). Delayed-type hypersensitivity in sheep induced by synthetic peptides of bovine leukemia virus encapsulated in Mannan-Coated Liposome. *The Journal of Veterinary Medical Science*, 65(4), 515–518. <http://www.ncbi.nlm.nih.gov/pubmed/12736435>.
- Opanasopit, P., Hyoudou, K., Nishikawa, M., Yamashita, F., & Hashida, M. (2002). Serum mannan binding protein inhibits mannosylated liposome-mediated transfection to macrophages. *Biochimica et Biophysica Acta (BBA) - General Subjects*, 1570(3), 203–209. [https://doi.org/10.1016/S0304-4165\(02\)00199-X](https://doi.org/10.1016/S0304-4165(02)00199-X).
- Orr, G. A., Rando, R. R., & Bangerter, F. W. (1979). Synthetic glycolipids and the lectin-mediated aggregation of liposomes*. *The Journal of Biological Chemistry*, 254(11), 4721–4725. <http://www.jbc.org/content/254/11/4721.full.pdf>.
- Perche, F., Gosset, D., Mevel, M., Miramon, M.-L., Yaouanc, J.-J., Pichon, C., Benvegnu, T., Jaffres, P.-A., & Midoux, P. (2011). Selective gene delivery in dendritic cells with mannosylated and hidrilyated lipopolyplexes. *Journal of Drug Targeting*, 19(5), 315–325. <https://doi.org/10.3109/1061186X.2010.504262>.
- Qiao, C., Liu, J., Yang, J., Li, Y., Weng, J., Shao, Y., et al. (2016). Enhanced non-inflammatory mediated immune responses by mannosylated zwitterionic-based cationic liposomes for HIV DNA vaccines. *Biomaterials*, 85(April), 1–17. <https://doi.org/10.1016/j.biomaterials.2016.01.054>.
- Song, X., Lin, Q., Guo, L., Fu, Y., Han, J., Ke, H., Sun, X., Gong, T., & Zhang, Z. (2015). Rifampicin loaded mannosylated cationic nanostructured lipid carriers for alveolar macrophage-specific delivery. *Pharmaceutical Research*, 32(5), 1741–1751. <https://doi.org/10.1007/s11095-014-1572-3>.
- Suzuki, S. (1997). Immunochemical Study on Mannans of Genus *Candida*. I. Structural Investigation of Antigenic Factors 1, 4, 5, 6, 8, 9, 11, 13, 13b and 34. *Current Topics in Medical Mycology* 8, (1–2), 57–70. <http://www.ncbi.nlm.nih.gov/pubmed/9504067>.
- Tseng, L.-P., Chiou, C.-J., Deng, M.-C., Huang, Y.-Y., & Der-Zen, L. (2010). Intranasal delivery of MANNAN-COATED liposomes enhances antibody responses to a Newcastle Disease Virus Vaccine. *Biomedical Engineering Applications Basis and Communications*, 22(01), 1–7. <https://doi.org/10.4015/S1016237210001773>.
- Tsuchiya, T., Fukazawa, Y., Taguchi, M., Nakase, T., & Shinoda, T. (1974). Serologic aspects on yeast classification. *Mycopathologia et Mycologia Applicata*, 53(1), 77–91. <http://www.ncbi.nlm.nih.gov/pubmed/4610378>.
- Ulrich, Sebastien, Boturyn, D., Marra, A., Renaudet, O., & Dumy, P. (2014). Oxime Ligation: A Chemoselective Click-Type Reaction for Accessing Multifunctional Biomolecular Constructs. *Chemistry - A European Journal*, 20(1), 34–41. <https://doi.org/10.1002/chem.201302426>.
- White, K. L., Rades, T., Furneaux, R. H., Tyler, P. C., & Hook, S. (2006). Mannosylated

- liposomes as antigen delivery vehicles for targeting to dendritic cells. *The Journal of Pharmacy and Pharmacology*, 58(6), 729–737. <https://doi.org/10.1211/jpp.58.6.0003>.
- Witoonsaridsilp, W., Paeratakul, O., Panyarachun, B., & Sarisuta, N. (2012). Development of mannosylated liposomes using synthesized N-Octadecyl-d-Mannopyranosylamine to enhance gastrointestinal permeability for protein delivery. *AAPS PharmSciTech*, 13(2), 699–706. <https://doi.org/10.1208/s12249-012-9788-1>.
- Xiong, M., Lei, Q., You, X., Gao, T., Song, X., Xia, Y., Ye, T., Zhang, L., Wang, N., & Luoting, Y. (2017). Mannosylated liposomes improve therapeutic effects of paclitaxel in Colon Cancer models. *Journal of Microencapsulation*, 34(6), 513–521. <https://doi.org/10.1080/02652048.2017.1339739>.
- Zachova, K., Krupka, M., & Raska, M. (2016). Antigen Cross-Presentation and Heat Shock Protein-Based Vaccines. *Archivum Immunologiae et Therapiae Experimentalis*, 64(1), 1–18. <https://doi.org/10.1007/s00005-015-0370-x>.

Application of Advanced Microscopic Methods to Study the Interaction of Carboxylated Fluorescent Nanodiamonds with Membrane Structures in THP-1 Cells: Activation of Inflammasome NLRP3 as the Result of Lysosome Destabilization

Pavína Turánek Knötigová,[†] Josef Mašek,[†] František Hubatka,[†] Jan Kotouček,[†] Pavel Kulich,[†] Pavína Šimečková,[†] Eliška Bartheldyová,[†] Miroslav Machala,[†] Tereza Švadláková,[‡] Jan Krejsek,[‡] Naděžda Vaškovicová,[§] Radim Skoupý,[§] Vladislav Krzyžánek,[§] Stuart Macaulay,^{||} Michael Katzuba,^{||} Ladislav Fekete,[⊥] Petr Ashcheulov,[⊥] Milan Raška,^{*,†,‡,§} Irena Kratochvílová,^{*,⊥,||} and Jaroslav Turánek^{*,†}

[†]Veterinary Research Institute, Brno 62100, Czech Republic

[‡]Faculty of Medicine, Department of Clinical Immunology and Allergology, Charles University, Hradec Králové 500 03, Czech Republic

[§]Institute of Scientific Instruments, Czech Academy of Sciences, Brno 61264, Czech Republic

^{||}Malvern Instruments, Great Malvern WR14 1XZ, U.K.

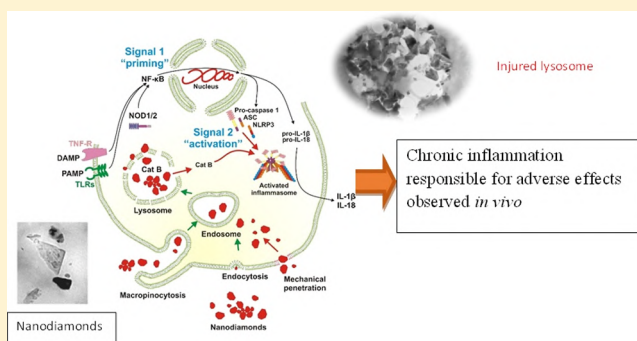
[⊥]Institute of Physics of the Czech Academy of Sciences, Na Slovance 2, CZ-182 21, Prague 8, Czech Republic

^{*}Department of Immunology, Faculty of Medicine and Dentistry, Palacky University Olomouc, Olomouc 775 15, Czech Republic

Supporting Information

ABSTRACT: Nanodiamonds (ND), especially fluorescent NDs, represent potentially applicable drug and probe carriers for *in vitro/in vivo* applications. The main purpose of this study was to relate physical–chemical properties of carboxylated NDs to their intracellular distribution and impact on membranes and cell immunity—activation of inflammasome in the *in vitro* THP-1 cell line model. Dynamic light scattering, nanoparticle tracking analysis, and microscopic methods were used to characterize ND particles and their intracellular distribution. Fluorescent NDs penetrated the cell membranes by both macropinocytosis and mechanical cutting through cell membranes. We proved accumulation of fluorescent NDs in lysosomes. In this case, lysosomes were destabilized and cathepsin B was released into the cytoplasm and triggered pathways leading to activation of inflammasome NLRP3, as detected in THP-1 cells. Activation of inflammasome by NDs represents an important event that could underlie the described toxicological effects *in vivo* induced by NDs. According to our knowledge, this is the first *in vitro* study demonstrating direct activation of inflammasome by NDs. These findings are important for understanding the mechanism(s) of action of ND complexes and explain the ambiguity of the existing toxicological data.

KEYWORDS: fluorescent nanodiamonds, cell immunopathology, nanodiamond intercellular distribution, inflammation, inflammasome NLRP3, AFM, TEM, cathodoluminescence, macropinocytosis, THP-1 cells, cathepsin B, lysosomal disruption



1. INTRODUCTION

Nanodiamonds (ND) have attracted a great deal of scientific attention for their potential in bioimaging and for their possible therapeutic applications due to their chemical inertness, useful surface properties, and stable fluorescence without photobleaching.^{1–8} The fluorescence properties of NDs, as well as their cathodoluminescence, are of special interest for the development of nanosensors for *in vivo* and *in vitro* applications.^{9–13} There is also increasing interest in

exploring the modification of the surface of NDs, and alteration of their functionality by the attachment of various biomolecules to mediate interaction with specific cellular targets.¹⁴ The broad area of applications includes the

Received: February 23, 2019

Revised: June 8, 2019

Accepted: June 11, 2019

Published: June 11, 2019

production of biosensors/biochips and biomedical nanorobots, drug, gene and protein carriers, protein purification, implant coating, and imaging probes.¹⁵ Functionalized ND can be extremely useful for tumor targeting, intravascular bioimaging, and diagnostic and therapeutic purposes.^{9,16,17} ND surface chemical modifications (e.g., by carboxylation, amination, PEGylation, biotinylation, etc.) could serve as a unique platform for bioconjugation.^{1,17}

The potential applications of NDs in medicine raise questions regarding biosafety assessment.^{18,19} Many papers addressed the important topics of ND biocompatibility and toxicity. Data on in vivo toxicity of NDs are limited and rather equivocal and conflicting. Although some reports indicate the safety of NDs documented in vitro using various cell lines as well as in vivo using murine animal models, several others have reported in vitro and in vivo toxicity and genotoxicity of various ND preparations.^{19–21} Cell-specific toxicity correlated with NDs in macrophages and lymphocytes^{22,23} has been reported recently. General cytotoxicity of NDs ranging in size from 2 to 10 nm was reported by in ref 24. The uptake of NDs into natural killer cells and monocytes has been studied in ref 25. ND concentration-dependent cytotoxic and inflammatory responses were described in the monoblastoid cell line U937 possibly via the TLR4 receptor and activation of the NF- κ B signaling pathway.²⁶ But more specifically the activation of inflammasome has not been shown before. As a whole, immunopathology seems to be the main phenomenon behind the observed toxic effect induced by NDs.

Therefore, in this work we used pure carboxylated fluorescence NDs of 100 nm in size to study the effect of ND on activation of inflammasome as the key event responsible for inducing tissue inflammation. To explain the specific behavior of ND in cells, we used advanced physicochemical methods [dynamic light scattering (DLS) and nanoparticle tracking analysis (NTA)] and microscopic methods [confocal microscopy, electron microscopy (EM), cathodoluminescence, and atomic force microscopy (AFM)]. The main purpose of this study was to relate the physical–chemical properties of carboxylated NDs to their effect on biological membranes and activation of inflammasome in vitro THP-1 cell line derived from human monocytes. Activation of inflammasome and uncontrolled chronic inflammation is responsible for a variety of immunopathologies. Chronic inflammation can be induced by a variety of nanoparticles which are difficult to remove from the organism and tend to accumulate in particular tissues and organs. NDs represent such particles, and activation of inflammasome can be assumed to be the main factor responsible for the observed in vivo toxic effect of NDs. According to our knowledge this is the first in vitro study demonstrating direct activation of inflammasome by NDs. Fluorescent NDs with proper chemical terminations can be used for monitoring the processes and states in the living cells but it should be taken into account that the cell can be destructed by the penetration of the ND. Finding the right biological application of technically very attractive diamond nanoparticles is a great challenge for the future.

2. EXPERIMENTAL SECTION

2.1. ND Particles. Fluorescent ND slurries denoted as ND-NV-100 nm were purchased from Adámas Nanotechnologies (Raleigh, NC, USA). (<http://adamasnano.com/fnd100nmndnv.html>). These were 1 mg/mL suspensions of

carboxylated ND in deionized water; their nominal average particle size was 100 nm.

2.2. DLS, Multiangle Light Scattering, and NTA. The batch measurements of the size distribution of the samples were carried out both by DLS (Zetasizer Ultra, Malvern, UK) and by the NTA technique using an instrument NanoSight NS500-HS (Malvern, UK) with a laser wavelength of 488 nm, sCMOS camera, and NTA 3.0 software. The effect of pH on the ζ potential of carboxylated NDs was measured using the Zetasizer Ultra a ζ -potential cuvette (DTS 1061, Malvern). Sodium phosphate buffer (10 mM; pH range 2–8) was used. Software ZS explorer was applied for calculation of particle concentration.

Multiangle light scattering (MALS) batch measurement was done by the instrument DAWN HELIOS II (Wyatt) at a concentration 20 μ g/mL in deionized water.

2.3. Electron Microscopy. **2.3.1. Transmission EM.** Samples of NDs were suspended in a drop of MilliQ water. The resulting suspension was covered with a carbon-coated grid (300 Old Mesch, Agar Scientific, Austria). The grid was removed from the suspension after 1 min and the residual water was dried with a strip of filtration paper. The samples were observed under a Philips 208 S Morgagni transmission electron microscope (FEI, Czech Republic) at 7500 \times magnification and at an accelerating voltage of 80 kV. The size of 100 prisms was measured.

The ultrathin section method was performed as follows: 3% glutaraldehyde-fixed THP-1 cells 24 h exposed to fND (10 μ g/mL) were centrifuged and the pellet was rinsed in Millonig buffer, postfixed in 1% OsO₄ solution in Millonig buffer, dehydrated in 50, 70, 90, and 100% ethanol, embedded in LR white resin (Sigma-Aldrich, Germany) and polymerized at 60 $^{\circ}$ C for 72 h. Ultrathin sections (the thickness of 70 nm) were cut with glass knives on a UC 7 ultramicrotome (UC 7, Leica, Austria). Afterwards, they were directly observed without being previously contrasted to prevent objectionable artifacts. The sections were examined under a Philips EM 208 S Morgagni transmission electron microscope (FEI, Czech Republic) at an accelerating voltage 80 kV.

2.3.2. Scanning EM and Freeze Fracture Techniques. A dense suspension of cells (density 10⁸ per mL) was frozen by a high pressure freezer Leica EM ICE (Leica Microsystems) on 3 mm gold carriers. The samples were totally freeze-dried in a high vacuum sputter coater Leica EM ACE 600 (Leica Microsystems) at a temperature -95 $^{\circ}$ C overnight. For imaging, the samples were transferred to a high resolution scanning EM (SEM) Magellan 400L (FEI) via cryo transfer system Leica EM VTC 100 (Leica Microsystems). The SEM is equipped with a detector MonoCL4 Plus (Gatan) for cathodoluminescence investigations. High resolution secondary electron images were captured at an acceleration voltage in the range 2–3 kV in a low dose, the cathodoluminescence investigations were performed at the acceleration voltage in the range 7–15 kV and the probe current of 6.4 nA.

For transmission EM (TEM) imaging, 70 nm sections of cells were prepared. This section size was considered optimum for TEM imaging because of a good contrast and resolution, while keeping an acceptable percentage of samples not destroyed by cutting and tearing by using large NDs (examples in Supporting Information).

2.3.3. Atomic Force Microscopy. NDs were characterized by a Dimension Icon AFM from Bruker Company. Standard tips Tap150al-g with a resonant frequency of 150 kHz and

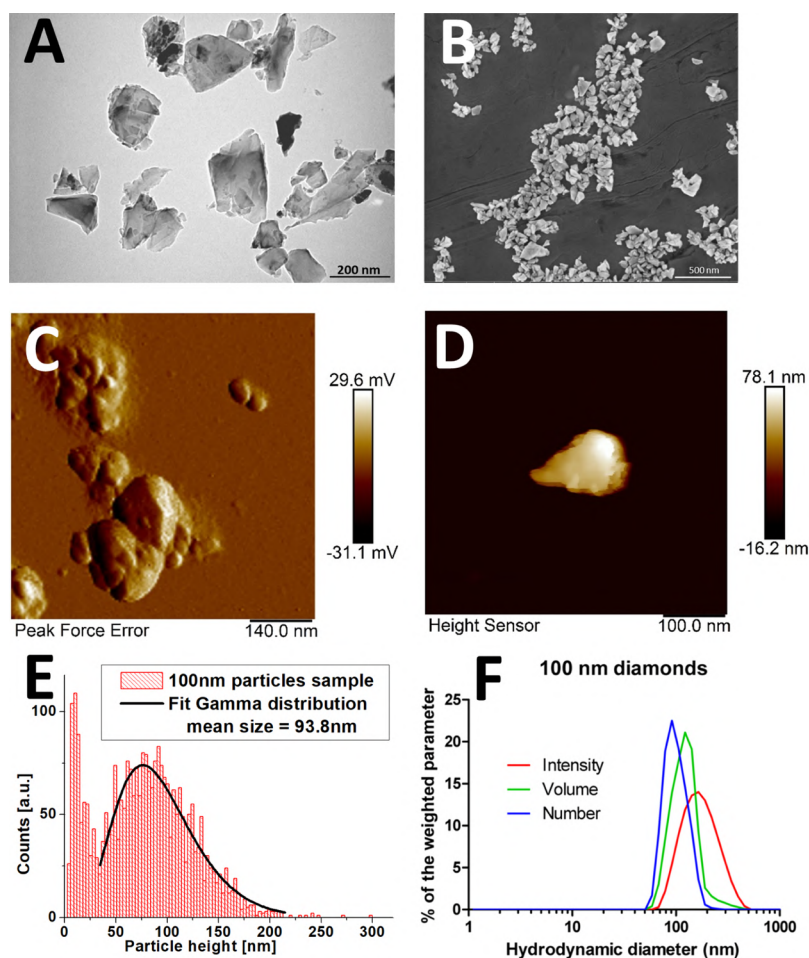


Figure 1. Characterization of ND—shape, size, and size distribution. Transmission and scanning electron micrographs of the 100 nm ND samples revealing their specific morphology and variability in their shape and size; (A) TEM detail of the structure of the 100 nm sample; (B) SEM of NDs. (C) Atomic force micrographs of the ND samples; (D) detail of the structure of the 100 nm ND sample; (E) size distribution of ND analyses by AFM; (F) the size distribution of the ND samples as determined by DLS (Zetasizer Nano-ZS, Malvern, UK); batch measurements, milliQ-water suspensions, Z-average (d.nm) 181.8, PDI 0.127.

nominal tip radius of 10 nm were used for the measurements. The particles were dissolved in ultra-pure deionized water and dropped on Si wafer. In the case of images for the analysis of the particle size distribution the areas of $5 \mu\text{m} \times 5 \mu\text{m}$ were depicted with a resolution of 512 points \times 512 points. All images were taken in the ScanAsyst measurement mode. The size of the particles was determined as the measured height of the particles.

2.4. Confocal Microscopy. A SP-2 confocal microscope (Leica) was used to visualize fluorescent ND in cells, colocalization studies of NDs with early endosomes and lysosomes, and release of cathepsin B from lysosomes. The images were scanned at 400 Hz using a 63 \times Leica oil immersion objective (numeric aperture, 1.4). An argon 488 nm laser was used for excitation of the Rab5a-GFP protein and LysoTracker, 561 nm laser was used for fluorescence excitation of NDs, and 458 nm laser was used for visualization of NDs in the reflectance mode.

2.4.1. Colocalization of NDs with Early Endosomes and Lysosomes. Early endosomes: THP-1 cells were transfected using CellLight[®] Rab5a-GFP *BacMam 2.0 (Molecular Probe, cat. No. C10586) according to the manufacturer's instructions, prior to the treatment with NDs. Lysosomes: THP-1 cells were incubated with 100 nM LysoTracker[®] Green DND-26

(molecular probe, Cat. no. L7526) 1 hour prior to observation by confocal microscopy, according to the manufacturer's instructions. The THP-1 cells were incubated with ND (final concentration 10 $\mu\text{g}/\text{mL}$ and observed in μ -slide 8 well ibiTreat (IBIDI, Martinsried, Germany) after 4 h incubation.

2.4.2. Release of Cathepsin B. Detection of cathepsin B was performed by a cathepsin B detection kit (Enzo Life Sciences) according to the manufacturer's protocol. CV-(RR)2 was used as the substrate for the cathepsin B cleavage. As a positive control, lysosomal disruptor Leu-Leu methyl ester hydrobromide (LLME) (Sigma-Aldrich) in the final concentration of 100 μM was used. THP-1 null cells were pretreated by a lysosomal disruptor for 2 h. THP-1 null cells not exposed to ND were used as a negative control.

2.5. Activation of NLRP3 (Inflammasome). The test was performed using HEK-Blue IL-1 β cells exactly according to the manufacturer manual (InvivoGen). See [Supporting Information](#) for details.

2.6. Raman Spectroscopy. Prior to measurements a suspension containing NDs has been drop-casted on the glass slide surface and dried under room temperature to obtain a 2 mm spot of NDs. Measurements have been carried out at room temperature using a Renishaw InVia Raman microscope under the following conditions: laser excitation wavelength of 488 nm

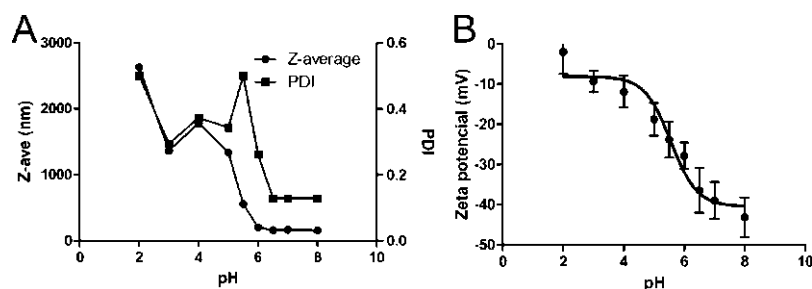


Figure 2. The effect of pH on ζ -potential of carboxylate NDs (100 nm) were dispersed in 10 mM sodium phosphate buffer with a pH ranging from 2 to 8. The size (expressed as Z-average) and polydispersity (PDI) (A) and ζ -potential (B) were measured at different pH values. Huckel approximation was used for calculation of the ζ -potential.

with laser power at sample of 6 mW, $\times 50$ Olympus objective, 65 μm slits, spot focus, and grating of 2400 lines/mm.

3. RESULTS

3.1. Electron Microscopy. NDs form irregular structures with flat, cuboidal, or block 3D shapes. EM and AFM are methods for detailed characterization of the shape, structure, and surface features of NDs. Individual particles were visualized, and their detailed size distribution over a wide range, importantly also below 20 nm calculated. Heterogeneity of ND preparations with respect to the particle morphology and size distribution is clearly evident by EM, as is the tendency of NDs to form clusters consisting of ND nanoparticles of various sizes. The irregular shapes and blade-like edges of NDs are clearly visible in the TEM image (Figure 1A) as well as the SEM image (Figure 1B). These features make NDs an ideal cutter of biological membranes, as demonstrated later in this study. The flat shape of NDs must also be considered as an important parameter for their separation by flow field fractionation (manuscript in preparation) and must be taken into account when the hydrodynamic radius (R_h) and the radius of gyration (R_g) are used in the characterization of their size distribution.

3.2. Atomic Force Microscopy. A detailed analysis of the size distribution of NDs was made by AFM equipped with software for size distribution analyses. Figure 1C shows representative micrographs of the ND preparation used for size distribution analyses and visualization of the surface details of NDs (Figure 1D). AFM analysis demonstrated a bimodal distribution of the ND size; the distribution curves are presented in Figure 1E. The first and dominant peak in the distribution curve represents larger particles. This peak, which is asymmetrical, was fitted to a γ -distribution with very good approximation. The second peak is produced by very small ND particles. The small peak of the particles present in the ND sample includes 580 particles that are smaller than 30 nm (the total number of analyzed particles is 2800) and represents 0.14% of the total volume of all particles.

The total volume of the small ND particles is very small and therefore difficult to observe by other methods [e.g., DLS, NTA, tunable resistive pulse sensing, and resonant mass measurement (RMM)]. The lower detection limit for nanoparticles is approximately 20–50 nm for the NTA, TRPS, and RMM methods. NDs are unique owing to their high refractive index and relatively high mass density, but in spite of the optimization of the settings of the instruments, we were not able to detect the fraction of smaller NDs by NTA, TRPS, and RMM.

If a basic model is considered in which the volume of the particle is taken as the cube of the height of the particle, the ND particles smaller than 10 nm make up only 0.04% of the total volume of all particles. The size distribution analysis showed a mean of 93.8 nm for the ND sample. The data obtained by manual measurement and analyses of micrographs obtained by EM yielded a mean of 91–100 nm for the ND preparation (histograms not shown). These values are in perfect agreement with the parameters specified by the manufacturer, but the information provided by the manufacturer does not mention the presence of small particles. A small portion of the larger ND was demonstrated as well.

Both TEM and AFM are suitable and precise methods for the characterization of NDs in dry form, but the study of aggregation phenomena is outside their main scope, and other methods must be applied for this purpose.

3.3. Characterization of NDs by DLS, NTA, and Raman Spectroscopy. In contrast to EM and AFM, the size of NDs measured by the DLS and NTA methods is expressed as a hydrodynamic radius (nm), which means that the shape of the particles is approximated as a spherical one. Differences in the size and character of the milieu, in which the particles are measured, (dry powder vs water dispersion) lead to differences in the measured size values. In spite of that NTA gave the data which are in good accordance with AFM analyses (NTA data is presented in the Supporting Information Figure S1). DLS has the advantages of high sensitivity, a wide dynamic range of size determination (0.6–6000 nm), and low consumption of the sample (as low as 12 μL when a microcuvette is used). On the other hand, complex samples with polymodal size distributions are difficult to analyze by this method. Moreover, larger particles can mask the presence of smaller ones owing to their stronger scattering of light, which produces a signal that can obscure the weaker light-scattering signals produced by small particles.

The size distribution of the ND samples was determined using DLS (Zetasizer Ultra, Malvern Instruments, UK). The signals were difficult to obtain from very small NDs, and it was necessary to prepare and analyze serial dilutions of the material to observe the marginal signals produced by very small NDs. These data are difficult to analyze quantitatively, and underestimation of the presence of small particles is evident as demonstrated by the analyses of particle numbers (Figure 1F). The number of ND particles was analyzed by DLS, and thQ value of 2.68×10^{10} nanoparticles per 1 mg of solid ND has been calculated by software ZS explorer.

Figure S1 shows histograms of the NTA results and summarizes the size distribution data for the ND preparation. Because the limits of size detection are in the range of 20–

2000 nm, the fraction of small NDs is difficult to observe owing to the low light-scattering signal produced by small NDs. Increasing the signal intensity and hence the sensitivity of the measurement would have decreased the quality of the data obtained for larger particles without improving the detection of small ones. Individual larger particles and particle clusters in the sample, which were also observed by AFM, were efficiently detected by NTA. In comparison to the AFM data, the NTA data suggest that a small proportion of the NDs do aggregate in spite of the relatively high ζ -potential of NDs, as demonstrated in Figure 2A,B.

Raman spectra obtained from 100 nm-sized fND demonstrate the presence of the sharp line located at 1332 cm^{-1} which is attributed to the sp^3 phase of carbon. For comparison, the Raman spectra of the 15 nm sized NDs display features attributed to the presence of the disordered carbon (broadband centered at 1340 cm^{-1}) and sp^2 -bonded carbon (broadband centered at $\sim 1580\text{ cm}^{-1}$) (see Supporting Information Figure S5).

3.4. Shape Analysis. The shape factor (p) was calculated using eq 1

$$p = R_g/R_h \quad (1)$$

The mean R_h (measured by DLS) and R_g (measured by MALS technique) values of the NDs were 39.8 and 48.3 nm, respectively. The shape factor (p) was calculated as 1.213; this value falls within the range 0.95–1.30, which is typical of “platy” particles. The theoretical value for a solid sphere is 0.778; a value of 0.816 is characteristic of a coil, and a value of 1.732 is characteristic of a rod.^{27,28} The obtained values are in good agreement with the shapes of individual ND particles observed by TEM, SEM, and AFM.

3.5. ζ -Potential of Carboxylated NDs. The presence of a carboxyl group endows NDs with a negative surface charge; due to the presence of this group, a negative ζ -potential value is expected in water milieu at basic and neutral pH values. The high negative ζ -potential of NDs prevents their aggregation (Figure 2A,B), and the NDs exist in a slurry presumably as individual particles. Zetasizer Ultra was used to determine the ζ -potential of NDs.

As expected, high negative values of ζ -potential were found for the ND samples, predicting high colloidal stability of the ND dispersions in water. This fact is important with respect to the analysis of size distribution by methods based on light scattering. In general, these methods cannot discriminate between monocomposite particles and aggregates of similar R_h formed by smaller particles or NDs with a size of approximately 100 nm occluded by very small (5–15 nm) NDs. Acidification of the water milieu leads to a rapid decrease in the ζ -potential, and this is accompanied by extensive aggregation as reflected by an increase in the size (Z -average) and PDI of the particles (Figure 2A,B). Because this effect begins to appear at a pH near 6, the possibility that the pH within lysosomes induces colloidal instability of the ND dispersion must be considered.

3.6. Localization of NDs in THP-1 Cells. The NDs present in THP-1 cells were either localized in vesicles that were identified by immunochemical staining as lysosomes or in the form of aggregates in the cytoplasm. Individual ND particles were observed in the cytoplasm. Rarely, some NDs were observed in the nucleus (see Supporting Information Figure S4). Clusters of NDs in the cytoplasm appeared as fluorescent spots when examined by confocal microscopy

(Figure 3A). The detailed structures of the ND clusters were revealed by TEM (Figure 3B). It should be noted that in the

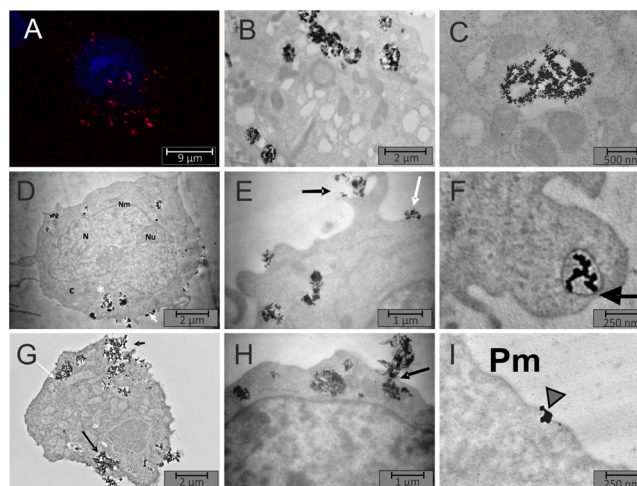


Figure 3. Penetration and intracellular localization of NDs in THP-1 cells revealed by confocal microscopy and TEM. TEM micrographs visualizing various steps of ND internalization by THP-1 cells. (A) Confocal microscopy pictures demonstrated cytoplasmic localization of fND (red spots). NDs were not localized in the nucleus (stained in blue). (B) TEM revealed localization of NDs in the cytoplasm and presumably NDs were found associated with vesicles. NDs were not localized in the nucleus. The presence of NDs in nuclei was demonstrated only sporadically in some cells (Figure S4) (C) Detailed picture of NDs associated with intracellular vesicles. (D) Overall view of the THP-1 cell showing adhesion of individual or aggregated NDs onto the cell membrane (white short arrow), aggregates of NDs in the cytoplasm (white asterisk). N—nucleus, Nu—nuclei, C—cytoplasm, and Nm—nucleic membrane. (E) Detailed picture of the internalization process of aggregated NDs via macropinocytosis (black arrows) and adhesion (white arrow). (F) Detailed picture of NDs inside of freshly formed pinocytotic vesicle (black arrow). (G) Overall view of the THP-1 cell after 24 h exposure to NDs. Formation of large aggregates of NDs in the cytoplasm (black arrow) and mechanical squeezing of mitochondrion (white arrow). Egestion of large aggregate of NDs out of cell (short black arrow). Detailed picture of mitochondrion—ND aggregate interaction in the Supporting Information (Figure S2). (H) Detailed picture of the ND cluster penetrating the cell membrane (black arrow). (I) Detailed picture of the small ND cluster and individual ND crossing cell membrane (grey arrow head) Concentration of fND was $10\text{ }\mu\text{g/mL}$. Incubation time 2 h with exception of (G) (incubation time 24 h).

cytoplasm there are various vesicles (e.g., endosomes, lysosomes, microsomes, transport vesicles, secretion vesicles, precursors of exosomes, etc.) differing in their content. Therefore their contrast in TEM is different. Most NDs were localized in the vesicles in close contact with the vesicle membrane. Some vesicles had intact structures, whereas others appeared to possess damaged membranes (Figure 3C–G). We observed a similar pattern of ND distribution in human lung A549 carcinoma cells (results not shown). The vesicles surrounding the NDs were identified as early endosomes and lysosomes by confocal microscopy of the samples in which Rab5a-GFP protein and LysoTracker were used as specific markers of early endosomes and lysosomes, respectively. NDs were present in some but not all lysosomes. ND clusters localized in the cytoplasm outside of lysosomes were not colocalized with LysoTracker-stained organelles. Injury and destabilization of the lysosomal membrane was visualized by

TEM and confirmed by enzymatic assay of cathepsin B activity in the cytoplasm after its release from endosomes and lysosomes destabilized by NDs.

Our TEM data demonstrate various ways in which NDs enter the cell. The initial step includes interaction of individual NDs or ND aggregates with the cell membrane and their adhesion to its surface (Figure 3, Supporting Information S2). Clusters of adhered NDs induce their internalization in a process that displays the morphological features of macropinocytosis (Figure 3D,F). Because of the sharp edges of NDs and the presence of ND aggregates, NDs can also penetrate the cell membrane directly and enter the cytoplasm (Figure 3F; Supporting Information Figure S3). Inside the cells, NDs are localized within and around the vesicles identified as endosomes and lysosomes, as demonstrated by TEM and confocal microscopy (Figures 3–5). TEM pictures demonstrating various localization of NDs and their interaction with cell membrane are presented in Figure S4.

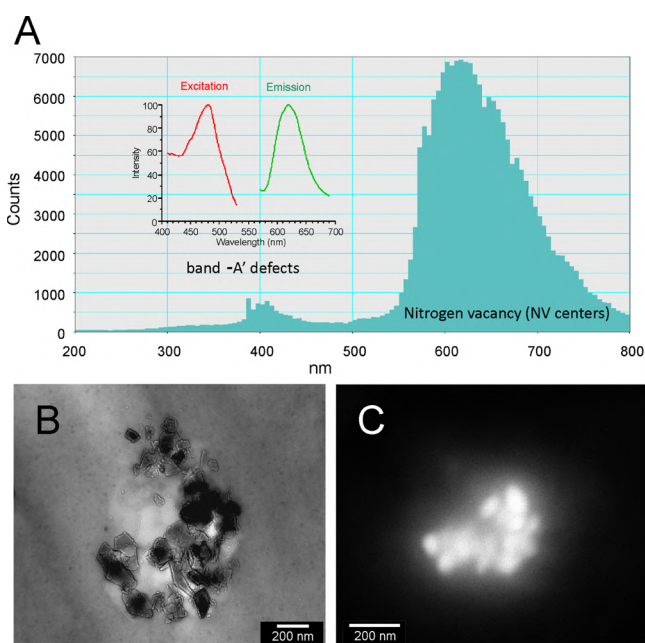


Figure 4. Visualization of fND in cell by application of EM with cathodoluminescence: (A) Cathodoluminescence spectrum of fluorescent NDs measured in an electron microscope and fluorescence spectrum (inset) of the same sample (B) detailed picture of intracellular vesicle coated by fluorescent NDs visualized by TEM. (C) Detailed picture of the cluster of fluorescent NDs associated with intracellular vesicle in THP-1 cells. NDs were visualized by SEM—cathodoluminescence. THP-1 cells were incubated with NDs (final concentration 10 $\mu\text{g}/\text{mL}$), and the specimen for TEM was prepared after 4 h incubation.

Cathodoluminescence is a unique property of fluorescent NDs and can be used to specifically visualize fND within cells by TEM. As demonstrated in Figure 4A, the fluorescence spectrum of fND is similar to the cathodoluminescence spectrum of the fND in imaged cells. Applications of confocal microscopy, monoclonal antibodies, and lysosomal fluorescent probes pointed to a fraction of lysosomes as intracellular structures containing fND. We used cathodoluminescence to confirm the localization of fND in intracellular vesicles, supposed to be lysosomes (Figure 4B,C). One must consider the fact that the number of fluorescent nitrogen-vacancy (NV)

centers in fND varies and that a small portion of the fND may contain low numbers of fluorescent NV centers; therefore, both their fluorescence and their cathodoluminescence can be very weak, and these fND are difficult to detect by these methods. Nevertheless, low fluorescent or nonfluorescent NDs can be visualized by reflectance confocal microscopy owing to the high refractive index of NDs (Figure 5).

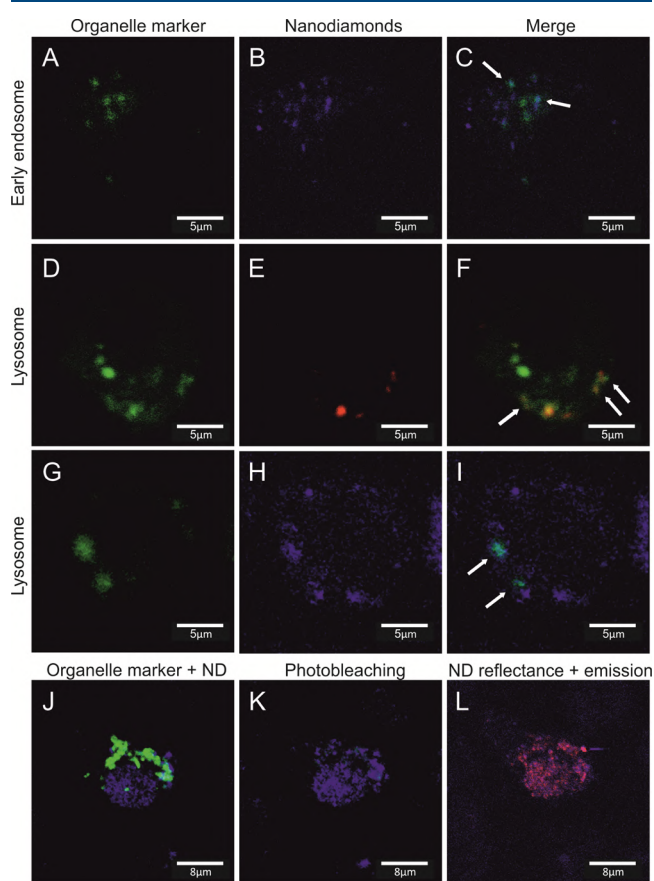


Figure 5. Colocalization of fND with early endosomes and lysosomes in THP-1 cells viewed by confocal microscopy. (A–C) colocalization of NDs with early endosomes, green (early endosome marker, cells were transfected by Rab5 protein), blue (visualization of ND using reflectance mode) (D–F) colocalization of NDs with lysosomes, green (LysoTracker was used as the lysosome marker), red (fluorescence signal of NDs). Lysosomes containing fND appeared as yellow-orange colored objects (G–I): colocalization of NDs with lysosomes, green (LysoTracker was used as lysosome marker), blue (visualization of NDs using reflectance mode) (J–K): photobleaching of a LysoTracker probe was used to clearly identify signals coming from the fluorescence probe of the lysosome and reflectance signal from NDs, whereas the fluorescence signal of LysoTracker as well as light reflected by the NDs is clearly visible before photobleaching (J), only the reflected light is observed after photobleaching (K), (L) colocalization of reflectance and fluorescence signal of internalized NDs (note that some ND are not fluorescent owing to the low content of NV centers). Concentration of fND 10 $\mu\text{g}/\text{mL}$ in incubation medium, incubation time 4 h.

3.7. Release of Cathepsin B from Lysosomes Destabilized by ND. The protease cathepsin B is localized in lysosomes, and under normal conditions is not present in detectable concentrations in the cytoplasm. Destabilization of lysosomes by various lysosomal disruptors leads to the release of cathepsin B into the cytoplasm and induces several

pathways, including pathways that lead to the stimulation of inflammasomes. We used a cell-penetrating fluorogenic substrate of cathepsin B to obtain evidence for the release of cathepsin B from lysosomes injured by NDs. Cathepsin B is not the component of early endosome, and injury to the membrane of early endosome did not cause its release into the cytoplasm. Identification of lysosomes and early endosomes as the organelles in which NDs are accumulated was approved by the colocalization study using a Lyso Tracker probe and Rab5a-GFP (Figure 5).

As a positive control, we used a disruptor -LLME, which is known to be a strong and selective lysosomal disruptor. NDs were visualized by confocal microscopy in the light scattering mode at wavelengths corresponding to the excitation spectrum of the fluorescent product of CV-(RR)₂ substrate cleavage by cathepsin B. After treatment with NDs at 10 $\mu\text{g}/\text{mL}$, most THP-1 cells became fluorescent (Figure 6).

The fluorescence was present in the cytoplasm but not in the nucleus. The fluorescence micrographs showed fluorescence signals both distributed throughout the cytoplasm and localized in intensely fluorescent spots. The observed fluorescence pattern suggests that several events occurred within the treated cells. First, the fluorogenic probe penetrated the slightly injured lysosomes that still contained molecules of cathepsin B. Second, cathepsin B was released into the cytoplasm from the lysosomes that were severely injured by NDs, giving rise to fluorescent staining with a disperse pattern. No substantial differences in the fluorescence patterns of THP-1 cells treated with NDs or with lysosomal disruptors that induce the release of cathepsin B were observed.

3.8. Stimulation of Inflammasomes in THP-1 Cells.

Stimulation of inflammasomes is a key event leading to the production of IL-1 β , which is the key proinflammatory cytokine. THP-1 cells are a well-accepted *in vitro* model for testing the induction of inflammasomes. NDs were able to induce inflammasome NRLP-3 in a dose-dependent manner in the range of ND 1–100 $\mu\text{g}/\text{mL}$. Representative results are presented in Figure 7.

4. DISCUSSION

The favorable physicochemical properties of NDs for construction of drug delivery systems and diagnostic preparations for *in vivo* imaging must be viewed from the perspective of biocompatibility. In this work we correlated physicochemical properties of ND particles with their penetration into cells, their intracellular distribution and their ability to induce activation of inflammasomes. For this purpose various modern microscopic and physicochemical methods were used in this work to fully characterize ND.^{29,30} As engineered nanoparticles, NDs are inevitably recognized by the immune system and are internalized by various mechanisms. Any persistence of NDs in tissues can lead to sustained activation of inflammasome resulting in chronic inflammation. Therefore, the ability of NDs to activate inflammasome can be assumed to be the main factor responsible for the toxicity of NDs observed *in vivo*.²⁹ Induction of inflammation is the key event that has an impact on the whole organism, and it may represent the general mechanism behind the observed adverse effects caused by NDs.

From a pharmacological point of view, aggregation of nanoparticles represents a serious problem for their possible application as drug carriers. Precise estimation of ND size distribution and their tendency to form aggregates in the

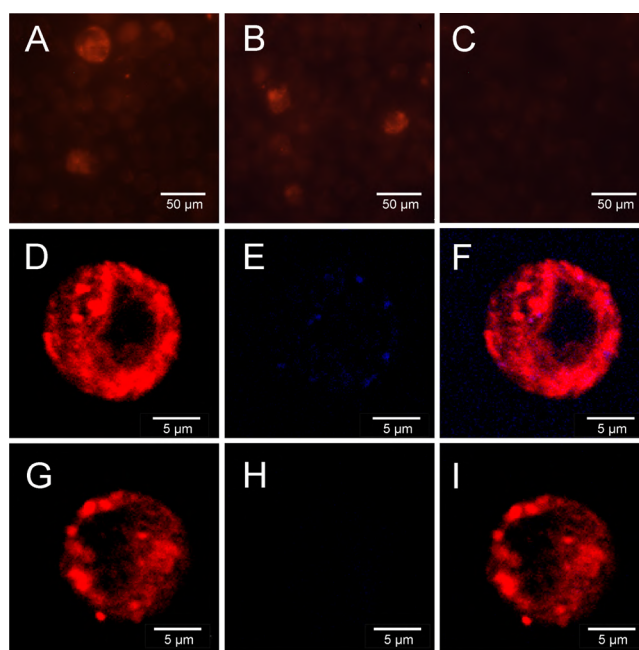


Figure 6. Release of cathepsin B into the cytoplasm in the THP-1 cell revealed by bright field and confocal fluorescence microscopy. Visualization of cathepsin B released into the cytoplasm from lysosomes injured by NDs (cathepsin B proteolytic activity was detected by fluorogenic product of CV-(RR)₂ substrate localized in the cytoplasm, red color). (A) release of cathepsin B after incubation of THP-1 cells with NDs visualized by bright field fluorescence microscopy. (B) release of cathepsin B after incubation of THP-1 cells with a lysosomal disruptor LLME visualized by fluorescence microscopy. (C) untreated control cells. (D–F): detailed picture of the THP-1 cell incubated with ND observed by confocal microscopy; (D) red fluorescence indicating cytosolic activity of cathepsin B, (E) blue reflectance signal of the NDs, (F) merge of (C,D). Visualization of fND in the cell by confocal reflection microscopy (scattering mode) (blue points represent ND scattered light. Wavelength of the light beam used for detection of fND was selected to be 458 nm, out of the wavelength range used for excitation of the fluorescence product generated from the substrate cleaved by cathepsin B; (G): detailed picture of THP-1 cell incubated with a LLME lysosomal disruptor observed by confocal microscopy; red fluorescence indicating cytosolic activity of cathepsin B; (H), blue—no reflectance signal observed. I—merged picture of G and H. Concentration of THP-1 cells was 10⁶ cells/mL. Concentration of fND was 10 $\mu\text{g}/\text{mL}$, incubation time 2 h.

biological milieu, is a requisite for all valid toxicological studies. Modification of NDs by carboxylation is one possible solution to suppress inherent tendency of NDs for aggregation owing to strong adhesive forces. Electrostatic repulsion because of negative ζ -potential of carboxylated ND diminishes their tendency for aggregation. This tendency is pH dependent (Figure 2) and can be further influenced *in vivo* by various components in biological fluids (e.g., proteins, peptides, and inorganic ions). It is of particular interest in the case of an organelle like lysosomes having mild acidic interior with pH around the value of 5.5–4.7. TEM and confocal microscopy visualizations of NDs accumulated in lysosomes confirmed the tendency of NDs to aggregate under mild acidic conditions inside lysosomes (Figures 3–5). Aggregation of NDs, to some extent, was also observed outside the cells in the cultivation medium. Carboxylated NDs behave like a cation exchanger binding proteins with a positive charge, it means that proteins

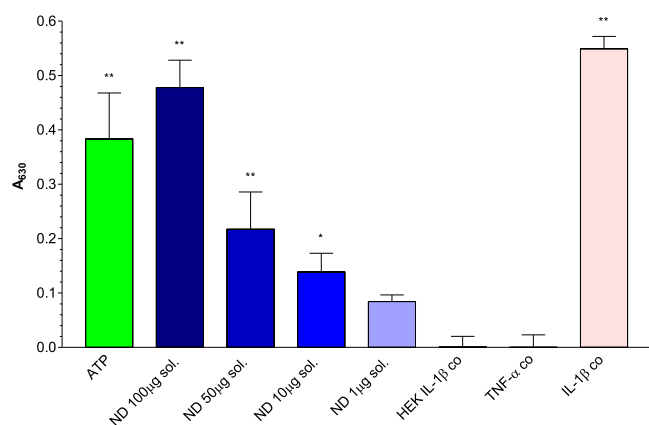


Figure 7. Stimulation of inflammasome NLRP-3 in THP-1 cells by fND. Activation of NLRP-3 was measured as conversion of proIL-1 β to IL-1 β . ND were tested in the concentration range 1–100 $\mu\text{g}/\text{mL}$ and dose dependency of IL-1 β production was demonstrated after 24 h incubation. ATP was used as a positive standard of NLRP-3 induction. IL-1 β was used as the positive control in the test. Dunnett's Multiple Comparison Test negative control column (HEK-Blue IL-1 β cells) versus the other columns * $p < 0.05$; ** $p < 0.01$; *** $p < 0.001$.

with low pI. Carboxylated NDs lost its negative charge, at a low pH, therefore the tendency to form protein corona via electrostatic interaction is lower. Nevertheless, the tendency to form protein corona is a general feature of nanoparticles, and NDs are no exception. Because in vitro data of ζ -potential dependence correlate well with the effect observed by TEM and confocal microscopy in cells, we can conclude that a lower pH in lysosomes contributes to ND aggregation. Of course, selective interaction of NDs (with or without biocorona) with surface proteins on intracellular vesicles cannot be excluded. But this is over the scope of this manuscript focused on activation of inflammasome.

The sharp edges of NDs produced by detonation technology make them potentially dangerous to cell membrane structures as demonstrated in Figures 3, 4, and 6. Cell membranes form compartments that separate various biochemical processes taking place inside the cell and are involved in a majority of the vital cell functions. Therefore, NDs can affect key cell structures and biochemical pathways, therefore the adverse effects can be induced, as observed in vitro and in vivo.^{19,21} The THP-1 cell line in vitro model provided us with experimental evidence pointing to the mechanism of toxic effects of NDs via activation of inflammasome NLRP3 (Figure 7).

Based on pH, ionic strength, and composition of water milieu NDs can exist as individually separated nanoparticles or can form aggregates of various sizes. NDs can enter the cytoplasm by (i) mechanical penetration through the cell membrane; (ii) by pinocytosis/macropinocytosis; (iii) by endocytosis/phagocytosis). Within the cell the NDs accumulate in lysosomes or form clusters in the cytoplasm. Interaction with other organelles is not yet proved, but influence of NDs on mitochondria must be considered too with respect to possible induction of oxidative stress, apoptosis, pyroptosis, and autophagy.^{29,31–33} Recently it was published that NDs at noncytotoxic concentrations were able to increase both total NO and ROS production in the A549 and BV-2 cells. The treatment negatively affected concentrations of high-energy phosphates, nicotinic coenzymes, and GSH, indicating an

imbalance of energy metabolism and mitochondrial functions and sustained oxidative/nitrosative stress.³²

On the molecular level interactions of proteins and other biomolecules with the surface of NDs can alter the conformations of proteins such as receptors, enzymes, structural proteins, hormones, and cell signaling molecules and can lead to alteration in or even a complete loss of their functionality.^{34,35} NDs are chemically inert; therefore, their possible adverse effects on cells result from mechanical injury of the cell membrane structures owing to thermal motion and the sharp edges of NDs. Injury of lysosomes induced by NDs is demonstrated by the release of the lysosomally-localized protease cathepsin B (Figure 5). Other organelles like mitochondria can also be mechanically disturbed by NDs presented in the cytoplasm (Figure 3G). Oxidative stress and apoptosis can be the results of adverse effects of NDs on mitochondria.³² A noncytotoxic dose may produce relevant biochemical alterations involving not only sustained oxidative/nitrosative stress, but also a profound imbalance in energy metabolism, mitochondrial functions, as well as triggering proinflammatory pathways.^{32,33,36} Altogether, the observed effect on the subcellular level can manifest in vivo in inflammation, as will be discussed below.

The above mentioned examples provide evidence for the ability of NDs to injure the membrane structures of exposed cells in vivo as well as in vitro. Blood coagulation and inflammation are two strong defense systems that are precisely controlled to prevent the possible lethal consequences of injury. Our data on the induction of inflammasomes (Figure 7) strongly suggest that inflammation instead of thromboembolism³⁷ is one of the mechanisms responsible for the observed toxicity of NDs in vivo described in the literature. The inflammasome concept was first introduced approximately 15 years ago.^{38–40} Priming and activation of these intracellular macromolecular complexes that sense cell stress or danger signals trigger the maturation of proinflammatory chemokines and cytokines, most notably IL-1 β and IL-18, and thereby initiate innate immune defense mechanisms. The role of inflammasomes in the development of autoinflammatory diseases^{41,42} must be considered in relation to NDs because of their potential to act as permanent inducers of inflammasomes, for example of NLRP3 (Figure 7). The complex role of inflammasomes in disease raises new questions about the application of NDs and in general all engineered bioresistant nanoparticles in medicine, especially with respect to their use as drug carriers that are resistant to biological degradation and rapid excretion from organisms. Accumulation of NDs in various organs such as lung, spleen, kidney, and liver can produce local concentrations of NDs that are sufficient to trigger inflammation, and consequently result in the pathological status of the affected tissues and organs.

By analogy with other engineered nanoparticles such as carbon nanotubes and endogenously produced crystalline structures such as cholesterol and urate crystals, we propose a scheme that describes, at the molecular and subcellular level, the mechanism responsible for the observed in vivo toxicity of ND (Figure 8). Our work demonstrated that the injury of the lysosomes by NDs is the central event that triggers the pathways leading to the activation of inflammasomes. Cathepsin B is released from the injured lysosomes, and its presence in the cytoplasm is a strong “signal 2” that induces the oligomerization of NLRP3. Various pathogen-associated molecular patterns (PAMPs) and damage-associated molecular

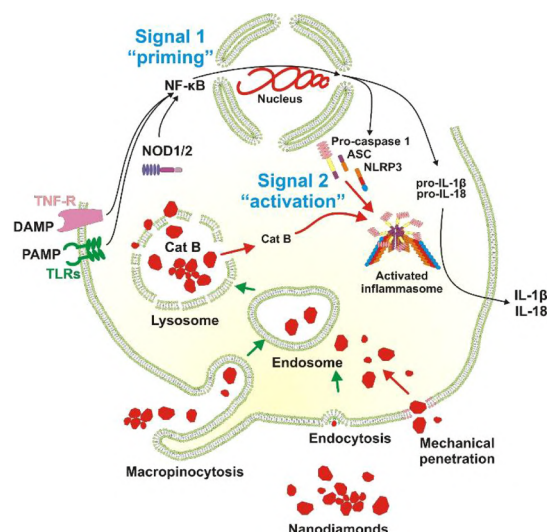


Figure 8. Schematic description of ND interaction with immune cells and mechanism of inflammasome activation. NDs enter the cytoplasm by mechanical penetration through the cell membrane, macropinocytosis, and endocytosis/phagocytosis. Sharp edges of NDs disrupt the membranes of lysosomes. Lysosomal content, including cathepsin B (CatB), is released into the cytoplasm providing the second signal triggering activation of inflammasome. The first signal is provided by various PAMP/DAMP via various cell receptors (e.g., TLRs and NOD1/2). This signal primes immune cells for activation of inflammasome. Therefore, bioresistant NDs accumulated in the tissue can induce chronic inflammation responsible for in vivo observed adverse and toxic effects.

patterns (DAMPs) provide the “signal 1”, which triggers the synthesis of proIL-1 β and proIL-18 together with that of inactive NLRP3 monomers. It is important to note that activation of inflammasomes by NDs is enhanced by various PAMPs, such as muramyl dipeptide, via NOD1/2 cytoplasmic receptors.⁴³ Because the mature cytokines IL-1 β and IL-18 are potent proinflammatory cytokines, their expression at high levels in organs and tissues such as lung, brain, bone marrow, spleen, and kidney could have disastrous consequences if left uncontrolled. For example, prolonged expression of these cytokines in the brain could lead to the malignancies observed in Alzheimer’s disease and other forms of dementia.⁴⁴

The fluorescent properties of fND, together with their cathodoluminescence^{45,46} make fND suitable probes for both confocal and EM. Quantum dots are of limited application because their fluorescence is quenched by osmium tetroxide fixation,²¹ limiting the applicability of quantum dots for multimodal imaging. Gold nanoparticles (AuNPs) lack the biosensing capabilities of NDs and are not easily distinguished from OsO₄-stained cytosolic lipid droplets based on their appearance in electron micrographs.⁴⁷ The unique fluorescence properties of fND make them appropriate markers for correlated optical/electron bioimaging, as demonstrated recently.⁴⁸ Our results show that the use of cathodoluminescence can extend the application of fND in multimodal optical/electron bioimaging.

5. CONCLUSIONS

NDs are expected as a tool for in vitro and in vivo imaging and are currently considered as new biocompatible nanocarriers for drugs. Surprisingly, the toxicological data published in the literature show a lack of complex understanding of the

mechanism(s) that govern the biodistribution of NDs in organisms, their penetration into cells and their effects on molecular structures, particularly on biological membranes. The main purpose of this study was to relate physical–chemical properties of carboxylated NDs (100 nm) to their intracellular distribution and impact on biological membranes and cell immunity—activation of inflammasome in vitro THP-1 cell line model. DLS, NTA, and microscopic methods (confocal microscopy, EM, cathodoluminescence, and AFM) were used to characterize ND particles and their intracellular distribution. According to our knowledge, this is the first in vitro study demonstrating direct activation of inflammasome by ND. It should be noted that our studies on standard carboxylated NDs do not directly imply the same effects in the case of ND particles with different chemical modifications of their surface. Specific surface modification can change ND behavior in the living cells, mainly when surface chemistry plays a key role in cell membrane interaction. Nevertheless, this surface modification can be altered in a complex environment of living cells (e.g., owing to action of enzymes and reactive oxygen species). In this case our description of ND behavior in living cells is relevant.

In this work we determined these important parameters which are crucial for interaction of ND particles with living cells:

1. The irregular shapes and blade-like edges of ND make ND an ideal cutter of biological membranes (EM).
2. In spite of relatively high ζ -potential, a small proportion of the ND exists in the aggregated state (NTA analysis).
3. Acidification of the water milieu leads to a rapid decrease in the ζ -potential of carboxylated ND which is accompanied by extensive aggregation. Because this effect begins to appear at a pH near 6, the possibility that value of pH within lysosomes and endosomes induces colloidal instability of the ND dispersion and must be considered.
4. As engineered nanoparticle NDs are inevitably recognized by the immune system, and internalization of NDs can destabilize endosomes and lysozymes in immune cells. Release of lysosomal content can induce cellular pathways leading to cytopathological processes. Cathepsin B released into the cytoplasm from injured lysozymes in combination with PAMP/DAMP molecules sensed by various membrane or cytosolic receptors (e.g., toll like receptors and NOD1/2) can trigger activation of inflammasome NLRP3 in tissue and induce chronic inflammation with pathological consequences.

There is no doubt that unique properties of fluorescent NDs make them excellent tools to study their fate and biodistribution in cells and tissues. The bioresistance of NDs and their ability to induce chronic inflammation in organisms well explains various toxic effects of NDs that have been observed and described in the literature using various in vivo animal models. Therefore, these features of NDs must be seriously considered and further studies focused on the long time effect of NDs on experimental animals are needed.

■ ASSOCIATED CONTENT

📄 Supporting Information

The Supporting Information is available free of charge on the ACS Publications website at DOI: 10.1021/acs.molpharmaceut.9b00225.

Size distribution of NDs measured by NTA, activation of NLRP3 (inflammasome), TEM detail of interaction of NDs cluster with mitochondrion in THP-1 cell, TEM penetration of the small cluster of NDs through the cell membrane, TEM cell nucleus with localized NDs, and Raman spectra of NDs (PDF)

AUTHOR INFORMATION

Corresponding Authors

*E-mail: milan.raska@upol.cz (M.R.).

*E-mail: krat@fzu.cz (I.K.).

*E-mail: turanek@vri.cz (J.T.).

ORCID

Tereza Švadláková: 0000-0002-1581-5531

Petr Ashcheulov: 0000-0001-8085-3609

Irena Kratochvílová: 0000-0002-6633-9432

Jaroslav Turánek: 0000-0001-8001-4047

Author Contributions

Contribution of two first authors was equal. Team headed by J.T., M.M., J.K., and M.R.—in vitro effect of nanodiamond on cell culture models. Team headed by J.T. and I.K.—physical-chemical characterization of NDs. P.T.K., P.Š., and T.Š.—in vitro tissue culture models. J.M., P.K., N.V., R.S., and V.K.—confocal microscopy, transmission, and SEM, cathodic luminescence. E.B. and S.M.—physical-chemical characterization of nanodiamond by DLS, NTA, fluorescence spectroscopy, and field flow fractionation. L.F.—characterization of nanodiamond by AFM. P.A.—Raman spectroscopy

Notes

The authors declare no competing financial interest.

ACKNOWLEDGMENTS

This work was supported by the Ministry of Education, Youth and Sports under grants OPVVV PO1 project “FIT” (Pharmacology, Immunotherapy, nanoToxicology) CZ.02.1.01/0.0/0.0/15_003/0000495 (J.T.); Project Centre of Excellence for Nanotoxicology CENATOX GAP503/12/G147 (M.M., J.T.) and Czech Ministry of Agriculture under grant MZE0002716202 (J.T., M.M.) and RO0518 (J.T., M.M.). The laboratories of AFM were also supported by European Structural and Investment Funds and the Czech Ministry of Education, Youth and Sports (project no. SOLID21—CZ.02.1.01/0.0/0.0/16_019/0000760) (I.K.). The laboratory at ISI was supported by CSF (project 17–15451S), MEYS CR (LO1212), its infrastructure by MEYS CR and EC (CZ.1.05/2.1.00/01.0017). Supported by the Ministry of Agriculture of the Czech Republic, institutional support MZE-RO0518 (J.T., M.M.). The kind support of the company Adamas (USA) regarding samples of nanodiamond is acknowledged. Special thanks to the project AdmireVet (CZ.1.05/2.1.00/01.0006—ED0006/01/01 from the Czech Ministry of Education, Youth and Sport) for permitting access to the scanning electron microscope. The authors acknowledged access to instruments in Education and Research Centre VRI-Malvern (join project of Veterinary Research Institute Brno and Malvern, UK) (J.T., S.M., M.K.) and in laboratory NanoPharm (join project of Veterinary Research Institute Brno, research centre ICRC and St. Anne Faculty Hospital Brno) (J.T.).

REFERENCES

- (1) Schrand, A. M.; Hens, S. A. C.; Shenderova, O. A. Nanodiamond Particles: Properties and Perspectives for Bioapplications. *Crit. Rev. Solid State Mater. Sci.* **2009**, *34*, 18–74.
- (2) Petraková, V.; Taylor, A.; Kratochvílová, I.; Fendrych, F.; Vacík, J.; Kučka, J.; Štursa, J.; Cígler, P.; Ledvina, M.; Fišerová, A.; Kneppo, P.; Nesládek, M. Luminescence of Nanodiamond Driven by Atomic Functionalization: Towards Novel Detection Principles. *Adv. Funct. Mater.* **2012**, *22*, 812–819.
- (3) Havlik, J.; Raabova, H.; Gulka, M.; Petrakova, V.; Krecmarova, M.; Masek, V.; Lousa, P.; Stursa, J.; Boyen, H.-G.; Nesladek, M.; Cigler, P. Benchtop Fluorination of Fluorescent Nanodiamonds on a Preparative Scale: Toward Unusually Hydrophilic Bright Particles. *Adv. Funct. Mater.* **2016**, *26*, 4134–4142.
- (4) Petrakova, V.; Benson, V.; Buncek, M.; Fiserova, A.; Ledvina, M.; Stursa, J.; Cigler, P.; Nesladek, M. Imaging of transfection and intracellular release of intact, non-labeled DNA using fluorescent nanodiamonds. *Nanoscale* **2016**, *8*, 12002–12012.
- (5) Kratochvílová, I.; Šebera, J.; Ashcheulov, P.; Golan, M.; Ledvina, M.; Míčová, J.; Mravec, F.; Kovalenko, A.; Zverev, D.; Yavkin, B.; Orlinskii, S.; Zálíš, S.; Fišerová, A.; Richter, J.; Šeřek, L.; Turánek, J. Magnetical and Optical Properties of Nanodiamonds Can Be Tuned by Particles Surface Chemistry: Theoretical and Experimental Study. *J. Phys. Chem. C* **2014**, *118*, 25245–25252.
- (6) Kratochvílová, I.; Kovalenko, A.; Fendrych, F.; Petraková, V.; Zálíš, S.; Nesládek, M. Tuning of nanodiamond particles' optical properties by structural defects and surface modifications: DFT modelling. *J. Mater. Chem.* **2011**, *21*, 18248–18255.
- (7) Kratochvílová, I.; Kovalenko, A.; Taylor, A.; Fendrych, F.; Rezáčková, V.; Vlček, J.; Zálíš, S.; Šebera, J.; Cígler, P.; Ledvina, M.; Nesládek, M. The fluorescence of variously terminated nanodiamond particles: Quantum chemical calculations. *Phys. Status Solidi A* **2010**, *207*, 2045–2048.
- (8) Kovalenko, A.; Petraková, V.; Ashcheulov, P.; Zálíš, S.; Nesládek, M.; Kraus, I.; Kratochvílová, I. Parameters affecting the luminescence of nanodiamond particles: Quantum chemical calculations. *Phys. Status Solidi A* **2012**, *209*, 1769–1773.
- (9) Turcheniuk, K.; Mochalin, V. N. Biomedical applications of nanodiamond. *Nanotechnology* **2017**, *28*, 252001.
- (10) Taylor, A. C.; Gonzalez, C. H.; Miller, B. S.; Edgington, R. J.; Ferretti, P.; Jackman, R. B. Surface functionalisation of nanodiamonds for human neural stem cell adhesion and proliferation. *Sci. Rep.* **2017**, *7*, 3707. DOI: 10.1038/s41598-017-07361-y
- (11) Mochalin, V. N.; Pentecost, A.; Li, X.-M.; Neitzel, I.; Nelson, M.; Wei, C.; He, T.; Guo, F.; Gogotsi, Y. Adsorption of Drugs on Nanodiamond: Toward Development of a Drug Delivery Platform. *Mol. Pharm.* **2013**, *10*, 3728–3735.
- (12) Toh, T.-B.; Lee, D.-K.; Hou, W.; Abdullah, L. N.; Nguyen, J.; Ho, D.; Chow, E. K.-H. Nanodiamond-Mitoxantrone Complexes Enhance Drug Retention in Chemoresistant Breast Cancer Cells. *Mol. Pharm.* **2014**, *11*, 2683–2691.
- (13) Adnan, A.; Lam, R.; Chen, H.; Lee, J.; Schaffer, D. J.; Barnard, A. S.; Schatz, G. C.; Ho, D.; Liu, W. K. Atomistic Simulation and Measurement of pH Dependent Cancer Therapeutic Interactions with Nanodiamond Carrier. *Mol. Pharm.* **2011**, *8*, 368–374.
- (14) Bray, K.; Cheung, L.; Hossain, K. R.; Aharonovich, I.; Valenzuela, S. M.; Shimoni, O. Versatile multicolor nanodiamond probes for intracellular imaging and targeted labeling. *J. Mater. Chem. B* **2018**, *6*, 3078–3084.
- (15) Mašek, J.; Bartheldyova, E.; Korvasova, Z.; Skrabalova, M.; Koudelka, S.; Kulich, P.; Kratochvílová, I.; Miller, A. D.; Ledvina, M.; Raska, M.; Turanek, J. Immobilization of histidine-tagged proteins on monodisperse metallochelation liposomes: Preparation and study of their structure. *Anal. Biochem.* **2011**, *408*, 95–104.
- (16) Shenderova, O. A.; Zhirnov, V. V.; Brenner, D. W. Carbon nanostructures. *Crit. Rev. Solid State Mater. Sci.* **2002**, *27*, 227–356.
- (17) Mochalin, V. N.; Shenderova, O.; Ho, D.; Gogotsi, Y. The properties and applications of nanodiamonds. *Nat. Nanotechnol.* **2012**, *7*, 11–23.

- (18) Silbajoris, R.; Huang, J. M.; Cheng, W.-Y.; Dailey, L.; Tal, T. L.; Jaspers, I.; Ghio, A. J.; Bromberg, P. A.; Samet, J. M. Nanodiamond particles induce IL-8 expression through a transcript stabilization mechanism in human airway epithelial cells. *Nanotoxicology* **2009**, *3*, 152–160.
- (19) Ema, M.; Hougaard, K. S.; Kishimoto, A.; Honda, K. Reproductive and developmental toxicity of carbon-based nanomaterials: A literature review. *Nanotoxicology* **2016**, *10*, 391–412.
- (20) Dworak, N.; Wnuk, M.; Zebrowski, J.; Bartosz, G.; Lewinska, A. Genotoxic and mutagenic activity of diamond nanoparticles in human peripheral lymphocytes in vitro. *Carbon* **2014**, *68*, 763–776.
- (21) Zhang, X.; Yin, J.; Kang, C.; Li, J.; Zhu, Y.; Li, W.; Huang, Q.; Zhu, Z. Biodistribution and toxicity of nanodiamonds in mice after intratracheal instillation. *Toxicol. Lett.* **2010**, *198*, 237–243.
- (22) Schrand, A. M.; Huang, H.; Carlson, C.; Schlager, J. J.; Ōsawa, E.; Hussain, S. M.; Dai, L. Are diamond nanoparticles cytotoxic? *J. Phys. Chem. B* **2007**, *111*, 2–7.
- (23) Thomas, V.; Halloran, B. A.; Ambalavanan, N.; Catledge, S. A.; Vohra, Y. K. In vitro studies on the effect of particle size on macrophage responses to nanodiamond wear debris. *Acta Biomater.* **2012**, *8*, 1939–1947.
- (24) Schrand, A. M.; Huang, H.; Carlson, C.; Schlager, J. J.; Ōsawa, E.; Hussain, S. M.; Dai, L. Are diamond nanoparticles cytotoxic? *J. Phys. Chem. B* **2007**, *111*, 2–7.
- (25) Suarez-Kelly, L. P.; Campbell, A. R.; Rampersaud, I. V.; Bumb, A.; Wang, M. S.; Butchar, J. P.; Tridandapani, S.; Yu, L.; Rampersaud, A. A.; Carson, W. E., III. Fluorescent nanodiamonds engage innate immune effector cells: A potential vehicle for targeted anti-tumor immunotherapy. *Nanomed. Nanotechnol. Biol. Med.* **2017**, *13*, 909–920.
- (26) Ibrahim, M.; Xue, Y.; Ostermann, M.; Sauter, A.; Steinmueller-Nethl, D.; Schwegler, S.; Krueger, A.; Cimpan, M. R.; Mustafa, K. In vitro cytotoxicity assessment of nanodiamond particles and their osteogenic potential. *J. Biomed. Mater. Res. A* **2018**, *106*, 1697–1707.
- (27) Burchard, W. *Static and Dynamic Light Scattering Approaches to Structure Determination of Biopolymers*; Royal Society of Chemistry ed.: Cambridge, 1992.
- (28) Baalousha, M.; Kammer, F. V. D.; Motelica-Heino, M.; Le Coustumer, P. 3D characterization of natural colloids by FIFFF-MALLS-TEM. *Anal. Bioanal. Chem.* **2005**, *383*, 549–556.
- (29) Khosravi, Y.; Salimi, A.; Pourahmad, J.; Naserzadeh, P.; Seydi, E. Inhalation exposure of nano diamond induced oxidative stress in lung, heart and brain. *Xenobiotica* **2018**, *48*, 860–866.
- (30) Lynch, I.; Dawson, K. A. Protein-nanoparticle interactions. *Nano Today* **2008**, *3*, 40–47.
- (31) Solomatin, A. S.; Yakovlev, R. Y.; Teplava, V. V.; Fedotcheva, N. I.; Kondrachova, M. N.; Kulakova, I. I.; Leonidov, N. B. Effect of detonation nanodiamond surface composition on physiological indicators of mitochondrial functions. *J. Nanoparticle Res.* **2018**, *20*, 1–16.
- (32) Fresta, C. G.; Chakraborty, A.; Wijesinghe, M. B.; Amorini, A. M.; Lazzarino, G.; Lazzarino, G.; Tavazzi, B.; Lunte, S. M.; Caraci, F.; Dhar, P.; Caruso, G. Non-toxic engineered carbon nanodiamond concentrations induce oxidative/nitrosative stress, imbalance of energy metabolism, and mitochondrial dysfunction in microglial and alveolar basal epithelial cells. *Cell Death Dis.* **2018**, *9*, 245.
- (33) Mytych, J.; Lewinska, A.; Zebrowski, J.; Wnuk, M. Nanodiamond-induced increase in ROS and RNS levels activates NF-kappa B and augments thiol pools in human hepatocytes. *Diamond Relat. Mater.* **2015**, *55*, 95–101.
- (34) Elsaesser, A.; Howard, C. V. Toxicology of nanoparticles. *Adv. Drug Delivery Rev.* **2012**, *64*, 129–137.
- (35) Lin, Y.-C.; Wu, K.-T.; Lin, Z.-R.; Perevedentseva, E.; Karmenyan, A.; Lin, M.-D.; Cheng, C.-L. Nanodiamond for biolabelling and toxicity evaluation in the zebrafish embryo in vivo. *J. Biophot.* **2016**, *9*, 827–836.
- (36) Xiang, Y.; Zhao, M.-m.; Sun, S.; Guo, X.-L.; Wang, Q.; Li, S.-A.; Lee, W.-H.; Zhang, Y. A high concentration of DMSO activates caspase-1 by increasing the cell membrane permeability of potassium. *Cytotechnology* **2018**, *70*, 313–320.
- (37) Kumari, S.; Singh, M. K.; Singh, S. K.; Grácio, J. J.; Dash, D. Nanodiamonds activate blood platelets and induce thromboembolism. *Nanomedicine* **2014**, *9*, 427–440.
- (38) Srinivasula, S. M.; Poyet, J.-L.; Razmara, M.; Datta, P.; Zhang, Z.; Alnemri, E. S. The PYRIN-CARD protein ASC is an activating adaptor for caspase-1. *J. Biol. Chem.* **2002**, *277*, 21119–21122.
- (39) Martinon, F.; Burns, K.; Tschopp, J. The inflammasome: A molecular platform triggering activation of inflammatory caspases and processing of proIL-beta. *Mol. Cell* **2002**, *10*, 417–426.
- (40) Patel, M. N.; Carroll, R. G.; Galván-Peña, S.; Mills, E. L.; Olden, R.; Triantafyllou, M.; Wolf, A. I.; Bryant, C. E.; Triantafyllou, K.; Masters, S. L. Inflammasome Priming in Sterile Inflammatory Disease. *Trends Mol. Med.* **2017**, *23*, 165–180.
- (41) Pellegrini, C.; Antonioli, L.; Lopez-Castejon, G.; Blandizzi, C.; Fornai, M. Canonical and Non-Canonical Activation of NLRP3 inflammasome at the Crossroad between immune Tolerance and intestinal inflammation. *Front. Immunol.* **2017**, *8*, 36.
- (42) Tan, M.-S.; Yu, J.-T.; Jiang, T.; Zhu, X.-C.; Tan, L. The NLRP3 Inflammasome in Alzheimer's Disease. *Mol. Neurobiol.* **2013**, *48*, 875–882.
- (43) Effenberg, R.; Turánek Knötišová, P.; Zyka, D.; Čelechovská, H.; Mašek, J.; Ārtheldyová, E.; Hubatka, F.; Koudelka, Š.; Lukáč, R.; Kovalová, A.; Šaman, D.; Křupka, M.; Barkoczišova, L.; Kosztyu, P.; Šebela, M.; Drož, L.; Hučko, M.; Kanášová, M.; Miller, A. D.; Raška, M.; Ledvina, M.; Turánek, J. Nonpyrogenic Molecular Adjuvants Based on norAbu-Muramyldipeptide and norAbu-Glucosaminyl Muramyldipeptide: Synthesis, Molecular Mechanisms of Action, and Biological Activities in Vitro and in Vivo. *J. Med. Chem.* **2017**, *60*, 7745–7763.
- (44) Fekete, L.; Kusova, K.; Petrak, V.; Kratochvilova, I. AFM topographies of densely packed nanoparticles: a quick way to determine the lateral size distribution by autocorrelation function analysis. *J. Nanopart. Res.* **2012**, *14*, 10.
- (45) Hemelaar, S. R.; de Boer, P.; Chipaux, M.; Zuidema, W.; Hamoh, T.; Martinez, F. P.; Nagl, A.; Hoogenboom, J. P.; Giepmans, B. N. G.; Schirhagl, R. Nanodiamonds as multi-purpose labels for microscopy. *Sci. Rep.* **2017**, *7*, 720.
- (46) Nagarajan, S.; Pioche-Durieu, C.; Tizei, L. H. G.; Fang, C.-Y.; Bertrand, J.-R.; Le Cam, E.; Chang, H.-C.; Treussart, F.; Kociak, M. Simultaneous cathodoluminescence and electron microscopy cytometry of cellular vesicles labeled with fluorescent nanodiamonds. *Nanoscale* **2016**, *8*, 11588–11594.
- (47) Yuan, Y.; Chen, Y.; Liu, J.-H.; Wang, H.; Liu, Y. Biodistribution and fate of nanodiamonds in vivo. *Diamond Relat. Mater.* **2009**, *18*, 95–100.
- (48) Lake, M. P.; Bouchard, L.-S. Targeted nanodiamonds for identification of subcellular protein assemblies in mammalian cells. *PLoS One* **2017**, *12*, No. e0179295.

Manuscript Number:

Title: Characterization and purification of the pentameric chimeric protein particles using Asymmetrical Flow Field-Flow Fractionation coupled with MALS/DLS/UV detector.

Article Type: Full length article

Keywords: Circovirus; Recombinant antigen; Asymmetrical flow Field-flow fractionation (AF4); Multi-angle dynamic light scattering (MADLS)

Corresponding Author: Dr. Jaroslav Turánek, Res. Prof.

Corresponding Author's Institution: Veterinary Research Institute

First Author: Jan Kotoucek

Order of Authors: Jan Kotoucek; Renata Héžova; Alena Vrábliková; František Hubatka; Pavel Kulich; Dierk Roessner; Stuart Macaulay; Milan Raška; Ivan Pšikal; Jaroslav Turánek

Abstract: Porcine circovirus causes the post-weaning multi-systemic wasting syndrome. Despite the existence of commercial vaccines, the development of more effective and cheaper vaccines is expected. The usage of chimeric antigens allows serological differentiation between naturally infected and vaccinated animals. In this work, recombinant pentameric vaccination protein particles spontaneously assembled from identical subunits - chimeric fusion proteins derived from circovirus capsid antigen Cap and a multimerizing subunit of mouse polyomavirus capsid protein VP1 were purified and characterized using Asymmetric Flow Field-Flow Fractionation (AF4) coupled with UV and MALS/DLS detector. Different elution profiles, including constant, linear, and exponential decrease cross-flow were tested. The optimal sample retention, separation efficiency, and resolution were assessed by the comparison of the hydrodynamic radius (R_h) measured by online DLS with the R_h values calculated from the full retention equation according to AF4 theory. The results show that the use of the combined elution profiles (exponential and constant cross-flow) reduces the time of the separation, undesirable sample-membrane interaction and yielded better resolution. The combination of two detectors MALS/DLS was used to determine the R_g/R_h ratio used for particle conformation analysis. Besides, the results show no self-associations of the individual pentameric particles into larger clusters and no sample degradation during the AF4 separation. The R_g/R_h ratios for different fractions are in good correlation with morphological analyses performed by transmission electron microscopy (TEM). Additional to the online analysis, the individual fractions were subjected to offline analysis including batch DLS, TEM, and SDS-PAGE followed by western blot.

Suggested Reviewers: Karsten Mäder

karsten.maeder@pharmazie.uni-halle.de

Expert in the filed of the design, processing, and characterization of nanoparticles.

Olivia Merkel
olivia.merkel@cup.uni-muenchen.de
Expert in the field of drug delivery and immunology.

Petr Malý
petr.maly@ibt.cas.cz
Expert in the field of protein particles and protein engineering.

Opposed Reviewers:

Research Data Related to this Submission

Title: Denaturation of the VP1-Cap
Repository: Mendeley Data
<https://data.mendeley.com/datasets/58gxprdf3t/draft?a=cc2f910c-6b0c-47f1-b2b6-f1189164fc2b>

Title: Thermal stability of the pentameric protein VP1-Cap.
Repository: Mendeley Data
<https://data.mendeley.com/datasets/58gxprdf3t/draft?a=cc2f910c-6b0c-47f1-b2b6-f1189164fc2b>

Characterization and purification of the pentameric chimeric protein particles using Asymmetrical Flow Field-Flow Fractionation coupled with MALS/DLS/UV detector.

Jan Kotoucek¹, Renata Hezova¹, Alena Vrablikova¹, Frantisek Hubatka¹, Pavel Kulich¹, Stuart Macaulay², Dierk Roessner³, Milan Raska^{1,4}, Ivan Psikal¹, Jaroslav Turanek^{1*}

¹*Veterinary Research Institute, Hudcova 70, 621 00 Brno, Czech Republic*

²*Malvern Panalytical Ltd. Enigma Business Park, Grovewood Road WR14 1XZ Great Malvern, United Kingdom*

³*Wyatt Technology Europe GmbH, Hochstraße 12a, D-56307, Dernbach, Germany*

⁴*Department of Immunology, Faculty of Medicine and Dentistry, Palacky University Olomouc, Hnevotínska 3, 775 15 Olomouc, Czech Republic*

Corresponding author:

Ass. prof. RNDr. Jaroslav Turanek, Res. Prof.

Department of Pharmacology and Immunotherapy

Veterinary Research Institute, Hudcova 70, 621 00 Brno, Czech Republic

E-mail: turanek@vri.cz

Phone: +420 533 331 311

Key words: Circovirus; Recombinant antigen; Asymmetrical flow Field-flow fractionation (AF4); Multi-angle dynamic light scattering (MADLS)

1 INTRODUCTION

Porcine circovirus (PCV) is one of the smallest animal viruses belonging to the genus *Circovirus*, family *Circoviridae*, and consists of a circular, single-stranded DNA with 1.7–2 kb in size. PCV virion is a nonenveloped, icosahedral particle of approximately 20 nm in diameter [1,2]. PCV2 is considered an infectious agent that causes several porcine circovirus-associated diseases (PCVAD). The clinical manifestation of PCVAD, post-weaning multi-systemic wasting syndrome (PMWS) [3] is characterized by chronic wasting and severely impaired weight gain in piglets 6 to 11 weeks old. This disease has had a significant economic impact on pork industries worldwide [4]. Vaccination is the most effective strategy to decrease the mortality rate and improve the growth in PCVAD-affected pig populations under field conditions [5]. Commercial PCV2 vaccines can be subdivided into three types, commonly referred to as the inactivated vaccine, chimeric virus vaccine, and a subunit vaccine. The present subunit vaccines (Ingelvac CircoFLEX (Boehringer Ingelheim Vetmedica), Circumvent (Intervet/Merck), and Porcilis PCV (Schering-Plow/Merck) are based on the capsid (Cap) protein of PCV2 produced in a baculovirus expression system (BEVS). For Porcilis PCV, a portion of the Cap protein is reported to be in the form of virus-like particles (VLPs) [6,7].

Despite the existence of commercial vaccines, there is still a strong effort to develop other effective vaccines for animal use that would be cheaper with the same or better efficacy. The significant commercial potential exists for BEVS technology to produce very rapidly large quantities of various proteins including chimeric proteins such as here reported PCV2b Cap protein fused with the C-terminus of the mouse polyomavirus (MPyV) capsid protein VP1, which forms a pentamer chimeric protein VP1-Cap allowing serological differentiation between infected (only Cap-reacting) and vaccinated (both VP1- and Cap-reacting) animals.

Based on the previous work of Fraiberk M. et al. 2017 [8] we produce, purify, and characterize giant chimeric pentamers of the mouse polyomavirus VP1 capsid protein carrying covalently bound porcine circovirus 2 capsid molecules (PCV2b Cap), VP1-Cap.

Purification and complex characterisation of antigens is the crucial step in vaccine development and industrial production. A variety of analytical techniques is used to characterize and purify proteins and protein particles, such as size exclusion chromatography, electrophoresis or ultracentrifugation. With respect to large recombinant antigen complexes like VLP or multimeric protein antigens, these techniques could have limitations including low selectivity, modification or aggregation of the sample during analysis and low sample recovery due to the interaction of the sample with the stationary phases. Relatively new Field-Flow Fractionation (FFF) separation technique is complementary to the above techniques [9]. The instrumentally most developed FFF sub-technique is the Asymmetric Flow Field-Flow fractionation (AF4) [10–12] which is used in a wide range of biological applications including the study of polymers [11,13], colloidal particles [14–16], virus-like particles [17–19], and proteins [17,20,21].

Unlike the above-mentioned techniques, AF4 has no stationary phase/packing material, which minimizes the sample-stationary phase interaction and shear degradation of the sample. AF4 has wide separation range in size from 1 nm up to micrometers and good compatibility with a variety of solvents [9,12]. In addition to separation and characterization, another advantage is the ability to analyse complex samples under conditions close to native ones, including

appropriate buffers of a given ionic strength [22]. Individual eluates of the sample can be collected in narrow fractions for additional “off-line” analysis using additional methods including electron microscopy for morphological analysis and western blotting and SDS-PAGE/western blot for the confirmation of purity and identity of our protein.

In this study, we used AF4 equipped with UV-DAD/MALS/DLS detectors for analysis and complex characterisation of new recombinant pentameric protein as a promising antigen for construction and industrial production of an anti-circovirus vaccine for pig.

2 THEORETICAL BACKGROUND

2.1 Determination of hydrodynamic radius base on the AF4 theory

The Asymmetric Flow Field-Flow Fractionation is the elution technique which is based on a different displacement of the sample in an empty trapezoidal channel. The technique uses two flows: *detector flow*, with a parabolic flow profile along the channel axis and the *cross flow*, perpendicular to the detector flow. Cross flow drives the sample towards the channel “accumulation” wall. The diffusion continuously forces the molecules and particles away from the accumulation wall until the equilibrium between cross flow and diffusion is reached resulting in a different displacement of the molecules and particles according to differences in hydrodynamic radii. The higher the sample's diffusion coefficient is, the greater is a distance from the accumulation wall resulting in higher velocity along the channel axis when the *detector flow* is applied. The samples elute in order of increasing hydrodynamic radius, which is called *normal elution* mode, applied to a size of approximately 1 μm . Separation of the particles with size up to 1 μm is carried in an opposite elution order, and it's called *steric elution* [23]. The retention time t_R of the sample can be approximated as the simplified equation [12]:

$$t_R = \frac{w^2 \pi \eta R_h}{kT} \ln \left(1 + \frac{\dot{V}_c}{\dot{V}} \right) \quad (1)$$

where w is the channel thickness, η is the viscosity of the mobile phase, R_h is the hydrodynamic radius, k is the Boltzmann's constant, T is the thermodynamic temperature, \dot{V} is the channel laminar *detector flow* and \dot{V}_c is the *cross flow*. The simplified equation (1) assuming elution without steric effect. With constant experimental parameters, the hydrodynamic radius can be determinate directly from retention time [12].

2.2 Determination of the radius of gyration

The size of the particles expressed as the *radius of gyration* is determinate using the Multi-Angle Light Scattering (MALS). The angular dependence of the intensity of the scattered light is evaluated using Berry formalism [12]:

$$\sqrt{\frac{Kc}{R_\theta}} = \frac{1}{\sqrt{MP(\theta)}} + A_2 c \sqrt{MP(\theta)} \quad (2)$$

where M is the molecular weight, $P(\theta)$ is the particle scattering function, A_2 is the second virial coefficient, c is the concentration, and K is the light scattering constant. The particle scattering function is approximated for the small angles as:

$$\lim_{\theta \rightarrow 0} P(\theta) = 1 - \frac{16\pi^2 n_0^2}{3\lambda_0^2} \sin\left(\frac{\theta}{2}\right) \langle R_g^2 \rangle \quad (3)$$

where λ_0 is a wavelength of the incident light in a solvent with a refractive index of n_0 . The $\sqrt{Kc/R(\theta)}$ is plotted against $\sin^2(\theta/2)$, the abscissa is constructed, and from the slope, the R_g is determinate [12,16].

2.3 Determination of the hydrodynamic radius

The size of the particles expressed as *hydrodynamic radius/diameter* is determinate using the Dynamic Light Scattering (DLS) technique. Using the Stokes-Einstein equation, the hydrodynamic radius (R_h) is determinate, assuming that the particles are compact spheres [24]:

$$R_h = \frac{kT}{6\pi\eta D} \quad (4)$$

where k is the Boltzmann's constant, T is the thermodynamic temperature, η is the viscosity of the medium, and D is the diffusion coefficient. The hydrodynamic radius is measured by a single angled detector, 173° for batch DLS, and 143° for the flow cell detector [24].

The intensity and number distributions are obtained from multi-angle dynamic light scattering (MADLS) which delivers an angular-independent particle size distribution with the increased resolution by combining scattering information from three angles (173° , 90° , and 13°) [24,25].

2.4 The ratio of the radius of gyration (R_g) and Hydrodynamic radius (R_h)

The R_g and the R_h of the sample can be obtained by MALS and DLS, respectively. The ratio provides information about the conformation of the sample, as shown in **Table 1**. The theoretical lower value of the ratio suggesting solid structures, the value increasing with less dense structures [13].

Table 1 – Table of the R_g/R_h ratio with the corresponding sample conformation.

R_g/R_h	Conformation
< 0.7	A highly expanded macromolecule or swollen microgel structure [13]
0.778	Hard sphere [26]
0.998	Soft sphere [27]
1.0-1.5	Branched molecule [28]
1.5-2.1	Random coil [29]
> 2	Rod like structure [30]

3 EXPERIMENTAL SECTION

3.1 Insertion of sequences of the capsid protein of porcine circovirus 2b (PCV2b) into universal baculovirus transfer vectors

For pentamer VP1-Cap, the entire PCV2b Cap sequence was amplified using PCR primers introducing BamHI sites to the 5' end and a His-tag (6 x His) and KpnI to the 3' end; the sequence was cloned into the pFastBac1-VP1 vector cleaved by BamHI and KpnI. The resulting

transfer vectors were termed pFastBac1-VP1-Cap-His. All transfer vectors were used to prepare recombinant baculoviruses. The molecular weight of the pentameric VP1-Cap-HIS protein is 356 kDa, monomer fusion protein has a molecular weight of 71 kDa, where VP1 has 45 kDa [8].

3.2 *Recombinant baculovirus preparation*

Recombinant baculoviruses were produced according to the manufacturer's instructions (ThermoFisher Scientific, Bac to Bac system). Briefly, *E. coli* DH10Bac containing a bacmid and helper vector were transformed using individual transfer vectors. Recombinant bacmid DNA from positive bacterial colonies was isolated (ThermoFisher Scientific, PureLink™ HiPure Plasmid DNA Miniprep Kit) and verified by PCR. Sf9 insect cells were transfected with bacmid DNA using lipofection (ThermoFisher Scientific, Celfectin II reagent). Recombinant baculoviruses released into the growth media (V_0) were harvested 72 hours after transfection and used for further multiplications by infection of insect cells to generate high-titre viral stocks [8].

3.3 *Generation high-titre viral stock and protein production in insect cells*

Sf9 cells (Gibco) were grown in suspension culture at 27.5 °C in SFM900II medium (Gibco) in New Brunswick temperature-controlled shaker. Baculoviruses were generated from recombinant bacmids according to the guidelines of the Bac-to-Bac protocol. To amplify the virus, $3.5 \cdot 10^7$ cells in 10 ml SFM900II medium supplemented with 1.5% FBS were infected with V_0 at a multiplicity of infection (MOI) = 0.1 in 50 ml TPP® TubeSpin bioreactor under rotation speed 200 rpm. After 4 days, the supernatant (V_1) was collected, and another $3.5 \cdot 10^7$ cells in 10 ml SFM900II medium supplemented with 1.5% FBS were infected with V_1 at MOI=5. Four days after incubation at 27.5 °C and 200 rpm supernatant (V_2) was collected. 2 ml of V_2 at MOI = 5 was used to infect $9 \cdot 10^8$ cells in 300 ml SFM900II medium in 600 ml TPP® TubeSpin bioreactor bottles at 140 rpm for protein production over 48 hours.

3.4 *Nuclear extract (NE) preparation*

Baculovirus-infected cells were harvested by centrifugation at 2000 g for 10 min; the cell pellet was resuspended in 40 ml ice-cold lysis buffer (137 mM NaCl, 10 mM Na₂HPO₄, and 1.8 mM KH₂PO₄) and allowed to swell on ice for 20 min with intermittent mixing. Centrifugation at 4000 g and 4 °C for 10 min was used to separate supernatant (CE1) and nuclei. The pellets with nuclei were washed twice with 10 ml of ice-cold lysis buffer, and the supernatant was collected (CE2, CE3) by centrifugation at 4000 g and 4°C for 10 min. The pellets with nuclei were redissolved in 10 ml of ice-cold NE buffer (20 mM HEPES 7.5 pH, 400 mM NaCl, 2 mM EDTA, and 1 mM DTT) and incubated on ice for 30 min. The supernatant (NE) was collected by centrifugation at 4000 g and 4 °C for 10 min. Nuclear extract was centrifuged at 210,000 x g (rotor SW 41 Ti) for 2 h at 10 °C and pellet were resuspended in PBS and stored at 4 °C for further analysis.

3.5 *SDS protein electrophoresis (SDS-PAGE) and Western blot analysis*

Approximately 100x concentrated (Pierce™ Protein concentrator PES) protein fractions were boiled in Laemmli sample buffer for 5 minutes and resolved in 12.5% SDS-polyacrylamide gel.

Separated proteins were stained with Coomassie blue (Sigma Aldrich). For Western blot analysis, proteins were electro-transferred onto a nitrocellulose membrane (Serva) in blotting buffer (0.3% Tris, 1.44% glycine, 20% methanol) at 15 V for 45 min. The membrane was incubated with 5% skim milk in Tris-buffered saline containing 0.05% Tween-20 (TBS-T) for 1 h, then stained with Anti-6X His tag HRP antibody (ab1187, ABCAM) for 1 h. The membrane was washed (3 x 10 minutes) in TBS-T after each incubation. Membranes were developed using Pierce ECL Western Blotting Substrate reagent (ThermoFisher Scientific) and analysed with Azure Biosystems C300 (Azure Biosystems, Inc.) and cSeries Capture Software.

3.6 *MADLS measurement*

The suspensions were measured using Low-volume quartz batch cuvette, ZEN2112 (Malvern Panalytical Ltd, UK), at the constant temperature of 25 °C, and using temperature ramp in a range from 20 to 80 °C with the step of 5 °C for stability measurements. Multi-Angle Dynamic Light Scattering measurements (MADLS®) were performed with a Zetasizer Ultra instrument (Malvern Panalytical Ltd, UK). The instrument was equipped with a 633 nm HeNe laser and had detection angles at 173°, 90°, and 13° respectively. The size distribution, z-average diameter, polydispersity index (PDI) and particle concentration (particles/ml) were obtained using ZS Xplorer software (Malvern Panalytical Ltd, UK).

3.7 *Transmission electron microscopy*

The suspension after fractionation was covered with a grid coated with Formvar film (Sigma-Aldrich, Czech Republic) and carbon (Agar Scientific, Austria). The grid was removed from the suspension after 1 min, and the residual water was dried with a strip of filtration paper. A drop of 2% aqueous-phospho-tungstic acid was placed onto the grid for a few seconds, and then excess stain was dried with filtration paper. Samples were observed under an electron microscope Philips 208 S Morgagni (FEI, Czech Republic) at 7 500× magnification and an accelerating voltage of 80 kV.

Immunogold labelling: The different suspensions of the pentamers were incubated with native primary antibodies PCV2Cap H9 (Exbio, Prague, Czech Republic), 1 hour at 60 °C and overnight keep at 4 °C. Then incubated for 1 hour at room temperature with gold particles conjugated with protein A (Sigma-Aldrich, GE). The immunogold-labelled pentamers were prepared for negative staining as described previously and observed under a transmission electron microscope.

3.8 *AF4 separation and analysis*

The Eclipse separation system (Eclipse AF4, Wyatt Technology Europe GmbH, Germany) was connected to an isocratic pump, degasser and autosampler with the temperature control unit (Agilent 1260 Infinity II, Agilent Technologies, Germany). The Short separation channel (SC with the channel length of 18 cm) was equipped with a trapezoidal wide polyethylene terephthalate spacer (Wyatt Technology Europe GmbH, Germany) with 350 µm thickness (M350) and regenerated cellulose membrane (cut-off 10 kDa). The actual thickness channel (293 µm) was determinate using channel high correlation base on a calculation using Scout DPS software version 2.0.0.9 (Wyatt Technology Europe GmbH, Germany). The calculation was based on the bovine albumin measurement. The separation system was connected to the UV-

VIS detector (Agilent 1260 Infinity II, Agilent Technologies), MALS detector DAWN HELEOS II, (Wyatt Technology Europe GmbH, Germany) equipped with a GaAs 658 nm laser and using 18 angular positions (between 15° and 160°) with DLS detector at angle 149°. Filtered (0.1 μm) and preserved (0.04% ProClin™ 300, Sigma-Aldrich) Tris buffer (Tris 50 mM and NaCl 150 mM) pH 7.4 was used as the carrier liquid. The separation was carried at a constant temperature of 25 °C (Thermos^[PRO] Wyatt Technology Europe GmbH, Germany). The sample was separated according to the following conditions. The *detector flow* was constant 1.0 ml/min, 50 μl of the sample was injected into the channel with 1.5 ml/min *cross flow* over 3 min in the *focus inject* mode (*inject flow* 0.2 ml/min) and further focused over 5 min with the same *cross flow*. The elution profile was divided into three different categories: *Constant* (**Fig. 1A**) *cross flow* of 0.1, 0.25, and 0.5 ml/min over 60 min. *Linear decreasing* (**Fig. 1B**) from the initial *cross flow* of 2.0 ml/min decreasing to 0.0 ml/min over 40, 60, and 80 minutes. *Exponential* (**Fig. 1C**) decreasing from the initial *cross flow* of 2.0 ml/min to 0.0 ml/min over 60 min with the different slope of 10, 20, and 30. Based on these experiments, the *Combined* (**Fig. 1D**) profile was created. Starting *cross flow* 2 ml/min with an exponential decrease to 0.25 ml/min over 20 minutes with the slope of 10, followed by the constant *cross flow* of 0.25 ml/min over 30 minutes. All elution profiles were extended by 10 minutes of elution and elution inject profile with *cross flow* 0.0 ml/min as a rinsing step.

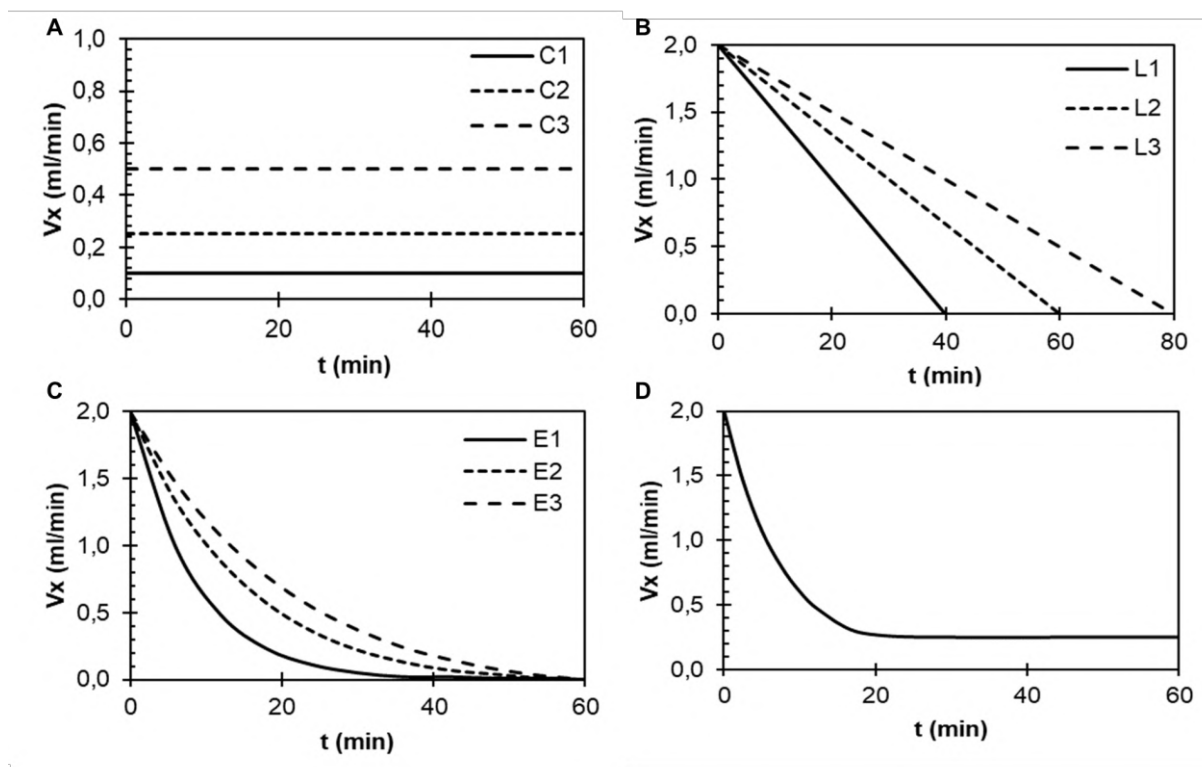


Fig. 1 – Plots of different cross flow profiles: (A) a constant cross flow profiles; (B) a decreasing linear profile; (C) exponential decreasing profiles with different slope $\tau_{1/2}$ 10, 20, and 30 for E1, E2, and E3 respectively; (D) a final cross flow profile.

The measurement was evaluated by the Astra software version 7.1.4.8 (Wyatt Technology Europe GmbH, Germany). The MALS detector (Wyatt Technology Europe GmbH, Germany) was calibrated with the HPLC grade toluene and normalized using isotropic scattered standard

1 mg/ml BSA in Tris buffer. The UV detector (Agilent 1260 Infinity II, Agilent Technologies) was set up at a wavelength of 280 nm and was used as a concentration source with the UV extinction coefficient of 0.6670 ml/(mg·cm).

3.9 Chemicals

All other chemicals, unless otherwise specified, were purchased from Sigma (St. Louis, MO). Ultrapure water was obtained from the Milli-Q® Reference Water Purification System (Merck KGaA, Darmstadt, GE).

4 RESULTS AND DISCUSSION

4.9 AF4 separation of pentameric protein particles using different cross flow profiles

Pentameric protein particles were separated using different, constant cross flow profile, according to **Fig. 1A**. Parameters for FFF separation were selected with respect to keeping the protein in its native state. DLS analysis demonstrates no thermally induced aggregation up to 50°C (see Fig. S1 in supporting information). **Fig. 2** shows three chromatograms, the full line represents the Rayleigh ratio at the angle of 90°, and the dashed line shows the UV absorbance signal for the wavelength of 280 nm. On the minor axis, the hydrodynamic radius based on the online DLS measurement is plotted (**Fig. 2A**), theoretical hydrodynamic radius based on full retention equation (1) is showed on (**Fig. 2B**), and (**Fig. 2C**) shows the radius of gyration. In general, the elution starts at 10th minute of the chromatogram (after the injection and focusing step) and is marked as a void peak. In the void peak, we can observe elution of species with strong UV absorbance and small light scattering signal, and this are protein impurities with small molar masses. The resolution between UV peak and peak of the light scattering signal from pentameric particles is increasing with higher cross flow. For the cross flow, 0.1 ml/min pentameric particles are co-eluting with protein impurities, which elute between 10 and 12 minutes. Hydrodynamic radius (**Fig. 2A**) starting at 35 nm and grows linearly to 80 nm (17th minute of elution). Then the hydrodynamic radius became scattered due to the presence of the aggregates and low intensity of the scattered light. The theoretical hydrodynamic radius (**Fig. 2B**) starts at 28 nm and rising to the 100 nm at the same elution time, which is in a relatively good correlation of the measured hydrodynamic values. The good correlation of the theoretical and measured hydrodynamic radius values indicated that the sample is eluting according to the FFF separation mechanism and that there are no interactions between the sample and membrane. The presence of the aggregates in the main peak is confirmed with the radius of gyration (**Fig. 2C**), which rapidly increases in the middle of the main peak from the gyration radius 50 nm to 300 nm. In the case of the constant cross flow 0.25 ml/min, the resolution between the main peak and void/protein peak (eluting between 10 and 12 minutes) is better compared to the cross flow 0.1 ml/min. The hydrodynamic radius from DLS (**Fig. 2A**) is relatively narrow, from 28 nm to 90 nm in the 30th minute of the elution, which is followed by a scattered signal from a larger component, aggregates. The presence of the aggregates is shown by the radius of gyration (**Fig. 2C**), growing linearly from 40 nm to 110 nm with a sharp rise up to 175 nm in the 30th minute of elution. The theoretical hydrodynamic radius (**Fig. 2B**), ranging from 20 nm to 130 nm. The deviation of the measured hydrodynamic radius from the calculated radius, especially at later elution times, maybe due to the beginning of the sample-membrane interaction. As the cross flow increases, the theoretical hydrodynamic data deviate from the measured radius to a greater extent. Higher cross flow can promote higher sample and membrane interaction; the sample remains in closer distance from the accumulation wall for a longer time, which is responsible for the undesirable interaction which may be a cause of the delayed elution compared to AF4 theory. The interaction is particularly evident in the case of the constants cross flow of 0.5 ml/min (C3). The hydrodynamic radius from DLS varies from 30 nm to 65 nm with the main peak eluting from time 18 minutes to approximately 40 minutes. The theoretical hydrodynamic radius goes from 25 nm up to 110 nm for the same elution time.

A relatively high portion of the sample is eluting, during the flush phase of the elution. At 70th minute of elution, the cross flow reaches a 0.0 ml/min, elution peak is marked as a released peak.

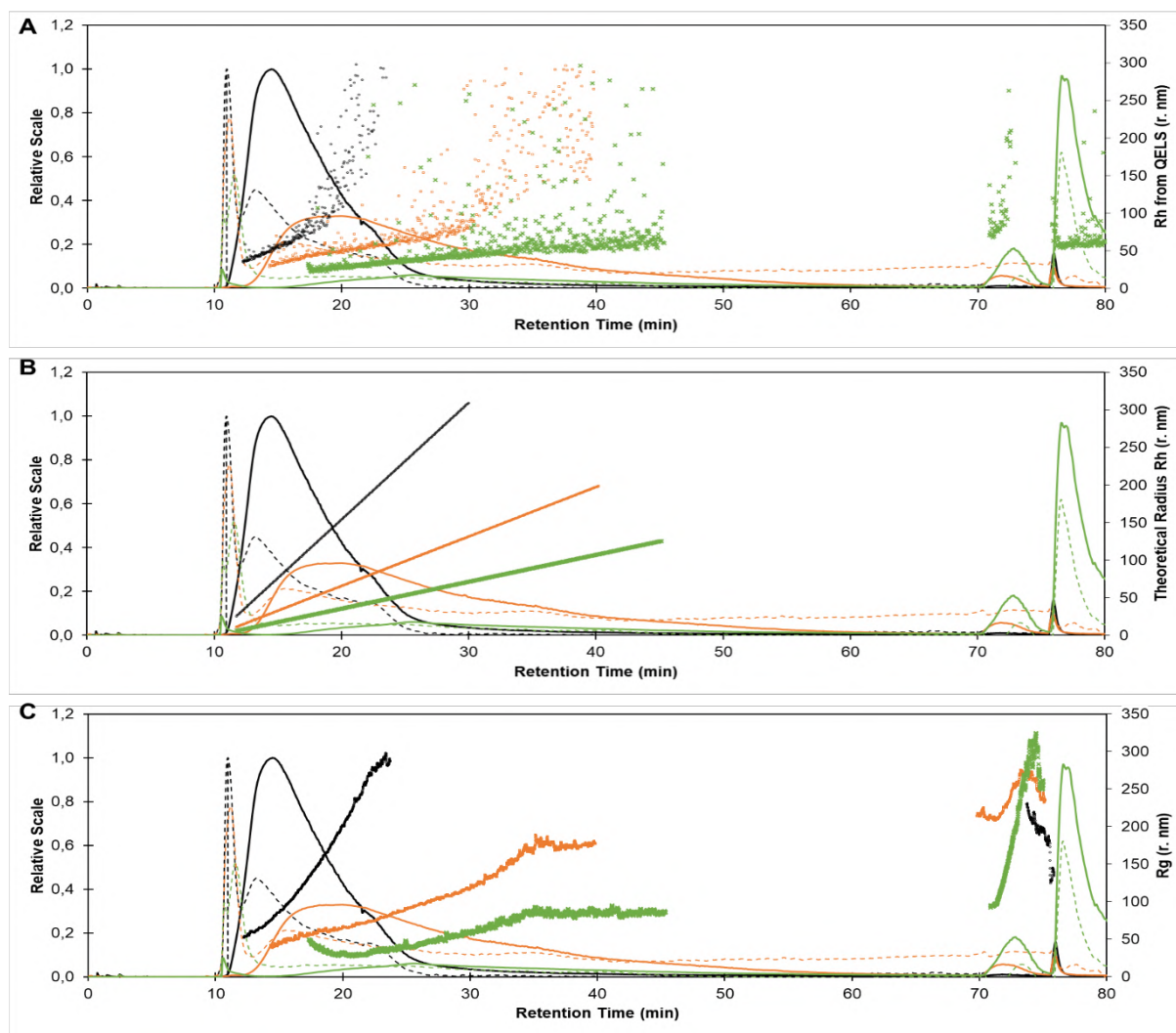


Fig. 2 – Chromatograms of different **constant** cross flow profiles: $C1 = 0.1$ ml/min Black (—), $C2 = 0.25$ Orange (—), and $C3 = 0.5$ Green (—). Left axis, the relative scale shows normalized data where the full line represents Rayleigh ratio, dashed line represents UV absorbance 280 nm, dots represent different radiuses on the right axis: (A) hydrodynamic radius based on online DLS measurement. (B) hydrodynamic radius based on the retention equation calculation. (C) The radius of gyration based on the MALS measurement.

The **Fig. 3** shows three different linear cross flow profiles starting at 2.0 ml/min and decreasing to 0.0 ml/min over 40, 60, and 80 minutes for L1 (black line), L2 (orange line), and L3 (green line) respectively. For all profiles, we can observe high resolution between the void peak (10th minute of the elution time) and the light scattering peak of the pentameric particles (40th to 90th minute of the elution time). In general, hydrodynamic radius (**Fig. 3A**) is scattered and is in range of 43~93 nm for L1, 33~99 nm for L2, and 38~99 nm for profile L3 in the elution time of 43~51, 49~70, and 61~88 minutes respectively. A larger portion of particles is released when the cross flow goes to 0.0 ml/min. The theoretical hydrodynamic radius (**Fig. 3B**) in the

same elution range is 75~255 nm for L1, 71~270 nm, and 92~285 nm for L3. With the decreasing slope of the cross flow, the main peak becomes wider. The theoretical R_h value indicates a higher sample-membrane interaction characterized by longer elution time of smaller particles. The **Fig. 3C** shows the radius of gyration, with narrow size distribution in the range from 50 nm to 100 nm and rapidly sharpening up to 250 nm for 0.0 ml/min of the cross flow. The sharp increase in the radius of gyration is the result of co-eluting aggregates. After the release peak, we observe a strong UV signal from protein impurities which are retaining in the channel due to the high cross flow of 2.0 ml/min at the beginning of the elution. The UV signal is negligible in the range of the elution of the main particles due to the low concentration of the sample in the elution peak. The release peak is relatively high compare to the chromatograms with other elution profiles.

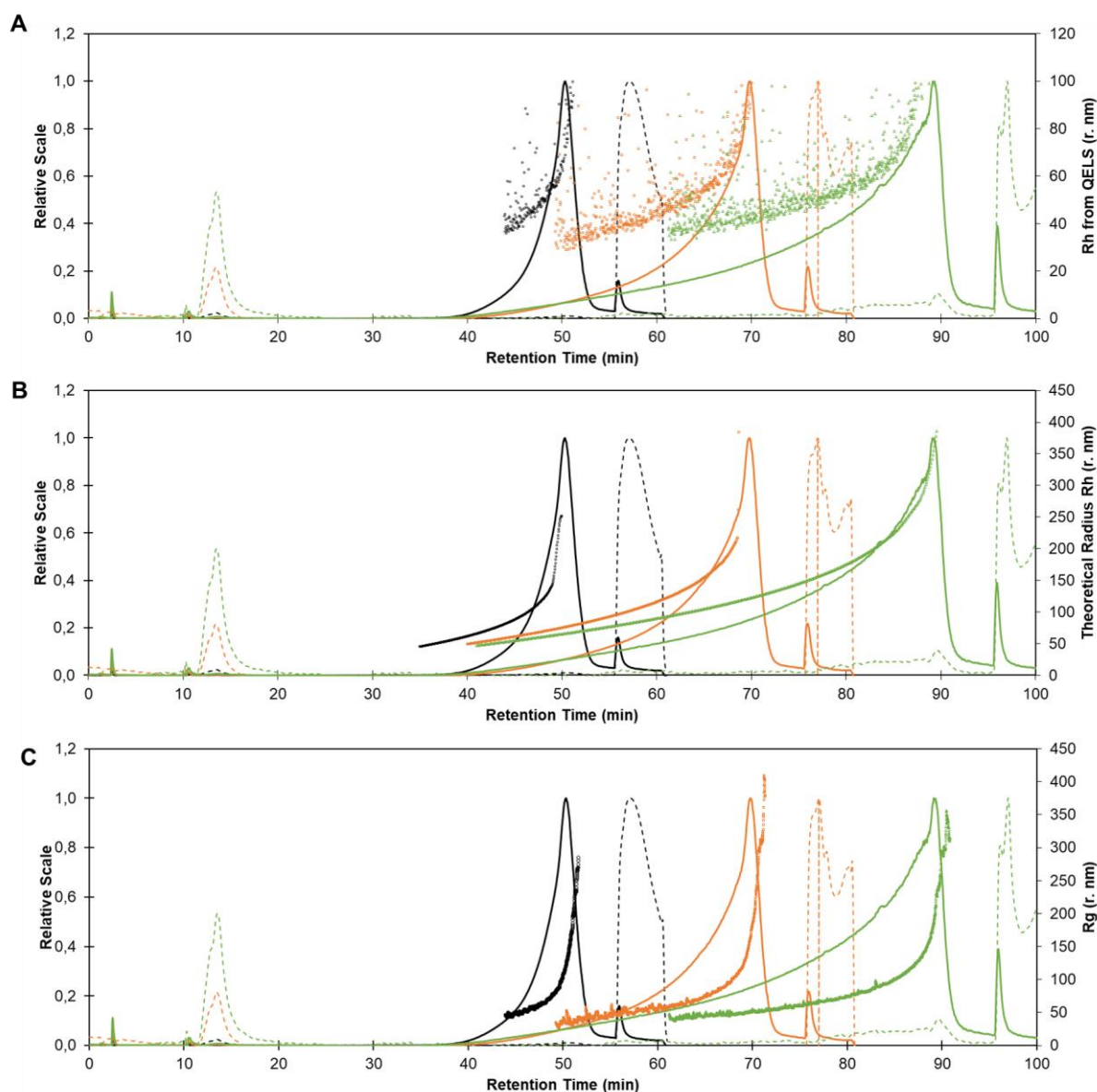


Fig. 3 – Chromatograms of different *linear* cross flow profiles: L1 Black (—), L2 Orange (—), and L3 Green (—). Left axis, the relative scale shows normalized data where the full line represents Rayleigh ratio, dashed line represents UV absorbance 280 nm, dots represent different radii on the right axis: (A) hydrodynamic radius based on online DLS

measurement. (B) hydrodynamic radius based on the retention equation calculation. (C) the radius of gyration based on the MALS measurement.

The **Fig. 4** below shows the same AF4 chromatograms with different exponential decreasing cross flow profiles starting at 2.0 ml/min and decreasing to 0.0 ml/min over the 60 minutes with a different slope of 10, 20, and 30 for E1 (black line), E2 (orange line), and E3 (green line) respectively. Exponential elution profiles having narrow hydrodynamic radius distribution (**Fig. 4A**) at the range of 33~70 nm (25~35 min) for E1, 28~85 nm (28~49 min) for E2, and 42~95 nm (29~55 min) for E3. Theoretical hydrodynamic radius (**Fig. 4B**) for the same elution range is 40~130 nm, 38~200 nm, and 35~210 nm with respect to individual elution profiles. The early eluting species of the pentameric protein particles of certain sizes are in good correlation with theoretical hydrodynamic radius. During later elution time the LS data becomes scattered because of co-eluting aggregates. For slope 20 and 30, the hydrodynamic radius distribution is narrower. The effect of the higher cross flow over a longer period of time increases the interaction of the sample and the membrane, resulting in longer sample retention in the channel and prolong elution. The radius of gyration (**Fig. 4C**) shows us the presence of large aggregates at the end of the light scattering peak. Narrow range from 40 nm to 100 nm is followed by a rapid increase up to 300 nm. No significant light scattering signal was observed for the released peak (75th minute of the elution).

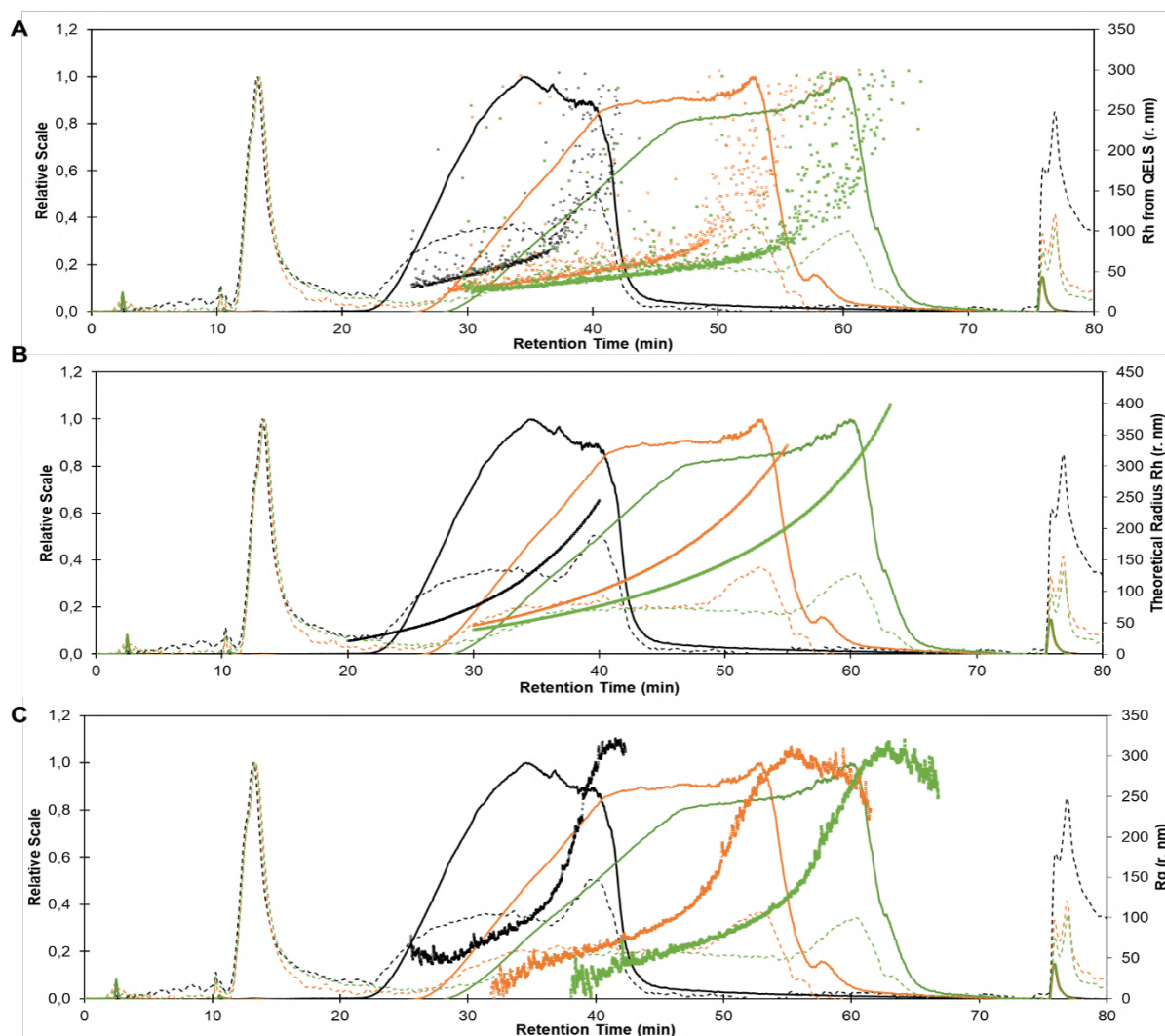


Fig. 4 – Chromatograms of different *exponential* cross flow profiles: E1 Black (—), E2 Orange (—), and E3 Green (—). Left axis, the relative scale shows normalized data where the full line represents Rayleigh ratio, dashed line represents UV absorbance 280 nm, dots represent different radiuses on the right axis: (A) hydrodynamic radius based on online DLS measurement. (B) hydrodynamic radius based on the retention equation calculation. (C) the radius of gyration based on the MALS measurement.

Base on the previous experiments with the different elution profiles (**Fig. 2**, **Fig. 3**, and **Fig. 4**), a combination of exponential decrease starting the 2 ml/min to 0.25 ml/min over 20 minutes with the slope of 10 followed by a constant cross flow of 0.25 ml/min over 30 minutes is showed in **Fig. 5**. The protein impurities not related to recombinant pentameric VP1-Cap elute within the first 10 minutes of elution. Strong UV peak is followed by elution of particles with hydrodynamic radius starting at 15 nm (**Fig. 5A**) ranging up to 100 nm. The theoretical hydrodynamic radius (**Fig. 5B**) is ranging from 20 nm up to 150 nm within the interval of the main peak (20-40 min of the elution). From the approximately 40th minute, the large aggregates with the radius ranging from 125 to approximately 300 nm start to elute. Light scattering data in this area are scattered due to the low concentration of aggregates. By measuring the radius of gyration (**Fig. 5C**), we can distinguish individual units of the pentameric particles. Pentameric particles start to be eluted in approximately 20th minute of the run, the starting R_g is

relatively constant and fluctuated around 25 ± 2 nm. Around 25th minutes, we can observe a sudden R_g increase with elution of super-unit pentameric structures with R_g ranging from 30 to 80 nm. Aggregates eluted at 40th-minute range from 110 nm to 180 nm. The **Fig. 5D** shows conformation plot with R_g to R_h ratio. For individual pentameric units, the ratio is in a range of 0.8 to approximately 1. The range value is convenient for the soft sphere conformation [27]. The R_g/R_h ratio gradually increases with the elution of the super-unit pentameric structures up to the value of 1.3, which corresponds to the branched structure [28] of randomly associated pentamers. The obtained values and structures are with a good agreement with structures obtained by transmission electron microscopy (Chyba! Nenalezen zdroj odkazů.**B, C, D**) where the individual pentameric particles have the longest axis of about 12 nm. The R_g/R_h ratio drops sharply after about 40 min of elution. The drop is due to a sudden increase in the value of the hydrodynamic radius. The ratio does not reflect the overall character of the sample but only reflects the scattered DLS signal of low concentrated aggregates.

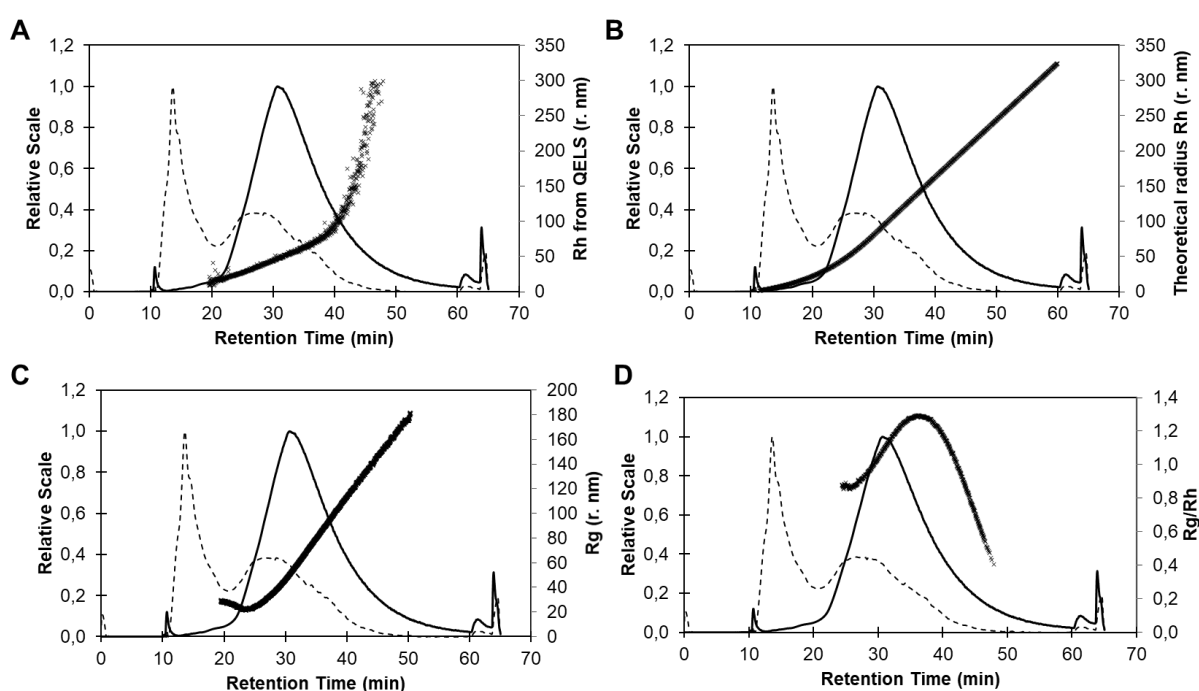


Fig. 5 – Chromatogram of final elution profile: Left axis, the relative scale shows normalized data where the full line represents Rayleigh ratio; dashed line represents UV absorbance at 280 nm, dots represent different radii on the right axis: (A) hydrodynamic radius based on online DLS measurement. (B) hydrodynamic radius based on the retention equation calculation. (C) the radius of gyration based on the MALS measurement. (D) the radius of gyration and hydrodynamic radius ratio based on the MALS/DLS measurement.

The theoretical values of R_h correspond to the measured values, especially for small, individual pentameric particles. As the size of the eluting particles increases, the measured and calculated values deviate. The deviation is smaller in the combined elution profile compared to the individual elution profiles. The cause of this deviation may be in the structure of individual self-associates of pentamers. The offline DLS analysis of the primary sample demonstrated the presence of individual pentamers as well as the existence of self-associates, and larger aggregates (**Fig. 6E and F**). According to the R_g/R_h ratio measurement (value > 1.3) and TEM

analysis (**Fig. 6C and D**), the self-associates of pentameric structures have a branched structure [28]. However, the calculated hydrodynamic radius is approximation on spherical particles, and only the individual pentameric protein particles meet the definition of a spherical particle (the spherical particles appear on EM analysis and R_g/R_h with a value of 0.8 corresponds to a soft sphere [27]). By comparing the DLS measurement of the primary sample with the individual fractions (**Table 2**), we could state that during AF4 separation, no further agglomerates are formed.

4.1 Batch analysis

Different fractions were collected based on the fractogram shown below (**Fig. 6A**) and subjugated further offline analysis. The **Fig. 6E** shows intensity and **Fig. 6F** number distribution of the MADLS measurement. Black, the full line represents a sample before fractionation (primary sample). The intensity distribution consists of three peaks with the first having maximum at 38 nm corresponding with the size of the single pentameric unit, a second peak with a maximum at 150 nm corresponding to the super-unit pentameric structures, and the third peak corresponding to larger aggregates with a diameter of approximately 400 nm. The light scattering signal from the first fraction was not sufficient for batch DLS analysis; the results are not listed. Fraction 2 (F2) shows a maximum at 37 nm, which corresponds to the first peak of the primary sample. With increasing elution time, the diameter is increased to 65 nm and 105 nm for F3 and F4 respectively. The Number distribution of the primary sample (**Fig. 6B**) shows that the majority of the particles have a diameter of about 38 nm. This corresponds to the concentration measurement listed in **Table 2** where the concentration increases with individual peaks of $2.97 \cdot 10^{13}$; $1.87 \cdot 10^{11}$, and $6.34 \cdot 10^{09}$ particles/ml for the first, second, and third population respectively. A similar trend is observed in individual fractions with respect to the AF4 dilution. Fraction F2 consists mainly of small individual pentameric protein units with z-average 38 nm and a concentration of $4.25 \cdot 10^{19}$ particles/ml. Fraction F3 with larger population (z-average of 64 nm) contains $2.00 \cdot 10^{10}$ particles/ml, and F4 (z-average 97 nm) with concentration of $3.59 \cdot 10^9$ particles/ml. The polydispersity index (PDI) in the primary sample is 0.265, indicating low polydispersity; however, the value is affected by the presence of three populations, which, like z-average value, in a sample with multiple populations, do not fully reflect the nature of the analyte. The polydispersity in the individual fraction is 0.301 for F2, 0.159 for F3, and 0.192 for F4. Low polydispersity values indicate that no larger particles co-elute within the individual fractions, especially in the fraction F3 and F4.

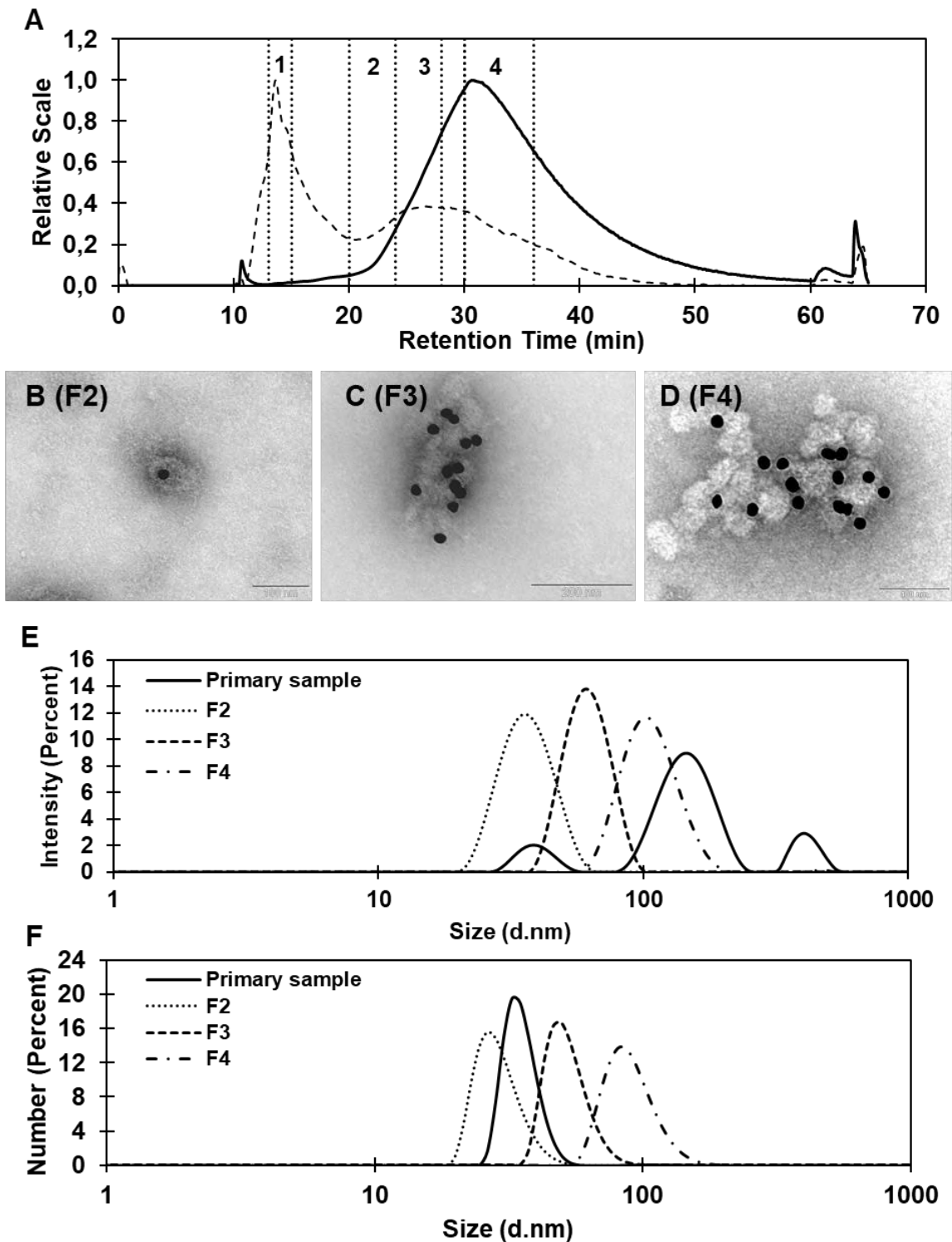


Fig. 6 – A) Fractogram with different marked fractions, the full line represents Rayleigh ratio; dashed line represents UV absorbance at 280 nm; B-D) EM image of the purified pentameric protein in different fractions after gold labelling. MADLS distribution of the intensity (E) and number (F). The Primary sample is a sample before purification, F2-F4 are individual fraction based on the fractogram.

Table 2 – Summary table of MADLS measurement.

	Concentration (particles/ml)			z-average (d. nm)	PDI
	Peak One	Peak Two	Peak Three		
Primary sample	$2.97 \pm 0.92 \cdot 10^{13}$	$1.87 \pm 0.43 \cdot 10^{11}$	$6.34 \pm 0.88 \cdot 10^{09}$	127±1	0.265±0.006
F2		$4.25 \pm 1.92 \cdot 10^{11}$		38±2	0.301±0.051
F3		$2.00 \pm 0.13 \cdot 10^{10}$		64±2	0.159±0.009
F4		$3.53 \pm 0.02 \cdot 10^{09}$		97±3	0.192±0.048

Analysis of individual TEM fractions shows both the structure of the individual pentamers corresponding to the R_g/R_h values and the preserved native nature of the protein pentameric particles. Gold nanoparticles with H9 antibody selectively bind to the pentameric Cap protein only in the native state in fractions F2, F3, and F4 (**Fig. 6B, C, and D** respectively). SDS-PAGE and WB analysis were performed on the concentrated fractions shown in the **Fig.7**. By selective staining for His-tag group by Anti-6X His, the purity of the individual fractions was demonstrated. In fraction F1, the band at 70 kDa (band corresponding to denatured pentameric protein particles) is not visible. Conversely, low molecular weight proteins are present, whose early elution time at given cross flow corresponds to the AF4 theory. The visible band is especially present in fractions F3 and F4. Fraction F2 containing the largest number of particles (**Table 2**) does not show such a proportion of individual His-Tag groups. This may be due to the structure of larger clusters of pentameric protein particles where the size expressed as z-average (**Table 2**) in F3 is about twice the fraction of F2 (z-average of F3 is 64 nm, and F2 is 38 nm). However, the volume of the particles, whose size will vary twice, will be eight times greater. Thus, larger particles, particles in fraction F3 and F4 have a much greater His Tag group density than the fraction F2 as seen in **Fig. 7A and B**. The **Fig. 7B** also shows pentameric doublet in fractions F3 and F4, a band of about 140 kDa, resulting from the conjugation of individual proteins during denaturation.

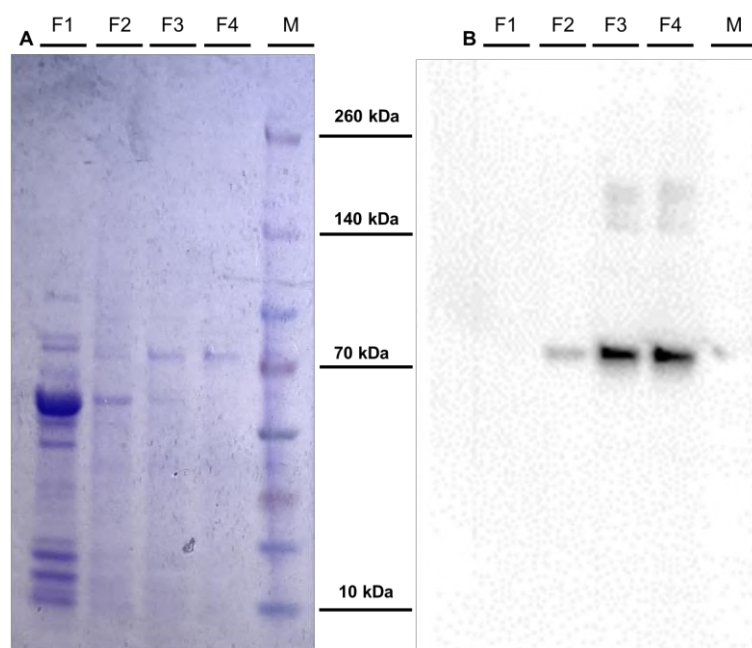


Fig. 7 – A) the sodium dodecyl sulphate–polyacrylamide gel electrophoresis (SDS-PAGE) stained with Coomassie blue; B) Western blot (WB) analysis of individual fractions.

5 CONCLUSIONS

Asymmetric Flow Field-Flow Fractionation system with UV, MALS and online DLS detection were used for separation and characterization of pentameric protein particles and their aggregates. Different elution profiles were tested to determine the optimal separation conditions. The exponential decrease in combination with constant cross flow profile was found to be most suitable for optimal separation because of reducing overall separation time while maintaining separation efficiency. Individual fractions were further subjected to offline DLS, TEM, and SDS-PAGE analysis. The overall purity and quality of the individual fractions were assessed by SDS-PAGE/western blot analysis. The measured particle size, expressed as the hydrodynamic radius, corresponds to the theoretical values, in particular for the elution of individual protein pentamers. The data suggests that the deviation is due to the structure of larger pentameric multicomplexes and minimal sample and membrane interactions. The values of R_g/R_h ratios corresponded to the structures visualised by offline TEM analysis in each fraction. By comparison, the offline DLS measurement of the primary sample and the fractions, we showed that no additional aggregates are generated due to AF4 separation. The immunogold labelling of individual fraction together with SDS-PAGE/western blot analysis showed preservation of the native structure of the pentameric antigen. Thus, AF4 working at native conditions proved themselves to be a technique suitable for the separation and analysis of the large recombinant protein complex composed of a carrier that forms the pentamer of a mouse polyomavirus VP1 capsid protein to which the porcine circovirus 2 capsid protein molecules are covalently attached. Therefore, the FFF method is also applicable as a part of rapid quality control analyses during biotechnological production of vaccines based on large recombinant antigens.

6 CONFLICTS OF INTEREST

There are no conflicts to declare.

7 ACKNOWLEDGEMENTS

This work was supported by the Ministry of Education, Youth and Sports OPVVV PO1 project “FIT” (Pharmacology, Immunotherapy, nanoToxicology) CZ.02.1.01/0.0/0.0/15_003/0000495 (JT, MR) and CEREBIT (Centre for Recombinant Biotechnology and Immunotherapy) CZ.02.1.01/0.0/0.0/16_025/0007397 (MR, JT); the Ministry of Agriculture of the Czech Republic, institutional support MZE-RO0518 (JT). Access to instruments in the laboratory NanoPharm (join project of Veterinary Research Institute, and International Clinical Research Center (FNUSA-ICRC) (JT) is acknowledged, as well as support by Education and Research Centre VRI-Malvern (JT, SM) and Education and Research Centre VRI-Wyatt (JT, DR).

8 REFERENCES

- [1] J. Gillespie, T. Opriessnig, X.J. Meng, K. Pelzer, V. Buechner-Maxwell, Porcine circovirus type 2 and porcine circovirus-associated disease, *J. Vet. Intern. Med.* 23 (2009) 1151–1163. <https://doi.org/10.1111/j.1939-1676.2009.0389.x>.
- [2] I. Tischer, H. Gelderblom, W. Vettermann, M.A. Koch, A very small porcine virus with circular single-stranded DNA, *Nature.* 295 (1982) 64–66. <https://doi.org/10.1038/295064a0>.
- [3] B.M. Meehan, F. McNeilly, D. Todd, S. Kennedy, V.A. Jewhurst, J.A. Ellis, L.E. Hassard, E.G. Clark, D.M. Haines, G.M. Allan, Characterization of novel circovirus DNAs associated with wasting syndromes in pigs, *J. Gen. Virol.* 79 (1998) 2171–2179. <https://doi.org/10.1099/0022-1317-79-9-2171>.
- [4] J. Segalés, G.M. Allan, M. Domingo, Porcine circovirus diseases, *Anim. Heal. Res. Rev.* 6 (2005) 119–142. <https://doi.org/10.1079/ahr2005106>.
- [5] V. Fachinger, R. Bischoff, S. Ben Jedidia, A. Saalmüller, K. Elbers, The effect of vaccination against porcine circovirus type 2 in pigs suffering from porcine respiratory disease complex, *Vaccine.* 26 (2008) 1488–1499. <https://doi.org/10.1016/j.vaccine.2007.11.053>.
- [6] N.M. Beach, X.-J. Meng, Efficacy and future prospects of commercially available and experimental vaccines against porcine circovirus type 2 (PCV2), *Virus Res.* 164 (2012) 33–42. <https://doi.org/10.1016/j.virusres.2011.09.041>.
- [7] X.J. Meng, *Circoviridae*, in: *Fields Virol. Sixth Ed.*, Wolters Kluwer Health Adis (ESP), 2013. <https://doi.org/10.1016/b978-012511340-3/50022-2>.
- [8] M. Fraiberk, M. Hájková, M. Krulová, M. Kojzarová, A. Drda Morávková, I. Pšikal, J. Forstová, Exploitation of stable nanostructures based on the mouse polyomavirus for development of a recombinant vaccine against porcine circovirus 2, *PLoS One.* 12 (2017) e0184870. <https://doi.org/10.1371/journal.pone.0184870>.
- [9] J.C. Giddings, A New Separation Concept Based on a Coupling of Concentration and Flow Nonuniformities, *Sep. Sci.* 1 (1966) 123–125. <https://doi.org/10.1080/01496396608049439>.

- [10] S. Podzimek, J. Machotova, J. Snuparek, M. Vecera, L. Prokupek, Characterization of molecular structure of acrylic copolymers prepared via emulsion polymerization using A4F-MALS technique, *J. Appl. Polym. Sci.* 131 (2014). <https://doi.org/10.1002/app.40995>.
- [11] S. Podzimek, J. Machotova, H. Zgoni, P. Bohacik, J. Snuparek, Application of A4F-MALS for the Characterization of Polymers Prepared by Emulsion Polymerization: Comparison of the Molecular Structure of Styrene-Acrylate and Methyl Methacrylate-Acrylate Copolymers, *Polym. - Plast. Technol. Eng.* 55 (2016) 1365–1372. <https://doi.org/10.1080/03602559.2016.1146957>.
- [12] S. Podzimek, Stepan Podzimek: Light scattering, size exclusion chromatography and asymmetric flow field flow fractionation. Powerful tools for the characterization of polymers, proteins and nanoparticles, *Anal. Bioanal. Chem.* 402 (2012) 1857–1858. <https://doi.org/10.1007/s00216-011-5607-x>.
- [13] P. Guo, Y. Li, J. An, S. Shen, H. Dou, Study on structure-function of starch by asymmetrical flow field-flow fractionation coupled with multiple detectors: A review, *Carbohydr. Polym.* 226 (2019). <https://doi.org/10.1016/j.carbpol.2019.115330>.
- [14] H. Zhang, D. Lyden, Asymmetric-flow field-flow fractionation technology for exomere and small extracellular vesicle separation and characterization, *Nat. Protoc.* 14 (2019) 1027–1053. <https://doi.org/10.1038/s41596-019-0126-x>.
- [15] S. Hupfeld, D. Ausbacher, M. Brandl, Asymmetric flow field-flow fractionation of liposomes: Optimization of fractionation variables, *J. Sep. Sci.* 32 (2009) 1465–1470. <https://doi.org/10.1002/jssc.200800626>.
- [16] S. Hupfeld, H.H. Moen, D. Ausbacher, H. Haas, M. Brandl, Liposome fractionation and size analysis by asymmetrical flow field-flow fractionation/multi-angle light scattering: influence of ionic strength and osmotic pressure of the carrier liquid, *Chem. Phys. Lipids.* 163 (2010) 141–147. <https://doi.org/10.1016/j.chemphyslip.2009.10.009>.
- [17] X. Zhang, Y. Li, S. Shen, S. Lee, H. Dou, Field-flow fractionation: A gentle separation and characterization technique in biomedicine, *TrAC - Trends Anal. Chem.* 108 (2018) 231–238. <https://doi.org/10.1016/j.trac.2018.09.005>.
- [18] R.N. Qureshi, W.T. Kok, Application of flow field-flow fractionation for the characterization of macromolecules of biological interest: A review, *Anal. Bioanal. Chem.* 399 (2011) 1401–1411. <https://doi.org/10.1007/s00216-010-4278-3>.
- [19] T. Bousse, D.A. Shore, C.S. Goldsmith, M.J. Hossain, Y. Jang, C.T. Davis, R.O. Donis, J. Stevens, Quantitation of influenza virus using field flow fractionation and multi-angle light scattering for quantifying influenza A particles, *J. Virol. Methods.* 193 (2013) 589–596. <https://doi.org/10.1016/j.jviromet.2013.07.026>.
- [20] W. Fraunhofer, G. Winter, The use of asymmetrical flow field-flow fractionation in pharmaceuticals and biopharmaceuticals, *Eur. J. Pharm. Biopharm.* 58 (2004) 369–383. <https://doi.org/10.1016/j.ejpb.2004.03.034>.
- [21] M. Lampi, H.M. Oksanen, F. Meier, E. Moldenhauer, M.M. Poranen, D.H. Bamford, K. Eskelin, Asymmetrical flow field-flow fractionation in purification of an enveloped bacteriophage $\phi 6$, *J. Chromatogr. B Anal. Technol. Biomed. Life Sci.* 1095 (2018) 251–257. <https://doi.org/10.1016/j.jchromb.2018.07.008>.
- [22] H. Dou, Y. Li, J. Choi, S. Huo, L. Ding, S. Shen, S. Lee, Asymmetrical flow field-flow fractionation coupled with multiple detections: A complementary approach in the characterization of egg yolk plasma, *J. Chromatogr. A.* 1465 (2016) 165–174. <https://doi.org/10.1016/j.chroma.2016.08.062>.

- [23] M.H. Moon, Flow field-flow fractionation: Recent applications for lipidomic and proteomic analysis, *TrAC - Trends Anal. Chem.* 118 (2019) 19–28. <https://doi.org/10.1016/j.trac.2019.05.024>.
- [24] P.C. Hiemenz, R. Rajagopalan, *Principles of Colloid and Surface Chemistry*, CRC Press, Taylor & Francis Group, 6000 Broken Sound Parkway NW, Suite 300, Boca Raton, FL 33487-2742, 1997. <https://doi.org/10.1201/9781315274287>.
- [25] P.G. Cummins, E.J. Staples, Particle size distributions determined by a "multiangle" analysis of photon correlation spectroscopy data, *Langmuir*. 3 (1987) 1109–1113. <https://doi.org/10.1021/la00078a040>.
- [26] A.K. Brewer, A.M. Striegel, Characterizing the size, shape, and compactness of a polydisperse prolate ellipsoidal particle via quadruple-detector hydrodynamic chromatography, *Analyst*. 136 (2011) 515–519. <https://doi.org/10.1039/c0an00738b>.
- [27] A.K. Brewer, A.M. Striegel, Particle size characterization by quadruple-detector hydrodynamic chromatography, *Anal. Bioanal. Chem.* 393 (2009) 295–302. <https://doi.org/10.1007/s00216-008-2319-y>.
- [28] C. Zielke, A. Stradner, L. Nilsson, Characterization of cereal β -glucan extracts: Conformation and structural aspects, *Food Hydrocoll.* 79 (2018) 218–227. <https://doi.org/10.1016/j.foodhyd.2017.12.036>.
- [29] J.R. Runyon, M. Ulmius, L. Nilsson, A perspective on the characterization of colloids and macromolecules using asymmetrical flow field-flow fractionation, *Colloids Surfaces A Physicochem. Eng. Asp.* 442 (2014) 25–33. <https://doi.org/10.1016/j.colsurfa.2013.04.010>.
- [30] T. Coviello, K. Kajiwara, W. Burchard, M. Dentini, V. Crescenzi, Solution properties of xanthan. 1. Dynamic and static light scattering from native and modified xanthans in dilute solutions, *Macromolecules*. 19 (1986) 2826–2831. <https://doi.org/10.1021/ma00165a027>.